University of Dublin

Trinity College

Doctoral Thesis

Characterization, Simulation and Optimization of Surface Etched Slotted Tunable Laser Diodes

---

Author:
Michael Wallace

Supervisor:
Prof. John Donegan

A thesis submitted in fulfilment of the requirements for the degree of Doctor of Philosophy

in the

Photonics Group

School of Physics

October 23, 2018

Declaration of Authorship

I, Michael Wallace, declare that this thesis titled, "Characterization, Simulation and Optimization of Surface Etched Slotted Tunable Laser Diodes" and the work presented in it are my own. I confirm that:

- This thesis has not been submitted as an exercise for a degree at this or any other university and it is entirely my own work.
- I agree to deposit this thesis in the University's open access institutional repository or allow the library to do so on my behalf, subject to Irish Copyright Legislation and Trinity College Library conditions of use and acknowledgement.
- Where I have consulted the published work of others, this is always clearly attributed.
- Where I have quoted from the work of others, the source is always given. With the exception of such quotations, this thesis is entirely my own work.
- I have acknowledged all main sources of help.
- Where the thesis is based on work done by myself jointly with others, I have made clear exactly what was done by others and what I have contributed myself.

Signed:

_____

Date:

_____

Summary

The past decades have seen near exponential growth in internet traffic. To meet this growth, optical communication networks continue to branch deeper into network architectures, replacing electrical based communication. In order to reduce deployment costs of such expansive networks, low-cost optical components integrated at ever-increasing densities are needed. Tunable semiconductor laser diodes represent an indispensable optical component in such networks, with significant research being undertaken to reduce their cost and complexity. Such laser diodes are sensitive to thermal fluctuations and with increasing component density this thermal behaviour becomes an important factor.

Previous research in the Trinity College Dublin semiconductor photonics group has yielded a low-cost laser diode design based on surface etched slotted gratings. In contrast to conventional low-order buried grating structures — used in distributed feedback and distributed Bragg reflector lasers — slotted grating structures can be fabricated without the need for re-growth or high resolution e-beam lithography. This slotted design has previously been implemented in the form of tunable laser arrays capable of covering the C-band with low linewidth and high SMSR. Furthermore, widely tunable lasers based on the vernier effect have also been demonstrated achieving $> 50\,\text{nm}$ tuning range. The research presented in this thesis builds upon the aforementioned work through experimental characterization, numerical simulation and optimization of these slotted laser diodes.

Firstly, the tuning behaviour of multi-section single mode slotted laser diodes is experimentally characterized in detail. This experimental characterisation yields a more rigorous tuning scheme for the various laser sections, replacing the previous ad hoc approach of avoiding mode hops. This tuning method is adopted to actively athermalize the laser relative to changing ambient temperatures. Continuously tuned athermal operation is demonstrated from $8\,^{\circ}\text{C}$ to $47\,^{\circ}\text{C}$ with a wavelength stability of $\pm 0.04\,\text{nm}/\pm 5\,\text{GHz}$ and a minimum SMSR of $37.5\,\text{dB}$. Utilizing dis-continuous tuning, extended athermal operation is also demonstrated from $10\,^{\circ}\text{C}$ up to $85\,^{\circ}\text{C}$, with a wavelength stability of $\pm 0.01\,\text{nm}/\pm 1.25\,\text{GHz}$ and a minimum SMSR of $38\,\text{dB}$. An

analytic predictive model for laser tuning is also developed utilizing surface temperature profile data measured via the CCD thermo-reflectance (CCD-TR) method. The model proves capable of predicting tuning maps matching experimental results to a high degree of accuracy.

A thermo-optic numerical model is subsequently developed (implemented using free and open source software), in order to accurately simulate a wide range of laser dynamics. This model utilizes the two-dimensional scattering matrix method (2D-SMM) to model the slotted gratings, the time-domain transfer matrix method (TD-TMM) to simulate the laser dynamics and the 3-D FEM solver FEniCS, to simulate the on-chip temperature distribution. The model is compared to a range of experimental measurements, including laser threshold, slope efficiency, linewidth, wavelength tuning maps and CCD-TR measured temperature, and shows good agreement. The model is also used to explain in detail the tuning dynamics of both single mode lasers and widely tunable Vernier lasers. Moreover, the performance experimentally observed in widely tunable Vernier lasers is investigated through simulation. The relatively high tuning current required for such lasers is attributed to the increasing carrier density in the mirror sections. This high carrier density is also identified as likely being detrimental to the linewidth and SMSR performance of such lasers.

Finally, a genetic algorithm is developed in order to optimize single mode slotted laser diodes, with a view to improving efficiency and temperature stability. The genetic algorithm incorporates the aforementioned 2D-SMM and TD-TMM to accurately guide the optimization process toward ideal solutions. Using the genetic algorithm, the previous iteration of laser array designs are re-optimized, yielding designs with significantly improved output power and stability at elevated temperatures. Furthermore, the genetic algorithm is applied to optimize a laser for low linewidth operation and a laser for direct modulation. The low linewidth design is theoretically capable of achieving a linewidth of $\leq$ 120 kHz; compatible with advanced modulation formats such as 16PSK and 16QAM. A directly modulated laser design achieves a theoretical performance of a -3 dB bandwidth of 30 GHz at 87.5 mA and clear opening in simulated eye-patterns. Importantly, all designs were limited to a slot width of $\geq$ 1.0 µm, enabling simple fabrication, potentially using photo-lithography.

Acknowledgements

I would like to express my sincere gratitude to my supervisor Professor John Donegan, for giving me the opportunity to undertake this research. Over the past four years, Professor Donegan's supervision has made this work possible and I thank him for all the invaluable advice, ideas, feedback, guidance and moral support, which were always readily available. This supervision was also complemented with a freedom to pursue my own research interests and put my own mark on the research — an opportunity which not all post graduate students are so lucky to be afforded with. Suffice it to say, the past four years have been an incredible learning experience for me, and I thank Professor Donegan wholeheartedly for this. Of course, this research would not have been possible without the funding provided by CONNECT, Science foundation Ireland and AMBER and I express my thanks for this.

I would also like to thank all the collaborating researchers who helped on this project. I would like to thank Prof. David McCloskey for all his work on the CCD-TR measurements. These measurements were also made possible by Simon Corbett, whose assistance is greatly appreciated. I would like to thank Rudi O' Reilly Meehan for his help with the laser athermalization experiments and Ryan Enright for his insights on this topic.

I would like to thank both Marta Nawrocka and Azat Abdullaev for introducing me to the experimental aspects of laser diodes and teaching me how to use the lab equipment. I thank Gaurav Jain, Robert McKenna and Kevin Brazel for their help with characterization. Furthermore, I would like to thank Jules Braddell for managing device fabrication runs and teaching me about said fabrication. I would like to thank Frank Bello for the many informative discussions on device modelling. I would also like to thank the photonics group and the school of Physics as a whole for all their help over the years.

Though not directly involved in the research, there are those without whom I would not have finished this undertaking. To my family I can not begin to express how much your support was appreciated over the years. I owe my parents a debt for all their moral (and financial) support which I can only hope to one day re-pay. Thank you both so much for your help and support, and I hope I was not too much of a burden in those last months writing up. To my father, thank you for all the invaluable proofreading — not to mention my morning porridge and coffee which you so masterfully prepared during my write up. To my mother, your unfaltering support and encouragement made a world of difference: if I'm taken care of *that* well when writing a thesis . . . maybe I should write another. A heartfelt thank you to my sister

Aileen; in those last months of intensive writing, watching with you your *awful* TV shows, was a much-needed respite from the thesis: I think I may have lost my mind without it!

I would like to thank my close friends and colleagues, Brian and Chuan. Thank you for your company over the past four years and all the great times.

I would also like to thank my housemates: Susan, Patrick and Michael. Thank you for a great four years and always giving feedback on my presentations.

Finally, this project made extensive use of free and open source software, which thousands of people across the world have developed. These people have spent countless hours of their spare time, developing and maintaining the software tools used in this work — I thank them for this.

Contents

List of Publications

A. Abdullaev et al. “Improved performance of tunable single-mode laser array based on high-order slotted surface grating”. *Opt. Express* 23.9 (May 2015), pp. 12072–12078. DOI: 10.1364/OE.23.012072.

I. Mathews et al. “Reducing thermal crosstalk in ten-channel tunable slotted-laser arrays”. *Opt. Express* 23.18 (Sept. 2015), pp. 23380–23393. DOI: 10.1364/OE.23.023380.

F. Bello et al. “Traveling Wave Analysis for a High-Order Grating, Partially Slotted Laser”. *IEEE Journal of Quantum Electronics* 51.11 (Nov. 2015), pp. 1–5. DOI: 10.1109/JQE.2015.2485219.

M. Wallace et al. “Athermal operation of a multi-section laser for optical communications”. *2017 Optical Fiber Communications Conference and Exhibition (OFC)*. Mar. 2017, pp. 1–3. DOI: https://doi.org/10.1364/OE.25.014414.

List of Figures

List of Tables

List of Abbreviations

AR / HR	Anti-Reflective / High-Reflective
CCD	Charge-Coupled Device
CCD-TR	CCD Thermo-Reflectance
CW	Continuous Wave
DBR	Distributed Bragg Reflector
DCN	Data Centre Network
DFB	Distributed Feedback
DWDM	Dense Wavelength Division Multiplexing
EA	Electro Absorption
EDFA	Erbium Doped Fibre Amplifier
FEM	Finite Element Method
FOSS	Free and Open Source Software
FSR	Free Spectral Range
FWHM	Full Width at Half Max
ICP	Inductively Coupled Plasma
IIR	Infinite Impulse Response
ITU-T	International Telecommunication Union-Telecommunication
Laser	Light Amplification by Stimulated Emission of Radiation
LED	Light Emitting Diode
LIV	Light Current Voltage
MQW	Multiple Quantum Well
ONU	Optical Network Unit
OOK	On-Off Keying
OSA	Optical Spectrum Analyser
PKS	Phase-shift Key Modulation
PIC	Photonic Integrated Circuit
PON	Passive Optical Network
QAM	Quadrature Amplitude Modulation
QCSE	Quantum Confined Stark Effect
QW	Quantum Well
SCH	Separate Confinement Heterostructure
SEM	Scanning Electron Microscope
SG-DBR	Sample Grating Distributed Bragg Reflector
SMSR	Side Mode Supression Ratio
SMM	Scattering Matrix Method
SOA	Semiconductor Optical Amplifier
TEC	Thermo-Electric Peltier Cooler
TD-TMM	Time Domain Transfer Matrix Method

TMM	Transfer Matrix Method
WDM	Wavelength Division Multiplexing

Physical Constants

Speed of Light	$c_0 = 2.997\,924\,58 \times 10^{8}\,\mathrm{m\,s^{-1}}$
Elementary charge	$q = 1.602\,176\,620\,8 \times 10^{-19}\,\mathrm{C}$
Planck's constant	$h = 6.626\,070\,04 \times 10^{-34}\,\mathrm{m^2\,kg\,s^{-1}}$
Boltzmann constant	$k_B = 1.380\,648\,52 \times 10^{-23}\,\mathrm{m^2\,kg\,s^{-2}\,K^{-1}}$

Chapter 1

Introduction

1.1 History of Optical Communications

The 1960s saw the emergence of two key advances that would make high speed optical communications feasible. The first of these was the development of the semiconductor laser diode by Hall et al. [1] in 1962 . These early homojunction laser diodes only functioned at $\sim 80\,\mathrm{K}$ and as a result were not suitable for any practical uses. With the development of liquid phase epitaxy (LPE), the first heterojunction lasers were fabricated, bringing semiconductor lasers closer to room temperature operation. It was not until the development of double heterostructure lasers that room temperature operation was realized in 1970 [2]. Double heterostructure lasers were rapidly commercialized for a variety of uses including optical communications. The second advancement which allowed for long distance communication based on optical signals was the development of a suitable material to transport light signals. This breakthrough was achieved in 1966 with the proposal of a method to improve fibre performance by removing impurities in glass which otherwise led to high attenuation in the order of $1000\,\mathrm{dB\,km^{-1}}$ [3]. By 1970, optical fibers with attenuation of $\sim 20\,\mathrm{dB\,km^{-1}}$ — low enough for communication purposes — were successfully developed by Corning Glass Works Inc.

These advancements heralded the deployment of the first fibre-optic networks — implemented over a range of wavelengths. In 1978, the first *fibre-to-the-home* solution using multi-mode fibers at 850 nm, as part of Japan's Hi OVIS project, was deployed. Soon thereafter, 1300 nm systems using single-mode fibres were implemented in 1981. By 1984 the first submarine fibres had been deployed by British Telecommunications PLC. Due to fibre attenuation, many of these early fibre networks relied on optical repeats for signal regeneration, making network deployment and upkeep costly [4].

In the late 1980s and early 1990s, the development of erbium doped fibre amplifiers (EDFAs) yielded a new generation of optical communication upon which modern

systems are based. The optical gain exhibited by EDFAs in the 1550 nm region saw the implementation of optical communication predominantly in the c-band (1530 to 1565 nm). Crucially, EDFAs allowed for the transmission of long reach signals without the need for signal regeneration, previously a barrier to widespread deployment.

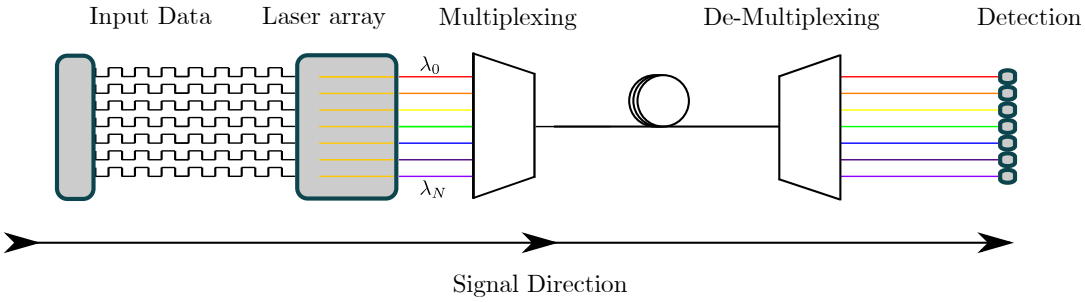

Figure 1.1: Wavelength Division Multiplexing.

In conjunction with EDFAs, the development of non-zero dispersion shifted fibres and dispersion management enabled a key technology of modern optical communication systems: wavelength division multiplexing (WDM). WDM transmits data in parallel by using several optical carriers each at a specific wavelength, as shown in Figure 1.1. The ability to send multiple signals over a single fibre has yielded dramatic increases in data rates. Dense wavelength division multiplexing (DWDM), a form of WDM with closely spaced carriers, is now commercially available achieving data rates upward of 20 Tb/s, and forms the backbone of modern optical communication networks [4, 5].

1.2 Challenges in modern optical networks

Despite the significant pace of progress, contemporary optical communication networks face a growing challenge in meeting the ever-increasing demand for data bandwidth. Data intensive services such as video streaming, cloud and gaming are currently causing a *capacity crunch*, driving a need for increases in data rates. Numerous emerging technologies, such as the internet of things and self driving cars also have the potential to dramatically increase network congestion often in unpredictable ways. In general, modern optical networks can be categorised by their transmission distance into short reach and long-haul networks each of which face unique challenges with numerous potential solutions.

1.2.1 Short reach networks

Short reach networks generally have transmission distances on the order of tens of kilometres. Short reach networks include access networks which connect end users to the metro and core. Access networks have in recent years seen significant adoption of optical networking in place of electrical, with a view to increasing capacity. In order to support a larger number of end users, access networks have sought to employ WDM passive optical networks (PON). WDM-PON, with channel spacing generally $\leq 100\,\mathrm{GHz}$ is seen as a key technology in expanding access capacity. By using a larger number of tightly spaced optical carriers, a larger number of end users can be supported at high data rates. However, with increasing spectral density the risk of channel crosstalk increases and as a result, each optical transmitter needs to be carefully controlled such that each carrier is at the appropriate wavelength. In particular, the thermally induced wavelength shift associated with semiconductor lasers is a challenge for DWDM systems. Given the large number of user optical network units (ONUs) required for fibre to the home applications, inventory cost also becomes a key factor. As such, balancing the performance and cost of optical components represents a crucial factor in the adaptation of PON access networks.

Another short reach network, which has seen significant growth, is that of inter- and intra-data centre networks (DCNs). In order to increase efficiency and capacity within data centres, electronic components will increasingly be replaced by optical solutions. Such architectures have been proposed with high energy efficiency, however, the use of optical components generally increases deployment cost [6]. Additionally, as data centres typically have size constraints, the spatial footprint of optical solutions becomes critical. Form factors such as C form-factor pluggable (CFP), consisting of several discrete optical components were rather large for DCN applications. In recent years, CFP2 and CFP4 have leveraged improved optical integration to double and quadruple port density over the original CFP [4]. In order to further reduce spatial footprint and cost, research into monolithic photonic integrated circuits (PICs) continues, seeking to integrate more optical components on a single chip. As photonic devices begin to be integrated at higher densities, thermal management again becomes an important consideration. As a result, there is a need for a detailed understanding of individual components' thermal behaviour, as well as new thermal management techniques. The viability of such PICs depends largely on the cost and reliability of the individual components therein and thus considerable effort is being undertaken to develop cheaper components for PICs.

1.2.2 Long-haul networks

Long-haul networks include metro and core, with transmission distances of hundreds or thousands of kilometres. In such networks, cost and power consumption are less critical than in short reach networks. Long-haul networks specifically face challenges in maximizing spectral efficiency and transmission distance. New high cardinality modulation formats in particular seek to improve spectral efficiency of long-haul networks. As core networks are already widely deployed, future advances in this context will likely focus on utilizing existing infrastructure in more efficient ways. Further advancements may also include: the implementation of integrated arrays for modulation and coherent reception, optical comb spectrum generation, and transponders capable of flexible data rates, tuned to required distance are also likely to be implemented in the coming years [4].

1.2.3 Advanced modulation formats

In order to further increase data capacity of WDM systems, increases in spectral efficiency are required in both short reach and long-haul networks. Limited by conventional modulation such as on-off keying (OOK), recent development of advanced modulation formats has yielded dramatic improvements in capacity. Such modulation formats allow for the encoding of multiple bits of data during a given symbol for a given wavelength channel, resulting in improved data rates per wavelength channel [4]. Phase-shift keying key modulation (PSK) is a widely implemented modulation technique which uses coherent detection to encode data in amplitude and phase. Commercially available formats include binary PSK, quadrature PSK, and 16-quadrature amplitude modulation (QAM) [4]. Figure 1.2 shows the main dimensions along which such coherent communication can increase capacity. In order to reach higher order constellation multiplicity, achieving low linewidth is a key goal for laser diodes.

Prior to more advanced coherent modulation, formats based on intensity modulation and direct detection (IM-DD) were the status quo. The emergence of coherent communication resulted in a shift of research focus away from IM-DD formats. However, the capacity crunch in short haul applications has seen a resurgence in research into IM-DD formats. Such formats offer cheap and energy-efficient alternatives to coherent detection, suitable for short reach networks. Advanced IM-DD formats include multi-level schemes such as 4 level pulse amplitude modulation (4-PAM) which have achieved 224 Gb/s [4].

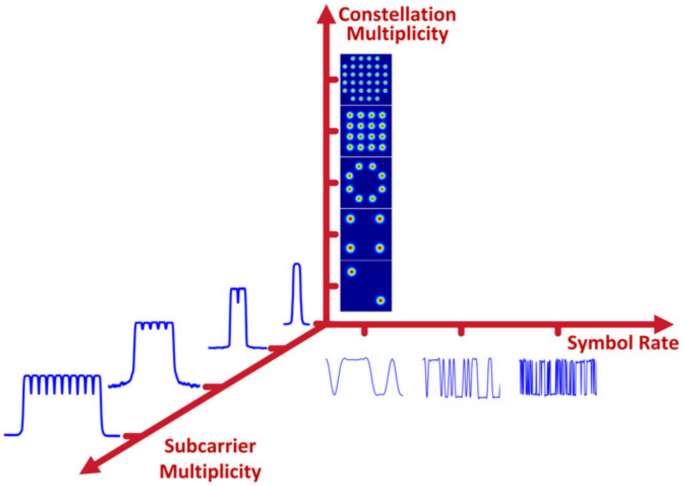

Figure 1.2: Dimensions along which capacity can be increased in coherent communication (from Agrell et al. [4]).

In order to facilitate increased capacity there is a need for next generation PIC components, in particular semiconductor laser diodes and EA modulators, to be compatible with cutting edge and emerging modulation formats.

1.3 Tunable laser diodes

Semiconductor laser diodes represent an essential optical component within optical networks, as they generate the optical carrier signal for the transmission of data. Given the frequency grid spacing defined by the international telegraph union telecommunication standardisation sector (ITU-T) of 12.5 GHz to 100 GHz and wider, DWDM systems can exceed 80 individual wavelength channels [7]. Such a large number of wavelength channels means that having an individual laser for each channel is not economically feasible. Instead, lasers capable of tuning to several channels are used, reducing the number of lasers required for a DWDM system. Several types of tunable lasers are used in current networks. As single lasers generally have tuning ranges on the order of nano meters, one approach is to combine several such lasers together with their combined tuning range covering the desired wavelength channels. Such early tunable laser arrays were demonstrated by Kudo et al. [8] in the 1990s, achieving 15.3 nm tuning range. More recent tunable arrays are now capable of fully covering the C-band [9]. Higher tuning ranges can be achieved by individual lasers, albeit with more complicated designs. Sample grating DBR (SG-DBR) lasers use several interrupted grating sections to generate super-modes, thereby extending the tuning range. They were first demonstrated in 1993 by Jayaraman, Chuang, and Coldren

[10], achieving 57 nm tuning with more than 30 dB SMSR. SG-DBR lasers are also capable of integration with other photonic components. Mason et al. [11] integrated SG-DBR lasers with SOAs to achieve output powers > 8 Bm and Akulova et al. [12] integrated EA modulators allowing for error-free transmission at 2.5 Gb/s for 350 km. Such SG-DBR lasers are now widely deployed in optical networks as a flexible wavelength source. Modulated grating Y-branch (MG-Y) lasers also tune via the vernier effect in order to obtain an extended tuning range. These lasers differ from SG-DBRs by having both gratings located on the same side of the gain section, thus avoiding the output light passing through the front reflector and being attenuated. Such lasers have been developed, attaining SMSR ≥ 40 dB, high output power ≥ 13 Bm and a low power variation < 1.5 dB [13]. A detailed review of the aforementioned tunable lasers can be found in Coldren et al. [14].

For the next generation of long haul communications new lasers designs capable of full band tunability, such as the digital supermode (DS)-DBR laser, have been investigated to replace fixed channel DFBs, achieving similar performance in terms of power and SMSR [15].

Although existing tunable laser solutions have achieved wide use in optical communications they generally involve complex and expensive fabrication. In long-haul systems where the price point of optical components do not have as large of a footprint, such complex lasers — fabricated through epitaxial re-growth, embedded grating structures and high resolution epitaxy — are well deployed and have become the de facto solution. However, as optical communication penetrates further into short reach networks and the number of devices increases, inventory cost begins to play a larger role and the mature laser designs suitable for established networks may not be ideal for emerging demands. There has been a concerted effort to reduce costs of these components while also maintaining efficiency as well as integrating more components on a single chip.

A key area of interest which has emerged is replacing embedded gratings with surface etched gratings. This removes the need for the aforementioned re-growth and high resolution epitaxy with a view to driving down costs. Recently, Yang et al. [16] demonstrated a monolithic PIC comprised of tunable single mode lasers, SOAs and multi-mode interference (MMI) couplers, using a simple slotted grating design. Cheap widely tunable lasers have also been demonstrated using a monolithic slotted grating design, demonstrating linewidth ≤ 800 kHz and fast wavelength switching between channels [17]. Surface grating laser designs have also been simulated for potential direct modulation applications in the 1.3 µm window, achieving a predicted 33 GHz modulation bandwidth at 100 mA [18]. Similar surface grating lasers have been

implemented in silicon photonics with an InGaAsP-Si hybrid single-mode laser based on slotted silicon waveguides achieving good performance with a threshold current of 21 mA, output power of 1.9 mW and side-mode suppression (SMSR) $\geq$ 35 dB [19]. The common themes of these recent efforts are low cost, simple fabrication, and monolithic integration. All of these attributes are increasingly seen as important for laser diodes to enable the next generation of optical communication networks.

1.4 Thesis scope and goals

With the above context and challenges in mind, research into cheap, simply fabricated, monolithic laser designs has been previously undertaken within the Trinity College Dublin semiconductor photonics (TCDSP) group. Out of this research, a platform for low cost laser diodes based on surface etched gratings has been developed. These lasers are designed to reduced cost in a number of ways. The ability to integrate the lasers with a range of optical components helps increase the number of functions per package thus reducing cost. In addition, the slotted grating simplifies manufacturing, potentially increasing yield and allowing for cheaper manufacturing methods. (Detailed costing in relation to the high-order surface grating laser have not been carried out by our group and for companies who sell lasers with similar structures, this information is proprietary and confidential.)

Most recently, the TCDSP group has demonstrated tunable laser arrays based on high order surface etched gratings, capable of covering the C-band and achieving linewidths compatible with advanced coherent modulation formats: star 16QAM and 8PSK [20]. In addition, lasers with monolithically integrated components in the form of SOAs and electro absorption modulators have been demonstrated using this platform [21, 22]. Widely tunable lasers based on the vernier effect were also fabricated achieving $>$ 50 nm tuning range with SMSR $\geq$ 30 dB for the majority of this range [23].

From this preceding work, a number of issues were highlighted. Chief among these was a need to understand in greater detail the physical behaviour observed in the fabricated devices. Of particular interest is the wavelength tuning behaviour of said lasers as well as the thermal dynamics underlying said tuning. In addition, areas where performance could be improved were identified and this thesis focuses on addressing these with a view to designing new slotted lasers with improved performance. With the above in mind, the overarching goals of this thesis are to:

- Experimentally investigate wavelength tuning of slotted laser diodes.

- Develop a high fidelity numerical model capable of explaining and predicting laser tuning behaviour as well as overall device performance.
- Iterate upon previous designs to improve performance of laser diodes for the next fabrication run.

With regard to the final goal above, design procedures for surface grating based lasers in the extant literature tend to rely on an ad hoc approach, simulating grating properties such as reflectivity over a limited range of design variables and choosing a suitable grating. A generalized approach to surface grating optimization is lacking and to our knowledge an efficient method fully covering the various design variables for a slotted grating while also encompassing the complexities introduced by them has not been demonstrated. As such, this thesis sets out to define an improved method whereby slotted grating laser diodes can be rigorously optimized, taking all degrees of freedom into account while being applicable for arbitrary laser performance requirements.

Thus far, attention has been focused on lasers within the context of optical communication networks. In addition to optical communications, semiconductor laser diodes have a number of wide-ranging applications, such as gas detection, measurement systems and atomic clocks. The slotted laser diodes presented herein also have potential application in these fields, though this research is primarily undertaken in the context of optical communications.

Chapter 2

Semiconductor Lasers

2.1 Introduction

Semiconductor laser diodes — as well as lasers in general — require a number of basic elements in order to operate. These include a:

- Gain medium.
- Pump source.
- Feedback mechanism, i.e. a mirror.
- Wavelength / frequency filter (single mode case).

A gain medium is required for the amplification of light through stimulated emission. In order for the gain medium to support stimulated emission, a *pump* source — generally optical or electrical — is needed to excite electrons to a higher energy level. Once excited, electrons can decay to a lower energy via stimulated emission, resulting in gain. In order for lasing to occur, the gain within a laser must be greater than the losses. To this end, a feedback mechanism is required to overcome loss from the gain medium. Typically, two mirrors fulfil this requirement, forming a cavity in which light is confined. Once an optical mode within a cavity has more gain than loss, lasing will occur. Laser cavities generally support a multitude of longitudinal modes at a number of wavelengths. In order to select a single cavity mode, a mechanism for filtering out competing modes is needed, normally in the form of a grating. These concepts will be introduced in this chapter, as well as common semiconductor laser diode structures and important properties thereof.

2.1.1 Energy bands in solids

In order to understand how a gain medium arises, we first consider the energy levels available to electrons in condensed matter such as semiconductors. Figure 2.1 shows

the progression of energy levels with an increasing number of atoms N. At low densities, as found in gases, energy levels of the electrons are discrete and are in effect the same as a single isolated atom. Moving away from this isolated atom case, as the number of atoms increases, the energy levels of the electrons of each atom are perturbed resulting in energy splitting. This splitting repeats itself as the number of atoms increases and in the case of a large number of atoms, as in solids, the discrete energy levels effectively becomes a continuous energy band. The splitting of the highest occupied atomic energy level forms the *valence band* with the next higher atomic level splitting to form the *conduction band*. Between the valence and conduction band there exists a *band gap*, which no electron can occupy.

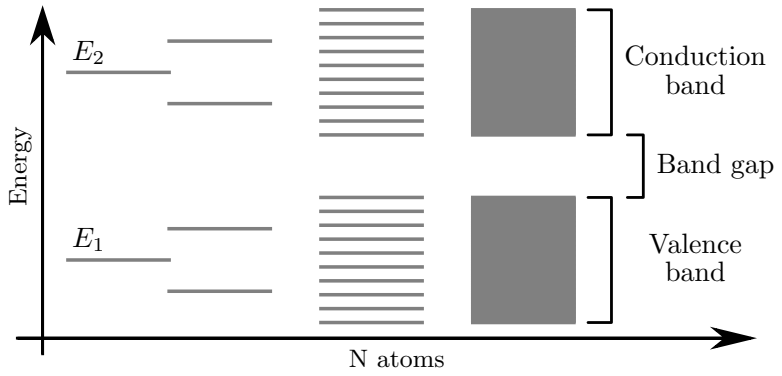

Figure 2.1: Change of energy levels from the single atom case to the band structures of crystals.

Plotting the valence and conduction band energy levels against their respective wave-vectors results in the band structure of semiconductors as shown in Figure 2.2. An important result of the E versus k diagram in Figure 2.2, is that not all energy levels can transition between one another, with energy transitions largely limited to vertical transitions only involving energy transfer. This is due to the fact that any other transition will involve a change in momentum k, and as the momentum of photons involved in these transitions is small compared with the momentum available to electrons and holes in bands, such transitions have a low probability. As a result, materials with direct band gaps, where E_c and E_v coincide at the same wavevector k, are required in order for optical transitions to occur efficiently between the bands. The region where light is generated through stimulated emission in a laser, known as the active region, is thus predominantly engineered with direct band gap materials. Such direct band gap materials include GaAs, InP and GaN, which are commonly used in the design of semiconductor lasers.

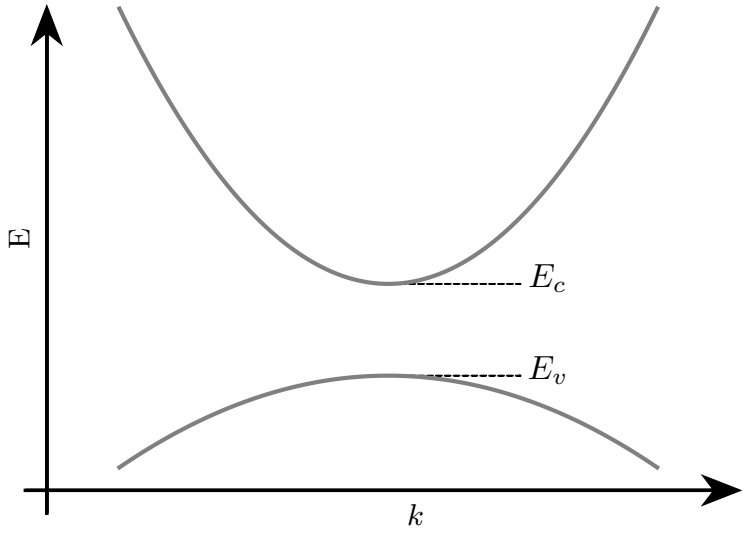

Figure 2.2: Electron energy vs. wave vector magnitude in a direct band gap material.

2.1.2 Heterostructures

In order to enable the operation of semiconductor lasers, the previously described band structures of solids can be engineered in numerous ways. Modern semiconductor lasers are based on the principle of a double heterostructure. In this scheme an active region is sandwiched between two layers of higher band gap energy. Figure 2.3 shows a simplified band structure of a double heterostructure in forward bias. Due to the high band gap confinement layers either side of the active region, electrons cannot escape into the p-type confinement layer and the holes cannot escape into the n-type layer. As such, they are forced to recombine in the active region.

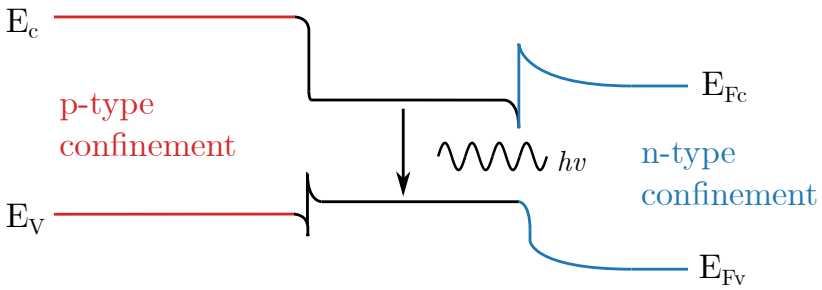

Figure 2.3: Double heterostructure band structure.

Decreasing the width of the active region close to or smaller than the de Broglie wavelength, such that quantum confinement occurs, results in a quantum well (QW).

This quantization has the effect of increasing the effective band gap energy as well as modifying the density of states as shown in Figure 2.4. The step-like behaviour increases the differential gain as the injected carriers have a narrower energy range. The gain can further be increased by introducing strain in the active region. This has the effect of reducing the density of states at the top of the valence band, allowing for population inversion to be obtained at a lower carrier density [24].

Although the carrier confinement is high in quantum wells, their narrow width means that optical confinement is relatively poor. To improve the optical confinement, separate confinement heterostructure quantum well (SCH-QW) structures are used. Such SCH-QWs have an additional waveguide around the quantum well, improving optical confinement. Finally, utilising multiple quantum wells (MQW), whereby several QWs are grown in series, further increases the optical gain. A strained SCH-MQW structure composed of five QWs forms the active region for all the proceeding results shown in this thesis (see Table 3.1, chapter 3 for details).

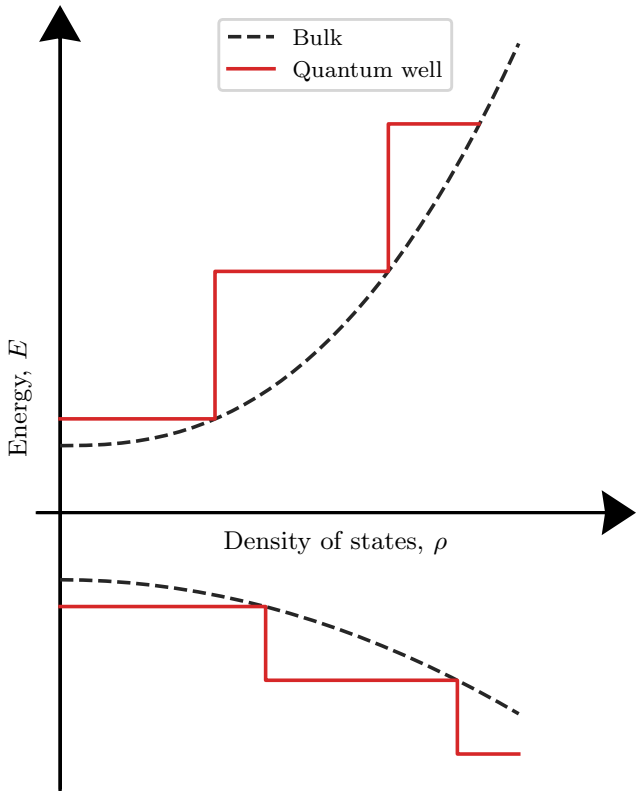

Figure 2.4: Density of states in a quantum well and bulk semiconductor.

2.1.3 Recombination and rate equations

Recombination

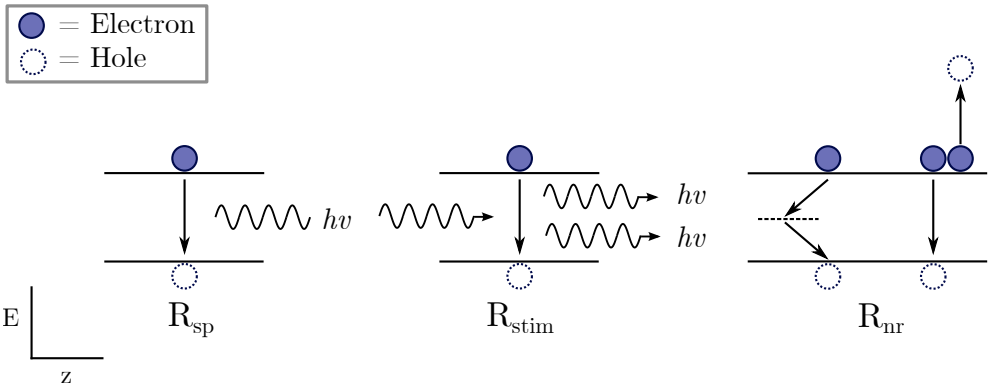

Figure 2.5: Primary paths of electron-hole recombination: spontaneous emission (R_{sp}), stimulated emission (R_{stim}) and non-radiative recombination (R_{nr}).

The two main light generating processes in laser diodes are spontaneous and stimulated emission. With the previously quantum well band structure in mind, these processes can be understood as shown in Figure 2.5. A detailed description of these processes is available in Coldren, Corzine, and Mashanovitch [25], from which the definitions in the following three paragraphs are sourced.

In the case of spontaneous emission (R_{sp}), an electron in the conduction band spontaneously decays to the valence band. The process of spontaneous emission is random by nature with random direction and phase, resulting in incoherent emission. This is the primary source of light in light emitting diodes (LEDs). The probability of a spontaneous recombination event occurring is proportional to the number of electrons (N) times number of holes (P), $N \times P$. As the total charge in undoped active regions remains constant, the spontaneous recombination rate is proportional to N^2.

The process of stimulated emission (R_{stim}) is also shown in Figure 2.5. An incident photon of energy hv perturbs the system, stimulating the recombination of an electron and hole with the generation of a new photon. Importantly, both photons have the same amplitude and phase. As this process cascades throughout the laser cavity, coherent light is created with high intensity.

In addition to radiative recombination, non-radiative recombination (R_{nr}) provides an alternate path through which conduction band electrons may decay. There are numerous such non-radiative paths, two of which are depicted in Figure 2.5. The first path is through defects within the active region material, which include point defects,

surfaces, and interfaces. This category of non-radiative decay is proportional to the number of carriers N. On the other hand, Auger recombination involves an excited conduction band electron decaying to fill a valence band hole. This differs from spontaneous emission because the energy is transferred as kinetic energy to another conduction band electron. In this case the process requires two electrons and a hole, and as a result is proportional to N^3.

Rate equations

In order for lasing to occur in a diode, there needs to be a population inversion, i.e. the number of electrons in the conduction band needs to be greater than the number in the valence band. This can be achieved by electrically pumping electrons from the valence band into the conduction band. Once this occurs, spontaneous emission will increase and seed the stimulated emission needed for lasing. In semiconductor lasers, electrically pumping the active region leads to an increase in carrier density given by

$$G_{gen} = \frac{I\eta_i}{Vq}, \tag{2.1}$$

where I is the injection current, η_i represents the injection efficiency, q is elementary charge and V is the active region volume. Combining the rate of carrier injection with the previously described possible paths of decay gives the rate equation

$$\frac{dN}{dt} = \frac{I\eta_i}{qV} - (AN + BN^2 + CN^3 + R_{stim}), \tag{2.2}$$

where A, B, C are the coefficients of non-radiative, bimolecular (spontaneous) and Auger recombination respectively [25]. The rate equation determines many of the dynamics of laser behaviour, both static and transient.

2.2 Fabry Pérot laser

The final requirement for a laser is longitudinal light confinement in the form of a cavity. The simplest case of this is a Fabry Pérot laser which is illustrated in Figure 2.6. In this device, light is confined to the gain medium by two reflecting surfaces. r_1 and r_2 are the amplitude reflectivity of the two cleaved facet mirrors, P_1 and P_2 are the powers leaving these mirrors. The blue arrows show a round trip of light confined to the active region with a field profile $U(x, y)$ as shown in red. Light

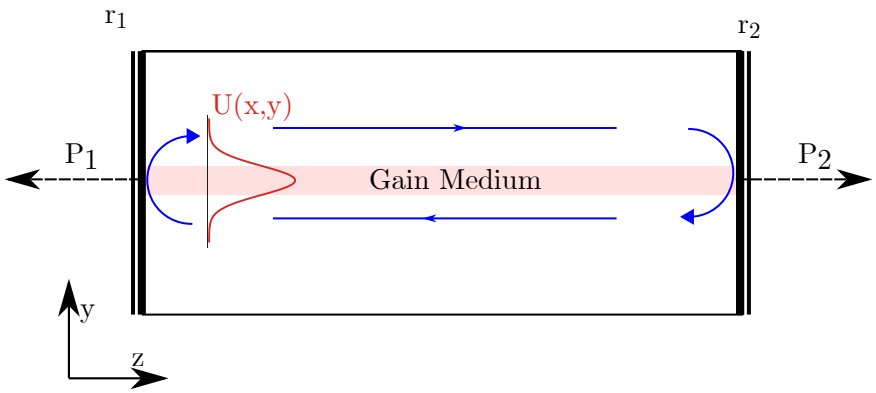

Figure 2.6: Fabry Pérot laser schematic.

in the cavity can be described by the propagation constant β:

$$\beta = \kappa_0 n'_{eff} + j\frac{g_{net}}{2} \tag{2.3a}$$

$$g_{net} = g\Gamma - \alpha_i, \tag{2.3b}$$

where α_i is the waveguide loss, Γ is the confinement factor, g_{net} is the net modal gain and κ_0 is the free space propagation constant ($\kappa_0 = \frac{2\pi}{\lambda}$) [25]. To achieve lasing, the net gain over a single round trip must equal the net loss, which includes the loss at the reflective boundaries r_1 and r_2. This will occur when

$$r_1 r_2 e^{-2i\beta L} = 1, \tag{2.4}$$

where L is the length of the Fabry Pérot cavity. Once this condition is met the laser is considered to be above threshold. Figure 2.7 shows the main changes when moving from a below threshold regime to an above threshold regime. Below threshold, carrier density in the active region increases with injection current. The carrier density will continue to increase until the gain is large enough to satisfy Equation 2.4. Once this occurs, the output power abruptly increases and the carrier density clamps at the value at threshold, as any additional carriers injected immediately decay via the stimulated emission which now dominates the light creation process within the QWs. The current at which this occurs is known as the threshold current (I_{th}) with a corresponding threshold carrier density of (N_{th}) as shown in Figure 2.7. Once above threshold, the output power increases approximately linearly. From Figure 2.7 the slope efficiency can be defined as the differential change in output power for a change in input power,

$$\eta_{se} = \frac{\Delta P}{\Delta I}, \tag{2.5}$$

measured in units of mW mA^{-1} [25]. It should be noted that the carrier density along the cavity is non-uniform and Figure 2.7 represents the approximate carrier density behaviour averaged over the length of the cavity.

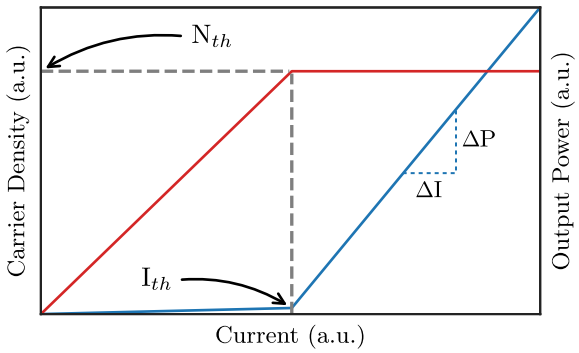

Figure 2.7: Typical threshold behaviour of a laser diode.

The lasing spectrum from a Fabry Pérot laser is largely determined by the cavity length. Wavelengths which have a constant phase after one round trip will add constructively and lase. The wavelengths which satisfy this condition are given by

$$\lambda_m = 2 \cdot \frac{n'_{eff} L}{m}, \tag{2.6}$$

where $m \in \mathbf{Z}$.

Figure 2.8 shows this condition where the vertical lines represent solutions to Equation 2.6 for an arbitrary cavity length. The wavelength of the longitudinal modes relative to the modal gain curve (green) will determine the power of each lasing mode. The gain curve plotted in Figure 2.8 was calculated using the parabolic approximation given in Westbrook [26]. An experimentally measured spectrum of a 400 µm long Fabry Pérot cavity is also shown in Figure 2.8 (bottom). The spectrum is strongly multi-mode, which is generally not suitable for optical communications. To obtain a single lasing wavelength, a method whereby competing modes are filtered out is required. This can be achieved by incorporating grating structures, which add a wavelength dependence to the reflectivity $r(\lambda)$ and thus can be used to select individual wavelengths.

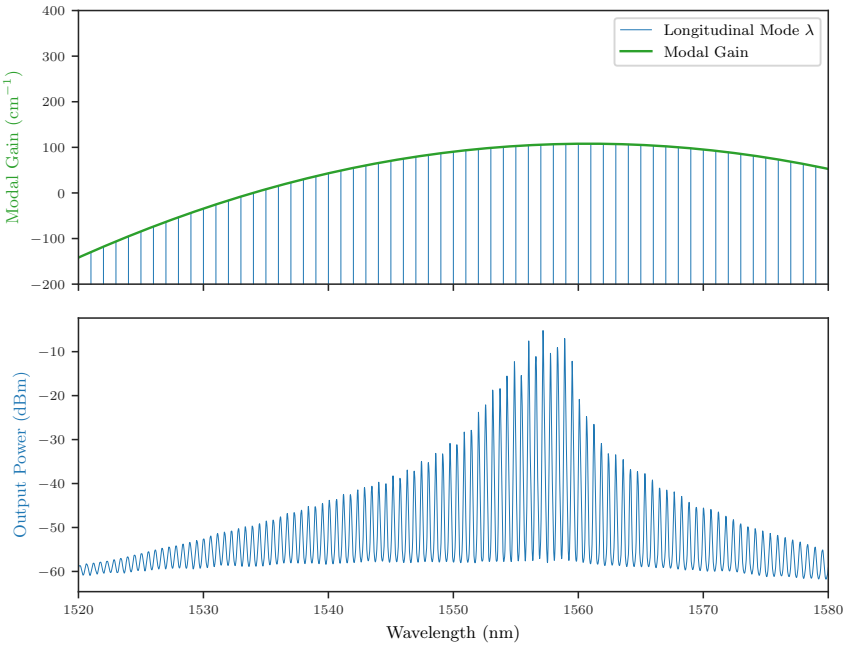

Figure 2.8: Fabry Pérot cavity's possible longitudinal modes and gain curve (top). Measured 400 µm Fabry Pérot lasing spectrum at 60 mA (bottom).

2.3 Single mode lasers

The multi-mode spectrum produced by Fabry Pérot lasers has a number of negative properties which make it ill-suited for fibre-optic communications. Considering a wavelength multiplexing system in which a number of independent signals need to be carried on their own unique wavelength, it is clear multi-mode spectra are not suitable. In addition, the dispersion which light experiences in optical fibres limits the use of Fabry Pérot lasers. In order to overcome dispersion it is necessary to produce a spectrally pure source with a narrow linewidth via single mode lasers. Grating structures play a pivotal role in enabling such single mode lasers.

2.3.1 Gratings

A grating consists of a periodic structure from which reflections add up constructively at a particular wavelength known as the Bragg wavelength. In laser diodes, these gratings take the form of structural variations which cause variations in the effective index, resulting in reflections. The amplitude of the reflection going from a material

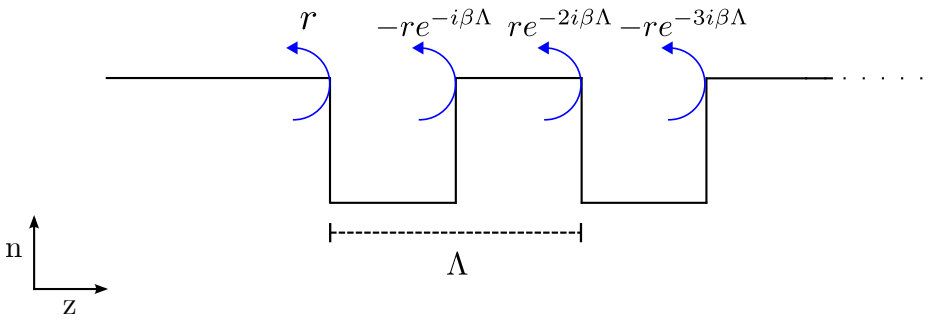

Figure 2.9: Typical grating structure, where changes in refractive index profile results in reflection.

of n_1 to one of n_2 can be approximated by the Fresnel equation as

$$r_{12} \approx \frac{n_1 - n_2}{n_1 + n_2}. \tag{2.7}$$

The periodicity of these reflections determines which wavelengths will be in phase upon reflection and add constructively, and which will be out of phase and add destructively. This is known as the Bragg condition and is described by the equation

$$\lambda_{Bragg} = 2n_{eff}\Lambda, \tag{2.8}$$

where λ_{Bragg} is the Bragg wavelength, Λ is the grating period and n_{eff} is the effective index of the fundamental mode [25]. Such a grating structure matching the Bragg condition is illustrated in Figure 2.9. The reflectivity peak of a grating can be tuned to a desired wavelength via the equation

$$\Lambda = \frac{\lambda}{2n_{eff}} \cdot m, \tag{2.9}$$

where $m \in \mathbf{Z}$. The integer m will be referred to as the *order* of the grating henceforth. The result of these constructively interfering reflections is a Bragg peak as shown in Figure 2.10. Generally, the bandwidth of such a Bragg peak is engineered to be narrower than the spacing of the longitudinal modes, ensuring that only one mode is supported by the cavity.

Semiconductor laser designs are generally categorized by the type of grating structure which they utilize. Two examples of single mode lasers which use different grating structures are distributed feedback lasers (DFBs) and distributed Bragg reflector lasers (DBRs) as shown in Figure 2.11a and 2.11b. In the case of the DBR laser, a grating known as a distributed Bragg reflector is used as a mirror on one side of the

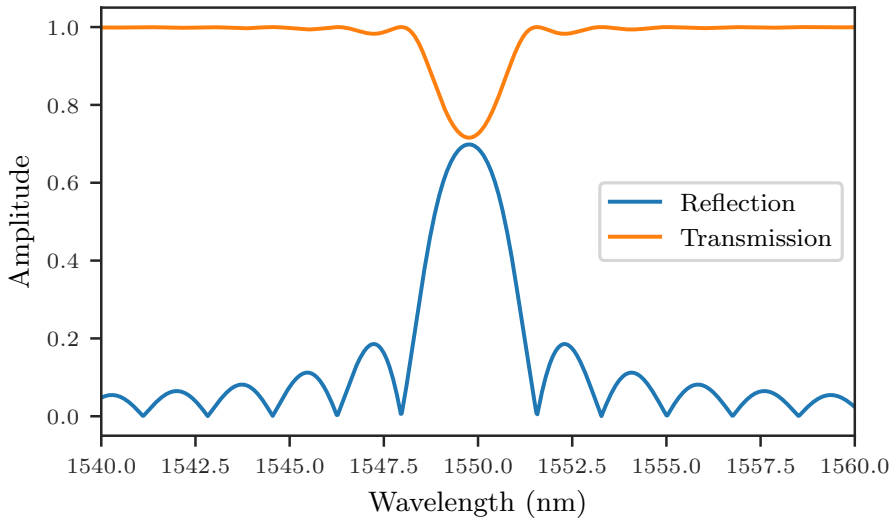

Figure 2.10: Bragg peak resulting from a periodic change in refractive index.

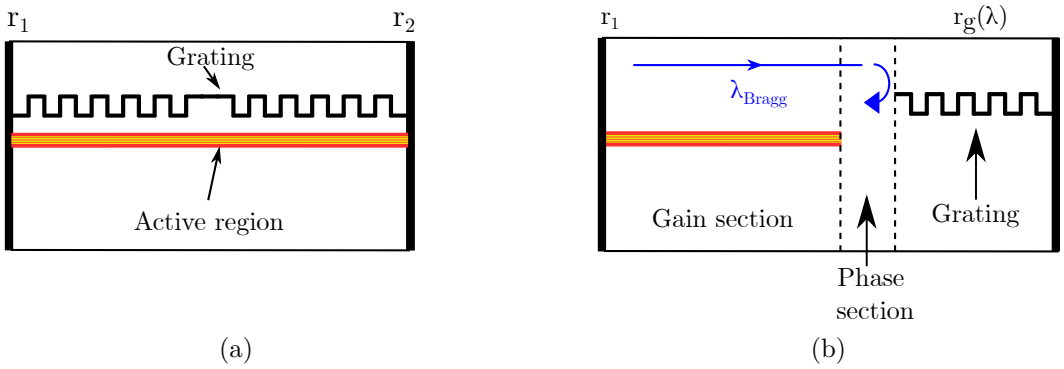

Figure 2.11: Longitudinal cavity cross sections of (a) DFB and (b) DBR lasers.

laser. The reflection peak of this grating will have a maximum at the Bragg wavelength. Modes near the maximum will have sufficiently low round trip losses for lasing to occur, whereas modes de-tuned from this peak will experience high loss and as a result not meet the threshold condition for lasing. In this way, single mode operation is achieved. In the case of the DFB the grating is formed across the whole active region and as in the DBR acts as a single mode selection mechanism. The effect of gratings when incorporated into a laser cavity is illustrated in Figure 2.12. The mirror loss is shown in red which is defined as

$$\alpha_m = \frac{1}{L_{eff}} \ln\left(\frac{1}{r_1 r_2(\lambda)}\right) \tag{2.10}$$

where L_{eff} is the effective cavity length. When the net gain for a longitudinal mode is larger than the mirror loss, lasing will occur [25]. From Figure 2.12 one can see that as the net gain increases, the longitudinal mode located at the minimum of the mirror loss (corresponding to the maximum of the Bragg peak) will be the first mode to achieve the threshold condition. As the carrier density is approximately

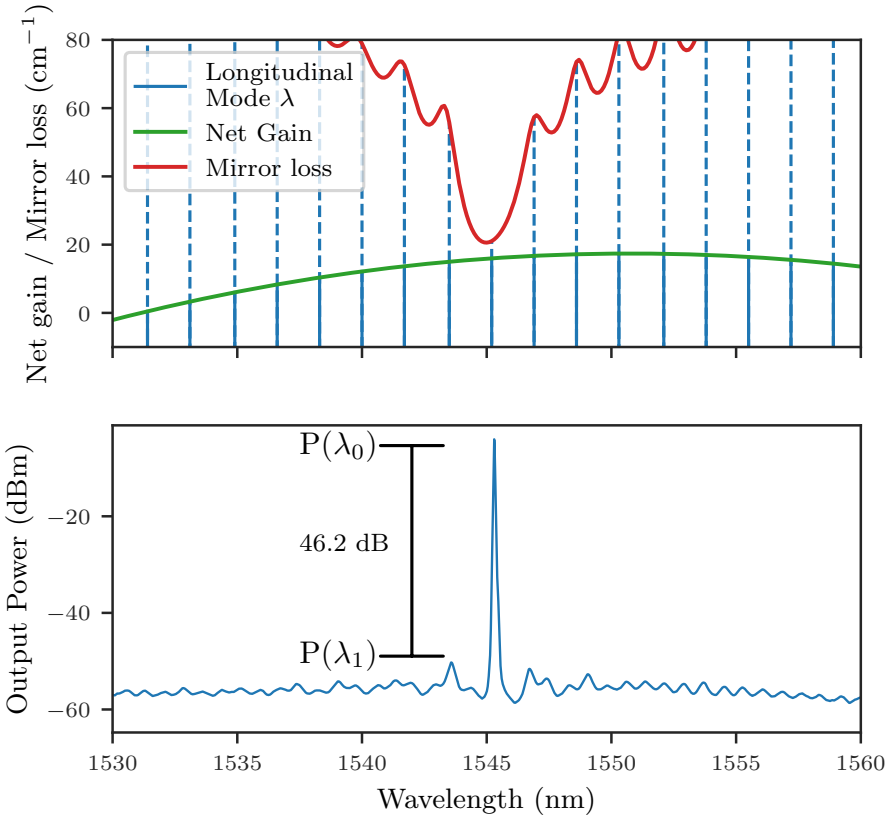

Figure 2.12: Effect of introducing a wavelength filter on lasing spectrum. Longitudinal modes experience different mirror loss; the mode with the lowest mirror loss reaching threshold first. In this way single mode lasing is achieved.

constant above threshold, the side modes will not reach threshold and thus only a single mode will dominate the lasing spectrum. An example of the resulting single mode lasing spectrum is seen in Figure 2.12 (bottom) where the dominant lasing mode is that located at the Bragg peak, and the side modes are suppressed. This introduces us to an important measure of single mode lasers: the side mode suppression ratio (SMSR). The SMSR is defined as the ratio between the dominant lasing mode and the second most powerful mode, given by

$$SMSR = \frac{P(\lambda_0)}{P(\lambda_1)}, \tag{2.11}$$

where $P(\lambda_0)$ is the power of the most dominant mode and $P(\lambda_1)$ is the power of the second most powerful mode, with a higher SMSR indicating better single mode operation.

An important consideration in lasers which have a cleaved facet, is the cleave error. Typically, the cleaving process is not particularly precise (varying on the order of micrometers), relative to the lasing wavelength. Because the cavity length has a random component arising from this cleave error, the wavelength of the longitudinal modes will also be random relative to the Bragg peak. As such, the ultimate SMSR of a cleaved facet laser has a random component, as the lasing longitudinal mode will not always coincide perfectly with the Bragg peak.

2.3.2 Laser linewidth

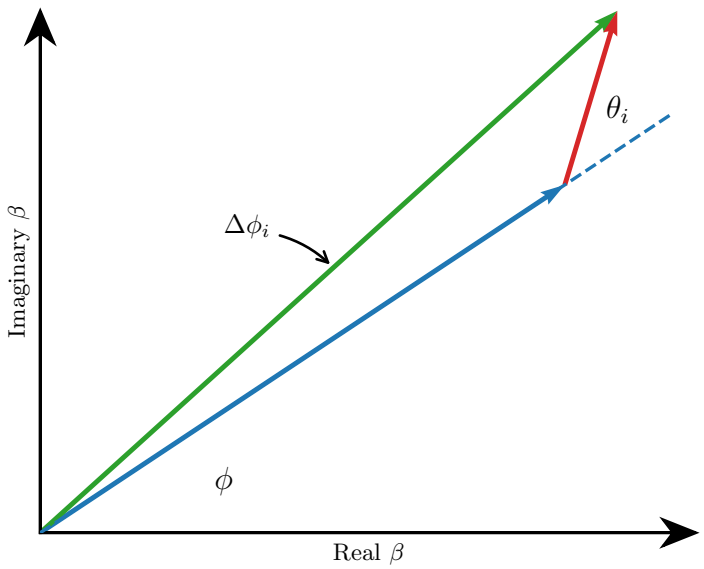

Figure 2.13: Effect of a spontaneous emission event on the field $\beta = I^{1/2}e^{i\phi}$.

In addition to the SMSR, the lasing mode's linewidth — typically defined as the full width at half max (FWHM) of the lasing mode's optical spectrum — is a key factor in optical communications. Due to optical signals undergoing dispersion within a fibre, a narrow linewidth is desirable to minimise this effect. The two main contributing factors to the broadening of the lasing mode's line-shape are spontaneous emission and carrier density variations. Henry [27] gives a detailed description of these effects, which is summarised in this subsection. The contribution from spontaneous emission can be illustrated by a phasor diagram as shown in Figure 2.13.

If we consider a field in a laser generated through stimulated emission,

$$\beta = I^{1/2} e^{(i\phi)}, \tag{2.12}$$

where I and ϕ are the intensity and phase respectively, a spontaneous emission event i will alter the field by

$$\Delta\beta_i = e^{(i\phi + i\theta_i)}, \tag{2.13}$$

where the magnitude is unity and the random phase of the spontaneous event is θ_i. From Figure 2.13 it follows that the change in phase due to the spontaneous emission is

$$\Delta\phi = I^{-1/2} \sin(\theta_i), \tag{2.14}$$

and accounts for the majority of spontaneous emission induced line broadening. From this the famous Schawlow-Townes equation can be derived. However, in order to fully account for linewidth, changes in refractive index n, caused by changes in carrier density within the cavity, need to be accounted for. The linewidth enhancement factor α was introduced by Henry [27], whereby the Schawlow-Townes equation becomes the *modified* Schawlow-Townes equation, generally given in terms of output power as

$$\Delta\nu = \frac{v_g^2 h\nu(\alpha_m + \alpha_i) n_{sp} \alpha_m}{8\pi P_o}(1 + \alpha^2), \tag{2.15}$$

where v_g is the group velocity, h is Plank's constant, g is the gain, n_{sp} is the spontaneous emission factor, α_m and α_i are the mirror and waveguide loss respectively and P_o is the output power; with the term $(1 + \alpha^2)$ accounting for changes in carrier density.

2.4 Laser tuning

2.4.1 Tuning schemes

In order to act as a source for multiple DWDM channels, it is desirable for laser diodes to have a large tuning range. Generally speaking, there are three main tuning patterns utilized, which are shown in Figure 2.14. The simplest of these is continuous tuning, whereby the laser wavelength tunes continuously and crucially without undergoing any mode hops over the range in question. From Figure 2.12 one can see that in order to maintain a single mode over a range of wavelengths, the longitudinal modes and the Bragg peak must be tuned in tandem. The single mode nature of continuous

tuning limits the achievable wavelength range, to the range which the longitudinal modes can be tuned over — generally up to $\sim 15\,\text{nm}$ [28].

If one allows for mode hops, the maximum achievable range is greatly increased as the only physical limit is the extent of the bandwidth of the optical gain. However, as shown in Figure 2.14, portions of the tuning range are not covered in such a discontinuous tuning scheme. In order to fully cover a large wavelength range, quasi-continuous tuning can be employed, whereby each mode can tune over a large enough wavelength such that their ranges overlap. Such tuning schemes allow for the full coverage of large tuning ranges $\sim 100\,\text{nm}$[28].

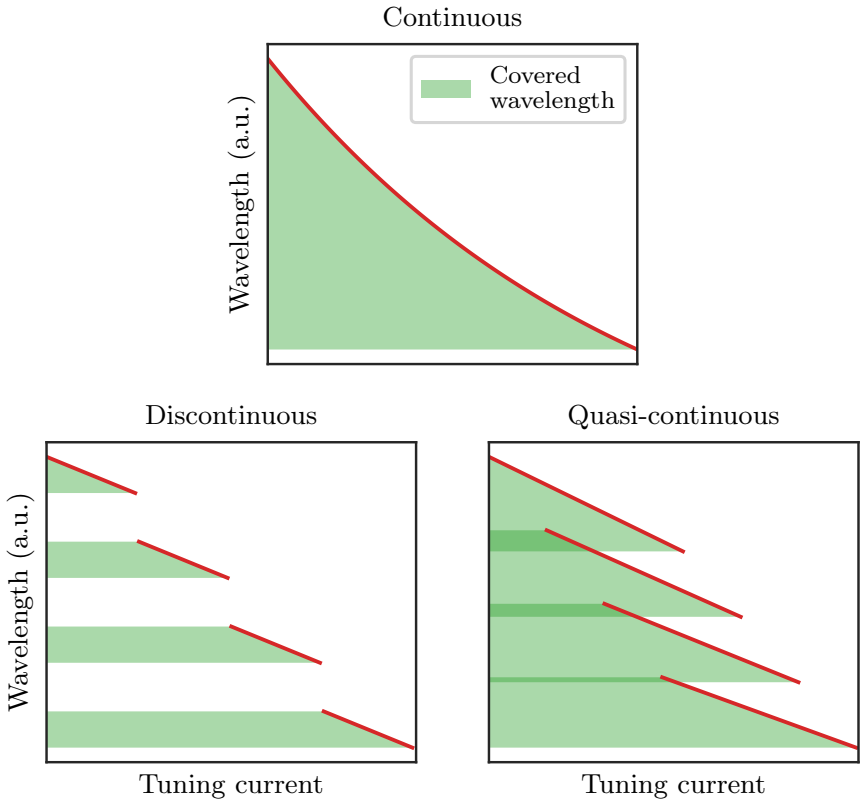

Figure 2.14: Various tuning schemes.

2.4.2 Wavelength tuning mechanisms

Free-carrier plasma effect

The most widely employed physical effect for tuning lasers is the free-carrier plasma effect. This effect causes a decrease in the refractive index of the semiconductor and hence a blue-shift in wavelength. The injection of carriers and holes into the

semiconductor leads to two sources of index change, Δn. The polarization of the injected carriers contributes most to this shift with a lesser contribution from the shift of the absorption edge [29]. In practice this effect is generally achieved by passivating a section of the laser diode, thus enabling high carrier densities to be injected and hence a larger Δn, typically up to ~ 0.04 [28].

Quantum confined stark effect

The quantum confined stark effect (QCSE) involves an electric field changing the refractive index. This field is applied by reverse biasing the pn-junction such that an electric field is produced within the quantum wells. The applied electric field results in a reduced band gap energy, reducing the refractive index. This effect generally produces refractive index changes less than the free-carrier plasma effect with Δn on the order of 1×10^{-2} to 1×10^{-3} [30].

Thermal tuning

An important tuning mechanism of semiconductor laser diodes is that of thermal tuning. Thermal tuning effects the lasing wavelength in two ways, directly through a change in the refractive index, Δn, and by increasing the band gap which red-shifts the gain spectrum. Thermal tuning generally produces a change in wavelength of $\sim 0.1\,\mathrm{nm\,^{\circ}C^{-1}}$ for the longitudinal modes and Bragg peak, while the change in band gap energy red-shifts the gain spectrum on the order of $\sim 0.5\,\mathrm{nm\,^{\circ}C^{-1}}$. This differential rate of tuning between the gain spectrum and cavity modes is an important consideration when designing laser diodes, particularly for operation at elevated temperatures.

When biased, laser diodes naturally undergo thermal tuning, arising from a number of sources. Below threshold, joule heating from material resistance is the predominant source of heating in and produces and $T \propto I^2$ dependence with additional sources of heating arising from absorbed spontaneous emission and non-radiative recombination. Above threshold free carrier absorption of coherent radiation in the active region also contributes to heating [31].

In practice, laser diodes are often thermally tuned via a Peltier element. Heating elements have also been integrated on chip to alter cavity temperatures in a controlled manner. From the perspective of PICs the effect of thermal induced tuning is becoming more important with increasing component density. The difficulty in thermally isolating components, means that there may be inter- and intra-component cross talk which may negatively affect performance.

2.4.3 Vernier tuning

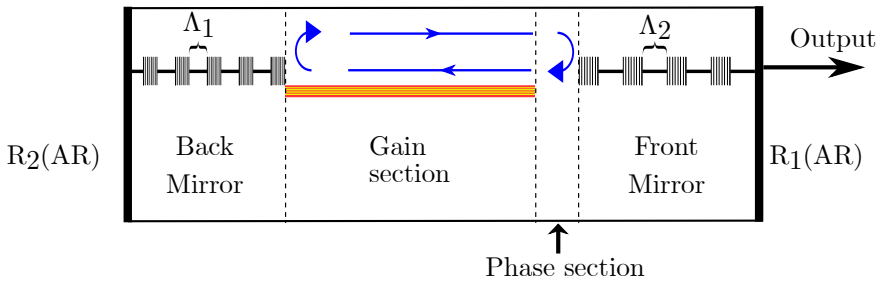

Figure 2.15: Schematic of a SG-DBR laser. Two gratings with differing periods Λ_1 and Λ_2 have reflection spectra with differing FSRs, resulting in a vernier effect.

The aforementioned tuning mechanisms when applied to DBR and DFB laser structures are limited in their tuning range by the maximum change in refractive index which each physical effect can induce. In order to exceed these limits, a wide number of laser designs have been developed which take advantage of the vernier effect to extend the tuning range [10, 32, 33, 34]. One example of a laser capable of vernier tuning is the sampled grating distributed Bragg reflector (SG-DBR) shown in Figure 2.15. Central to the functioning of such a laser is the inclusion of two grating structures, each with differing periods Λ_1 and Λ_2. By selecting the appropriate periodicity, a reflection spectrum as shown in Figure 2.16 can be achieved, where the blue and red lines represent the reflection spectra of the two gratings of period Λ_1 and Λ_2. The resulting product is seen in Figure 2.16 (bottom), where the largest peak will lase. As a result of the difference in spacing of the super-modes, a small change in the wavelength of one reflection spectrum can yield a much larger wavelength shift in the lasing spectrum. The right-hand side of Figure 2.15 shows the effect of shifting the wavelength of Λ_1 by 0.5 nm which translates to a significantly larger shift in lasing wavelength of -3 nm.

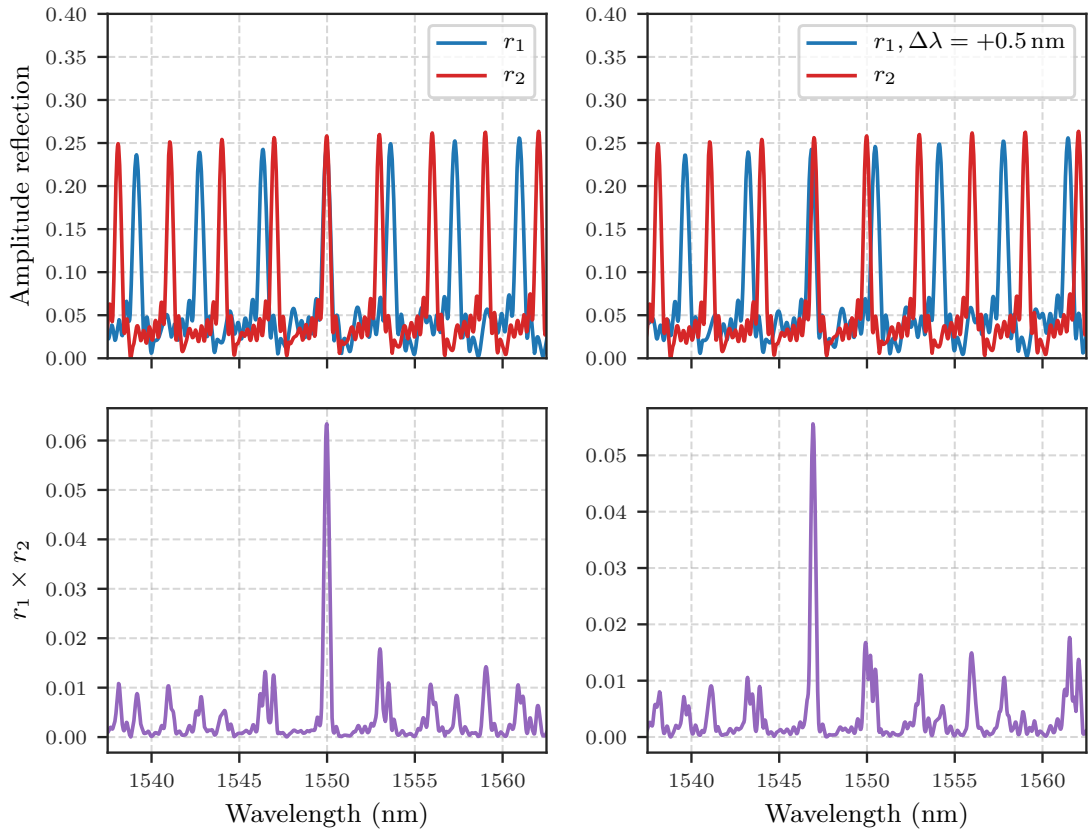

Figure 2.16: Illustration of vernier effect: reflection spectra produced by gratings in Figure 2.15 (top), spectra multiplied together where the largest peak determines the lasing mode (bottom). By tuning one of the spectra by a small wavelength a large wavelength change is achieved in the lasing mode.

2.5 Conclusions

In this chapter, the fundamentals of semiconductor laser diodes have been introduced. Conventional laser designs such as DFBs, DBRs and SG-DBRs, and the theory behind their gratings have been introduced. Various important properties of lasers including slope efficiency, linewidth and SMSR have been also been described.

The lasers presented in this thesis differ from the conventional lasers discussed thus far. In place of embedded gratings, slotted gratings are etched into the surface of the waveguide ridge, providing feedback and wavelength filtering. In the following chapter these slotted gratings and the theory behind them will be introduced. The method used to simulate the optical properties of slotted gratings will be discussed. In addition, the most recent design work which our group has undertaken and the laser fabrication process will also be introduced.

Chapter 3

Modelling, design and fabrication of slotted gratings

In conventional DFB and DBR laser diodes, gratings are embedded within the waveguide structure. As a result, radiation loss is generally small and a simple lossless one-dimensional (1D) transfer matrix method (TMM) can be used to simulate gratings. The lasers presented in this thesis, however, are formed by etching into the waveguide structure and this introduces radiation loss. Previously, Lu et al. [35] have shown the need to use the two-dimensional (2D) scattering matrix method (SMM) to analyse the slot characteristics in slotted single-mode semiconductor lasers. In this work the CAvity Modelling FRamework (CAMFR)[1] implementation of the 2D-SMM is used. In this chapter the basic principle behind the 2D-SMM and its application in designing slotted gratings will be introduced. Moreover, slotted gratings previously designed using the SMM will be discussed. Finally, the fabrication process for slotted grating lasers will be described.

3.1 2D scattering matrix method

In order to design an efficient single mode laser, the reflectivity, transmission, loss and bandwidth associated with the grating needs to be accurately modelled. To this end, the 2D scattering matrix method (2D-SMM) is used [36]. The 2D-SMM is based on the principle of eigenmode expansion and the use of scattering matrices. In a structure where the optical refractive index does not vary in the z direction, the solutions of

[1]CAMFR was developed by the photonics group of the Department of Information Technology (INTEC) at Ghent University in Belgium.

Maxwell's equations take the form

$$\begin{aligned} \mathbf{E}(x,y,z) &= \mathbf{E}(x,y)e^{(i\beta z)}, \\ \mathbf{H}(x,y,z) &= \mathbf{H}(x,y)e^{(i\beta z)}. \end{aligned} \tag{3.1}$$

In this form, $\mathbf{E}(x,y)$ and β are the eigenfunction and eigenvalue of the solution which has a simple harmonic z-dependence [37]. As eigenmodes, these equations satisfy the eigenvalue problem

$$(\nabla_t^2 + \omega^2\mu\epsilon)\mathbf{E} = \beta^2\mathbf{E}, \tag{3.2}$$

derivable from Maxwell's equations. We can express any solution of Maxwell's equations in terms of a superposition of the forward and backward propagating modes as

$$\begin{aligned} \mathbf{E}(x,y,z) &= \sum_{k=1}^{M} \left(a_k e^{(i\beta_k z)} + b_k e^{(-i\beta_k z)}\right) \mathbf{E}_k(x,y) \\ \mathbf{H}(x,y,z) &= \sum_{k=1}^{M} \left(a_k e^{(i\beta_k z)} + b_k e^{(-i\beta_k z)}\right) \mathbf{H}_k(x,y). \end{aligned} \tag{3.3}$$

In a linear medium where M goes to infinity, this set of equations represents an exact solution to Maxwell's equations. In a computational implementation, the number of modes is finite, but this truncation nevertheless yields accurate results [37].

Changes in the z direction (as occur in a grating) are modelled using the mode-matching technique and scattering matrices. The mode-matching technique is applied to the interface between two adjacent sections, requiring tangential components of the field $\mathbf{E}_t$ and $\frac{d\mathbf{E}_t}{dz}$ to be continuous. Once the mode matching technique has been applied to a single interface, the reflectivity and transmission of a stack of interfaces is calculated using the SMM. The SMM relates the outward propagating field of a structure to the inward propagating fields as follows:

$$\begin{bmatrix} b_1 \\ b_2 \end{bmatrix} = \begin{bmatrix} S_{11} & S_{12} \\ S_{21} & S_{22} \end{bmatrix} \cdot \begin{bmatrix} a_1 \\ a_2 \end{bmatrix}. \tag{3.4}$$

For a segment with no discontinuities, as shown is Figure 3.1a, the elements of the scattering matrix are

$$\begin{aligned} S_{11} &= S_{22} = 0 \\ S_{12} &= S_{21} = e^{-i\beta L}, \end{aligned} \tag{3.5}$$

where β is the propagation constant and L is the length of the segment. In the case of an effective index change at a dielectric interface, as shown in Figure 3.1b, the

elements of the scattering matrix are

$$\begin{aligned} S_{11} &= \frac{b_1}{a_1}|_{a_2=0} = r_{12} & \qquad S_{12} &= \frac{b_1}{a_2}|_{a_1=0} = t_{21} \\ S_{21} &= \frac{b_2}{a_1}|_{a_2=0} = t_{12} & \qquad S_{22} &= \frac{b_2}{a_2}|_{a_1=0} = r_{21}, \end{aligned} \tag{3.6}$$

where r_{ij} and t_{ij} are the reflection and transmission going from a material of refractive index n_i to n_j as shown in Figure 3.1b [25]. Using this method, the reflection and transmission spectra of a field incident on a grating can be accurately simulated, taking into account radiation loss. An in depth description of this model as well as its implementation in the form of CAMFR can be read in Bienstman [37].

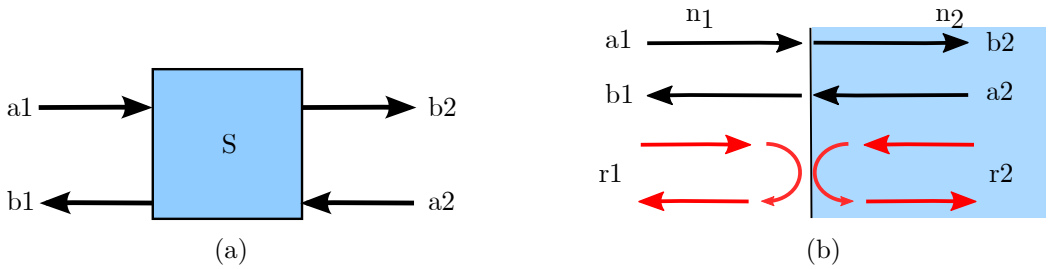

Figure 3.1: (a) Scattering matrix junction, (b) Dielectric interface.

3.2 Single mode slotted lasers

In modern optical communication networks, DFBs, DBRs and SG-DBRs represent the predominant in-plane single mode lasers. Together, these lasers cover many of the requirements for optical network applications, including low noise, tunability over the C-Band and good single mode operation. However, the fabrication of such lasers requires a grating to be patterned within the waveguide structure, with re-growth steps subsequently being necessary. In addition, low order gratings which require high resolution lithography, are generally used in these conventional lasers. The aforementioned factors increase both the complexity and the overall cost of fabrication. To address these issues, a simpler fabrication process can be adopted, whereby gratings are etched directly into the surface of a Fabry Pérot laser, forming a surface grating mirror. A three-dimensional (3D) schematic of a single mode slotted laser is shown in Figure 3.2. The laser consists of two electrically isolated sections; the gain section consists of an active region waveguide while the grating region consists of the slotted surface gratings. One advantage of the slotted laser design is that the laser is not dependent on reflection from the output facet, with the feedback provided by

the grating. This allows one to monolithically integrate various photonic components on a single chip. For instance, in Lu et al. [22] an electro absorption modulator was integrated and in Abdullaev et al. [21] an array of lasers was integrated with semiconductor optical amplifiers (OSAs). The successful demonstration of such components makes the integration of more complicated circuits possible. Thus, with only a single wafer growth, complex PIC structures can be relatively easily fabricated.

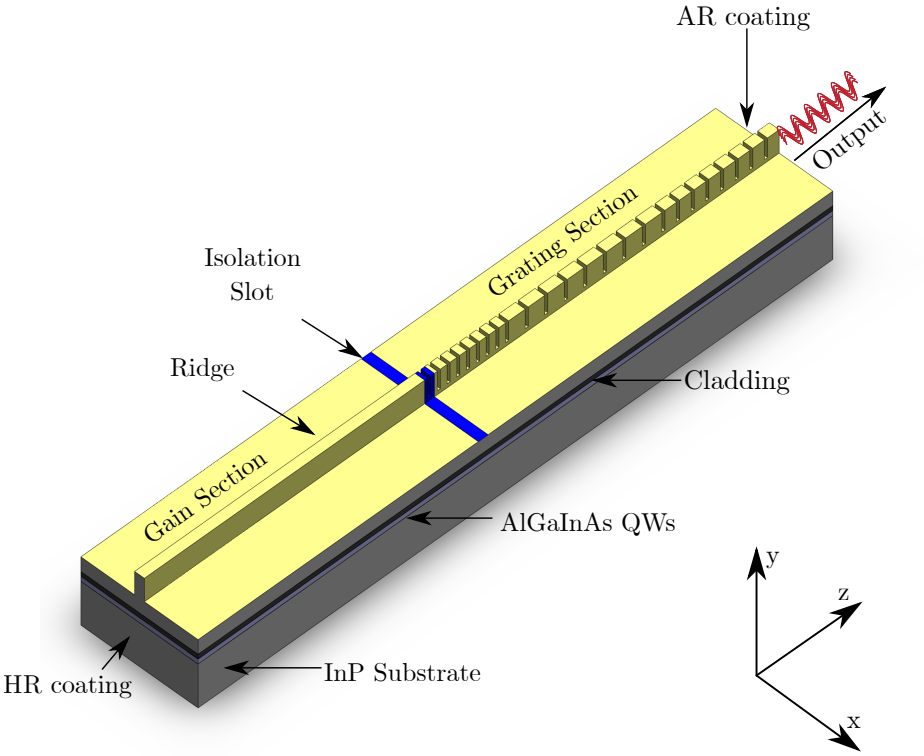

Figure 3.2: Slotted single mode laser with two electrically isolated sections.

3.2.1 Slotted grating design

Etching into the surface resolves the issue of re-growth — in order to reduce the required lithographic resolution, the surface grating is designed to be of high order, with the slot size generally set $\geq 1\,\mu m$ and a slot spacing of several microns. This high order grating can be fabricated with cheaper photo-lithography[2]. As with a DBR, the grating acts as a mode selection mechanism to obtain single mode lasing. The change in structure relative to conventional DBR and DFB gratings, requires us to re-examine some fundamental parameters when designing the slotted grating.

[2]It should be noted that the lasers presented in this thesis are in fact fabricated via e-beam lithography due to foundry limitations (see section 3.4).

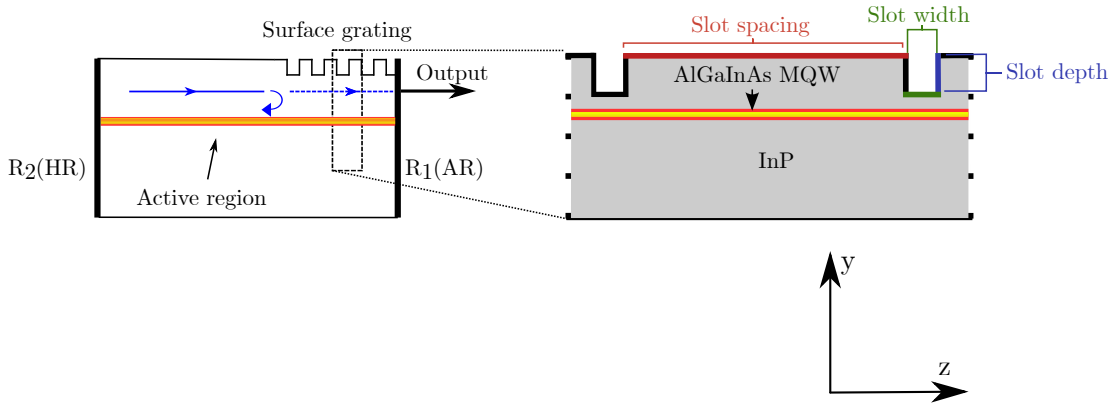

Figure 3.3: y,z plane of the cavity structure, illustrating the various slot parameters.

These parameters include, slot width, slot spacing, slot depth and the total number of slots, as shown is Figure 3.3. These parameters need to be chosen carefully, in order to produce sufficient reflection and a narrow reflection bandwidth.

Perhaps the most important parameter for single mode performance is the grating periodicity. The grating period is defined by the Bragg condition from Equation 2.9, with the period order m set to integer values; ensuring single mode lasing at the defined wavelength. Once the grating period Λ is defined, the slot width and slot spacing are related by

$$\Lambda = \Lambda_s + \Lambda_w, \tag{3.7}$$

where Λ_s is the slot spacing and Λ_w is the slot width. The slot width and spacing is again chosen to satisfy the Bragg condition,

$$\begin{aligned} \Lambda_s &= (m_s) \cdot \frac{\lambda_{Bragg}}{2n_s} \\ \Lambda_w &= (m_w) \cdot \frac{\lambda_{Bragg}}{2n_w}, \end{aligned} \tag{3.8}$$

where m_s and m_w are multiples of half integers (henceforth referred to as the slot spacing order and width order) n_w and n_s are the effective indices of the un-slotted and slotted waveguide respectively [38].

We now have a method whereby the grating period can be defined, however the final value which this will take in the case of slotted lasers is somewhat more complicated than embedded gratings. To illustrate this, Figure 3.4 shows the simulated field profile when encountering a slotted grating within a cavity. As a portion of the field is lost through the slot, the field is reduced immediately after the slot. As a result, the field requires a certain distance in order to recover and interact with the

next slot. The result of this is seen in the simulation shown in Figure 3.5 where the peak reflectivity has been simulated with changing period and slot width.

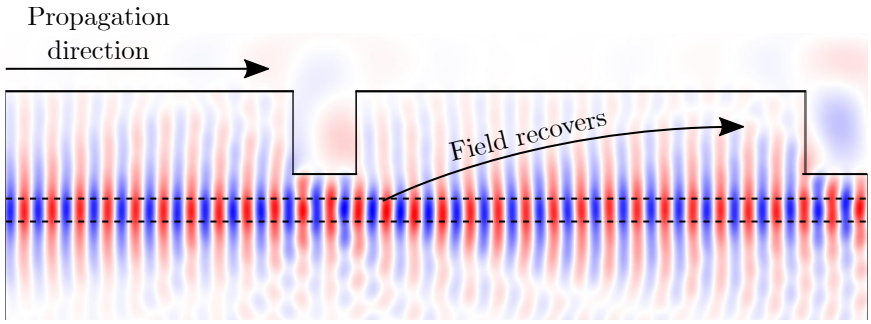

Figure 3.4: Simulated TE field profile.

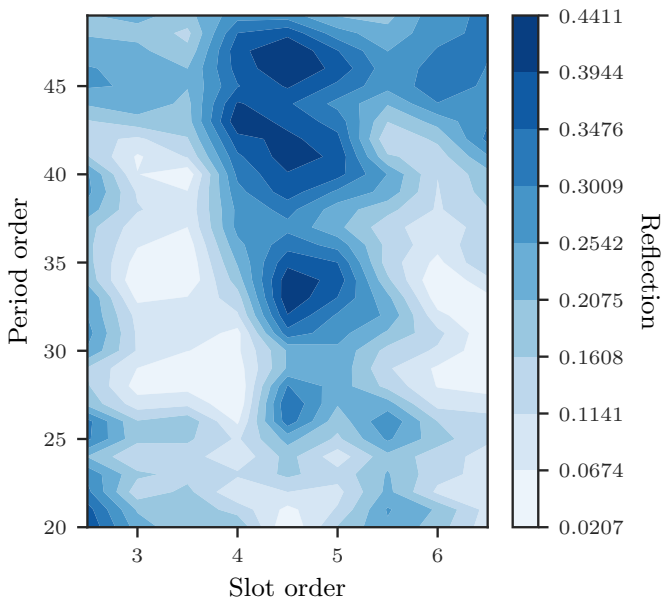

Figure 3.5: Contour plot of simulated amplitude reflection versus slot period order and slot width order for 20 slots, etched to 1.35 µm.

From this map it can be seen that lower order periods have less reflectivity, and below $m = 30$, the reflectivity is too low to be used in a laser structure. From this reflection map, the grating order was previously chosen to be 37 and the slot order was chosen as 4.5, thus providing sufficient reflection. However, a negative consequence of using such high order periods is a narrowing of the free spectral range (FSR) — the distance between successive Bragg wavelengths. The FSR can be calculated as

$$\Delta\lambda = \frac{\lambda^2}{2n_g\Lambda}, \tag{3.9}$$

where n_g is the group refractive index. From this equation, the FSR of a 37^{th} order grating is $\sim 40\,\text{nm}$, which is on the order of the gain bandwidth. As a result, the FSR reflection peaks receive gain and may compete with the desired lasing mode.

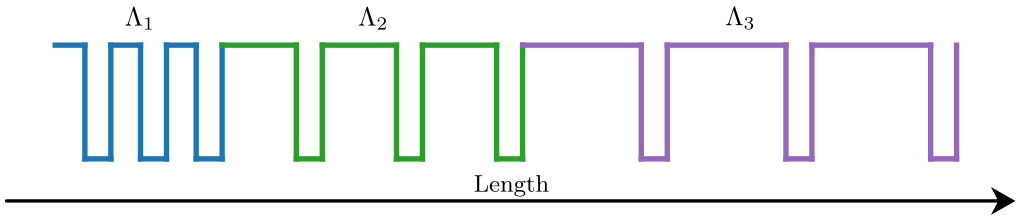

Figure 3.6: Schematic of a multiple period grating: in this case a three period grating. Individual colours correspond to the distinct grating periods.

In order to overcome competition from FSR peaks, a grating structure as shown in Figure 3.6 has been developed. The multiple sub gratings with differing periods, are all designed such that a Bragg peak occurs at the desired lasing wavelength, however, as the period changes there will be 3 distinct FSR spacings arising from the grating resulting in a reduced FSR peak reflectivity. This effect can be seen in Figure 3.7 where the simulated reflectivity of the 1510 nm and 1590 nm Bragg peaks are suppressed for a grating with three periods, as compared to the one period case. The effect on the lasing spectrum is experimentally measured in Figure 3.8 where the one period grating suffers from mode competition at $\sim 1575\,\text{nm}$, whereas the three period grating does not. By employing such multiple period gratings, we have successfully fabricated laser array capable of covering the C-band with SMSR $\geq 50\,\text{dB}$ [21].

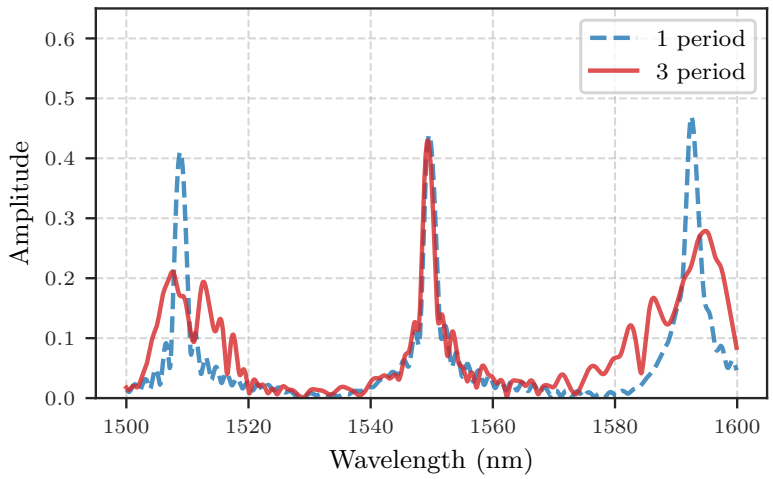

Figure 3.7: Reflectivity spectrum of a 1 and 3 period slotted grating. FSR reflection peaks are significantly reduces in amplitude in the 3 period grating.

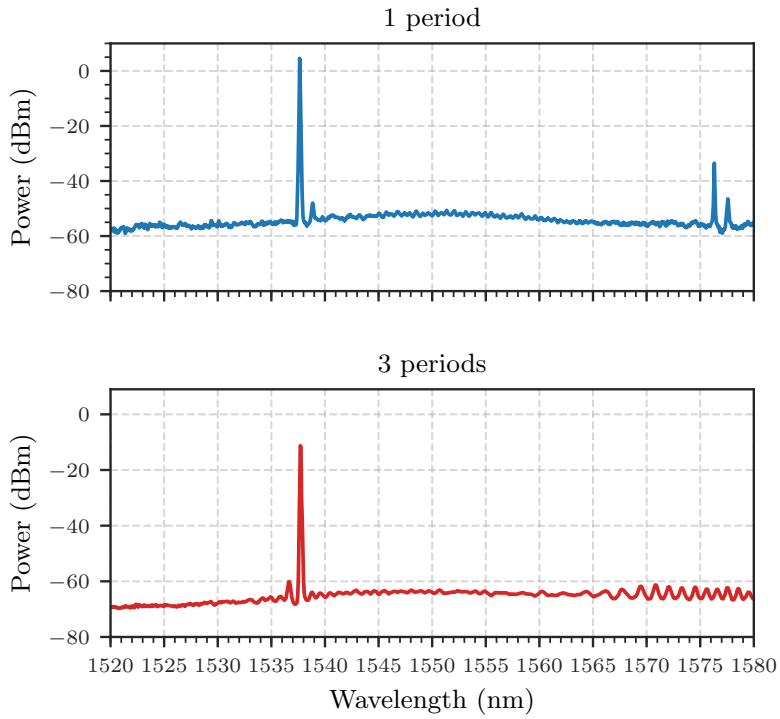

Figure 3.8: Measured lasing spectrum of a laser with a one period grating (top) compared with a three period grating laser (bottom). The competing mode resulting from the FSR reflection peak is significantly suppressed in the three period grating laser.

3.3 Widely tunable vernier lasers

In addition to single mode slotted lasers, the concept of a widely tunable laser utilizing slotted gratings, has also been investigated. Such widely tunable slotted lasers are analogous to the SG-DBR introduced in chapter 2, the main difference being that in place of sampled gratings deeply etched slots are employed. Figure 3.9 shows the schematic of such a widely tunable slotted laser. Similar to an SG-DBR, two gratings with different periodicities form the mirrors of the cavity, resulting in reflection spectra with differing FSRs. This allows one to utilize the vernier effect to tune over wide wavelength ranges (see Figure 2.16). The period of the back and front sections are determined using Equation 3.9, whereby a suitably narrow FSR must be engineered such that it is possible to tune into the required number of wavelength channels. As the FSR is $\propto \Lambda^{-1}$, a relatively large grating period must be chosen. In order to limit the length of the grating, the reflectivity per unit length needs to be increased. This is achieved by etching slots to a depth of 1.85 µm allowing for sufficient reflectivity to be achieved with ~ 9 slots. A detailed description concerning the design of these widely tunable vernier lasers can be read in Nawrocka [23].

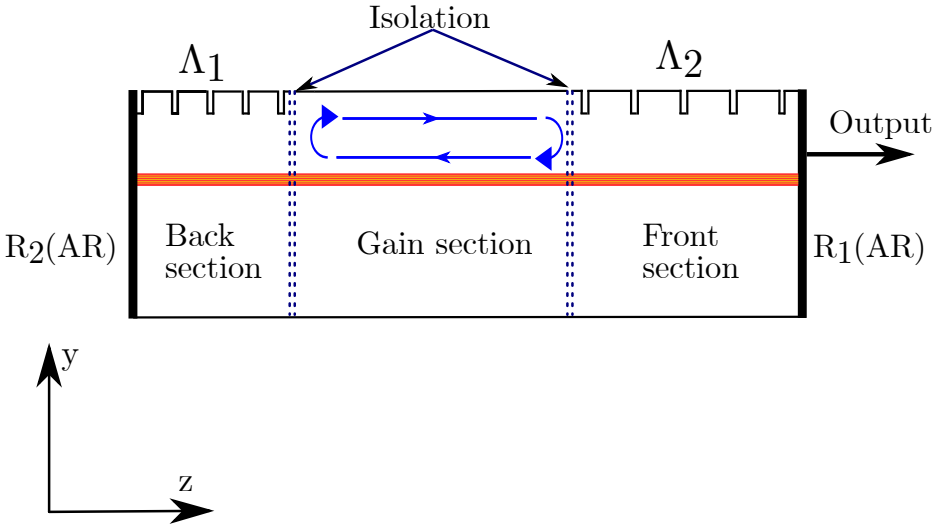

Figure 3.9: Slotted vernier laser schematic.

3.4 Laser fabrication

The experimentally measured laser diodes presented in this thesis were fabricated on a commercial wafer supplied by IQE PLC, the specifications of which are contained in Table 3.1. The wafer contains an active region consisting of five AlGaInAs quantum

wells with an emission peak at $\sim 1530\,\text{nm}$. Above the QWs there is: a $1.6\,\mu\text{m}$ thick p-doped InP layer, a $50\,\text{nm}$ thick p-doped InGaAsP layer, and a $200\,\text{nm}$ InGaAs contact layer. All devices presented in this thesis were fabricated in an external foundry[3]. The laser fabrication process for a single mode slotted laser is illustrated in Figure 3.10 where the main features are fabricated in the following sequence: slots and ridge, SiO_2 isolation layer, gold contact deposition.

Fabrication first involves forming the slots and ridge via two inductively coupled plasma (ICP) etch steps using Cl_2 and N_2 gas. The main steps involved in the single mode laser slot fabrication are as follows:

1. Silicon nitride (SiN) layer is deposited using a plasma enhanced chemical vapour deposition process (PECVD).
2. e-beam lithography is used to define the slots.
3. Deposition of SiO_2 to prevent etching of slots during first ICP etch.
4. First ICP etch to a depth of $0.5\,\mu\text{m}$.
5. Removal of SiO_2 to allow etching of defined slot patterns.
6. Second ICP etch to a depth of $1.35\,\mu\text{m}$.

The sum of the two etch processes results in a ridge depth of $1.85\,\mu\text{m}$ while the slots are $1.35\,\mu\text{m}$ deep. Once the etching process is complete, the laser is contacted. This is achieved by first depositing an SiO_2 isolation layer which is etched away on the top of the ridge, with a gold contact being subsequently deposited. The laser bars are then cleaved and the resulting facets coated in high reflection (HR) and anti-reflection (AR) films, before the chip is eutectic bonded onto an AlN carrier. The result of this fabrication process can be seen in Figure 3.11 where a single slot was imaged using a scanning electron microscope (SEM). One can see from the SEM the waveguide ridge has a rough surface on the lateral faces: the effect of this on waveguide loss is not clear and may have reduced performance on recent devices.

[3]CST Global Ltd

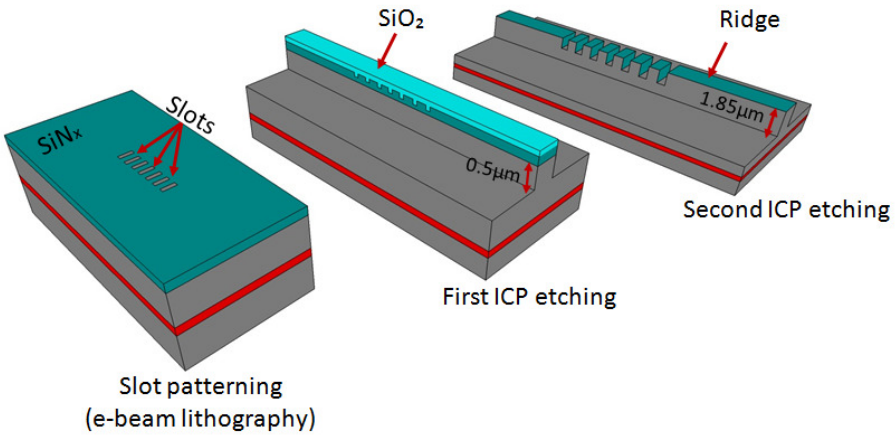

Figure 3.10: Overview of the slotted laser diode fabrication process. The absence of any re-growth reduces the complexity and number of steps required.

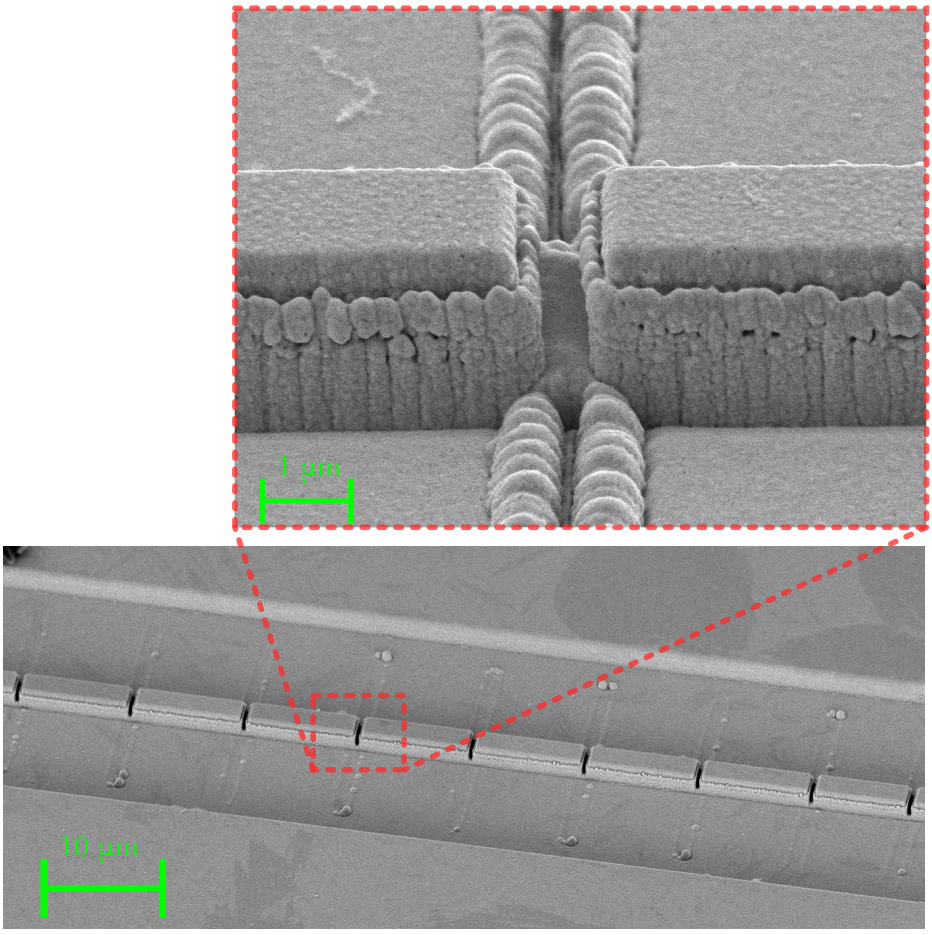

Figure 3.11: SEM image of a slotted grating (bottom) and a single slot (top).

Table 3.1: Specifications for the IQE wafer.

Layer	Material	Group	Repeat	Mole Fraction (x)	Mole Fraction (y)	Strain (ppm)	PL (nm)	Thickness µm	Dopant	Type	CV Level (cm^3)
16	GaIn(x)As	-	-	0.530	-	0	-	0.2	Zinc	P	$> 1.5 \times 10^{19}$
15	GaIn(x)As(y)P	-	-	0.71	0.62	0	1300 ±50	0.05	Zinc	P	$> 3 \times 10^{18}$
14	InP	-	-	-	-	-	-	0.1	Zinc	P	$> 1.5 \times 10^{18}$
13	InP	-	-	-	-	-	-	1.5	Zinc	P	$= 1.0 \times 10^{18}$
12	GaIn(x)As(y)P	-	-	0.85	0.33	0	1100 ± 20	0.02	Zinc	P	$= 1.0 \times 10^{18}$
11	InP	-	-	-	-	-	-	0.05	Zinc	P	$= 7.0 \times 10^{17}$
10	[Al(x)Ga]In(y)As	-	-	0.9	0.53	0	-	0.06	Zinc	P	$= 4.0 \times 10^{17}$
9	[Al(x)Ga]In(y)As	-	-	0.72 to 0.9	0.53	0	-	0.06	Undoped	-	-
8	[Al(x)Ga]In(y)As	-	-	0.44	0.49	-3000	1100 ± 20	0.01	Undoped	-	-
7	[Al(x)Ga]In(y)As	1	5	0.24	0.71	12000	1530	0.06	Undoped	-	-
6	[Al(x)Ga]In(y)As	1	5	0.44	0.49	-3000	1100 ± 20	0.01	Undoped	-	-
5	[Al(x)Ga]In(y)As	-	-	0.9 to 0.72	0.53	0	-	0.06	Undoped	-	-
4	[Al(x)Ga]In(y)As	-	-	0.9	0.53	0	-	0.06	Silicon	N	$= 1.0 \times 10^{18}$
3	[Al(x)Ga]In(y)As	-	-	0.86 to 0.9	0.53	0	-	0.01	Silicon	N	$= 1.0 \times 10^{18}$
2	InP	-	-	-	0	-	-	0.5	Silicon	N	$= 1.0 \times 10^{18}$
1	InP	-	-	-	0	-	-	0.3	Silicon	N	$= 3 \times 10^{18}$
⋮	SUBSTRATE										

3.5 Conclusions

In this chapter, slotted surface grating laser diodes have been introduced. The 2D-SMM has been described and its application to simulating slotted gratings discussed. The more recent single mode laser design for arrays and the concept of multi-period gratings and their importance have been described. Moreover, the slotted Vernier laser design has been introduced. Finally, the method whereby the lasers presented in this thesis were fabricated has been presented.

The following chapter provides a detailed characterisation of the tuning of these slotted laser diodes and investigates tuning schemes enabled by the isolation of grating and gains sections.

Chapter 4

Laser tuning and athermal stabilization

4.1 Introduction

In the previous chapter, the design of slotted grating laser diodes was introduced. In this design, the laser comprises two distinct sections, a gain section, and a grating section. These sections are electrically isolated allowing for individual control of the bias current in each section. In this chapter the tuning behaviour associated with such multi-section lasers is experimentally investigated and various applications thereof explored.

One particular application is the concept of athermalising the laser. In typical DWDM systems, wavelength stability is obtained by cooling the laser using thermo-electric coolers (TECs). This leads to expensive packaging costs and high energy consumption, which also reduces scalability. One solution to this is to athermalise the laser diode, making its lasing wavelength insensitive to temperature change by varying the currents across the laser sections, provided that the necessary optical power for the optical link and device reliability is realised at elevated temperatures. In order to athermalise a laser, it is necessary to control the thermal drift of mirror loss and cavity modes, and offset these against each other [39]. Although the design and fabrication of such lasers initially proved difficult [40], the performance and wavelength stability of athermal tunable lasers has improved significantly in recent years [41], with recent work by Zhu et al. [42] achieving wavelength accuracy of $\pm$ 3 GHz over a 15 to 70 °C range. This required control over the current supplied to 5 sections of the DS-DBR laser and feedback from a centralised shared wavelength locker [43].

An alternative to tunable lasers is materials based athermalisation, in which a waveguide consisting of two or more materials is engineered to balance the confinement factor with the thermo-optic coefficient such that the thermal drift is close to zero [39].

Towards this, materials-based athermal ring resonators [44] and DBR gratings [45] have been demonstrated in the literature. Furthermore, if athermalising a full WDM laser array, it is necessary to take thermal crosstalk between adjacent lasers into account, since this has been shown to be a significant issue in PICs [46].

While various athermal control schemes for tunable lasers have been proposed, these often add an extra layer of fabrication complexity to what are already comparatively high-cost lasers. Thus, this research has sought to implement athermal control for a low-cost, multi-section, high order grating laser under continuous wave operation, which is relevant to a wide range of cost-sensitive photonics applications. In order to achieve this, detailed characterisation of laser tuning behaviour needs to be undertaken. Also investigated, is the fundamental operation of these multi-section slotted lasers through the development of a phenomenological model and through thermoreflectance measurements.

4.2 Experimental Set up

4.2.1 Instrumentation

Figure 4.1 shows the experimental set up used to characterize the spectral and output power characteristics of the laser diodes. The lasers are operated on a copper heat sink, the temperature of which is controlled by a TEC. The different sections of the laser are supplied with independent injection currents from a Keithley 2400, Lightwave LDX-3200 and LDX-3210 source meters. In order to measure spectral properties, the output of the laser is coupled into a lensed optical fibre. The light passes through a 90/10 beam splitter with 90% detected by an Agilent 86140B Optical Spectrum Analyser (OSA) and 10% detected by a Keithley 6485 Picoammeter. The power reading of the picoammeter is used to adjust the fiber position until maximum coupling efficiency is achieved.

The output spectrum is recorded using an Agilent 86140B OSA with a maximum bandwidth of 0.06 nm being used with a sensitivity of -75 dBm. To measure the absolute power from a device, a germanium photo-diode is placed in front of the laser and the photocurrent is measured to obtain the output power.

4.2.2 Laser Characterisation

Using the set-up in Figure 4.1, spectral and light-current (L-I) characterisation of the laser diodes can be undertaken. Figure 4.2 shows L-I curves and measured output

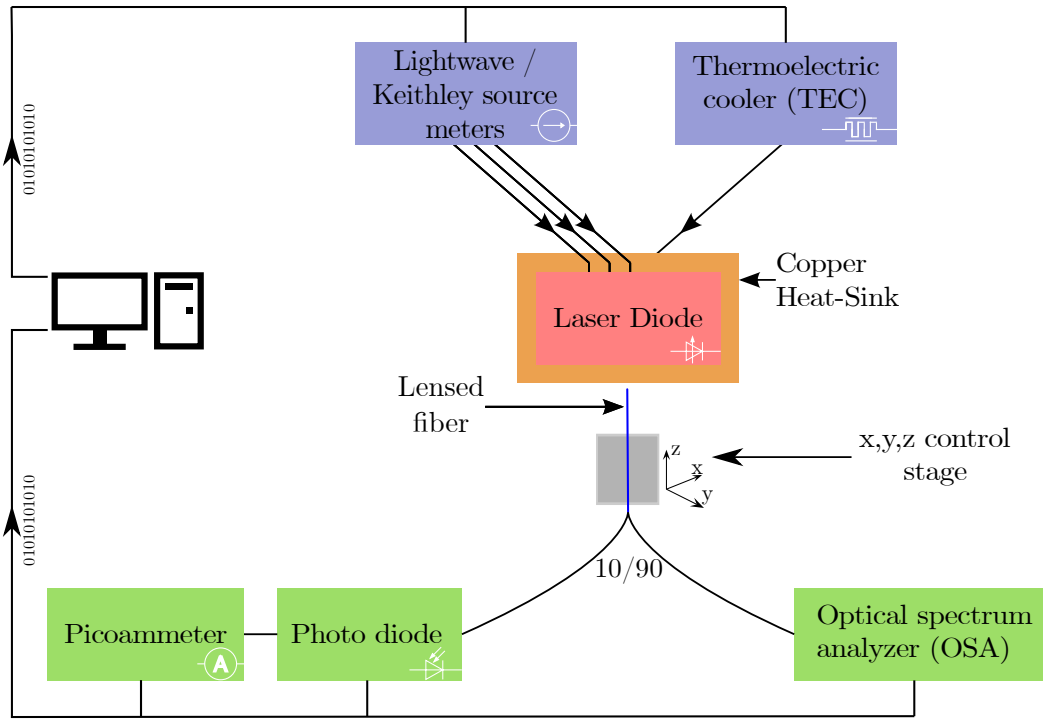

Figure 4.1: Experimental set up.

spectra for a 400 µm slotted laser diode array containing an integrated SOAs for each laser. Lasers were set on a TEC and tested under continuous wave (CW) conditions at 20 °C. The SOA section was left unbiased as its main effect is to raise the power output. Figure 4.2b shows the spectra of an array of 12 lasers where grating and gain sections are biased at a total of 100 mA, with each section at the equal current density. From this we can see that the SMSR performance varies from laser to laser. This variation is a result of the random nature of cleave error as discussed in chapter 2. The electrical isolation between the grating and gain section allows us to rectify this error by either tuning the grating section to shift the Bragg peak or tuning the gain section to shift the longitudinal modes to the optimal wavelength. The result of this tuning can be seen in Figure 4.3 where the c-band is covered with ≥ 47 dB SMSR. In this case the gain or grating section was tuned in an ad hoc manner to achieve better performance. The wider implications of this multi-section tuning are now investigated through detailed experimental characterisation and modelling.

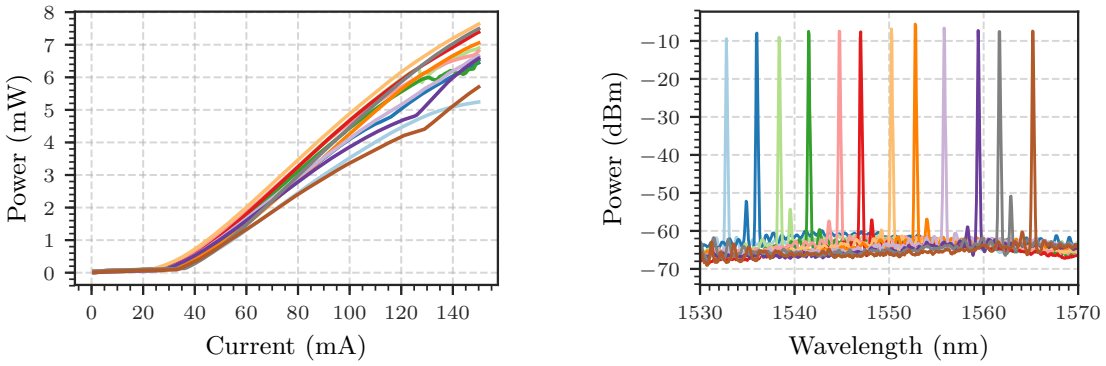

(a) LIV curves for an array of slotted lasers covering the C-band frequency range.

(b) Corresponing device spectra at injection current of 100 mA each.

Figure 4.2: 400 µm device performance.

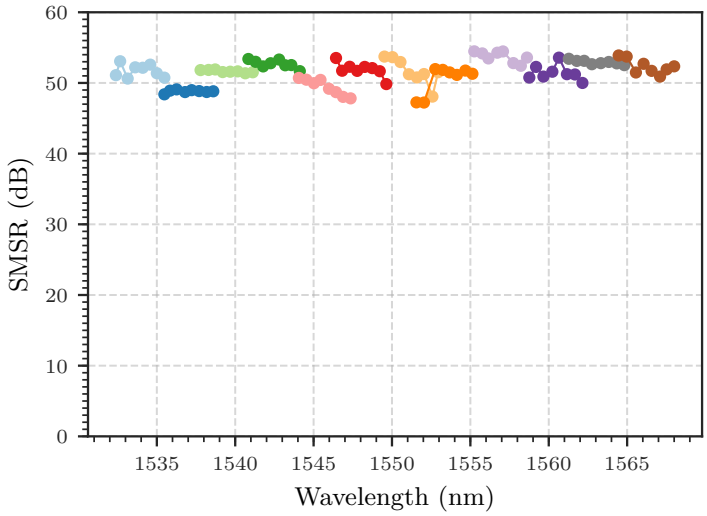

Figure 4.3: SMSR of a 400 µm cavity length array of 12 lasers temperature-tuned over the C-band. SMSR is maintained close to or above 50 dB over the tuning range.

4.3 Laser tuning

Figure 4.4 shows the shift in wavelength with respect to a range of grating and gain currents, for three different laser cavity lengths of 400 µm, 700 µm and 1000 µm. The tuning maps are recorded by sweeping the grating and gain currents and reading the peak wavelength on the optical spectrum analyser, while maintaining the submount at a constant temperature of 20 °C using the TEC. The discontinuities seen in the tuning maps correspond to the laser changing from lasing at one mode to another. These "mode hops" are caused by either the longitudinal modes or the Bragg peak shifting such that a side mode adjacent to the lasing mode coincides with the Bragg peak, resulting in a higher round trip gain for the competing side mode. Once the competing side mode has the highest round trip gain it will start to lase, resulting in the observed wavelength jump. The effect of such a mode hope on SMSR can be seen in Figure 4.5 which shows the SMSR corresponding to the 400 µm laser in Figure 4.4a. Regions close to a mode hop are seen to have reduced SMSR as the competing modes each have almost equivalent round trip gain.

From Figure 4.4, the rate of mode hops with grating current is seen to increase with cavity length. This is due to longer cavity length lasers having a narrower mode spacing and as such, a higher number of modes will be traversed by the Bragg peak as its wavelength shifts. For instance, in the case of the 400 µm length laser, which has a mode spacing of ~ 1.2 nm, a shift in the Bragg peak of 2 nm would result in a maximum of 1 mode hop. On the other hand, in the case of the 1000 µm length laser, which has a mode spacing of ~ 0.4 nm, a shift in the Bragg peak of 2 nm would result in a maximum of 5 mode hops. This results in longer cavity length lasers having a higher number of mode hops, as seen in Figure 4.4.

Figure 4.6a shows the tuning map for a 1000 µm cavity laser. The overlaid solid blue line represents the current path for which the gain and grating sections are biased at equal current density, i.e. the equivalent bias currents of the laser if the gain and grating regions were not isolated and were contacted with a single contact pad. One might assume that if gain and grating regions are biased at equal current density, the different tuning effects in each section would be equivalent. However, we can see from the tuning map that this cannot be the case as the laser undergoes a mode hop at a gain current of ~ 220 mA and grating current of ~ 75 mA as indicated by the blue circle in Figure 4.6a and Figure 4.6b. As the mode spacing is $\sim$0.4 nm, far smaller than the gain peak bandwidth, this tuning is purely due to index tuning. From this we can deduce that the longitudinal modes and Bragg peak are being tuned at different rates and thus, the gain and grating sections have some non-uniform physical

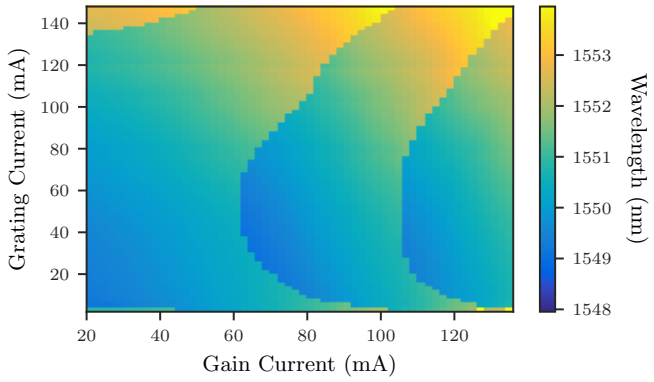

(a) Wavelength tuning map for a laser with 400 µm cavity length.

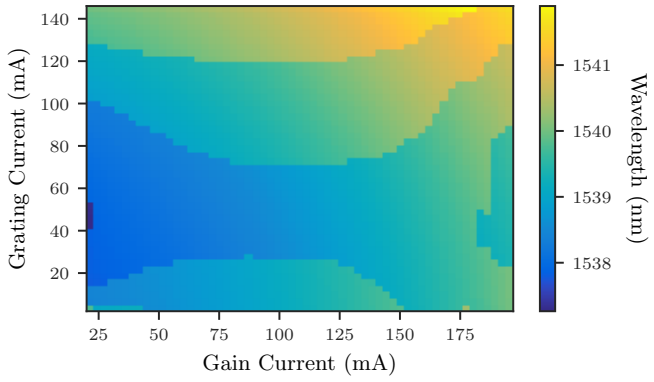

(b) Wavelength tuning map for a laser with 700 µm cavity length.

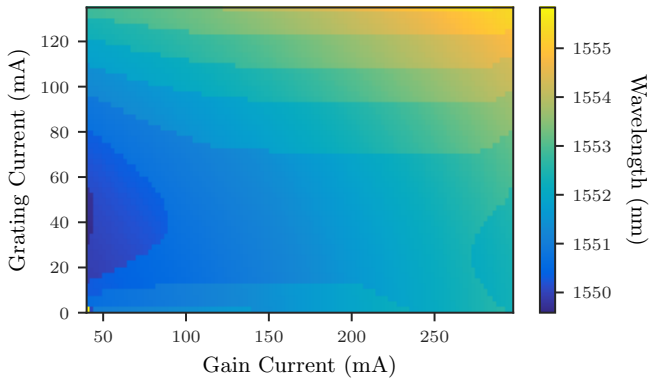

(c) Wavelength tuning map for a laser with 1000 µm cavity length.

Figure 4.4: Wavelength tuning maps of differing cavity lengths.

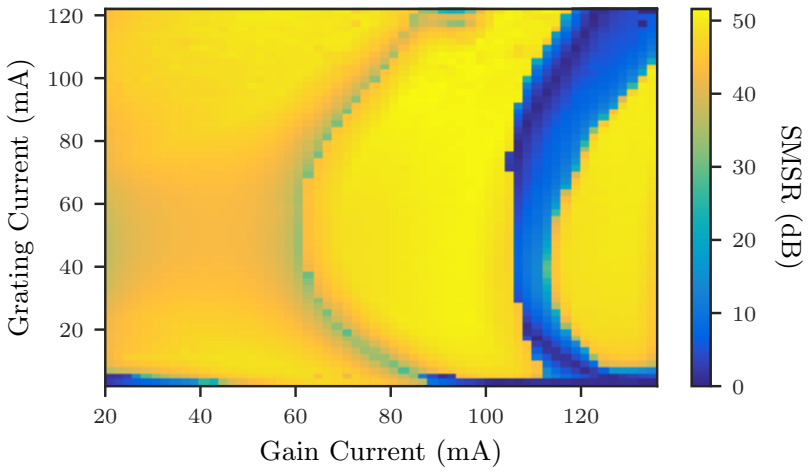

Figure 4.5: SMSR map for a laser with 400 µm cavity length.

property between them, despite having uniform injection current density. This non-uniformity is numerically examined in greater detail in chapter 5, subsection 5.6.3. Additionally, the red circle indicates a region where the laser is operating close to a mode hop resulting in an unstable lasing wavelength due to mode-hops. Naturally these discontinuities pose a problem for operating the laser in any optical communication system as the mode spacing of a 1000 µm laser is ~ 0.4 nm, significantly larger than the channel spacing of 0.1 nm specified in the highest density DWDM systems. As such, any mode hops would result in interference with neighbouring channels or a loss of signal at the receiver side of the network.

Figure 4.7a shows the corresponding map for output power found by sweeping the grating and gain currents and reading photo-current on the picoammeter. Again the solid blue line shows the current path for which the gain and grating regions are biased at equal current density. The corresponding output power along this path is shown in Figure 4.7 where one can see the jump in power at the mode hop as indicated by the blue circle.

In order to overcome the aforementioned performance issues associated with biasing the laser uniformly, we can take advantage of the isolated gain and grating sections to create a biasing scheme as show in Figure 4.8a. The solid red line shows the updated current path where gain and grating sections are biased at different current densities in order to avoid any mode hops. Figure 4.8b shows the corresponding lasing wavelength along this current path, where no mode hops occur and the laser tunes continuously. This tuning mechanism enables reliable operation of the laser

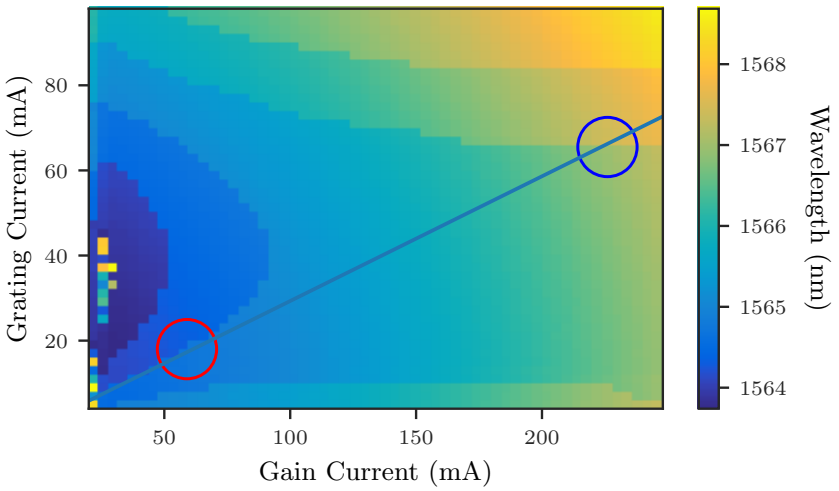

(a) Wavelength tuning map, solid blue line represents gain and grating sections under equal current density.

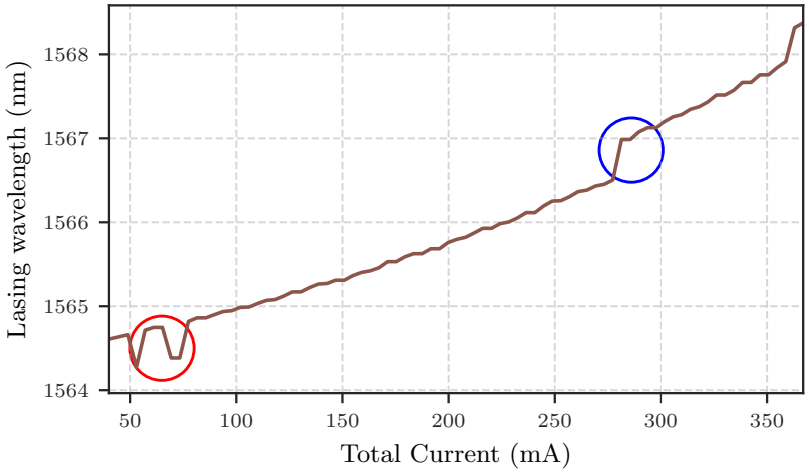

(b) Wavelength along solid blue line on the tuning map.

Figure 4.6: Wavelength tuning of a 1000 µm cavity length device.

diodes over a large current range and as such, over a larger current induced wavelength tuning range. We now turn our focus to applying this improved tuning with a view to stabilising the wavelength of laser arrays.

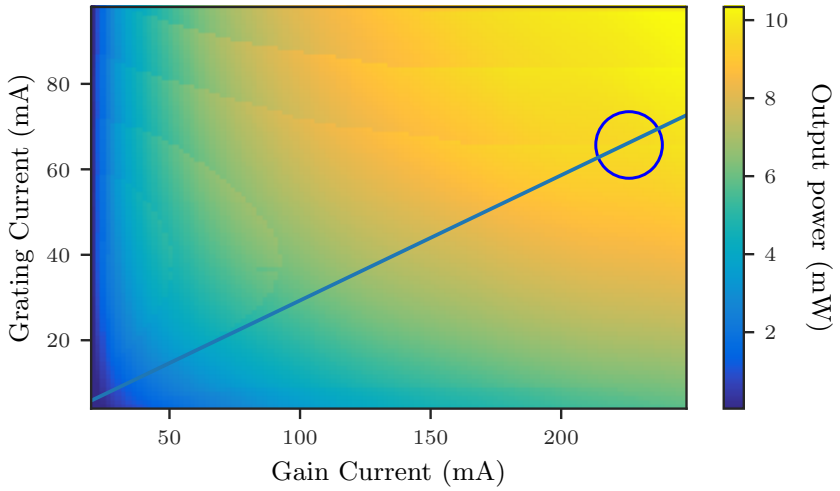

(a) Output power map, solid blue line represents gain and grating sections under equal current density.

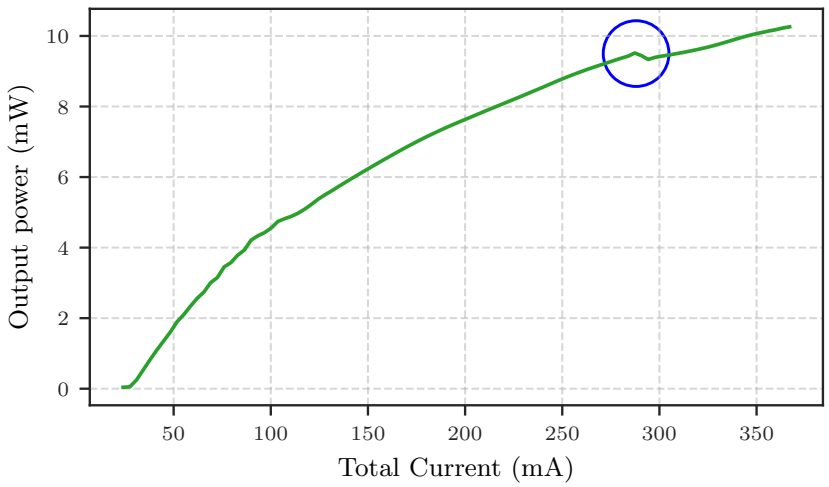

(b) Output power along solid blue line on the tuning map.

Figure 4.7: Output power of a 1000 µm device.

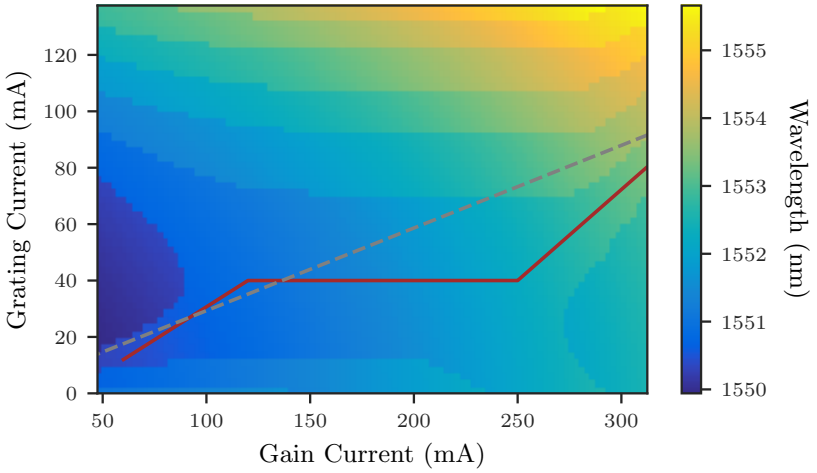

(a) Wavelength tuning map, solid red line represents improved tuning path, dashed gray line represents gain and grating sections under equal current density.

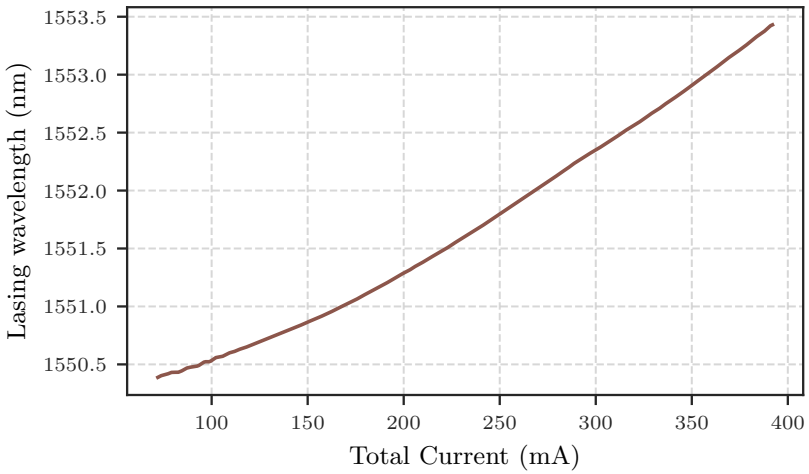

(b) Wavelength along solid brown line (improved tuning path) on tuning map.

Figure 4.8: 1000 µm device showing an improved tuning path.

4.4 Athermal operation

In conventional optical communication systems, a laser diode's wavelength is stabilised with the use of a TEC to maintain a constant laser temperature. Without such a thermal control, the laser temperature and thus wavelength will change with ambient temperature fluctuations. The characterisation of the tuning behaviour has thus far allowed us to improve and extend the single mode injection current tuning of the laser array. From this extended tuning we can develop control schemes to counteract laser wavelength drift with changes in ambient temperature.

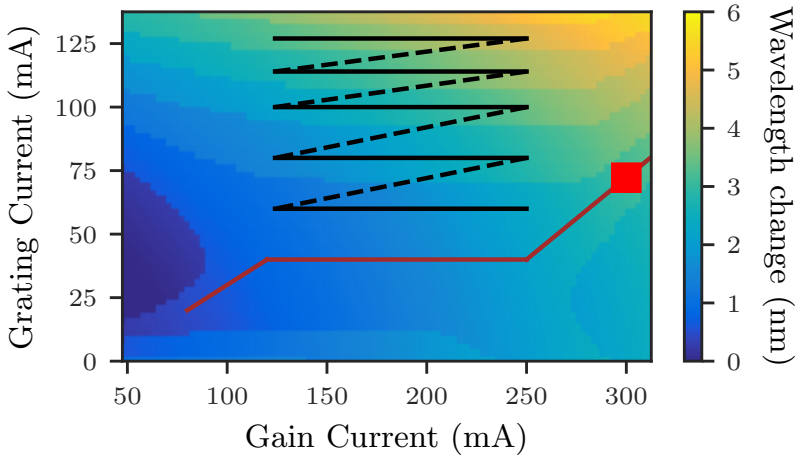

Figure 4.9: Experimental tuning map for a 1000 µm long laser cavity at 20 °C, where black and red lines represent discontinuous and continuous current paths, respectively. The red square corresponds to an ambient temperature of 20 °C during athermal operation.

The features of the tuning maps suggest two distinct control schemes, which we refer to as continuous and discontinuous tuning. In the continuous scheme, which is applied to a 1000 µm cavity laser, the longitudinal mode is not switched at any stage. This tuning path is similar to the path previously introduced in Figure 4.8a. The SOA is used to maintain stable power levels: as the SOA is outside of the laser cavity, it is sufficient to characterise a single SOA section on the laser array for output power against injection current and use this to compensate for changes in power for any cavity length. The tuning path is shown in Figure 4.9 where the red square indicates the point in the tuning path at 20 °C. We simulate changes in ambient temperature by changing the temperature of the copper heat sink using the Peltier element. As the laser wavelength drifts at $\sim 0.1\,\mathrm{nm\,°C^{-1}}$ we tune the laser via the injection current path to compensate. Note that as the wavelength red-shifts with

increasing temperature, the currents follow the red path from right to left. Figure 4.10 shows the wavelength, section currents and SMSR for the slotted device along this current path. This method yielded athermal operation up to 47 °C with a wavelength stability of ±0.04 nm / 5 GHz and a minimum SMSR of 37.5 dB. An output power stability of ±0.35 dBm was achieved as seen in Figure 4.12a, which also shows the wall plug efficiency during athermal operation. Achieving stability above 47 °C using this scheme proved problematic, as using higher gain section currents resulted in less stable behaviour, in large part due to the gain peak red-shifting leading to mode competition from the adjacent Bragg peak.

Rather than avoiding mode hops, the discontinuous control scheme utilises this behaviour to increase the range of athermal performance, switching the longitudinal mode by changing the current in the grating section. Once the device is lasing on one of these modes, the gain section is tuned to keep the mode wavelength stable, with continuous athermal performance for a 10 °C temperature range. When this 10 °C range is exceeded, the algorithm switches to a new mode by increasing or decreasing the grating current as required. As mode hops are no longer avoided, it is possible to utilise larger grating currents in this scheme to achieve athermal performance over an extended temperature range.

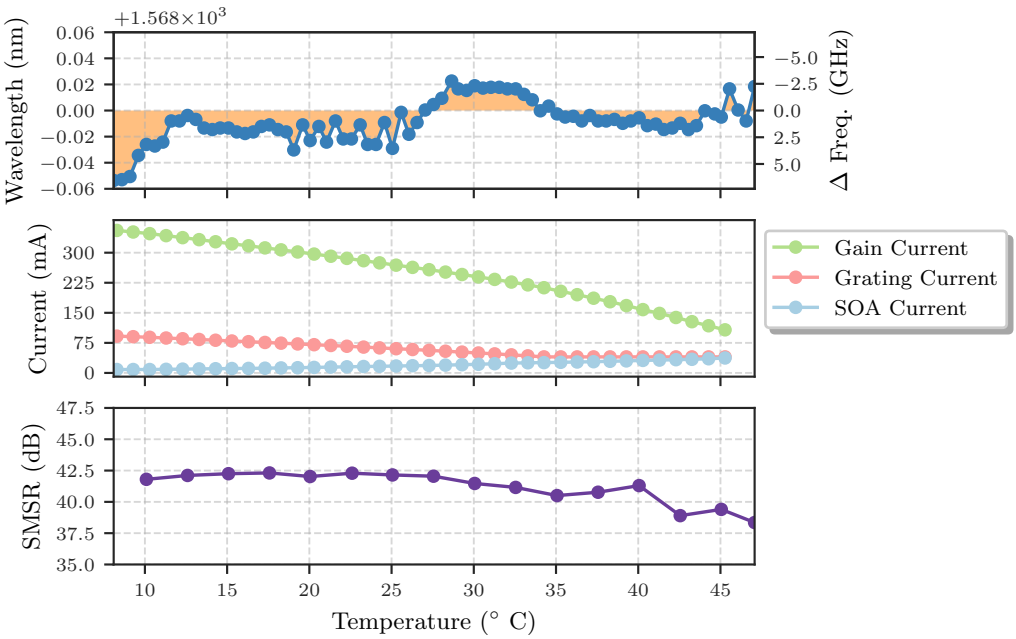

Figure 4.10: Wavelength tuning performance for continuous tuning scheme showing wavelength stability (top), applied currents (middle), SMSR (bottom).

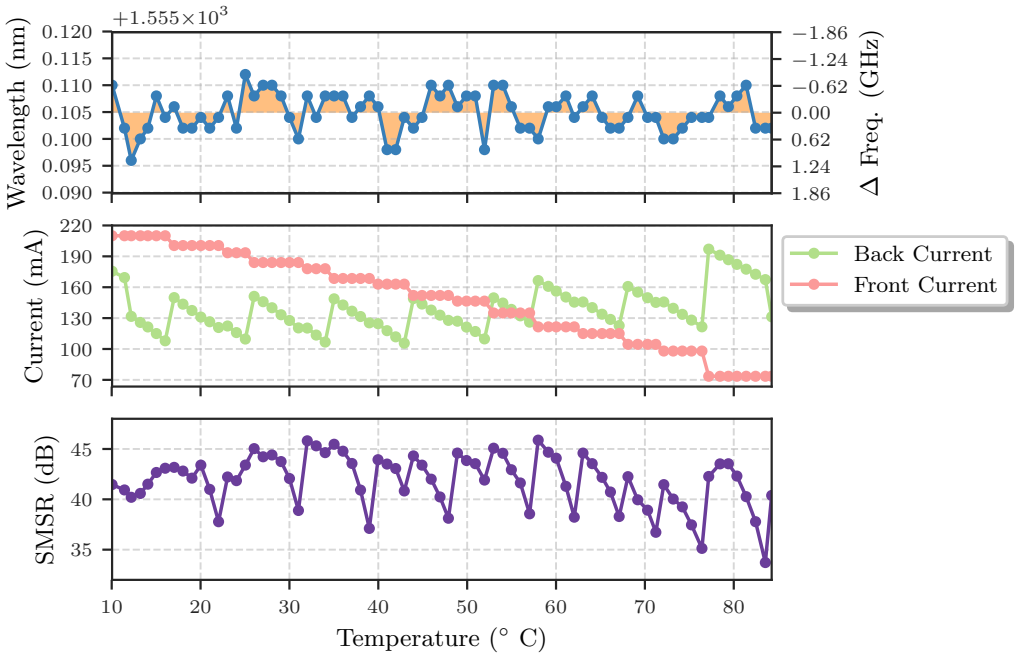

Figure 4.11: Wavelength tuning performance for the discontinuous tuning schemes showing wavelength stability (top), applied currents (middle) and SMSR (bottom) .

The black lines on the tuning map in Figure 4.9 are indicative of the tuning currents, where the dashed black line show the jumps in current. Figure 4.11 shows the wavelength, section currents and SMSR for the slotted device along its current path. This method yields extended athermal operation from 10 °C up to 85 °C (note: we did not operate the TEC below 10 °C to avoid water condensation on our unpackaged devices), with a wavelength stability of ±0.01 nm/±1.25 GHz and a minimum SMSR of 38 dB. This performance is equivalent to experiments on more complex DS-DBR devices [42] but has the additional benefit of being achieved on our low cost devices. It should be noted that as we are switching modes to maintain stable wavelength, there is a transient wavelength response associated with each mode hop, during which the wavelength is not stable. The wavelength measurements shown do not have the necessary temporal resolution to characterise these transient effects as they are generally in the order of micro seconds for such devices. Such transients in lasing wavelengths are not desirable in DWDM systems where the lasing wavelength is required to be stable at all times and fluctuations in laser power can cause damage to components in the network.

Additionally, output power was kept above 10 dBm with a maximum of 13.1 dBm as seen in Figure 4.12b. The wall plug efficiency in Figure 4.12 does not take the TEC

power into account, since the TEC is only used to simulate various ambient conditions and is not used for temperature control. We observe a maximum wall-plug efficiency at higher temperatures, as the currents used for stabilization of the laser are lower.

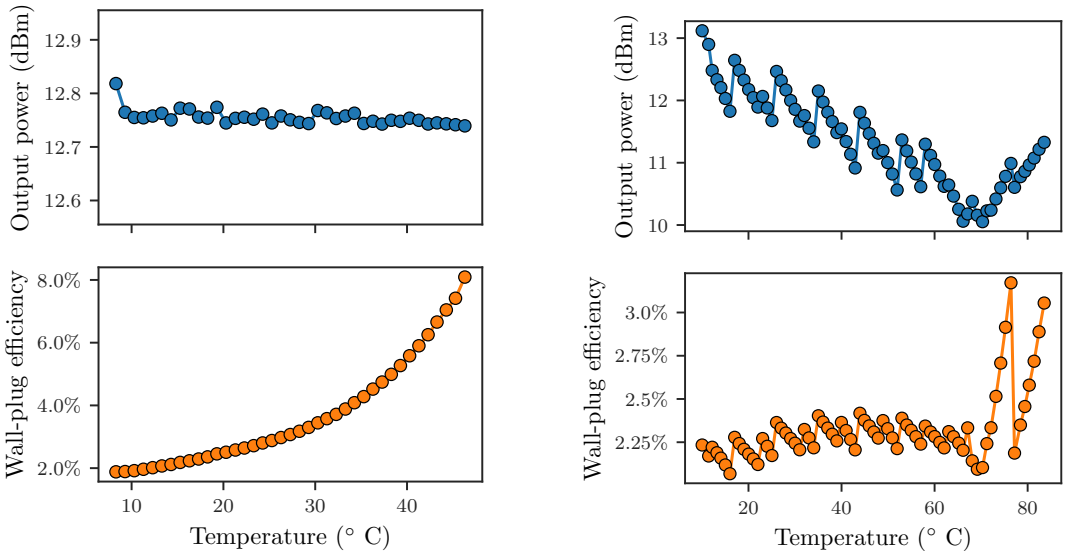

Figure 4.12: Output power (top), wall-plug efficiency (bottom) for (a) the continuous tuning scheme with the output power stabilised using the SOA and (b) the discontinuous tuning scheme.

For some WDM systems, it is necessary to operate an array of lasers rather than a single device. Figure 4.13 extends the discontinuous control scheme to three lasers on a 12 laser array, which span $\sim$ 28.5 nm. In this case, the wavelength stability drops to $\pm$ 1.75 GHz (which is still within the spacing required by DWDM), while the maximum temperature decreases to 80 °C on the blue end of the array. Thus, it should be possible to athermalise a full laser array: however, the thermal cross-talk between adjacent lasers would be a significant factor in the successful operation of this system. Taking this crosstalk into account will require further modelling, building on our previous work [46].

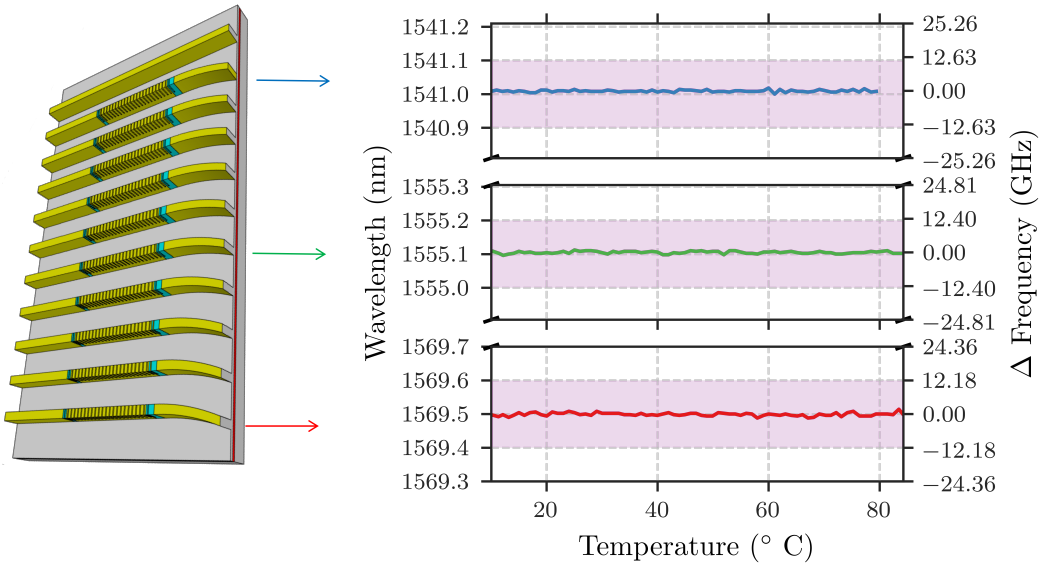

Figure 4.13: Wavelength tuning performance for three lasers (numbers 1, 6 and 12) in a 12-laser array at a heat sink temperature of 20°C. For comparison, shaded regions represent the maximum spectral excursion of ±12.5 GHz allowed for a 50 GHz channel spacing next-generation passive optical network 2 (NG-PON2) transmitter [47].

4.5 CCD-TR surface temperature measurements

As we have moved away from a simple uniform tuning protocol, we can expect the athermal tuning to result in more asymmetric behaviour over the length of the cavity. Therefore, it is instructive to experimentally study the temperature distributions in each section of the laser during operation. While the operating temperature of each section can be found using wavelength measurements of the laser output, these only provide a spatially averaged temperature within each section. However, since the various laser sections are not thermally isolated, it is likely that temperature gradients will exist along the waveguide during athermal operation. Measuring the surface temperature distribution directly proves difficult using traditional techniques: infrared (IR) thermography has poor resolution (5-10 µm) and struggles with the low emissivity of the gold contacted laser, while the micro-thermocouples used in scanning thermal microscopy (SThM) absorb the light of light-emitting surfaces, resulting in measurement errors [48].

Herein, we obtain temperature fields across the device using CCD based thermoreflectance imaging (CCD-TR) [49]. CCD-TR does not face the aforementioned issues and provides images of the temperature field at up to 250 nm resolution.

4.5.1 CCD-TR method

Thermoreflectance microscopy is based on measuring the relative change in the reflectivity of a sample as a function of a change in temperature. The method relies on the reflectivity of said material having a large enough dependency on temperature to be measurable via a CCD sensor. Over small temperature excursions, this relation between reflectivity and temperature change can be approximated as first order, i.e.:

$$\frac{\Delta R}{R} = \left(\frac{1}{R}\frac{\partial R}{\partial T}\right)\Delta T = \kappa \Delta T, \tag{4.1}$$

where $\Delta R/R$ is the relative change in reflectivity, ΔT is the surface temperature change, and κ is the temperature-dependent thermoreflectance coefficient, typically in the range 10×10^{-3} to $10 \times 10^{-4}\,\mathrm{K}^{-1}$ [50]. In our case, the laser diodes are contacted with a layer of gold which has a thermoreflectance coefficient measured to be $\sim 2.2 \times 10^{-4}\,\mathrm{K}^{-1}$ at 515 nm.

Due to this weak dependence, lock-in detection is required to extract small signals from the noisy signal. Figure 4.14 shows the schematic of the CCD-TR set up used for the proceeding measurements. The CCD-TR method specifically operates using a periodic current source and a phase locked CCD camera in a standard microscope configuration. Each pixel effectively becomes a locked-in detector, which allows for wide-field thermal imaging with up to 250 nm resolution in a standard optical microscope (20x magnification, NA=0.65).

The maximum theoretical sensitivity of a CCD-TR measurement is $\kappa/2^b$ where b bit depth of the camera. For our case, $b = 12$ gives a maximum sensitivity $\sim 1\,\mathrm{K}$, assuming ideal measurement conditions. In practice this sensitivity is not achieved for a single measurement. In order to increase to signal-to-noise ratio, the frames captured from the camera are averaged, scaling the sensitivity as $1/\sqrt{N}$ where N is the number of thermal cycles. The number of averages required were on the order of N =1000 which gave sufficient temperature resolution.

Because the CCD-TR relies on the difference between successive images, the stability of the sample being measured becomes critical. Post processing techniques such as image stabilization can be used to correct for vibrations. An image stabilization algorithm is described in Appendix B which is used in later CCD-TR measurements in chapter 5. Vibrations can be reduced in future by implementing anti-vibration tables.

Full details of the technique and the application space are provided in the comprehensive review by Farzaneh et al. [48].

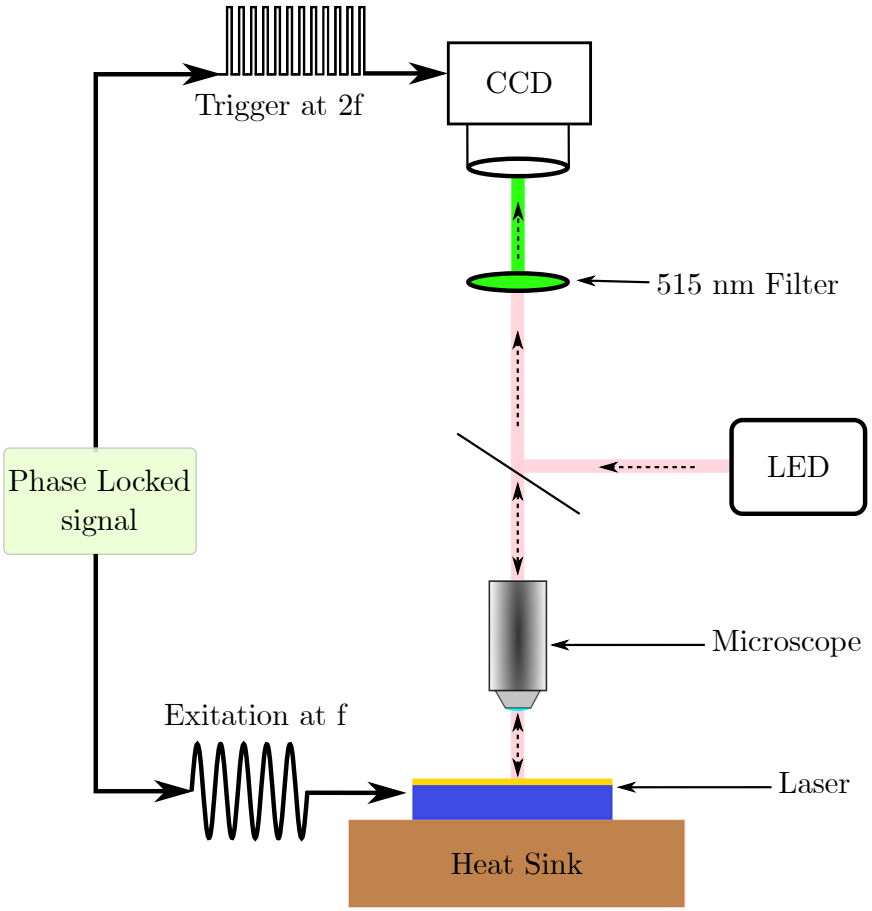

Figure 4.14: CCD-TR set up.

Table 4.1: Mean temperatures across the gain and SOA section, along with the resultant temperature gradient across the grating section.

T_{TEC} [$^{\circ}C$]	I_{gain} [mA]	$I_{grating}$ [mA]	I_{SOA} [mA]	ΔT_{gain} [$^{\circ}C$]	ΔT_{SOA} [$^{\circ}C$]	dT/dx [mK/μm]
15	180	50	20	22	6	-29.6
20	154	50	22.4	18.7	5.2	-4.1
25	124.4	50	26	15.5	8.6	-2.2
30	88.8	50	31.5	11.2	12.5	-1
35	40.4	50	41.4	5	18.5	+1.3

Figure 4.15 shows CCD-TR images of a 700 µm laser at ambient temperatures of (a) 15, (b) 25 and (c) 35°C, each of which consists of three images 150 µm x 250 µm in size stitched together. At each temperature, the current in the gain, grating and SOA sections are chosen in line with the continuous athermal tuning scheme to maintain constant output power and wavelength. The CCD-TR technique yields surface plots of differential reflectivity, which can be converted to temperature by performing a steady state calibration on the gold sections to find the thermoreflectance coefficient ($\kappa =$

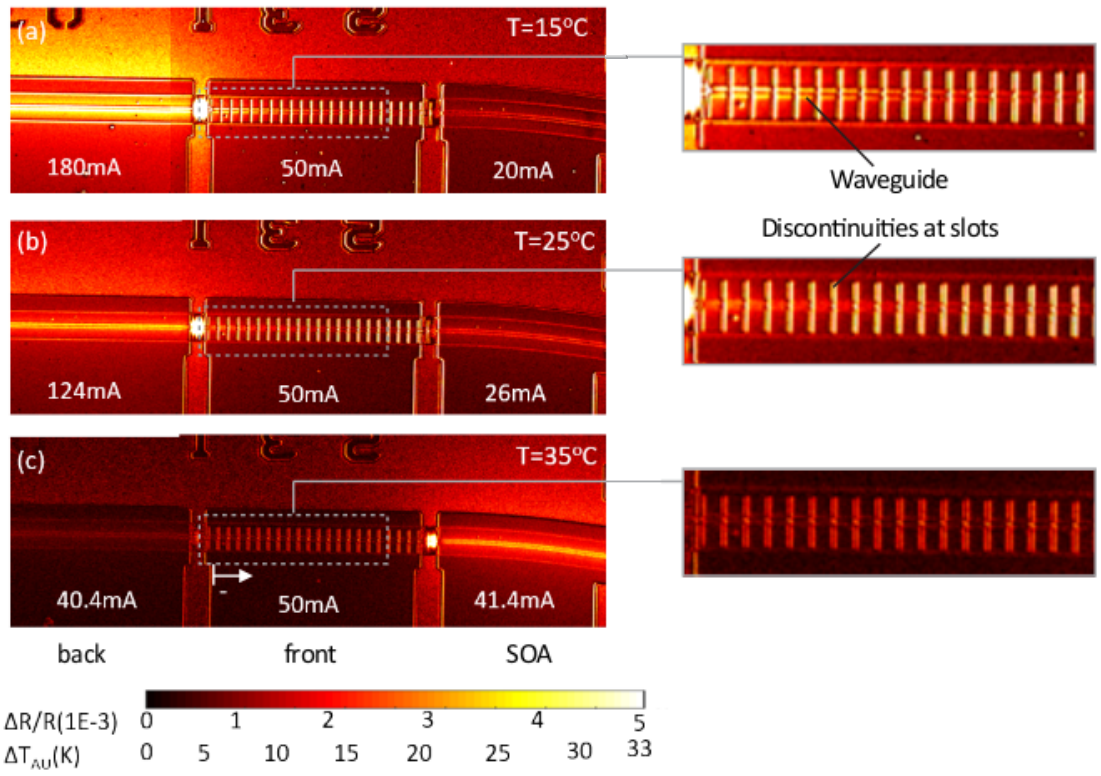

Figure 4.15: CCD-TR images: temperature profile of three section laser operating athermally at ambient temperatures of (a) 15°C, (b) 25°C and (c) 35°C. Inset are the currents to each section to maintain athermal performance. $\Delta R/R$ is the relative change in reflectivity and ΔT is the amplitude of the temperature increase from the ambient temperature in each case. Magnified views of the grating sections are also provided.

-1.5×10^{-4} [1/K]). At each of these operating conditions, we observe very different temperature distributions across the waveguide. For the range of current densities used in these CCD-TR experiments, we observe relatively constant temperatures in the gain and SOA sections, but observe temperature gradients across the grating section. These are more obvious in the magnified images of the grating section in Figure 4.15.

In these images, we also observe regions of apparently significantly elevated temperature at the slots and around the laser contact pads. These measured temperature spikes are artefacts due to a drawback of CCD-TR; namely that changes in reflectivity due to changes in height or material are equated to changes in temperature. Since the grating is etched into the structure, sharp discontinuities are observed due to the 1.35 µm deep slots, which can be removed from the temperature distribution via low-pass filtering. Table 4.1 tabulates this thermal gradient, along with the steady state

temperature of the gain and SOA sections.

In order to determine the significance of these gradients, the reflectivity on the grating was simulated using the 2D-SMM over a range of experimentally measured gradients. Figure 4.16 shows the reflectivity spectrum at different gradients, the influence of which is seen to have a negligible effect on the shape of the Bragg peak and as such, the gradients induced by the tuning protocols will not deteriorate device performance in this regard.

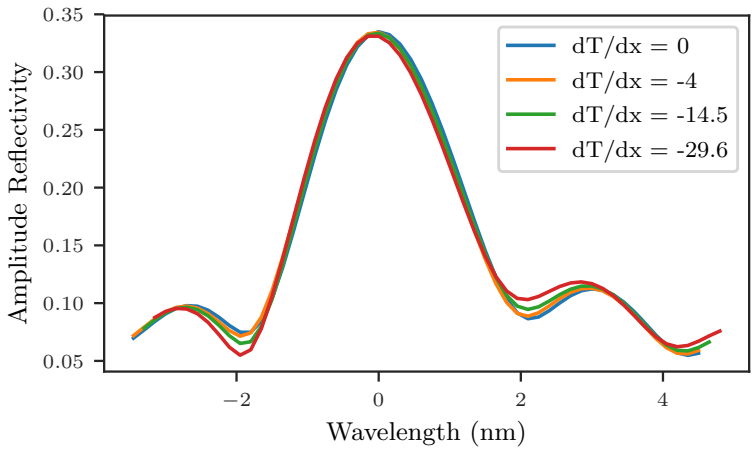

Figure 4.16: Simulated grating reflectivity for experimentally measured thermal gradients ($\mathrm{mK\,\mu m^{-1}}$), thermal gradients induced by the athermal tuning have a negligible effect on the grating reflection spectrum.

4.6 Device modelling

The preceding characterisation of multi section lasers has given us insight into the tuning behaviour and yielded methods to compensate for non-uniform tuning effects and thermal drift. We now wish to gain a better understanding of the physical processes involved and develop a model to predict multi-section laser wavelength tuning. As we are modelling 2D tuning maps for numerous devices, the significant run time of existing discretised time domain models, as described in [51], becomes an issue. To this end we have developed the following analytical model with the goal of reproducing the tuning maps of multi-section devices with minimal run-time.

4.6.1 Model theory

To find the tuning behaviour of the laser it is necessary to solve for the wavelength shift of the Bragg peak ($\Delta\lambda_{Bragg}$) and the shift in the wavelength of longitudinal modes of the cavity ($\Delta\lambda_L$). The grating structure in the laser is etched into the waveguide and as such, a fraction of the field profile will be radiated from of the grating. This loss requires us to use the 2D-SMM (discussed in chapter 3) to calculate the reflectivity and transmission spectra of the grating.

Table 4.2: Analytical model parameters

Parameter	*Symbol and unit*	*Values*
Active layer thickness	d (µm)	0.03
Active layer width	w (µm)	2
Non-radiative linear recombination	A ($10^8\,s^{-1}$)	1
Bimolecular recombination	B ($10^{-10}\,cm^3s^{-1}$)	1
Auger recombination	C ($10^{-30}\,cm^6s^{-1}$)	7.0
Waveguide loss	α_i (cm^{-1})	28
Transparency carrier density	N_{tr} ($10^{18}\,cm^{-3}$)	1.9
Differential gain	$^{dg}/_{dN}$ ($10^{-17}\,cm^2$)	1.2
Effective index change with carrier density	$^{dn}/_{dN}$ ($10\times10^{-21}\,cm^3$)	-3.65
Spontaneous emission contribution	$R'_{sp}\sim(10\times10^{23}\,cm^{-3})$	1.02
Gain saturation coefficient	ϵ_0 ($10^{-16}\,cm^3$)	6
Group index	n_g	3.6
Confinement factor	Γ	0.05
Injection efficiency	η_i	0.8
Grating reflectivity	r1	∼0.4
Back facet reflectivity	r2	0.95
$g(\lambda)$ parameters		
	b_1 ($cm^{-1}nm^{-2}$)	0.05
	b_2 ($10\times10^{-17}\,nm\,cm^3$)	-2.7
	b_3 ($nm°C^{-1}$)	0.5

The physical effects contributing to the wavelength shift of the reflection peak and longitudinal modes are split into carrier and thermal and solved separately. The wavelength shift due to carrier density changes is found by considering the grating and gain sections separately and solving the carrier and photon density rate equations, given by

$$\begin{aligned}\frac{dN}{dt}=0&=\frac{\eta_i I}{qV}-R(N)-v_g g(N)P,\\ \frac{dP}{dt}=0&=(\Gamma v_g g(N)-\frac{1}{\tau})P+\Gamma R'_{sp}+P_i,\end{aligned}\tag{4.2}$$

where η_i is the injection efficiency, I is the injection current, q is electron charge, V is the active region volume, v_g is the group velocity, Γ is the confinement factor, R'_{sp} is the spontaneous emission contribution and P_i is the rate of photons entering the grating from the gain section when above threshold [25]. P_i is calculated assuming the steady state approximation $P_i = \frac{n_i(I-I_{th})}{qg_{th}VL}$ where I_{th} is the threshold current, g_{th} is the threshold gain and L is the length of the grating [25]. Values for these constants can be found in Bello et al. [51] and Coldren, Corzine, and Mashanovitch [25]. $R(N) = AN + BN^2 + CN^3$ where A is the non-radiative linear recombination, B is the Bimolecular recombination and C is the Auger recombination coefficient. The photon lifetime τ can be defined in terms of the waveguide and mirror losses, while the gain $g(N)$ is described as a linear function of the grating section carrier density, i.e.

$$\tau = \frac{1}{v_g(\alpha_i + \alpha_m)}, \qquad g(N) = \frac{dg}{dN}\frac{N - N_{tr}}{1 + \epsilon P}, \tag{4.3}$$

where α_i is the waveguide loss, α_m is the minimum mirror loss at the Bragg peak, N_{tr} is the carrier density at transparency and $\epsilon = \epsilon_0\Gamma$, where ϵ_0 is the non-linear gain saturation coefficient. Solving for the roots of Equation 4.2 yields the average carrier and photon density of the grating section, $N_{grating}$ and $P_{grating}$. The change in the Bragg peak wavelength due to the carrier density change is

$$\Delta\lambda_N = \frac{dn}{dN}\frac{N - N_{tr}}{n_g}\lambda, \tag{4.4}$$

with λ set to the approximate lasing wavelength of 1.55 µm in this case.

As a first pass, the temperature of the grating section is found empirically via a quadratic fit of current versus wavelength data, yielding $\Delta\lambda_T = \Delta T d\lambda/dT$, where $\frac{d\lambda}{dT} = 0.09\ nm/^\circ C$. Note that this measurement only provides a spatially averaged temperature along this laser section. From Figure 4.15 we have found that there are non-negligible thermal gradients present along the individual sections. This thermal cross-talk needs to be taken into account to accurately predict tuning behaviour. Using CCD-TR measurements, a temperature gradient transverse to the waveguide was measured and normalised as $\Delta T_n(y) = \Delta T(y)/\Delta T(0)$, where y is the transverse distance from the waveguide. This normalised profile is then used to approximate the thermal gradients present along both sections for the required range of injection currents. This approach implicitly assumes that the thermal profiles scale linearly with temperature. These thermal gradients are then added to the averaged section temperatures. The wavelength shift of the Bragg peak is now simply the sum of the carrier density and thermal induced wavelength shifts, $\Delta\lambda_{Bragg} = \Delta\lambda_T + \Delta\lambda_N$.

The wavelength shift of the longitudinal modes is found similarly to that of the Bragg peak shift. The average carrier and photon density of the gain region, N_{gain} and P_{gain} are calculated using Equation 4.2. In order to account for feedback from the grating section, we set $P_i = RP_{grating}$ where R is the power reflectivity of the grating. We then proceed to calculate the wavelength shift of the longitudinal modes in the same manner as for the Bragg peak. Finally, the longitudinal mode which will ultimately lase is found by calculating the round trip gain of each mode as

$$g_{round} = r_1(\lambda) \times r_2 e^{g(\lambda)L}, \tag{4.5}$$

where $r_1(\lambda)$ and r_2 are the grating and end facet reflectivities respectively. In order to accurately model the gain, $g(\lambda)$ is approximated as $g(\lambda) = \frac{dg}{dN}(N - N_{tr}) - b_1[\lambda - (\lambda_o - b_2(N - N_{tr}) - b_3(\Delta T))]$ where b_1 sets the gain spectrum width and b_2 and b_3 account for gain peak de-tuning due to carrier density and temperature changes respectively. Now the mode with the highest g_{round} will correspond to the lasing mode. Finally, this process is iterated for a range of grating and gain input currents to yield a tuning map of wavelength with respect to the currents injected in each section. The SMSR is calculated via the standard analytical approach, which can be found in Coldren, Corzine, and Mashanovitch [25], and is elaborated on in section 6.2.1. Values of the simulation parameters are listed in Table 4.2.

4.6.2 Simulation results

The experimental and simulated tuning maps are compared in Figure 4.17a and 4.17b respectively. The model reproduces both the wavelength shift and the location of the mode hops. Figure 4.17c shows the wavelength shift across the current paths shown as dashed lines in Figure 4.17b; first assuming uniform temperature, then taking gradients into account. This shows that the temperature distributions obtained using CCD-TR are essential in order to capture the thermal cross-talk between adjacent sections and faithfully model the laser tuning behaviour. We observe good agreement between the experimental and simulated results, although the model tends to slightly under-predict the wavelength shift due to temperature effects at currents in excess of 240 mA. This is likely due to the analytical approach not taking non-uniform photon density profiles within the grating into account, which can become significant at high gain section injection currents.

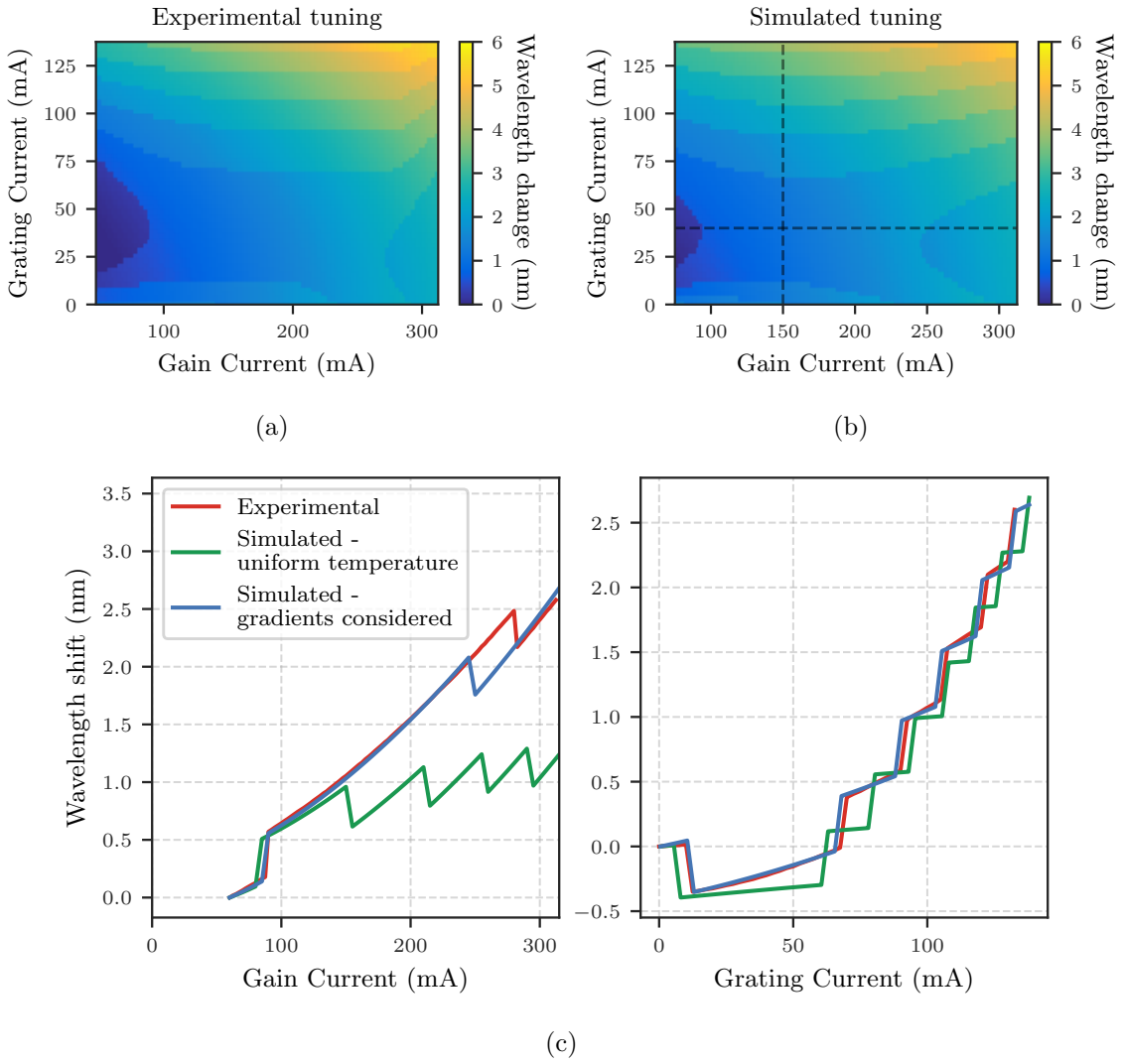

Figure 4.17: Analytical simulation of laser behaviour: (a) experimental tuning map for a 1000 µm long laser cavity at 20 °C, where black and red lines represent discontinuous and continuous current paths, respectively, (b) corresponding simulated map, (c) Wavelength shift across the paths highlighted on (b), with and without temperature gradients.

Figure 4.18 compares the modelled currents and SMSR for the discontinuous tuning scheme. For a given laser design, the simulation provides an approximate prediction of required injection currents necessary to maintain athermal performance over a given temperature range, as well as the expected SMSR behaviour. The model overestimates the SMSR in some cases, likely due to the multi mode nature of mode competition which is not encompassed fully by our analytical approach.

We can further use the model to study the effect of cleave error and to better understand the occurrence of mode hops during normal laser operation. Figure 4.19 shows the tuning maps of a 1000 µm cavity laser for a range of cleave errors. The

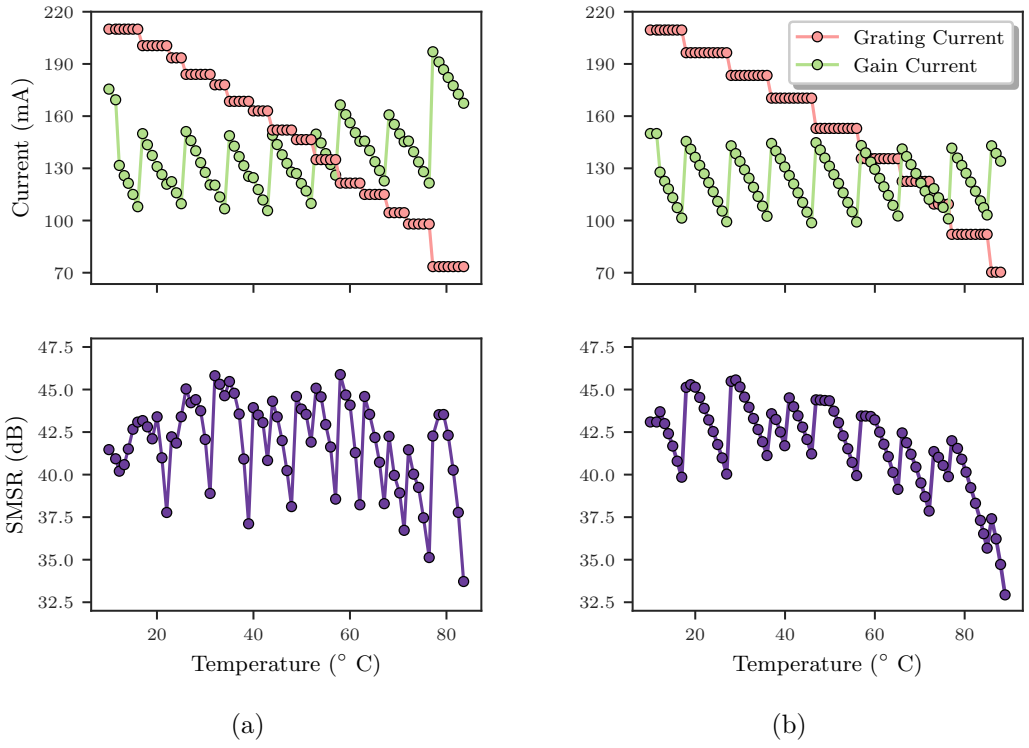

Figure 4.18: Discontinuous tuning schemes, showing applied currents and SMSR found by (a) experiment and (b) simulation.

change in cavity length caused by cleave error is set equivalent to a change in phase of the longitudinal modes from 0π to 2π. Again the grey dashed line represents uniform current injection over all sections. From the 0π phase case we can see that the saddle shape becomes very narrow at gain current $\sim 140\,\mathrm{mA}$, grating current $35\,\mathrm{mA}$. In this case any tuning paths chosen to avoid mode would have very little room for error. As the phase changes, the two mode hop regions circled in red merge and the saddle feature is extended. As the phase is further increased, the saddle feature compresses until at 2π the map is equivalent to 0π. From this we can see that choosing appropriate tuning paths is non-trivial and each device needs to be characterised to account for the change of the tuning map with cleave error.

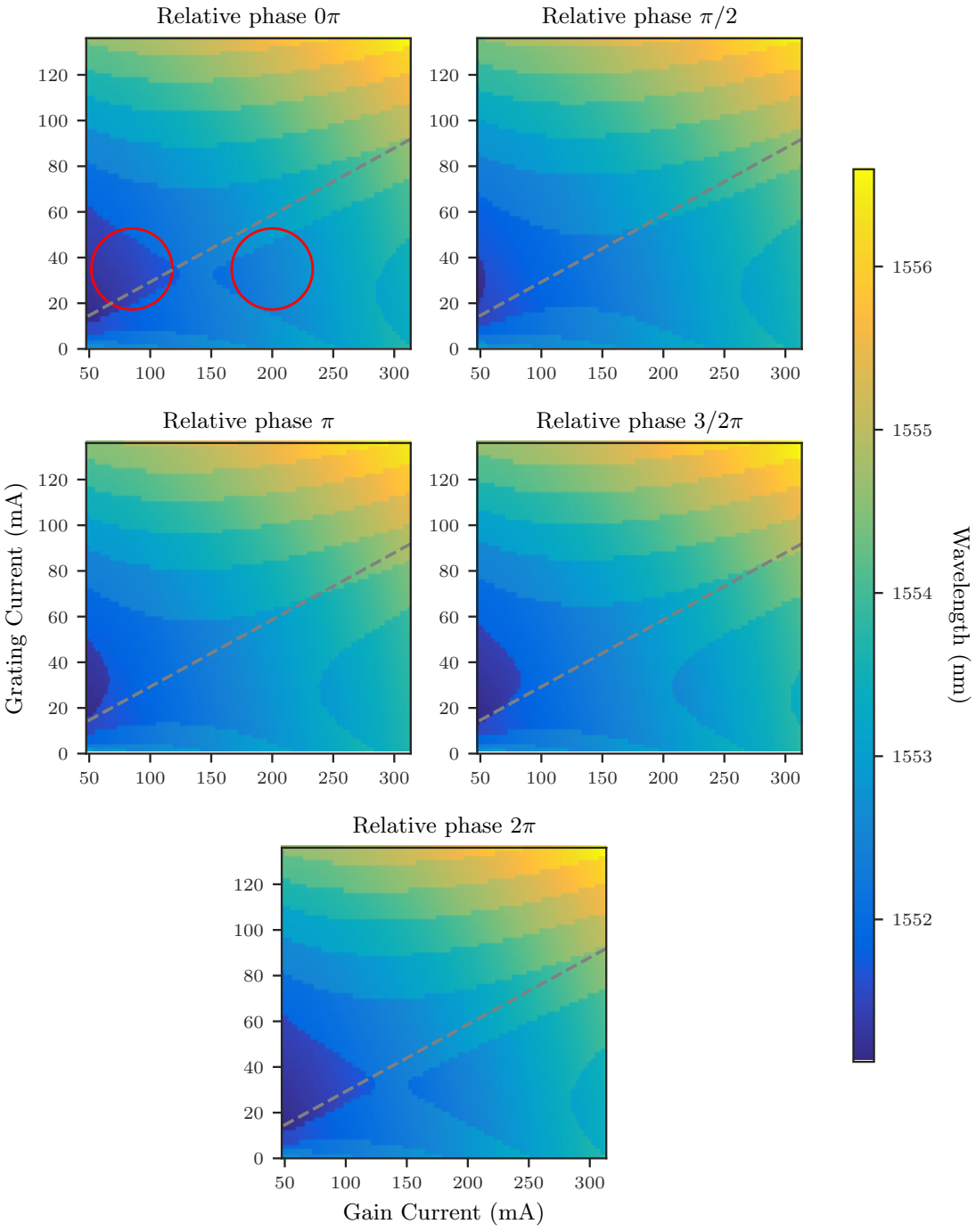

Figure 4.19: Wavelength tuning maps with a varying cleave error corresponding to a phase change from 0π to 2π. Grey dashed line represents uniform injection currents.

4.7 Conclusion

This chapter has laid the groundwork for understanding the multi-section laser tuning through experimental tuning map measurements. These maps revealed a number of tuning regimes and shed light on the occurrences of mode-hops under uniform injection current. A tuning scheme which avoids these mode hops was implemented utilizing the independent tuning capabilities of the electrically isolated laser sections. Elaborating on this tuning scheme, two athermal bias current control procedures for a three section slotted single mode laser were developed. These achieved the same wavelength stability and temperature ranges as have been demonstrated for DS-DBR lasers but on lasers with a simpler fabrication. Additionally, an analytical model was developed that yields current tuning maps that are in close agreement with the experimental results at lower gain section currents. To validate the assumptions made by this model, the CCD-TR technique has been used to experimentally measure the temperature distribution along a multi-section laser. These plots reveal significant temperature gradients along the laser, while implementing such a gradient significantly improves the agreement between experiment and model. These findings may inform high-fidelity future simulations of athermal multi-section devices, allowing for the optimal design of low-cost lasers for athermal WDM applications.

The model has proven accurate at predicting laser tuning whilst the analytic approach allows for simulation run times on the order of minutes for tuning maps. However, inherent to the model are certain drawbacks. Firstly, the analytic approach of the model sacrifices accuracy. As our model only discretises the cavity into two sections any non-uniformities within the sections are not accounted for. This naturally means the model is limited in terms of providing photon and carrier density profiles along the cavity and additionally cannot accurately simulate transient effects, modulation dynamics, linewidth and a range of other parameters. Secondly, the model relies heavily on experimentally determined parameters. For example the change of wavelength with injection current $d\lambda/dI$ is accounted for by a polynomial curve fitted to experimental measurements. In addition to this the CCD-TR is used to account for thermal cross-talk. This is not ideal as any non-negligible changes to epitaxial structure, i.e. solder layer thickness, sub-mount material or thickness, substrate thickness, would require new CCD-TR measurements to characterise the thermal dissipation from the laser cavity and new measurements of $d\lambda/dI$.

To address these issues, in the following chapter a discretised thermo-optic model is developed to better simulate laser behaviour.

Chapter 5

Thermo-optic laser model

5.1 Introduction

In the previous chapter the tuning behaviour of single mode lasers was investigated though experimental and analytical modelling of tuning maps. Additionally, the use of the CCD-TR technique revealed inter-section cross talk in the form of thermal gradients which altered the lasers' tuning behaviour. In terms of predicting this tuning behaviour the analytic model was effective, but is limited in certain regards. For example laser output power is not accurately calculated due to the grating region having both gain and distributed loss from the slots. As such, a more accurate method of calculating laser performance is developed in this chapter, whereby a discretised optical model calculates the optical and carrier dynamics, and a thermal model solves for the on-chip temperature distributions.

5.2 Time domain transfer matrix method

The TD-TMM is based on discretising the laser cavity into a number of longitudinal subsections and solving for wave propagation and laser rate equations within these subsections, with the approximation that the physical parameters within each subsection are homogeneous. The starting point for this model is expressing the transfer matrix in a time variant form in order to solve for the wave propagation.

5.2.1 Transfer matrix formulation

The static transfer matrix relates the backward and forward travelling fields at one port to that of another, given by

$$\begin{bmatrix} E_F(k+1) \\ E_B(k+1) \end{bmatrix} = \begin{bmatrix} A_k \end{bmatrix} \begin{bmatrix} E_F(k) \\ E_B(k) \end{bmatrix}, \tag{5.1}$$

where E_F and E_B are the forward and backwards travelling fields respectively, and A_k is the 2x2 transfer matrix [25].

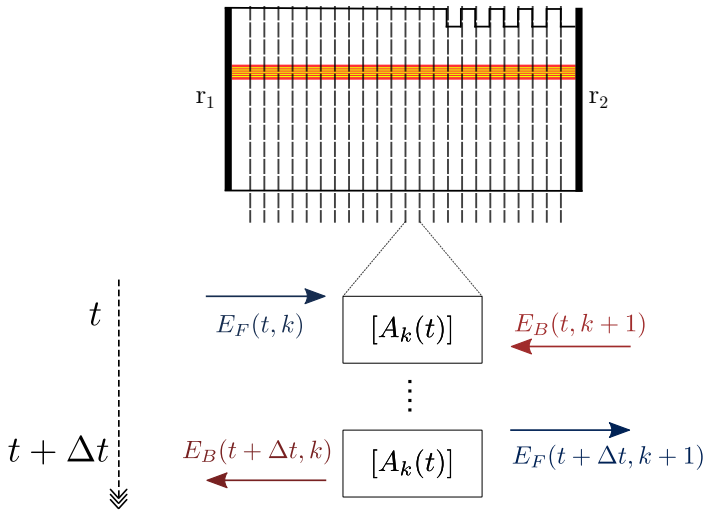

Figure 5.1: Basic principle of the time domain transfer matrix method.

Equation 5.1 describes the static case where we are simply relating the field at one side of the cavity to the other. The TD-TMM requires the transfer matrix to relate the forward and backward travelling fields both spatially and temporally [52]. This is achieved by writing the transfer matrix in a time dependent form,

$$\begin{bmatrix} E_F(t+\Delta t, k+1) \\ E_B(t, k+1) \end{bmatrix} = \begin{bmatrix} A_k \end{bmatrix} \begin{bmatrix} E_F(t, k) \\ E_B(t+\Delta t, k) \end{bmatrix}. \tag{5.2}$$

Multiplying the right-hand side out gives

$$\begin{aligned} E_F(t+\Delta t, k+1) &= a_{11}(t,k)E_F(t,k) + a_{12}(t,k)E_B(t+\Delta t, k) \\ E_B(t, k+1) &= a_{21}(t,k)E_F(t,k) + a_{22}(t,k)E_B(t+\Delta t, k), \end{aligned} \tag{5.3}$$

where $a_{i,j}$ are the elements of the transfer matrix A_k. In order to formulate the left hand side of the equation in terms of $(t + \Delta t)$ the equation is re-arranged as follows:

$$\begin{aligned} E_F(t+\Delta t, k+1) &= a_{11}(t,k)E_F(t,k) + a_{12}(t,k)E_B(t+\Delta t, k) \\ E_B(t+\Delta, k) &= (E_B(t, k+1) - a_{21}(t,k)E_F(t,k))/a_{22}(t,k). \end{aligned} \tag{5.4}$$

This is the governing equation for the propagation of the field within the cavity. Figure 5.1 gives an overview of the discretisation used, where Equation 5.4 solves for $E_F(t + \Delta t, k + 1)$ and $E_B(t + \Delta, k)$.

Prior to running a simulation we need to construct the transfer matrix for each subsection within the cavity. The general form of these transfer matrices is

$$A_k = \begin{bmatrix} a_{11} & a_{12} \\ a_{21} & a_{22} \end{bmatrix}. \tag{5.5}$$

As seen in Figure 5.1 there are two types of subsections to be considered for the transfer matrix when applied to the slotted design. Firstly, a homogeneous subsection as found throughout the gain section, and secondly a subsection where an index change results in a reflective interface, caused by the slots in the grating section. The transfer matrix for homogeneous subsections as shown in Figure 5.2, is given by

$$A_{gain} = \begin{bmatrix} e^{i\beta z} & 0 \\ 0 & e^{-i\beta z} \end{bmatrix}, \tag{5.6}$$

in which the propagation constant is

$$\beta = n_{eff}k_0 + i(\Gamma g - \alpha_i)/2, \tag{5.7}$$

where n_{eff} is the effective index, k_0 is the wave vector, Γ is the confinement factor, g is the gain and α_i is the waveguide loss. The transfer matrix for a reflective interface, as represented in Figure 5.3, is constructed as follows:

$$A_{slot} = \frac{1}{t_{12}} \begin{bmatrix} 1 & -r_{21} \\ r_{12} & t_{12}t_{21} - r_{12}r_{21} \end{bmatrix}, \tag{5.8}$$

where r_{ij} and t_{ij} represent the reflection and transmission of the interface respectively and are related as

$$\begin{aligned} t_{12} &= \sqrt{1 - r_{12}^2} \\ t_{21} &= \sqrt{1 - r_{21}^2}. \end{aligned} \tag{5.9}$$

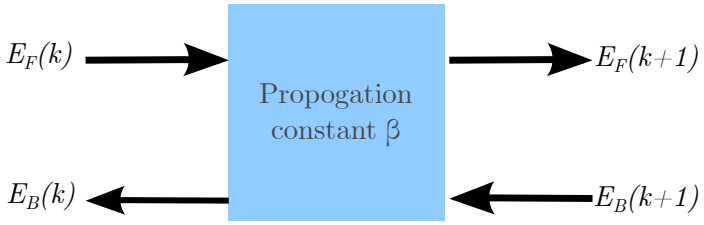

Figure 5.2: Homogeneous segment.

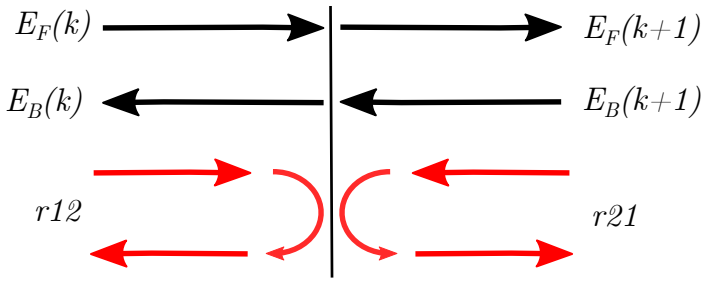

Figure 5.3: Reflective interface, in our case this interface is a slot etched into the waveguide ridge.

As the matrix given by Equation 5.8 has zero length, it does not satisfy the condition $\Delta z = \Delta t\ \nu_g$. Therefore, we multiply by the adjacent homogeneous section in between two adjacent slots, i.e:

$$A_{slot} = \frac{1}{t_{12}} \begin{bmatrix} 1 & -r_{21} \\ r_{12} & t_{12}t_{21} - r_{12}r_{21} \end{bmatrix} \begin{bmatrix} e^{i\beta z} & 0 \\ 0 & e^{-i\beta z} \end{bmatrix}. \tag{5.10}$$

This sets a minimum required resolution for the simulation equal to the grating period. Finally, the boundary condition for the propagating wave is defined by

$$\begin{aligned} E_F(k=0) &= r_1 E_B(k=0), \\ E_B(k=L) &= r_2 E_F(k=L), \end{aligned} \tag{5.11}$$

where r_1 and r_2 are the back and front facet reflectivity respectively. As was discussed in chapter 3, the non-negligible radiation loss associated with slotted gratings means the transfer matrix method is not an ideal tool for simulating reflectivity and transmission. Generally, gratings are modelled by setting the matrix elements for a reflection feature equal to

$$A_{slot} = \begin{bmatrix} \frac{n_2+n_1}{2n_2} & \frac{n_2-n_1}{2n_2} \\ \frac{n_2-n_1}{2n_2} & \frac{n_2+n_1}{2n_2} \end{bmatrix} \tag{5.12}$$

where n_1, n_2 are the refractive indexes of the dielectrics which form the grating feature. As conventional DFBs and DBRs have their gratings embedded in the waveguide, this approximation normally is valid. However, in our case it is not applicable as loss is non-negligible. Instead, the reflection and transmission spectrum are first calculated via the 2D-SMM. The reflection and transmission spectrum, as calculated by the TMM, can then be matched to the 2D-SMM by setting the appropriate values for r and α_s, where α_s is the loss of a slot which is accounted for in the propagation

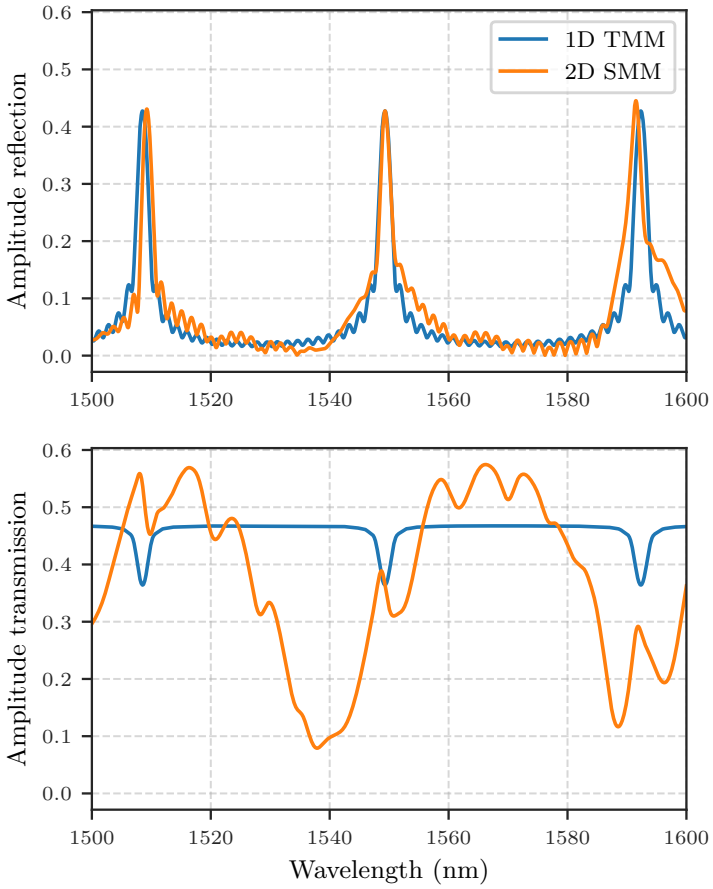

Figure 5.4: Comparison of 2D-SMM against 1D-TMM simulated spectrum. Amplitude reflection in the 1D case matches the 2D results well (Top). Transmission of the 2D case only matches the one 1D case close to the Bragg peak (Bottom).

constant of Equation 5.8, which gives

$$A_{slot} = \frac{1}{t}\begin{bmatrix} 1 & -r \\ r & t^2 - r^2 \end{bmatrix}\begin{bmatrix} e^{iz(\beta - i\alpha_s/2)} & 0 \\ 0 & e^{-iz(\beta - i\alpha_s/2)} \end{bmatrix}. \tag{5.13}$$

This ensures that the 1D-TMM produces accurate reflection and transmission, provided the lasing mode is near the Bragg peak. The results of this can be seen in Figure 5.4 where the Bragg reflection peak of the 1D-TMM and the 2D-SMM at 1550 nm match closely. The transmission in Figure 5.4 is not seen to match for the majority of the spectrum. Crucially, however, the transmission at the 1550 nm Bragg peak does match in both cases. As long as lasing occurs at the desired wavelength, i.e. the Bragg peak, the simulation will return accurate results. If the simulated lasing mode changes to one of the adjacent FSR peaks we can see from Figure 5.4 that the

transmission from said mode may be over or under estimated relative to the 2D-SMM transmission.

5.2.2 Rate equations

In conjunction with solving for the propagating waves, we also need to solve for the photon and carrier densities, gain and spontaneous emission within each discrete subsection in the simulation. The photon density is given by the solution of the optical field in each subsection

$$S_k = (|E_{F,k}|^2 + |E_{B,k}|^2)/v_g. \tag{5.14}$$

The carrier density in each subsection is then updated as

$$N(t+dt,k) = N(t,k) + \Delta t[\eta \frac{I(t,k)}{qV} - R(N(t,k)) - \nu_g g(t,k) S_k], \tag{5.15}$$

where η_i is the injection efficiency, I is the injection current, q is electron charge, V is the active region volume, Γ is the confinement factor, R is the rate of spontaneous recombination given by

$$R(N) = AN + BN^2 + CN^3, \tag{5.16}$$

where A is the Non-radiative linear recombination, B is the Bimolecular recombination and C is Auger recombination coefficient. In order to include thermal effects we take the same approach as Han et al. [53] by adjusting Equation 5.16 with a characteristic temperature T_0 which takes into account changes in $R(N)$ with temperature as follows:

$$R(N) = e^{\gamma(1-\frac{T}{T_0})}(AN + BN^2 + CN^3), \tag{5.17}$$

$$\gamma = T_0 \frac{E_A}{k_B}, \tag{5.18}$$

where $E_A = 0.06\,\text{eV}$ is the activation energy taken from Saidi et al. [54] and k_B is Boltzmann's constant.

5.2.3 Gain

The gain is approximated as a linear function of carrier density set relative to the carrier density at transparency N_o, given by

$$g(N_k, S_k) = \frac{T_0}{T} \frac{dg}{dN} \frac{(N_k - \frac{T}{T_0} N_o)}{1 + \epsilon S_k}, \tag{5.19}$$

where $\epsilon = \epsilon_0\Gamma$ and ϵ_0 is the fundamental saturation coefficient. dg/dN is the differential gain and gives the rate of change of gain with carrier density. We have again adopted the approach from Han et al. [53] to account for changes in dg/dN and N_0 with temperature.

As we are modelling laser tuning over the C-band, it is necessary take gain dispersion across this wavelength range into account. As this model is working in the time domain, we make use of an infinite impulse response digital filter (IIR) to model gain dispersion. A given IIR has a characteristic frequency response, and by choosing the appropriate IIR filter one can achieve a response in the frequency domain which approximates the gain spectrum. In this model we use the same Lorentzian filter used by Li, Huang, and Li [55], which has a frequency response of the form

$$|\mathcal{H}(\omega)|^2 = \frac{(1-\eta)^2}{1+\eta^2-2\eta\cos[(\omega+\delta_g dt)]}, \tag{5.20}$$

where $0 \leq \eta \leq 1$ sets the width of the filter and δ_g sets the relative wavelength/frequency of the gain peak as

$$\delta_g = (\omega_0 - \omega_g), \tag{5.21}$$

where ω_0 is the reference angular frequency and ω_g is angular frequency of the gain spectrum's peak. The IIR filter with frequency response of Equation 5.20 corresponds to filter coefficients of,

$$\begin{aligned} a &= \eta e^{i(\omega_0-\omega_g)dt}, \\ b &= 1-\eta, \end{aligned} \tag{5.22}$$

the proof for which can be seen in Appendix A. The digital filter is then implemented by updating the field in each subsection as follows:

$$\begin{aligned} E_F(t) &= bE_F(t) + aE_F(t-\Delta t), \\ E_B(t) &= bE_B(t) + aE_B(t-\Delta t). \end{aligned} \tag{5.23}$$

The weighting parameter η is fit to experimentally measured gain spectra close to threshold. These gain spectra were previously measured using the Fourier series expansion method described in Guo et al. [56] and are presented in Abdullayev [20] and Nawrocka [23]. The accuracy of the digital filter can be seen in Figure 5.5. The digital filter overestimates the gain at higher frequencies and underestimates the gain at lower frequencies somewhat, although, overall the fit is accurate enough for the

cases presented in this work.

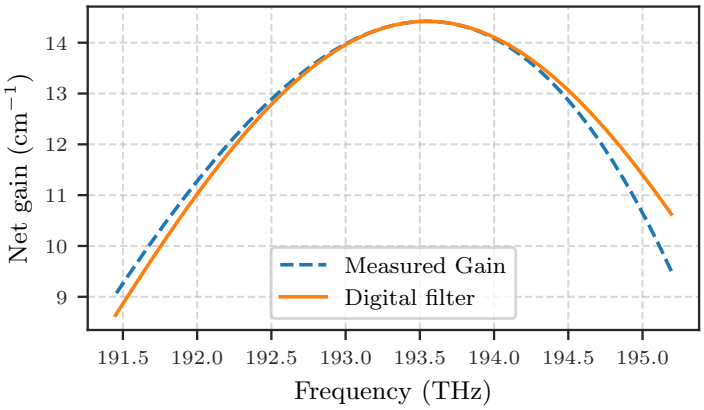

Figure 5.5: Frequency response of the gain filter vs. experimental data.

In addition to accounting for gain dispersion, the wavelength shift in peak gain due to changes in carrier density and temperature cannot be ignored if the model is to accurately predict lasing wavelength. These effects are included as follows:

$$\omega_g(T,N) = \omega_g(N_0,T_0) + \frac{d\omega}{dT}(T-T_0) + \frac{d\omega}{dN}(N-N_0), \tag{5.24}$$

where $\omega_g(N_0,T_0)$ is the peak of the gain curved as measured at N_0 and T_0, $^{d\omega}/_{dN}$ and $^{d\omega}/_{dT}$ are the rate of change of peak gain with carrier density and temperature respectively, approximated as being linear.

5.2.4 Spontaneous emission

The rate of spontaneous emission per unit time is formulated as random Gaussian noise satisfying the correlation

$$\begin{aligned} \langle s_{F,B}(t,k)s^*_{F,B}(k^{'},t^{'})\rangle &= \frac{\beta_g(BN^2)v_g}{\nu_{sp}}\delta(k-k^{'})\delta(t-t^{'}), \\ \langle s_{F,B}(t,k)s_{F,B}(k^{'},t^{'})\rangle &= 0, \end{aligned} \tag{5.25}$$

where β_g the geometric spontaneous coupling factor which determines the fraction of spontaneous emission coupled from the quantum wells into the waveguide, B is the bimolecular recombination coefficient, N is the carrier density, and ν_{sp} is the bandwidth of the spontaneous emission, taken as 12.49 THz (100 nm), typical for such devices [25]. Spontaneous emission is used to seed the electric field at the start

of the simulation and is subsequently added at the end of each loop, accounting for the spontaneous emission noise.

Table 5.1: TD-TMM model parameters

Parameter	*Symbol and unit*	*Values*
Active layer thickness	d (µm)	0.03
Active layer width	w (µm)	2
Non-radiative linear recombination	A ($10^8\,s^{-1}$)	1 ‡
Bimolecular recombination	B ($10^{-10}\,cm^3s^{-1}$)	1 ‡
Auger recombination	C ($10^{-30}\,cm^6s^{-1}$)	7.0 ‡
Waveguide loss	α_i (cm^{-1})	28 †
Transparency carrier density	N_{tr} ($10^{18}\,cm^{-3}$)	1.9 †
Differential gain	$^{dg}/_{dN}$ ($10^{-17}\,cm^2$)	1.2 †
Gain freq. shift with N	$^{d\omega}/_{dN}$ ($10^{-6}\,rad\,cm^{-3}$)	2.0 †
Gain freq. shift with T	$^{d\omega}/_{dT}$ ($10^{12}\,rad°C^{-1}$)	2.7 †
Linewidth enhancement fact.	α	3 †
Geometric spontaneous coupling factor	β_g (10^{-4})	1.2 †
Fundamental saturation coefficient	ϵ_0 ($10^{-16}\,cm^3$)	6 ‡
Group index	n_g	3.6 ‡
Confinement factor	Γ	0.05 *
Injection efficiency	η_i	0.7 to 0.8 †

* Calculated
† Experimentally measured
‡ Taken from literature

5.2.5 Effective index

In order to accurately account for the tuning dynamics of the laser, changes in refractive index due to temperature and carrier density are included. The thermally induced change in effective index is calculated as

$$\Delta n_{eff} = \frac{dn_{eff}}{dT}(T - T_0), \tag{5.26}$$

where dn_{eff}/dT is the rate of change of effective index with temperature, measured as 2.4×10^{-4}, and T_0 is the reference temperature.

Effective index changes due to the free carrier plasma effect are accounted for via

$$\Delta n_{eff} = \frac{\alpha\lambda}{4\pi}\frac{dg}{dN}(N - N_{tr}), \tag{5.27}$$

where α is the linewidth enhancement factor [55].

5.2.6 Output

Finally, the output of the laser from the front and back facet is

$$\begin{aligned} E_1 &= \sqrt{(1-r_1^2)}E_B(k=0), \\ E_2 &= \sqrt{(1-r_2^2)}E_F(k=L), \end{aligned} \tag{5.28}$$

where $r_{1|2}$ are the facet reflectivities. The lasing spectrum of the laser is calculated by taking the Fourier transform of $E_{1|2}$. The output power from the facet is then given as

$$P_{1|2} = h\nu w d \frac{\left|E_{1|2}\right|^2}{\Gamma}, \tag{5.29}$$

where w is the waveguide width and d is the total height of the MQWs. Figure 5.6 shows a flow chart of the TD-TMM algorithm.

5.3 Implementation

A specific objective when implementing this model was to ensure ease of use and make the module intuitive for future users. To this end, we have implemented the front end of the module in Python, which has a number of advantages in line with the aforementioned goals. These include: dynamic typing, verbose/readable syntax, wide user base/adoption and a wide library of scientific tools. A disadvantage of using Python — inherent to its nature as an interpreted language — is that it is slower than lower level compiled languages such as C. Although libraries such as NumPy bring python up to speed with comparable scientific languages such as MATLAB, OCTAVE or Julia, there are still significant performance gains possible by implementing numerically intensive portions code in a compiled language. Fortunately, this functionality is readily available, as Python has a number of modules which facilitate extending code with languages such as C++, Fortran etc. With this in mind, the computationally demanding TD-TMM algorithm is implemented and compiled in FORTRAN and imported as a Python module using the Python module F2PY [57]. The Python front end is used for the defining physical parameters, device structure, post processing etc. with these being passed to the compiled FORTRAN code at run-time, ensuring maximum performance.

The python front end has been implemented in an object oriented manner in order to enable fast prototyping of simulations, code legibility and ease of use. An example of

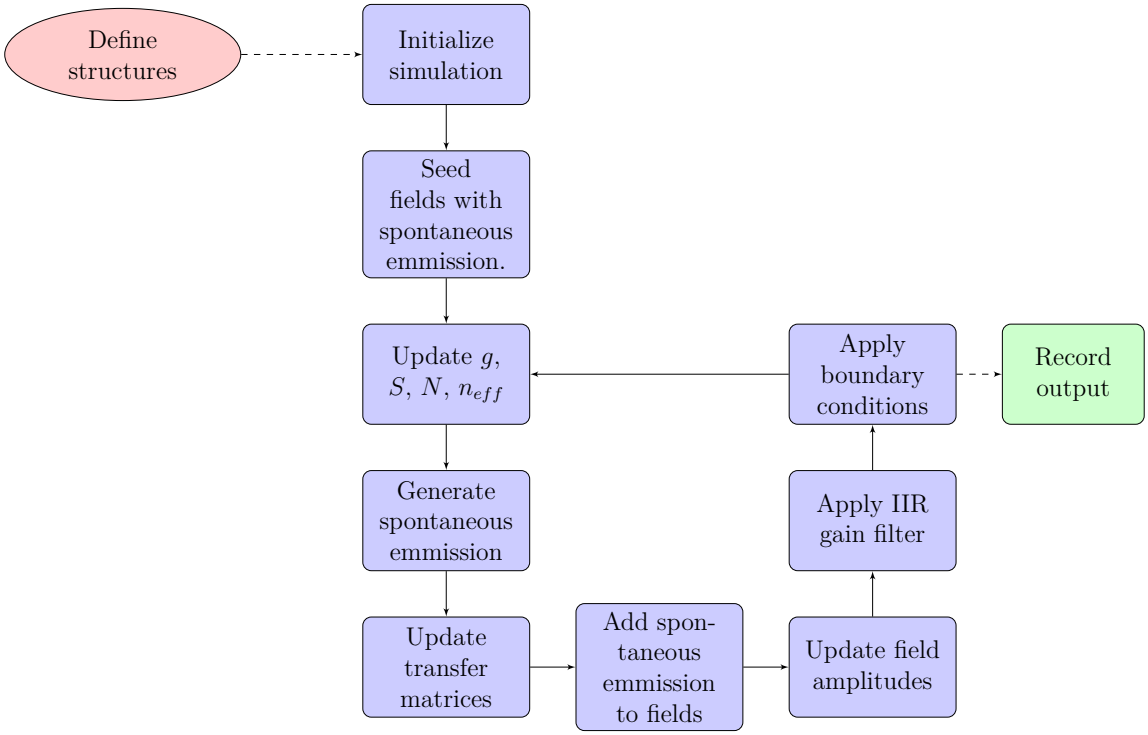

Figure 5.6: TD-TMM algorithm.

a simulation can be seen in Listing 5.1. In this code we define gain and grating objects. From these objects one can build more complex cavity structures. The cavity shape and boundary condition (facets) are passed to the simulation which is then executed. Once our simulation parameters are defined, any properties of the gain and grating section can be manipulated, for example in Listing 5.1 the injection current is changed in lines 32-33. The module allows for any parameters to be dynamically changed, for instance slot number, period, linewidth enhancement factor, differential gain etc. The individual sections can also be supplied with arbitrary modulation functions, which proves useful for simulation direct modulation dynamics. When the *run* method of our simulation is called, the cavity is automatically re-built to take into account any changes made to the sections before running the TD-TMM algorithm.

```
import tdtmm as tdtmm

# Laser structure
cavity_length = 400
lasing_wavelength = 1.55
grating_period = 37 * lasing_wavelength / (2*3.2)
slot_number = 24
grating_length = grating_period*slot_number
gain_length =    cavity_length - grating_length

# Definding individual sections
grating =  tdtmm.grating(period=grating_period,slot_number=
    slot_number, r = 0.032,l = 0.025,injection_current = 40)
gain    =  tdtmm.waveguide(length=gain_length,injection_current =
    100)

sections = [gain,front]
facets = tdtmm.facets(0.95,0.05)

# Simulation properties
runtime = 1
resolution = grating_period

# Defining simulation
simulation = tdtmm.simulation(runtime, ref_wavelength=1.55,
    resolution=resolution)

simulation.cavity(sections,facets)

simulation.run()

# Post processing
wavelength_1, power_dBm_1 = simulation.return_spectrum()

# Change injection current
grating.injection_current =  100.0
gain.injection_current =  40.0

simulation.run()
wavelength_2, power_dBm_2 = simulation.return_spectrum()
```

Listing 5.1: Example of a simple laser simulation at two differing injection currents.

5.4 Modelling results

The TD-TMM has been used to simulate a range of behaviour. Where possible, the results of the model are compared with experimentally measured lasers.

5.4.1 Static results

Spectra

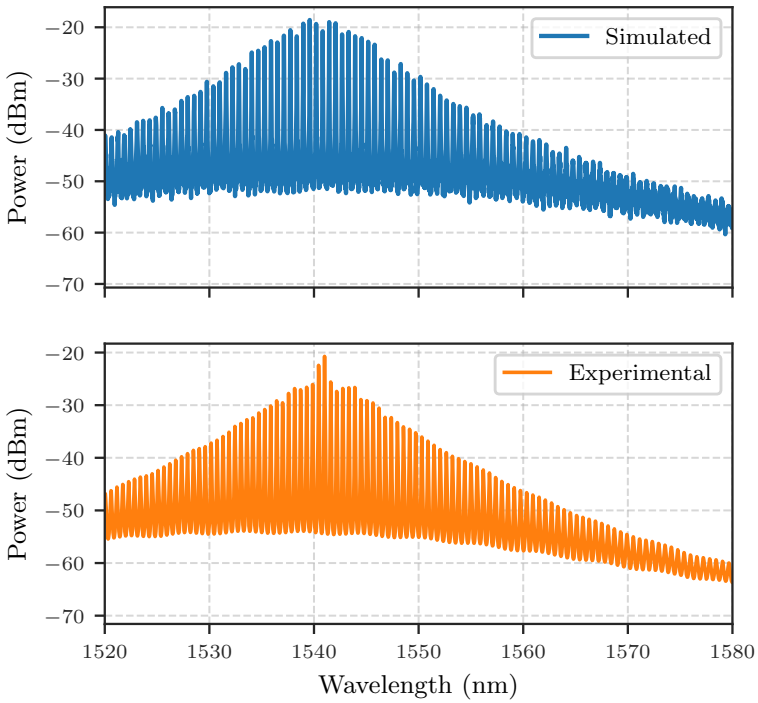

Figure 5.7: Output spectrum of a 400 µm Fabry Pérot laser: simulated (top) compared with experimental (bottom).

The simulated lasing spectrum is obtained by taking the Fourier transform of the output field given by Equation 5.28, with the power then given by Equation 5.29. Figure 5.7 shows the simulated output spectrum of a 400 µm Fabry Pérot laser biased just above threshold. The shape of the simulated spectrum closely matches the experimental spectrum. As the spectrum of a Fabry Pérot laser is a function of the gain profile, the Lorentzian digital filter approximation of the gain dispersion is shown to be accurate over the wavelength range considered.

Adding a grating into Fabry Pérot cavity now simulates the single mode slotted lasers. Figure 5.8 shows the simulated output spectrum of an array of 700 µm single

mode slotted lasers with 24 slots of period $\sim 8.96\,\mu m$. Importantly the spectra allows one to determine lasing wavelength and SMSR.

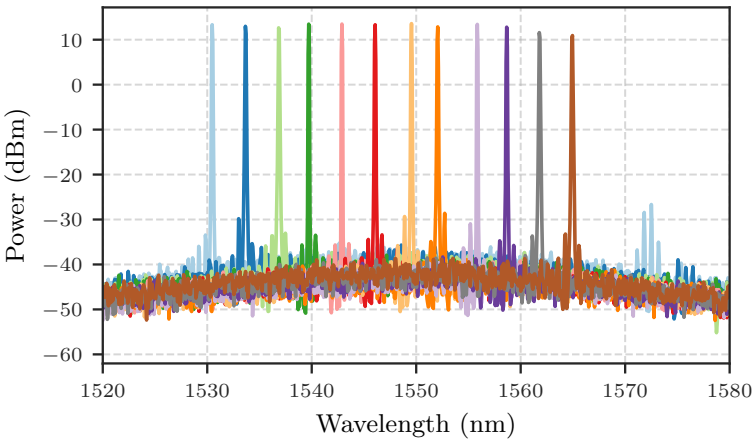

Figure 5.8: Simulated output spectrum of an array of 12, 700 µm cavity length lasers.

Photon and Carrier Density profiles

As our model is discretised in the propagation direction we can calculate the carrier and photon density profiles along the laser cavity. The profiles for 400 µm, 700 µm and 1000 µm length single mode lasers are shown in Figure 5.9. Of note is the high level of loss which the lasers experience in the grating section (the position of which is indicated by dashed lines), as can be seen by the decrease in photon density which ultimately reduces output power.

Linewidth

An important parameter when considering laser performance for single mode lasers is the linewidth or FWHM of the lasing mode. Figure 5.10 shows the simulated emission profile of a 400 µm cavity length single mode slotted laser and the corresponding Lorentzian fit from which a linewidth of 3.74 MHz is extracted. In comparison, the experimental linewidth — measured using the delayed self-heterodyne method [58] — matches closely; with the Lorentzian component of a Voigt fit having a linewidth of 4.04 MHz. For a 700 µm cavity length laser Figure 5.11 again shows good agreement between simulation and experiment with a linewidth of 1.19 MHz and 1.29 MHz.

Although such simulations are an accurate method for determining linewidth, in cases where a number of linewidth evaluations are required they are not practical due

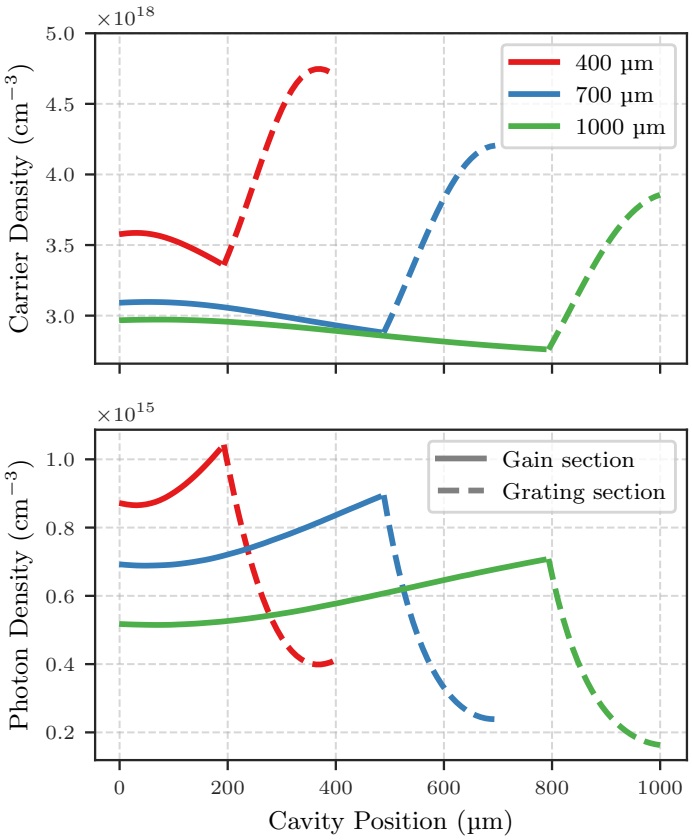

Figure 5.9: Simulated carrier and photon density profiles for lasers with cavity lengths of 400 µm, 700 µm and 1000 µm, biased at 100 mA each. Solid and dashed lines represent the gain and grating sections respectively.

to the required run time associated with them. This can be readily seen as follows: the simulation run in order to produce Figure 5.10 was discretised at $\Delta t = 9.56 \times 10^{-5}$ ns, a sampling frequency of $f_s = 1.045 \times 10^{13}$ Hz. The frequency resolution is given by

$$\Delta f = f_s/N, \tag{5.30}$$

where N is the number of samples. In order to obtain a frequency resolution of 150 kHz one would need 1.045×10^8 samples. At $\sim$ 60000 iterations per seconds the time for simulating the linewidth of one particular laser under a particular set of conditions is on the order of hours. As such, performing linewidth simulations is better served

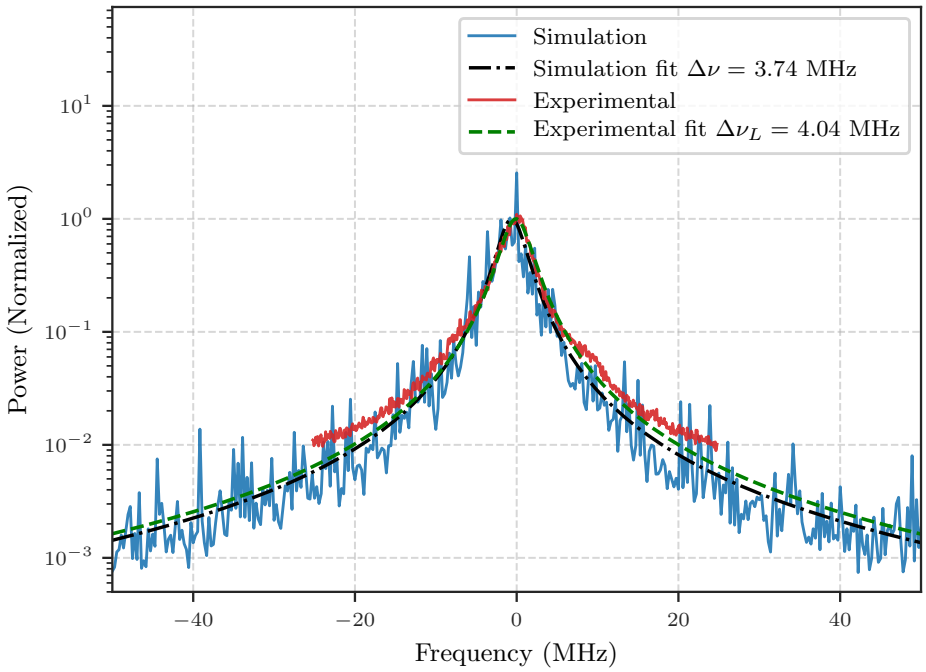

Figure 5.10: Simulated linewidth of a 400 µm slotted laser at 100 mA bias current. Simulated linewidth of the laser is fitted to a Lorentzian with FWHM = 3.74 MHz. Experimental data is fitted with a Voigt profile with the Lorentzian component FWHM = 4.04 MHz

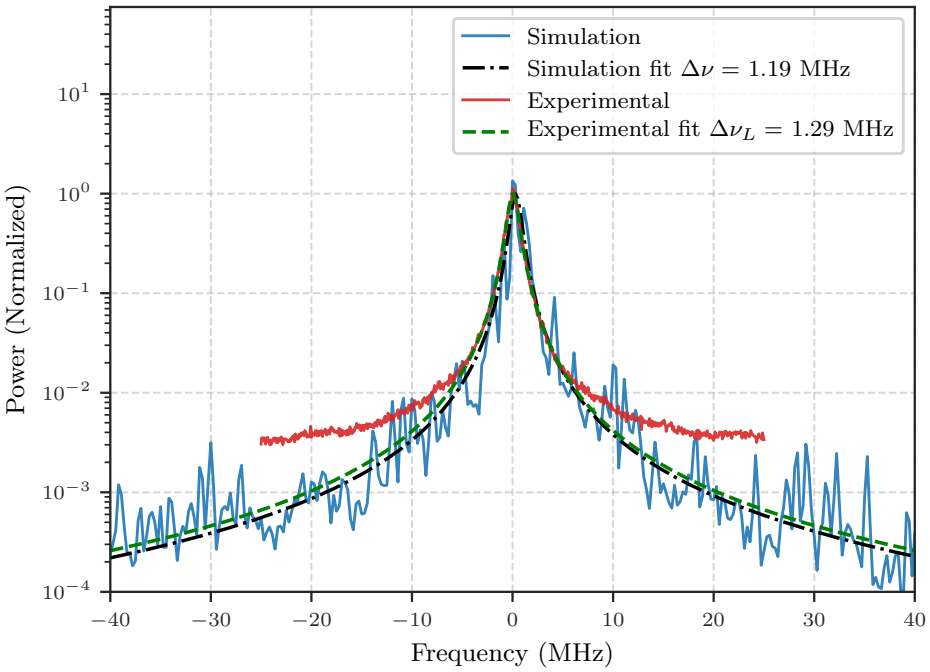

Figure 5.11: Simulated linewidth of a 700 µm slotted laser at 100 mA bias current. Simulated linewidth of the laser is fitted to a Lorentzian with FWHM = 1.19 MHz. Experimental data is fitted with a Voigt profile with an extracted Lorentzian component of FWHM = 1.29 MHz

using the modified Schawlow-Townes equation, formulated in terms of photon density,

$$\Delta\nu_{FW} = \frac{(\Gamma R'_{sp})^2}{4\pi S}(1+\alpha), \tag{5.31}$$

where S is the average photon density in the cavity (calculated with the TD-TMM), R_{sp} is the spontaneous emission rate, and α is the linewidth enhancement factor [25]. As calculating the photon density S only takes seconds, this is an efficient method for calculating the laser linewidth. The result of this can be seen in Figure 5.12 where linewidth vs. injection current is simulated for a 700 µm length laser. Simulated values are somewhat underestimated relative to experimental values in this case, though the overall trend is correct. Figure 5.13 shows the simulated and experimental linewidth for a 1000 µm laser, in this case simulated linewidth values match closely with experimental values. Experimental linewidth was again measured using the delayed self-heterodyne method [58].

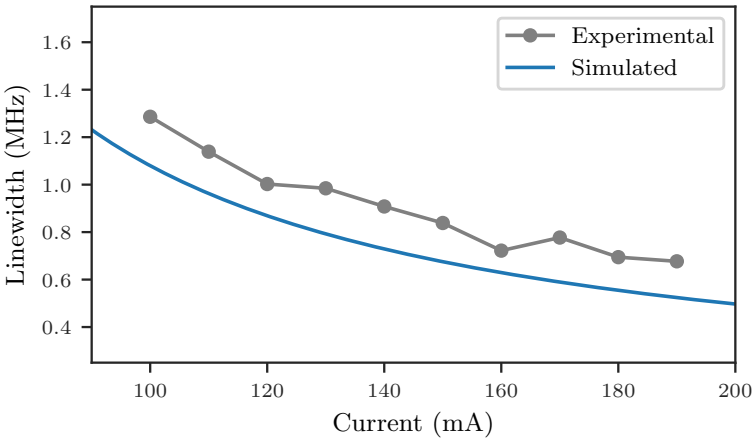

Figure 5.12: Simulated (modified Schawlow-Townes equation) and experimental linewidth of a 700 µm slotted laser.

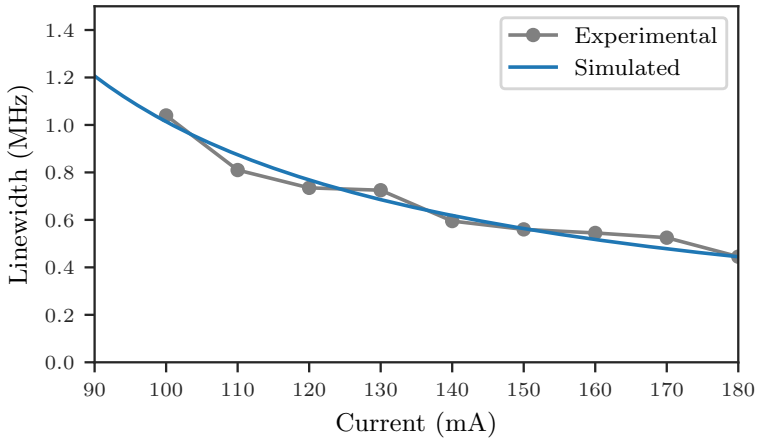

Figure 5.13: Simulated (modified Schawlow-Townes equation) and experimental linewidth of a 1000 µm slotted laser.

5.4.2 Transient results

A further motivation for developing the TD-TMM is to simulate laser transient dynamics. When simulating the static case, as shown previously, the simulation is run until the laser reaches steady state. Before the laser reaches steady state however, there is a turn on delay during which the laser undergoes relaxation oscillations. Figure 5.14 shows this transient response for single mode slotted lasers of differing cavity lengths. The 400 µm long laser is naturally seen to have the fastest response, and starts to lase at $\sim$ 0.25 ns, quickly reaching stable single mode performance thereafter. As the laser cavity gets longer, this stabilization time becomes longer. In the case of the 1000 µm laser, lasing does not start until $\sim$ 0.5 ns, with the SMSR taking considerably longer to reach a steady value relative to shorter cavity lengths. The initial relaxation oscillation is an important feature in this transient phenomenon, as its frequency is the natural resonant frequency of the cavity. This resonant frequency will produce the highest modulation response under direct modulation and for such applications it is desirable to increase the relaxation oscillation frequency of the cavity. Taking the Fourier transform of the output during this relaxation oscillation gives us the resonant frequency of the laser as seen in Figure 5.15 where the first peaks (marked by squares), correspond to the frequency of the relaxation oscillation. From the plot we can see the resonant frequency of the laser decreasing as the cavity length increases.

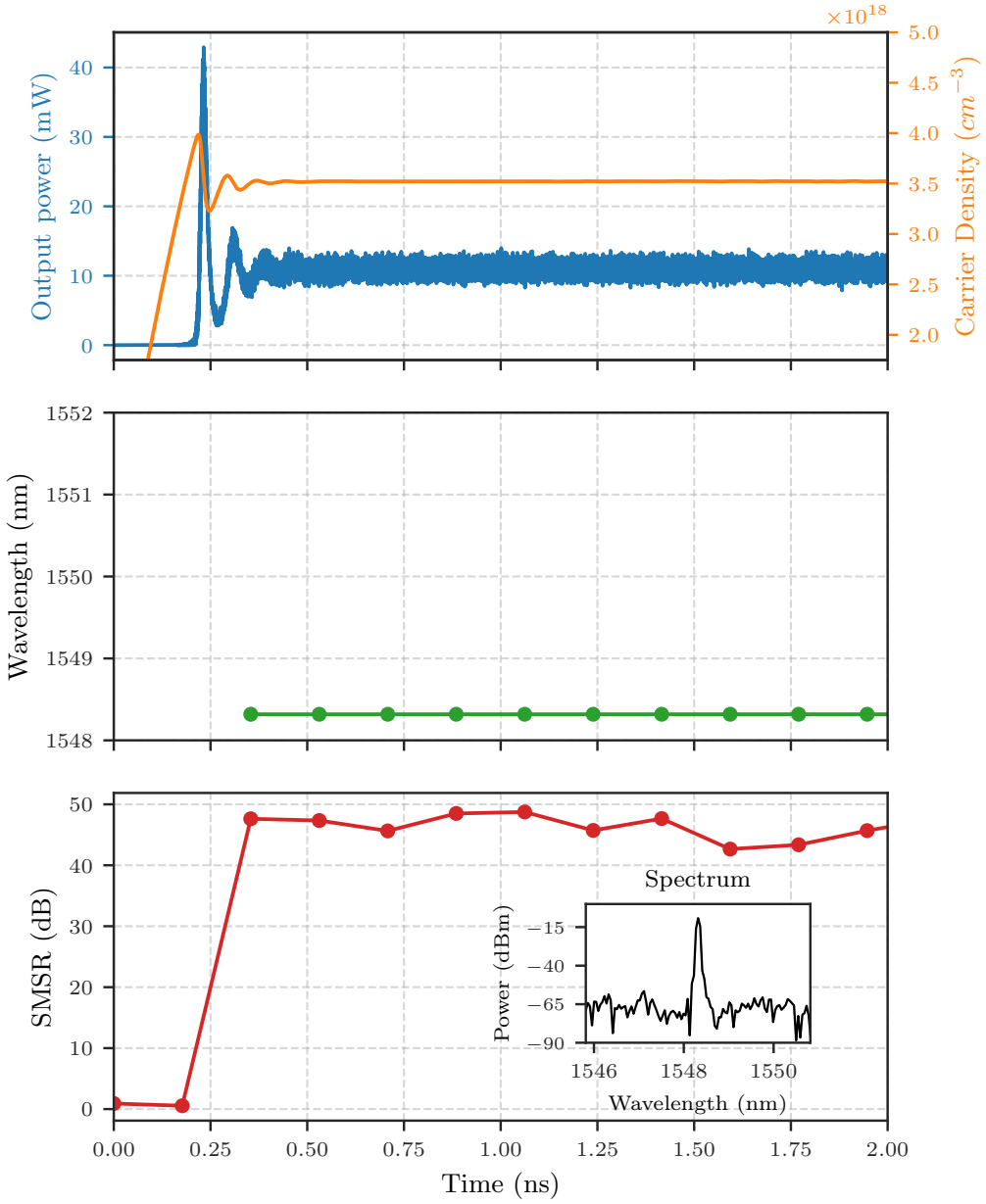

(a) 400 µm cavity length.

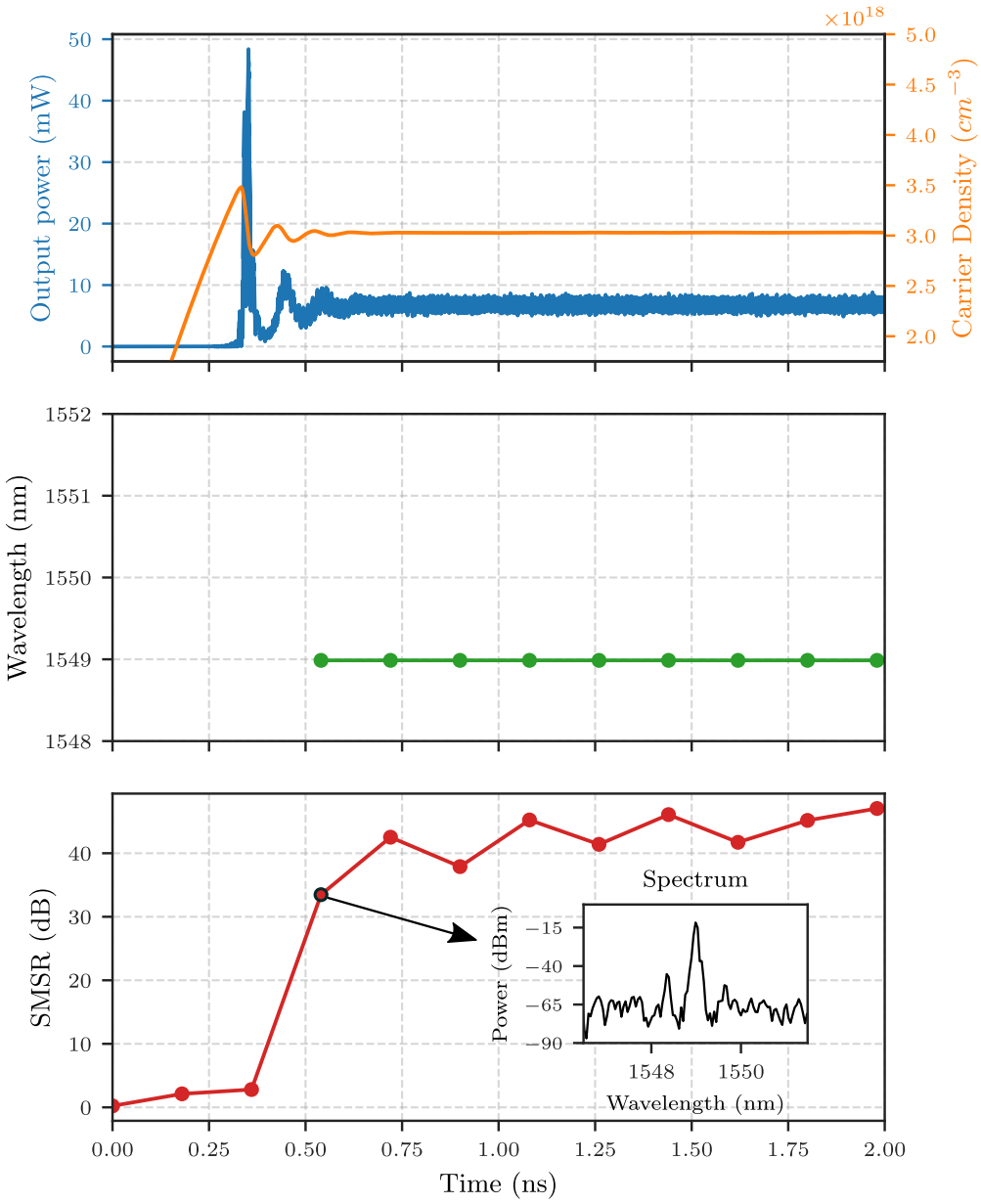

(b) 700 µm cavity length.

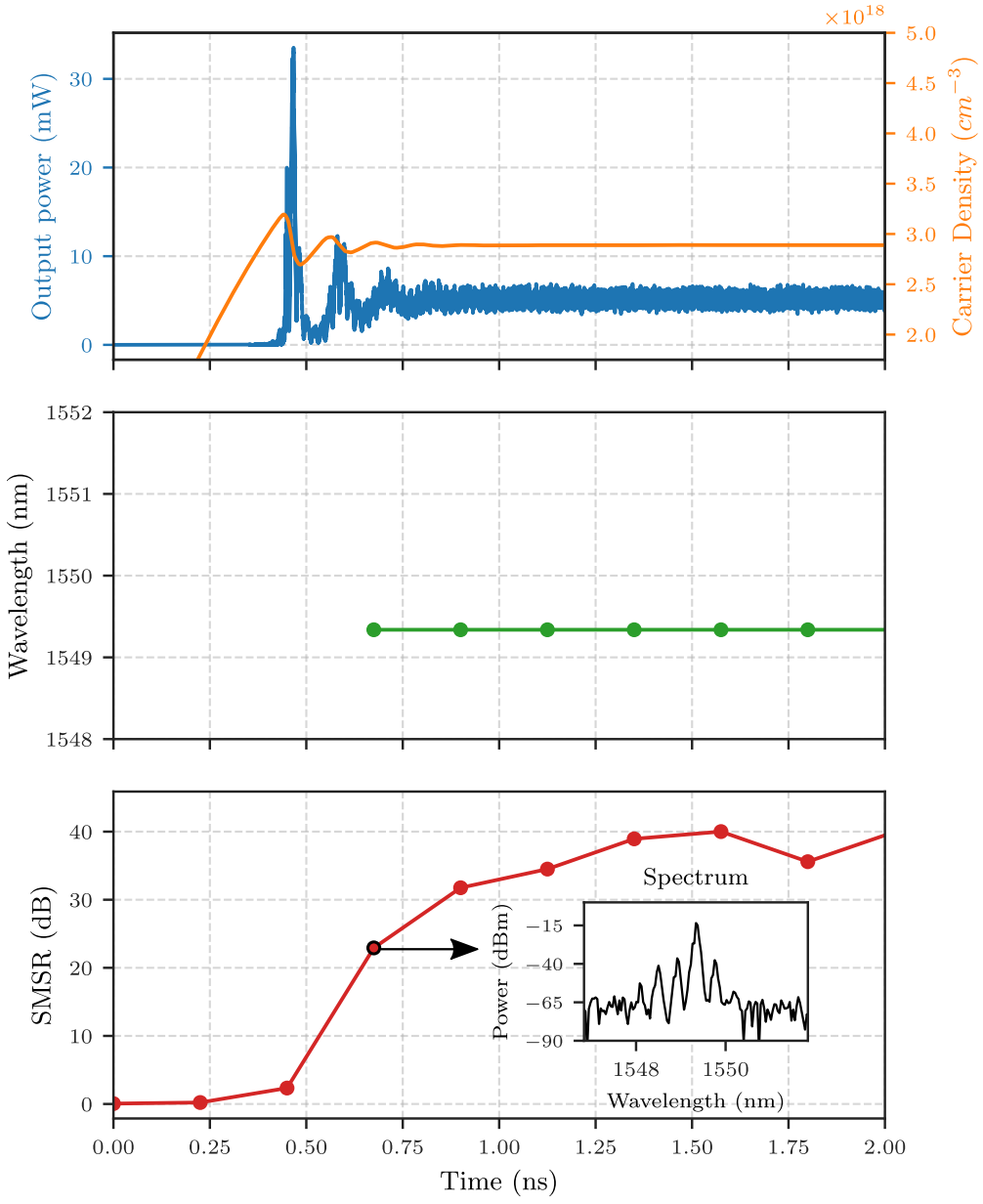

(c) 1000 µm cavity length.

Figure 5.14: Simulated transient response of cavity lengths (a) 400 µm, (b) 700 µm, (c) 1000 µm; each at 100 mA bias current.

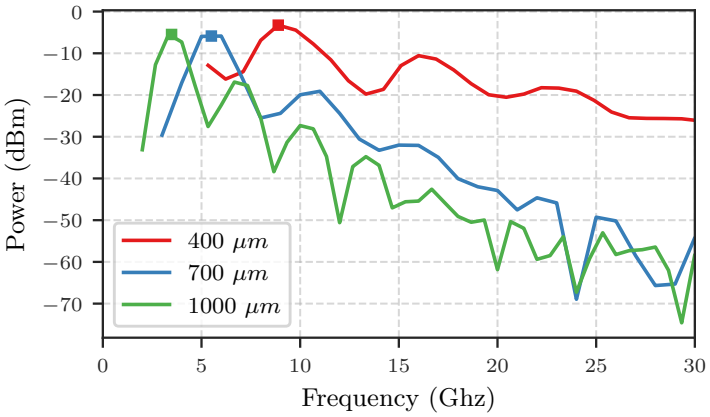

Figure 5.15: Simulated radio frequency spectra.

5.4.3 Laser modulation

The TD-TMM can also be used to explicitly simulate the modulation response by modulating the current of the laser over a range of frequencies during the simulation and evaluating the response at each frequency. Figure 5.16 shows the simulated modulation response of the three different cavity length slotted lasers. The currents correspond to the DC offset bias, around which the current is modulated, and is chosen in each simulation to be $\sim$ 2, 3, 4 and 5 times laser threshold. In each simulation the resonance peak and 3 dB bandwidth increase with current and decreases with cavity length. The trend is more clearly illustrated in Figure 5.17, which shows the 3 dB bandwidth as a function of current for the three cavity lengths.

It is also possible to simulate the eye diagrams for each of the laser, as shown in Figure 5.18a, Figure 5.18b and Figure 5.18c, in order to determine the suitability of the lasers for direct modulation at a given frequency. Distortion in the eye diagrams is seen for each cavity length, becoming more severe with increasing cavity length. In addition, the large overshoot in power seen for each cavity will lead to a large transient chirp.

Thus far we have simulated the performance of 400 µm, 700 µm and 1000 µm cavity length lasers, taking into account purely the optical dynamics included by the TD-TMM. We will now describe the method by which we incorporate thermal behaviour of the lasers.

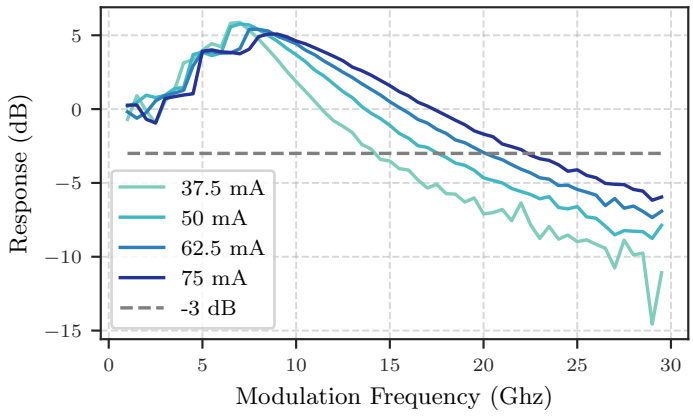

(a) 400 µm long cavity.

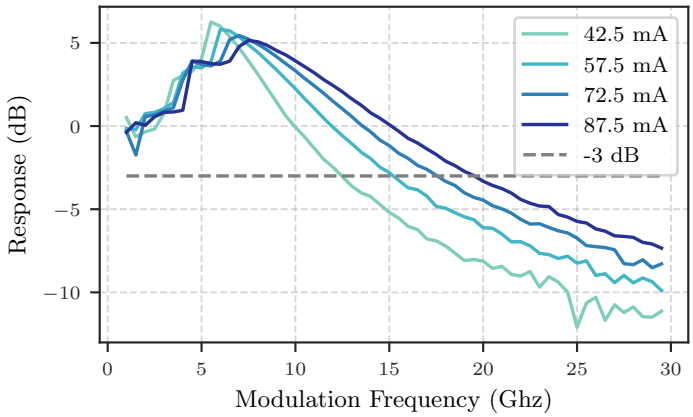

(b) 700 µm long cavity.

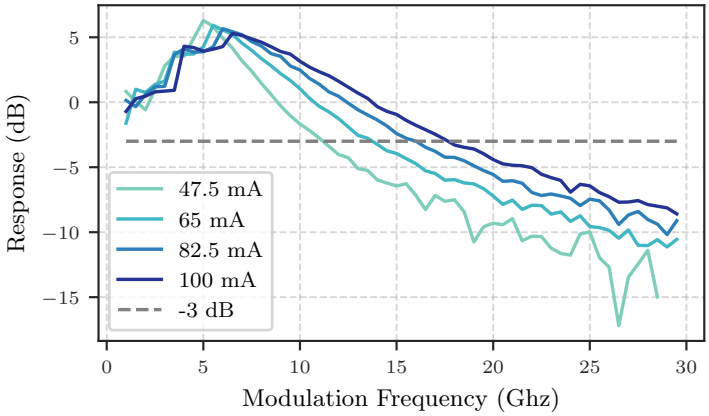

(c) 1000 µm long cavity.

Figure 5.16: Simulated modulation response for three differing laser cavity lengths.

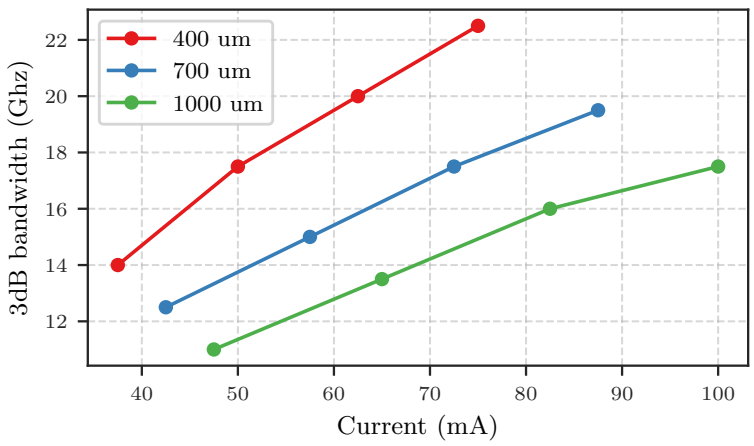

Figure 5.17: Simulated 3 dB bandwidth with varying cavity length.

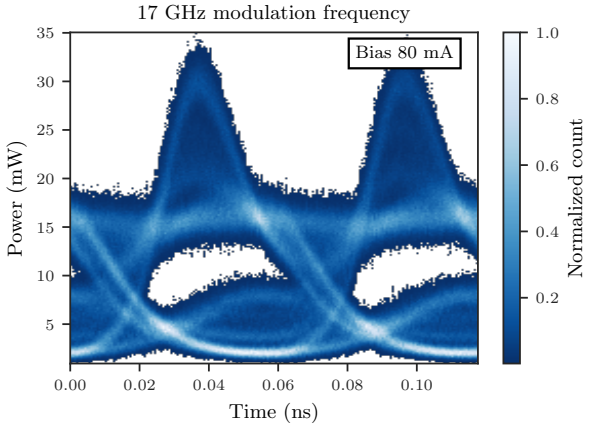

(a)

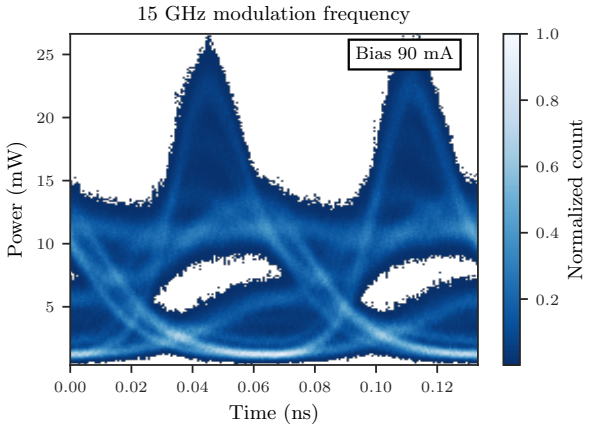

(b)

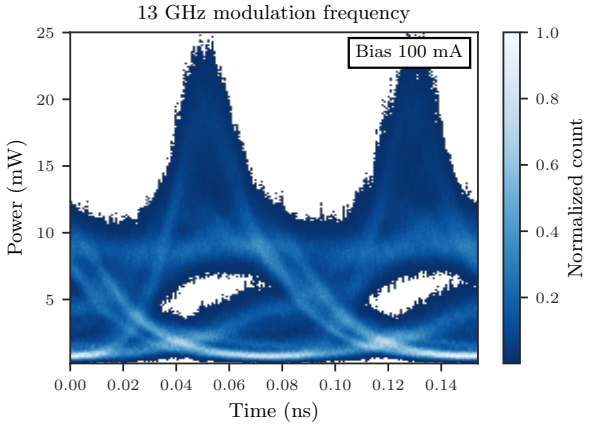

(c)

Figure 5.18: Simulated eye diagrams for cavity lengths: (a) 400 µm, (b) 700 µm, (c) 1000 µm.

5.5 Thermal model

In order to accurately solve the thermal behaviour of multi-section lasers, it is desirable to solve the heat equation in 3D. To do this, we use the finite element method (FEM).

5.5.1 FEM solvers — FEniCS

Commercially popular FEM solvers include COMSOL, ANSYS and Abaqus. Such proprietary solvers have been successfully implemented in the past [59] to simulate thermal behaviour of laser diodes, although to the best of our knowledge no such models have been implemented on purely free and open source software (FOSS). In keeping with our TD-TMM implementation we aim to implement the thermal model using FOSS. A number of FOSS FEM solvers exist, of which we considered FreeFem++, MOOSE, Elmer deal.II and FEniCS. Ultimately FEniCS was chosen as a suitable solver for a number of reasons. As FEniCS has Python bindings, it is possible to monolithically integrate the FEM solver with the TD-TMM optical model, which is primarily implemented in Python. In addition: FEniCS has an in-built analysis platform for rapid visualisation of results, the FEM solver has parallel capabilities in the form of MPI as well as automatic mesh partitioning, the project has extensive documentation and an active community. Although a meshing component, mshr, is included in FEniCS we instead used the more mature mesh generating feature of SALOME in order to generate FEM meshes. SALOME is an open-source software platform providing pre- and post-processing solutions for numerical simulations. Python bindings are also included in SALOME which allows us to fully automate geometry and mesh generation in the simulation — an example of the resulting mesh for laser is shown in Figure 5.19. The relevant publications relating to FEniCS and its constituent components are as follows: FEniCS [60, 61], DOLFIN [62, 63], FCC [64, 65, 66], UFL [67, 68], FIAT [69, 70], UFC [71, 72].

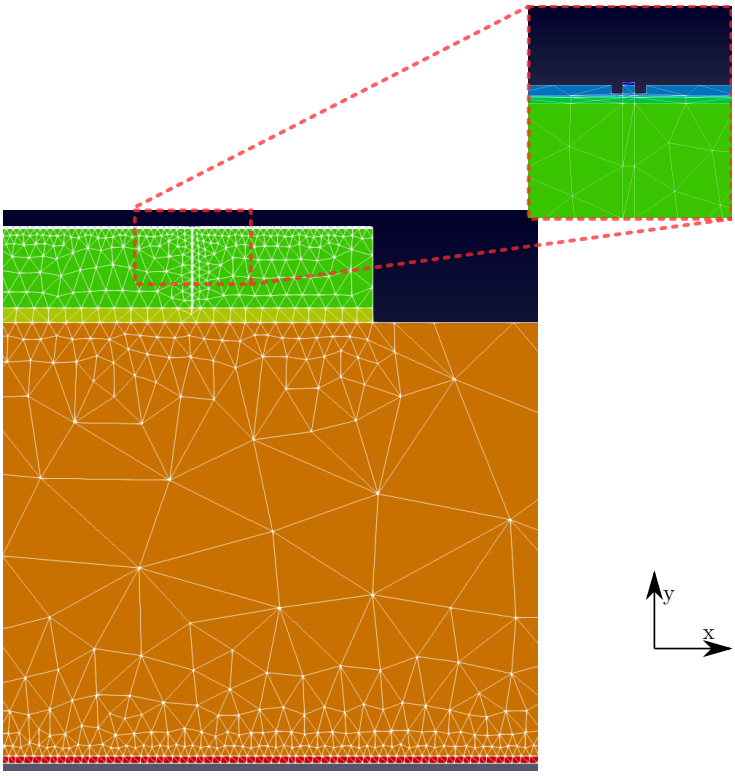

(a) x, y plane

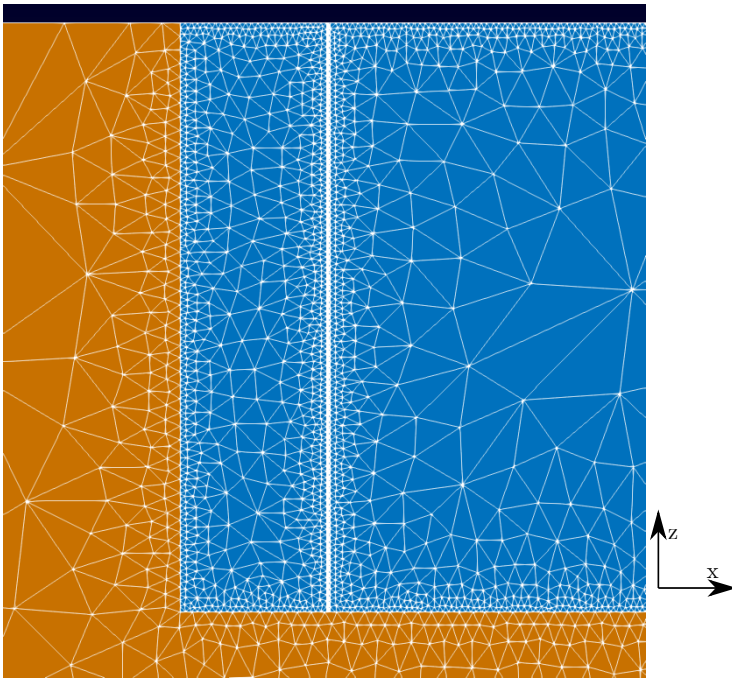

(b) x, z plane

Figure 5.19: Mesh generated by SALOME.

5.6 Optical and Thermal model coupling

5.6.1 Theory

The heat conduction equation is given as

$$\frac{\partial T(x,y,z,t)}{\partial t} = \frac{K}{\rho C}\nabla^2 T(x,y,z,t) + \frac{Q(x,y,z,t)}{\rho C}, \tag{5.32}$$

where T is the temperature, K is the thermal conductivity, C is the specific heat, ρ is density, and Q is the heat generation. x, y, z correspond to spatial co-ordinates and t is time. In the steady state case we can let

$$\frac{\partial T(x,y,z,t)}{\partial t} = 0, \tag{5.33}$$

in which case the heat equation reduces to

$$K\nabla^2 T(x,y,z) = -Q(x,y,z,t). \tag{5.34}$$

The heat generation term in each layer, Q_i is defined for three layer types. For the InP layers we define Q_i is defined as joule heating by

$$Q_i = j^2\rho_i \tag{5.35}$$

where j is the current density and ρ_i is the ohmic resistivity. For the active region, we follow the approach taken in Han et al. [59] and Kobayashi and Furukawa [31], which give

$$Q_A = \frac{V_j(1-\eta_{sp}f_{sp})}{d_A}[d_A R(z) + (j - d_A eR(z))(1-\eta_i)], \tag{5.36}$$

where d_A is the height of the active region, V_j is the junction voltage, η_{sp} and η_i are the internal quantum efficiencies of spontaneous emission and stimulated emission respectively, f_{sp} is the ratio of spontaneous emission absorbed by the cladding layers relative to the total spontaneous emission from the active region. From time domain simulations, we know that laser cavity asymmetries (due to the position of grating at the laser output end and the HR and AR coatings at the back and front of the laser) produce asymmetries in photon and carrier density profiles along the cavity. These profiles are taken into account by the current density, which is

$$j = qd[g(z)\nu_g S(z) + R(z)], \tag{5.37}$$

where $R(z)$ is given previously in Equation 5.17 and $g(z)$ and $S(z)$ are the gain and photon density profiles respectively as calculated from the TD-TMM.

Finally, resistive heating from the gold contact is also taken into account as

$$Q_g = \frac{j^2 \rho_{con}}{d_g}, \tag{5.38}$$

where d_g is the thickness of the gold and ρ_{con} is the resistance of the contact. Table 5.2 shows the values for each of the layers considered in the thermal simulation, where the smallest layers in the epitaxial structure with negligible impact are omitted. The epitaxial structure of the laser can be seen in Figure 5.20. In addition to the physical layers associated with the chip, the air interface between the chip and the copper heat sink must be accounted for. This is done by adding an effective layer between the copper and AlN carrier, with a thermal resistance calibrated by biasing a single 700 µm length laser at 100 mA and matching to simulation. Although the surface of the AlN carrier is likely a predominant source of variation in thermal behaviour from chip to chip, we use the same calibrated value for the sake of consistency.

Table 5.2: Physical parameters for each layer.

Material	Doping	Height (µm)	Conductivity K ($\mathrm{W\,m^{-1}\,K^{-1}}$)	Resistivity ρ ($\Omega\,\mathrm{m}$)	Resistance ρ_g ($\Omega\mathrm{m}^2$)
Au	–	1	300	–	1.0×10^{-10}
InP	P	1.8	68	7.6×10^{-4}	–
AlGaInAs	–	0.34	5	1×10^{-4}	–
InP	N	120	68	2.4×10^{-4}	–
Solder	–	20	20	–	–
AlN	–	600	180	–	–

5.6.2 Results

The temperature distribution in the laser can now be solved incorporating outputs from the TD-TMM. The calculated temperature profiles along the laser cavity can then be input into the TD-TMM in order to provide a full thermo-optic model of laser performance.

Light-current curves

In order to verify our model we first take the simplest case of a Fabry Pérot laser. Figure 5.21 shows the L-I curve of a ~ 400 µm Fabry Pérot laser for a range of different

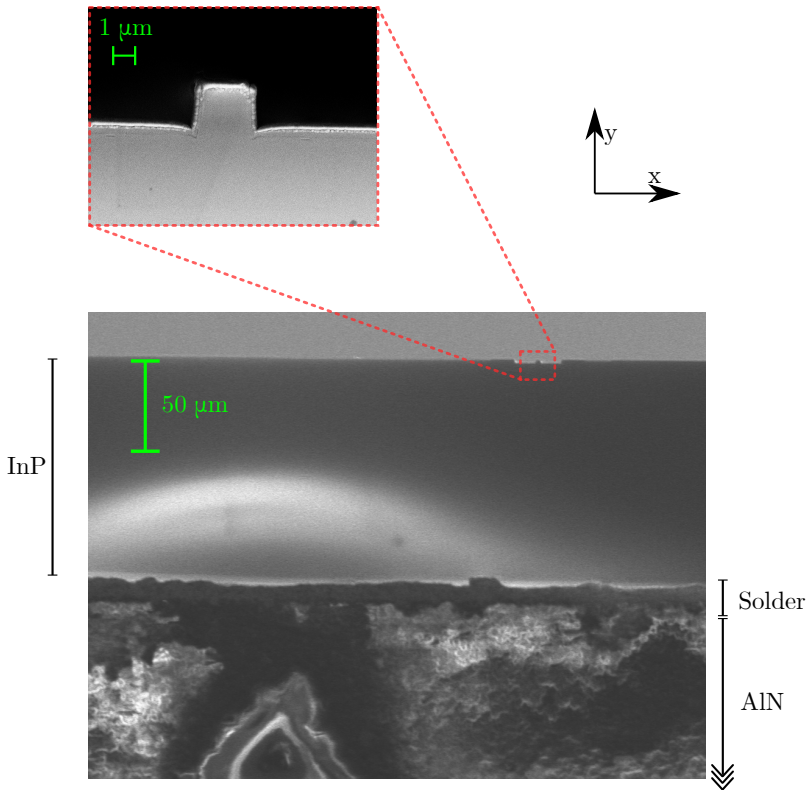

Figure 5.20: Scanning electron microscope (SEM) image of a laser face on. Height of different epitaxial layers can be seen, where the solder layer in particular varies along the width of the chip.

heat sink temperature compared with corresponding experimentally measured L-I curves. The slope efficiencies and thresholds of simulation and experiment are seen to match closely. In general, semiconductor lasers performance does, however, vary from chip to chip, with several varying factors influencing laser performance. These can include: waveguide loss α_i, quality of cleave, quality of the HR and AR coatings, injection efficiency and the accuracy of the etching process forming the waveguide. Although in this case the L-Is shown agree well, one can expect variation between the measured performance and simulated devices.

Figure 5.22 shows simulated L-I with increasing heatsink temperature for a 700 µm single mode slotted laser. The bottom plot shows a comparison of experimentally measured L-Is. The model accurately predicts the increase in laser threshold. However, in this particular case the slope efficiency for the simulated case overestimates power by $\sim 10\%$. A likely cause is variation in grating fabrication accuracy, as the laser's output power has a t^2 dependence where t is the grating transmission.

We now wish to further verify the thermal model by measuring the laser temperature and compare with predicted values. The most common method employed to

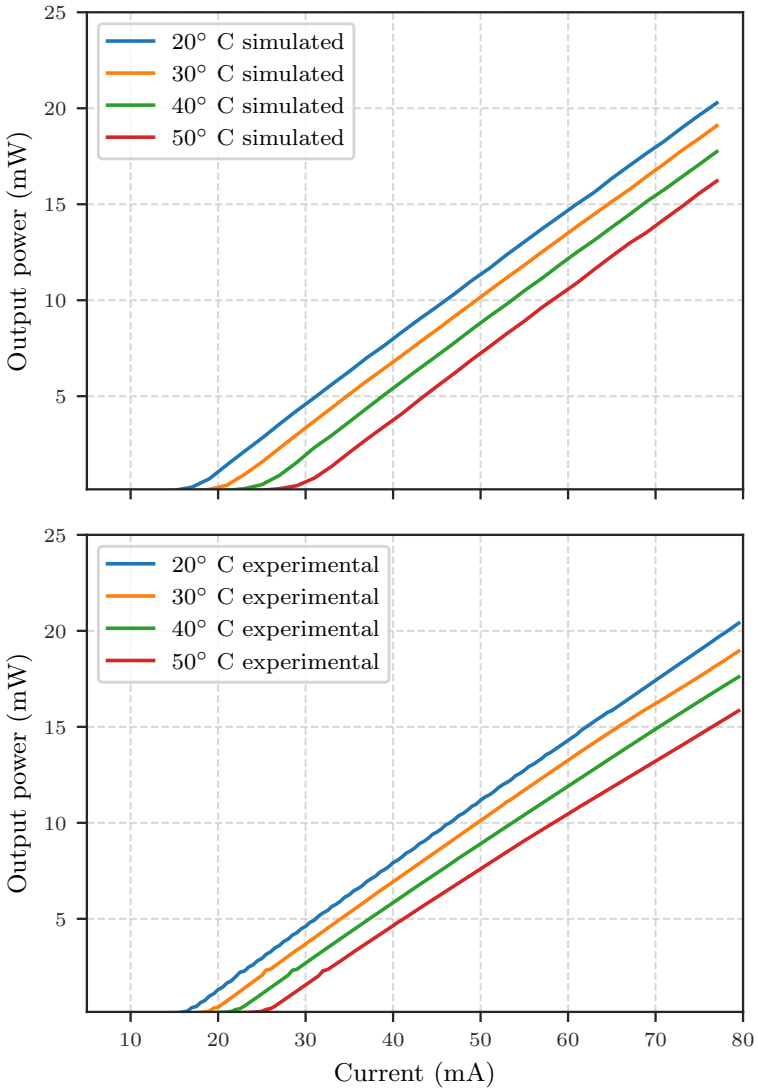

Figure 5.21: Simulated and measured L-I curves of a 400 µm Fabry Pérot laser.

measure laser temperature is to characterise the change in wavelength with temperature $\partial\lambda/\partial T$ and apply this to determine an average wavelength change from the cavity. In Figure 5.23 the modelled wavelength shift, and hence temperature, is seen to match the experimentally measured wavelength shift.

In order to more rigorously verify our model it was also desirable to compare simulated temperatures to directly measured temperature values. To this end, the CCD-TR method was employed to measure the temperature of a laser under a range of injection currents. An example of the resulting map can be seen in Figure 5.25. Regions with differing material to gold, in this case SiO_2, have been shaded white to

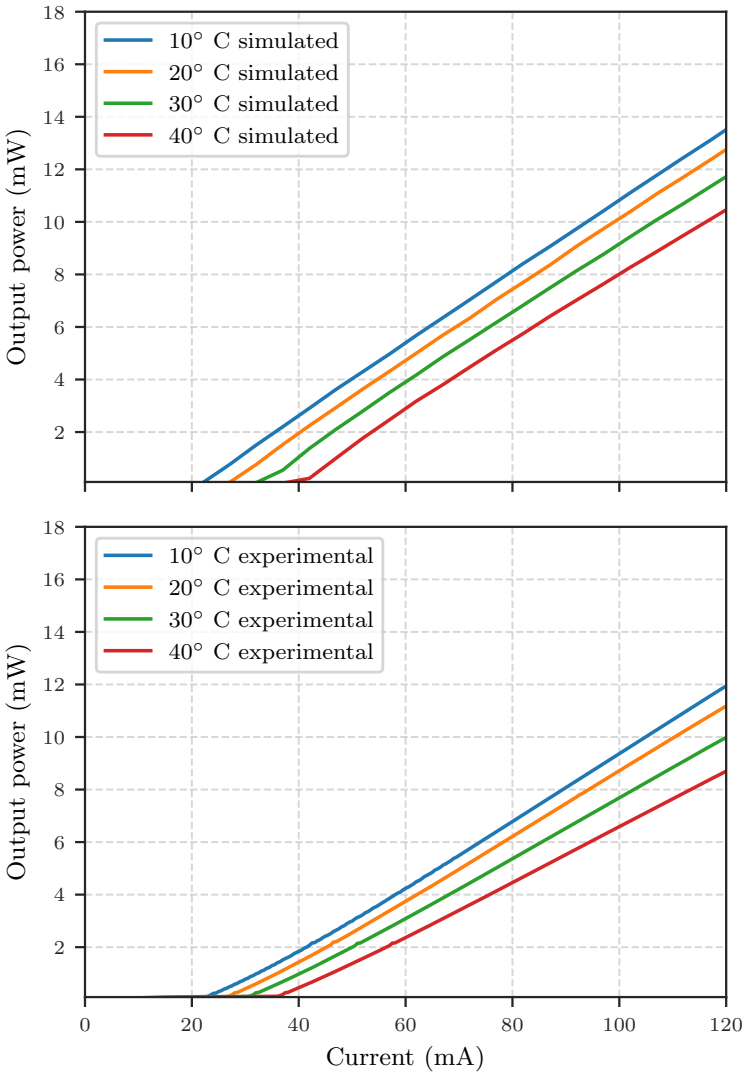

Figure 5.22: Simulated (top) and experimental (bottom) L-I curves of a 700 µm length laser with increasing temperature.

avoid misinterpretation. As the CCD-TR method is based on comparing changes in reflectivity between a series of recorded frames any vibrations of the sample during measurement will cause artefacts which hinder measurements of small or narrow features as in the case of the 2 µm wide cavities we fabricate. To overcome this an image stabilization algorithm was developed which is discussed further in Appendix B. Figure 5.24 shows the averaged measured cavity temperature compared with the averaged simulated cavity temperature for a range of injection currents. Simulated temperatures agree well with experimental values, although due to the more challenging nature of CCD-TR measurements the experimental data is somewhat less smooth than the wavelength measurements in Figure 5.23.

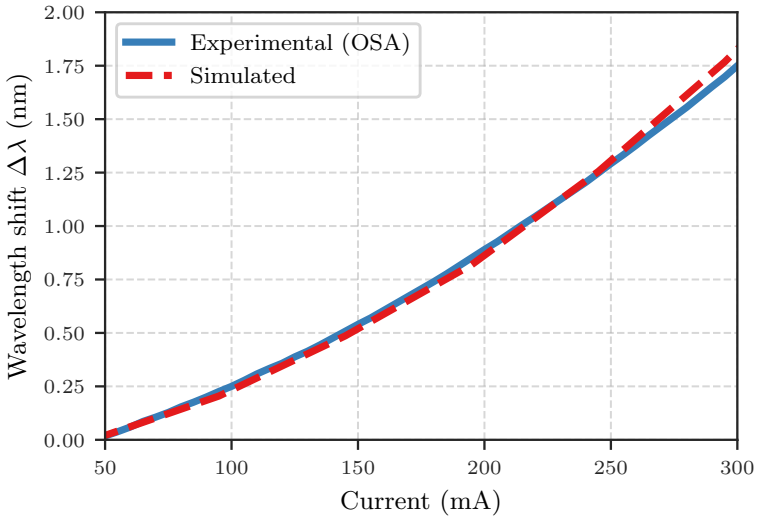

Figure 5.23: Simulated and measured wavelength shift of a 400 µm cavity length laser.

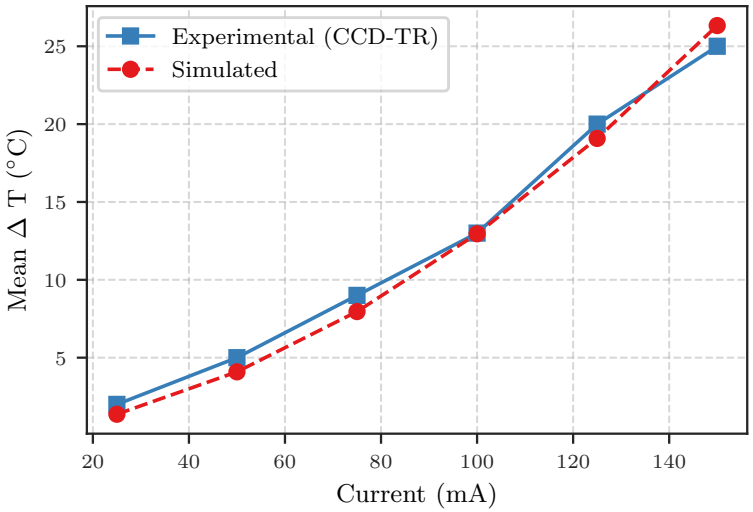

Figure 5.24: Simulated temperature of a 400 µm slotted laser compared to CCD-TR measurements.

As discussed in chapter 3, the use of high order gratings introduced a challenge in terms of mode competition arising from free spectral range reflection peaks. Previously we described the use of IIR digital filters to simulate gain dispersion and as a result we can use our model to simulate the maximum temperature at which a given laser will perform reliably at its designed wavelength before jumping to the next FSR peak. Figure 5.26 shows the simulated wavelength vs. heat sink temperature compared with experimentally determined values. One can see that the 1-period design is

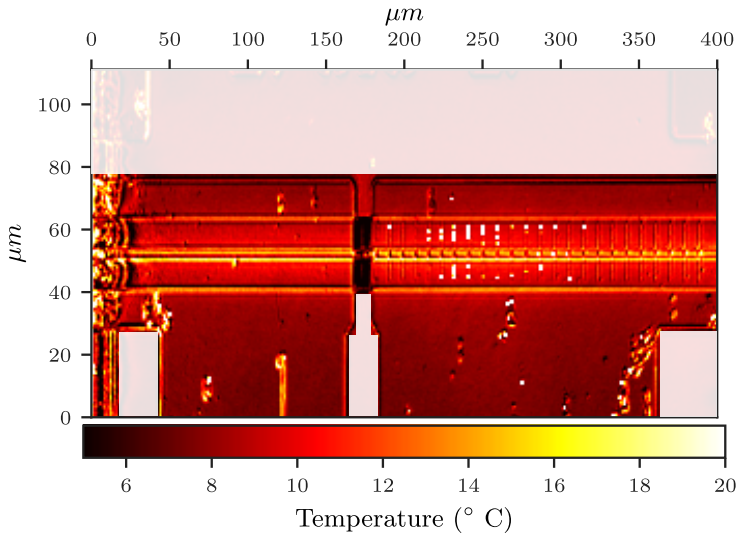

Figure 5.25: CCD-TR map of a 400 µm laser at 100 mA corrisponding to the measurement in Figure 5.24.

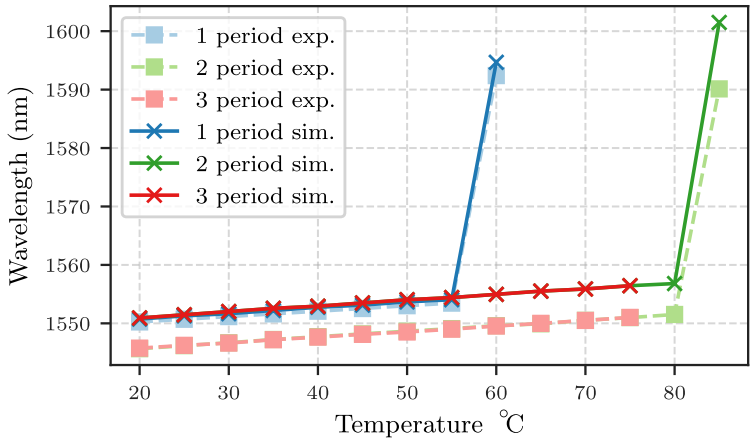

Figure 5.26: Simulated and experimental lasing wavelength of 400 µm length single mode lasers with one, two and three period gratings over a range of heat sink temperatures. The temperature at which the lasing wavelength jumps increases with the number of periods used in the grating as a result of increasing FSR peak suppression.

most susceptible to FSR mode competition, operating only up to 55 °C before the lasing wavelength jumps. The 2-period laser shows vastly improved operating range only switching wavelength at 85 °C while the 3-period laser does not undergo any mode hop over the temperature range considered. One should note the difference in predicted lasing wavelength for the 2-period and 3-period case, relative to the 1-period case. This is likely due to the fact that these lasers were from a different fabrication run

than the 1-period laser and were found to have a higher threshold than the previous fabrication from which the 1-period result is taken. This higher threshold results in a higher carrier density, which in turn blue shifts the lasing wavelength. For the sake of consistency we use the parameters from Table 5.1 for all simulations, because to use unique parameters for each chip would require re-characterisation of material properties using the Fourier expansion method. In any case, the model faithfully reproduces the phenomenon of mode competition from FSR reflection peaks and as a result can be used to verify future laser designs at high temperatures.

5.6.3 Tuning maps

We now wish to use the thermo-optic model to predict multi-section laser wavelength tuning. In chapter 3, two laser types were introduced, single mode lasers, and widely tunable vernier-based lasers, both of which can be simulated using the thermo-optic model. We will start with the simpler, single mode lasers and simulate their tuning behaviour and compare with experiment.

Figure 5.27, Figure 5.28 and Figure 5.29 show the simulated and experimental wavelength tuning map of a 400 µm, 700 µm and 1000 µm length laser respectively, at a submount temperature of 20 °C. The tuning maps of the three cavity lengths have four distinct regions where mode hopping occurs.

At high grating injection currents, the mode hops arise due to thermal effects. As the grating heats up the Bragg wavelength red shifts until the next longitudinal mode coincides with the Bragg peak, resulting in a mode hop. The inverse of the aforementioned mode hop is seen at higher gain section currents. As the gain sections increases in temperature, the longitudinal modes red shift. The lasing wavelength tunes continuously until a lower wavelength mode eventually coincides with the Bragg peak resulting in a mode hop to lower wavelengths. At low grating currents we also see mode hops which blue shift the lasing wavelength. In this case, the mode hops are simply a result of increasing carrier density in the grating region blue shifting the Bragg peak.

A fourth distinct region of mode hopping is seen in the 1000 µm cavity length laser at low gain section currents. As the gain section current is increased, a mode hops occurs which red shifts the lasing wavelength. However, somewhat counter intuitively, we note that although current is injected into the gain section the mode hop is caused by the Bragg peak red shifting, i.e. injecting current into the gain section is changing the resonant wavelength of the grating. In order to understand this we can extract the photon and carrier density profiles at the currents for which this tuning is occurring.

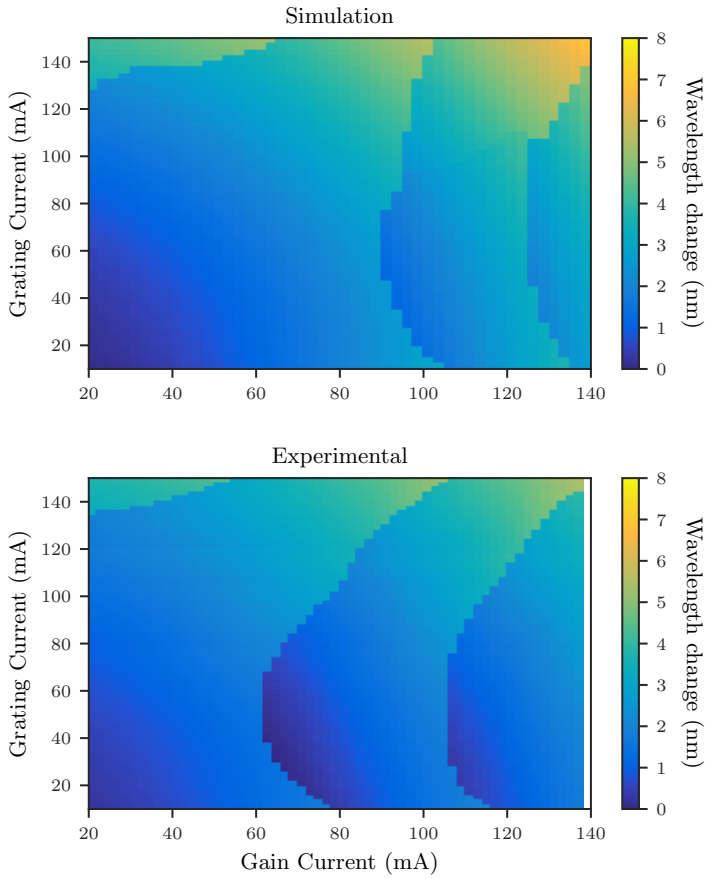

Figure 5.27: Wavelength map of a 400 µm length laser: simulation (top), experimental measurement (bottom).

Figure 5.30 shows the density profiles of the grating section corresponding to currents indicated by star markers in Figure 5.29 where we are keeping the grating at a constant current and varying the gain section current. We can see that as the current in the gain section is increased the photon density in the grating increases, and as a result the carrier density decreases. This decrease in carrier density leads to a red shift of the Bragg peak and consequently a red shifted mode hop seen in the tuning maps. This effect explains the observation alluded to in chapter 4: that uniform injection of the laser resulted in non-uniform tuning over the cavity, as inferred by the mode hops observed.

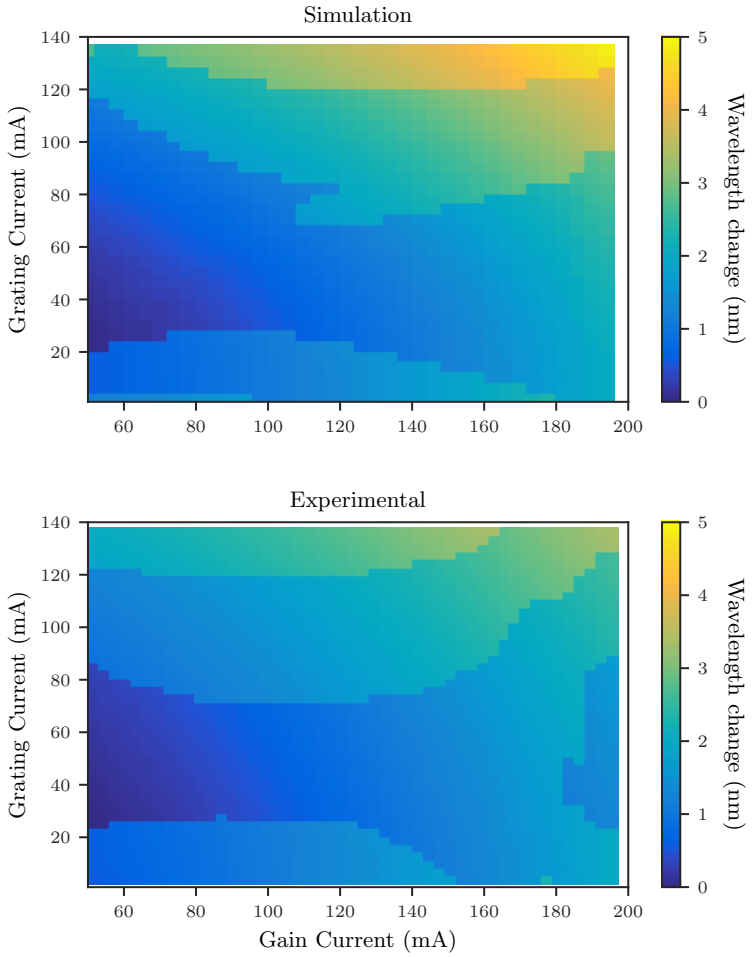

Figure 5.28: Wavelength map of a 700 µm length laser: simulation (top), experimental measurement (bottom).

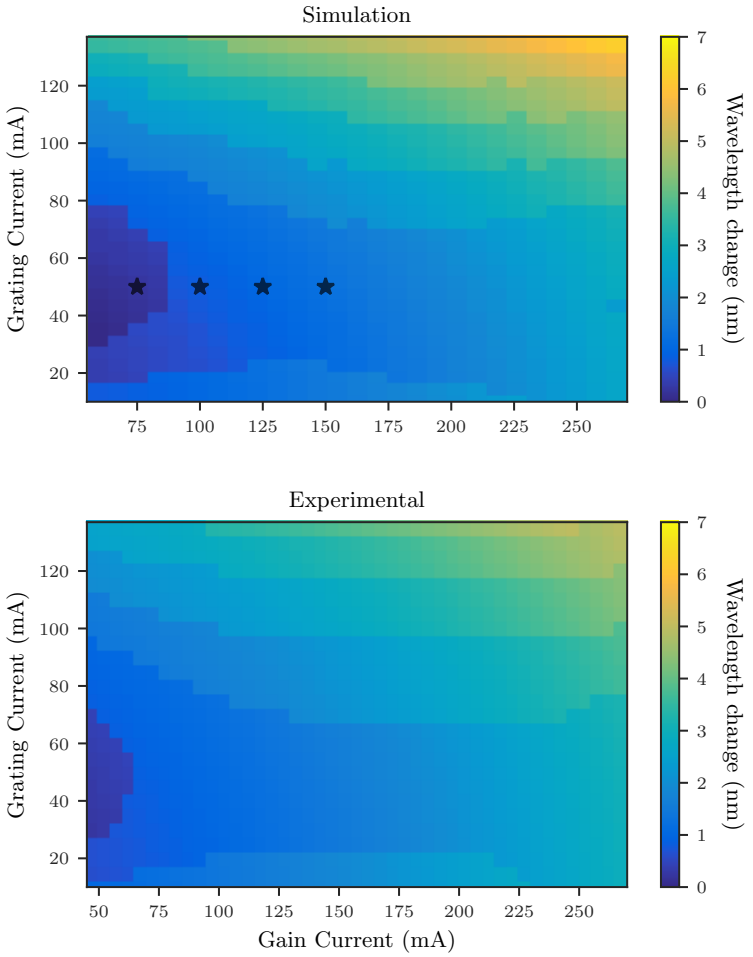

Figure 5.29: Wavelength map of a 1000 µm length laser: simulation (top), experimental measurement (bottom). Star markers correspond to the currents simulated in Figure 5.30.

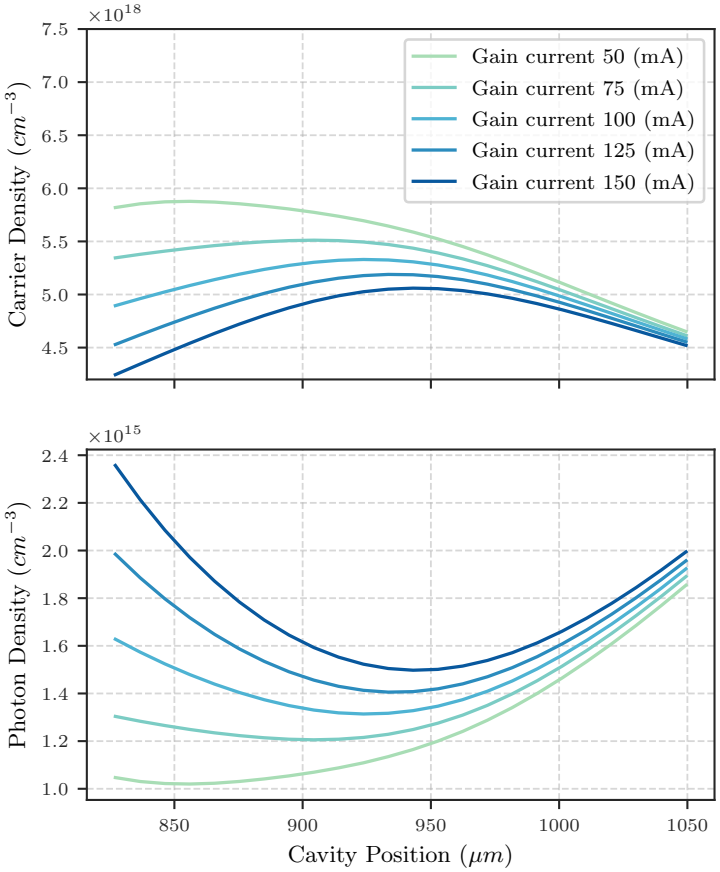

Figure 5.30: Carrier and photon density profiles within the grating section under varying gain section currents. Injecting the gain section is seen to decrease the grating section's carrier density.

5.6.4 Vernier lasers

As discussed in chapter 3 widely tunable slotted vernier lasers, similar to SG-DBRs have previously been fabricated. These lasers were capable of being tuned across the C-band with SMSR $\geq$ 30 dB. For these lasers a number of different tuning regions were observed [23]. We can apply the thermo-optic model to better understand this tuning and predict performance.

Front period 70 µm Back period 80 µm

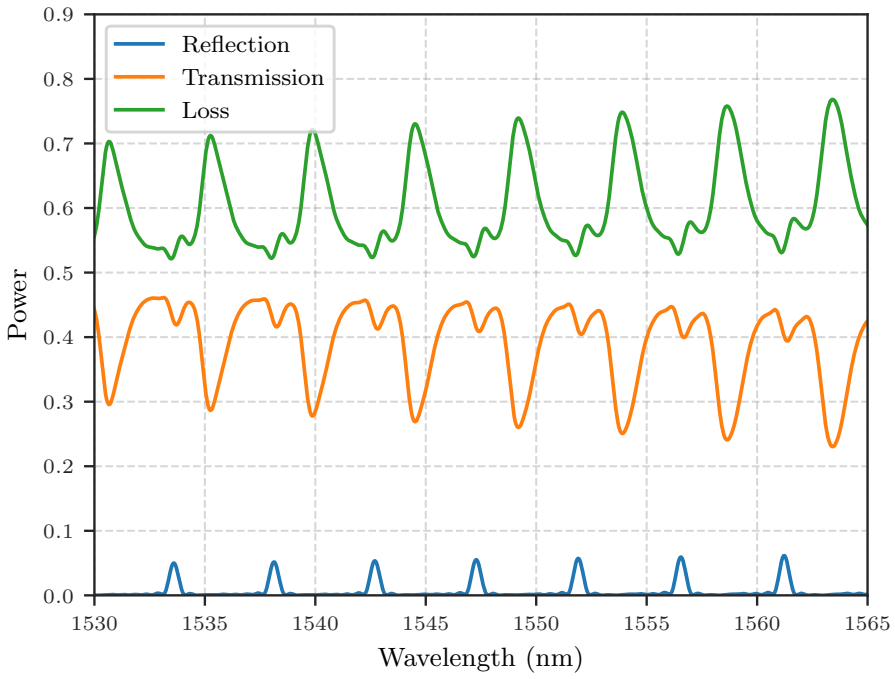

Figure 5.31: Simulated power reflectivity, transmission and loss for a 9 slot grating of period 80 µm.

In this section we consider a vernier laser with slot periods of 70 µm for the front mirror and 80 µm for the back mirror. The FSRs are 4.9 nm and 4.3 nm for the front and back mirror, respectively. The gratings both consist of nine slots each. The simulated optical properties of such a grating is shown in figure Figure 5.31. Figure 5.32 shows the experimentally measured wavelength and SMSR of the laser, compared with simulated values in Figure 5.33. The tuning wavelength of the simulation is seen to match well with the experimental case reproducing the tuning trends accurately. As in the single mode case, the tuning map has a "saddle" feature — in this case the middle of this feature is at Front and Back current $\sim$ 100 mA. Although similar to the tuning previously described for the single mode case, a key difference is that

there is no strong coupling effect between the front and back sections as was seen in for the gain and grating section previously. Rather, all the tuning behaviour arises from the injected current in each individual section with minimal crosstalk. At lower currents, the front and back section are tuned primarily due to increasing carrier density. As the current to each section increases, the thermal tuning at some point exceeds the carrier density tuning. The midpoint of the "saddle" feature corresponds to the currents at which both carrier and thermal tuning are approximately equal to one another, beyond which thermal tuning begins to dominate. This tuning pattern results in a limiting factor for efficiency, in so far as the tuning between channels must be in regions with injection current $\geq 100\,\mathrm{mA}$.

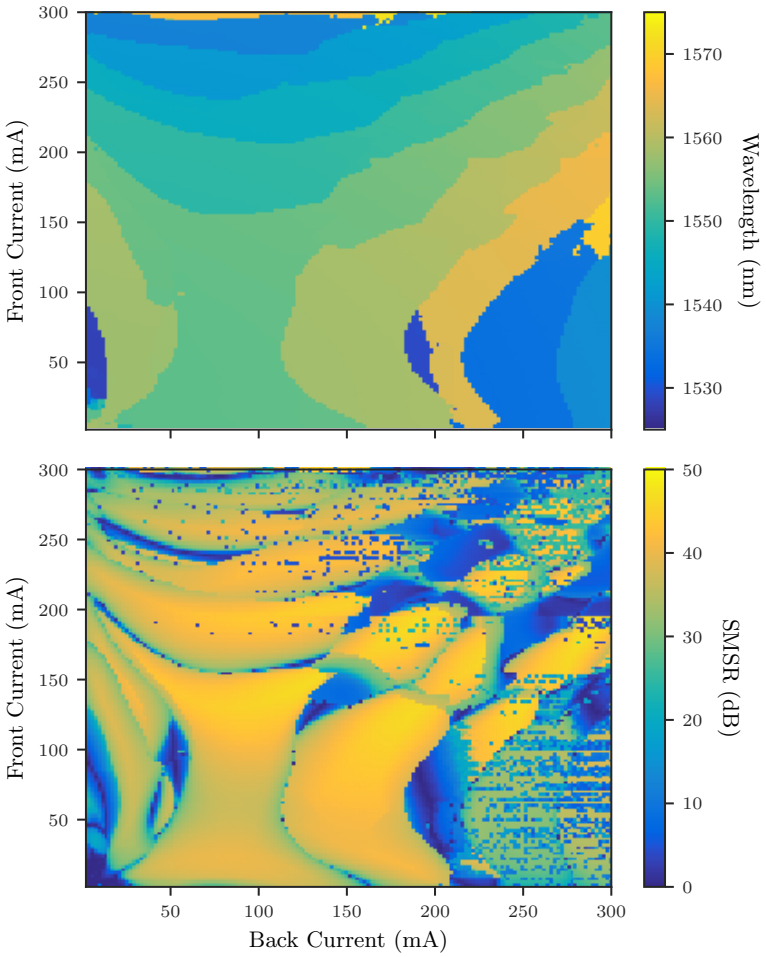

Figure 5.32: Experimental tuning map of wavelength (top) and SMSR (bottom).

Once above 100 mA however, the tuning process is still rather inefficient requiring $\geq 250\,\mathrm{mA}$ in order to tune certain channels. Examining the simulated profile of the

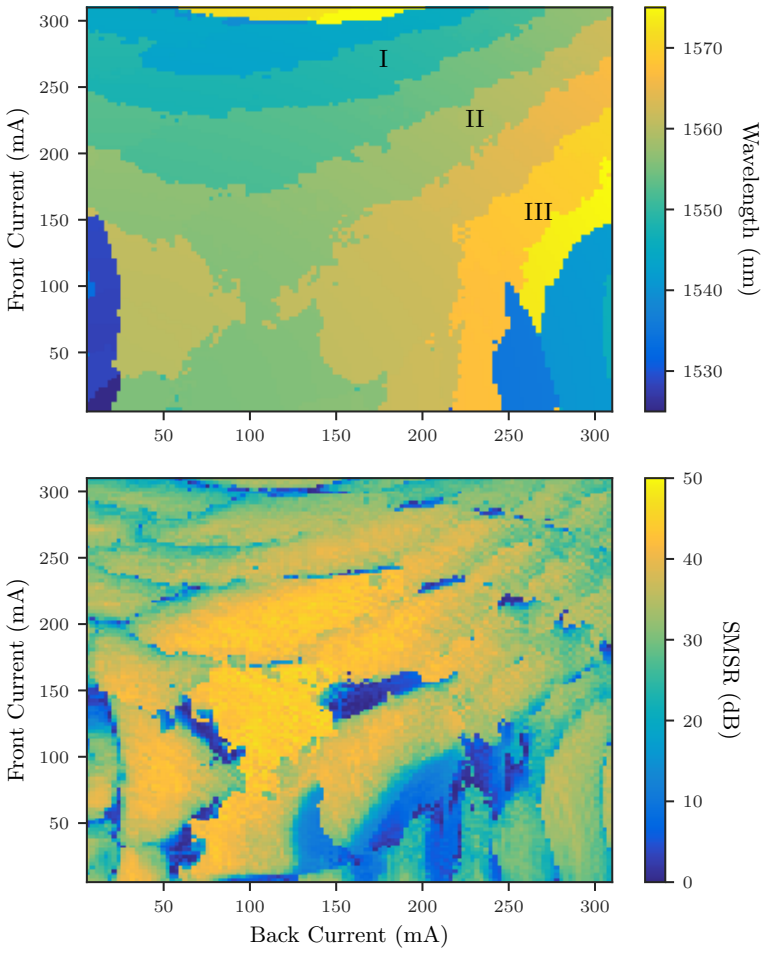

Figure 5.33: Simulated tuning map of wavelength (top) and SMSR (bottom).

cavity in detail can shed light on this inefficiency. Consider the current co-ordinates shown by Roman numerals on Figure 5.33, that correspond to three distinct wavelength channels. For each of these co-ordinates we have simulated the thermal, carrier and photon density profiles along the cavity. Figure 5.34 shows the surface of the laser as calculated via the FEM. The inefficiency in tuning leads to considerably large temperatures in the gratings when tuning between super-modes, reaching up to $\sim 77\,^{\circ}\mathrm{C}$.

Extracting the profiles along the cavity gives the temperature, photon density and carrier density as plotted in Figure 5.35. This plot reveals a prohibitive consequence of direct current injection on tuning efficiency. The carrier density in the bottom plot is seen to increase with mirror injection current. This is in contrast to the usual approximation that the carrier density is constant once the laser is above threshold (see Figure 2.7, chapter 2). This is due to the fact that the radiation loss within the mirror

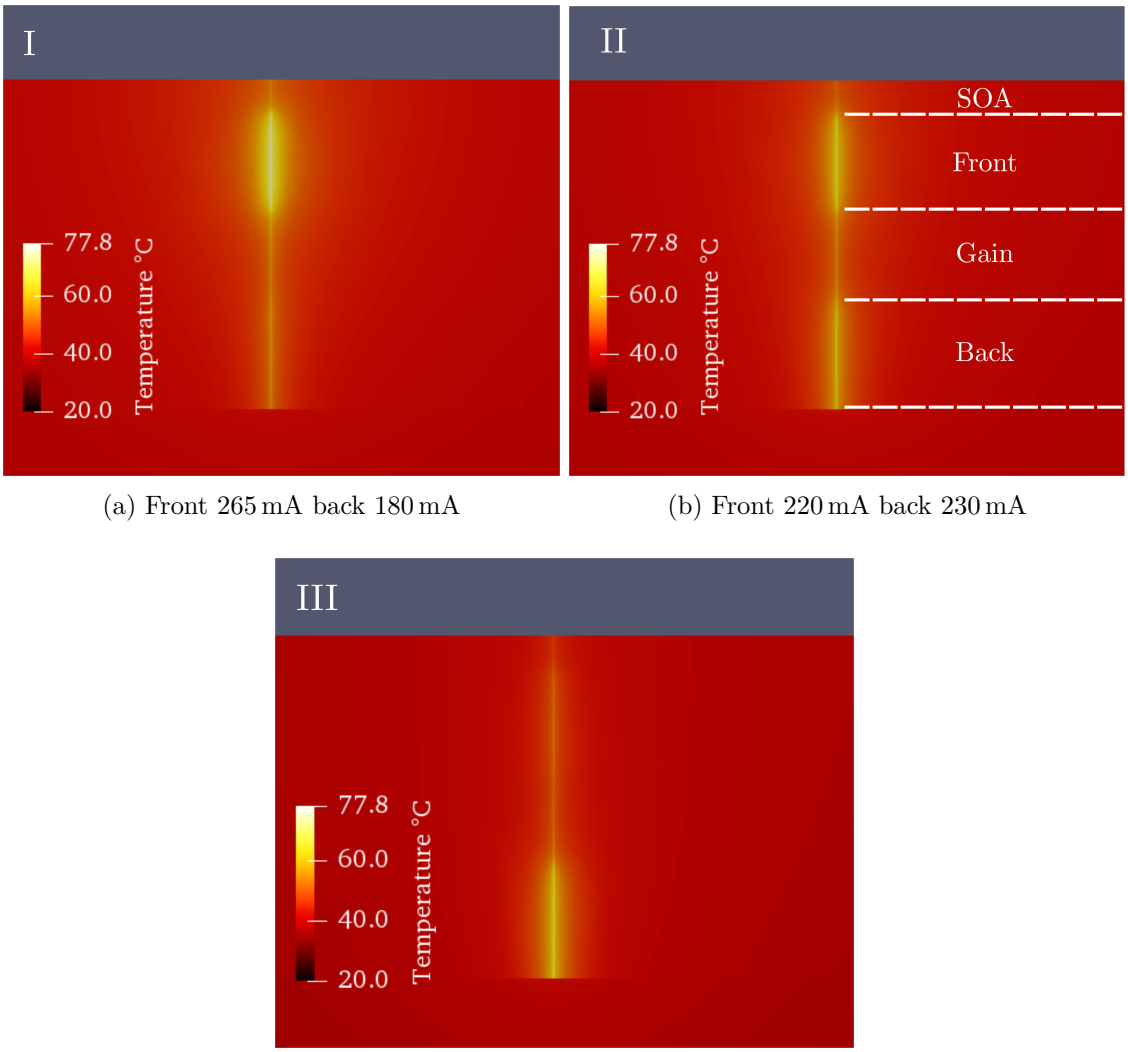

(a) Front 265 mA back 180 mA

(b) Front 220 mA back 230 mA

(c) Front 150 mA back 264 mA

Figure 5.34: Simulated temperature distributions for the three supermodes labelled in Figure 5.35.

sections is quite large; a result of etching deep slots. As such, the gain is not saturated within the gratings and the carrier density can increase with injection current. This can also be understood by considering the grating individually in terms of its net cavity gain and loss. A cavity is considered above threshold when the net cavity gain equals the loss, and as the grating section has a relatively large amount of loss, it will have a higher threshold. The carrier density is thus free to increase with current as it's loss keeps it below threshold. The increase in carrier density results in a negative change in the effective refractive index due to the free carrier plasma effect which counteracts the positive refractive index change induced via thermal tuning. The two tuning effects are counterbalancing one another reducing the overall efficiency of the thermal tuning, resulting in the high injection currents and temperatures required.

Considering the tuning of the front section in Figure 5.35 from I to III, we can calculate the contribution to the refractive index change from the individual physical effects, as can be seen in Figure 5.36. Despite the high injection current the carrier density induced Δn_{eff} is still significant, reducing the efficiency of the thermal tuning to a large degree. The lasing spectrum at each current co-ordinate is also shown in Figure 5.37 where the degradation in SMSR is largely due to competing super-modes. This degraded SMSR is likely due to the high carrier density in the mirror sections resulting in an increase in spontaneous emission ($R_{sp} \propto N^2$).

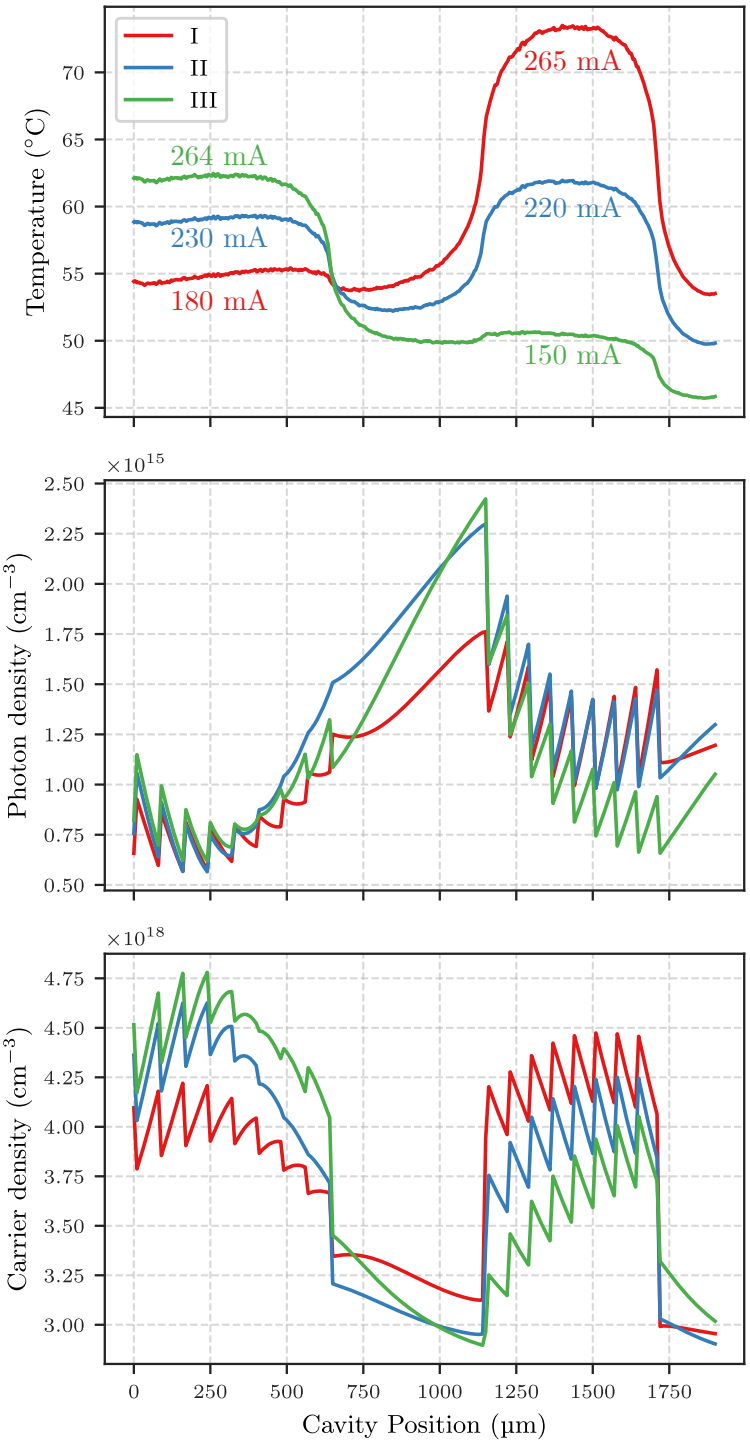

Figure 5.35: Simulated profiles in the laser cavity for the three supermodes labelled in Figure 5.35, (top) temperature, (middle) photon density, (bottom) carrier density. The Front/Back section currents for I, II and III are 265/180, 220/230 and 150/264 mA respectively with a constant gain and SOA current of 120 mA and 30 mA respectively.

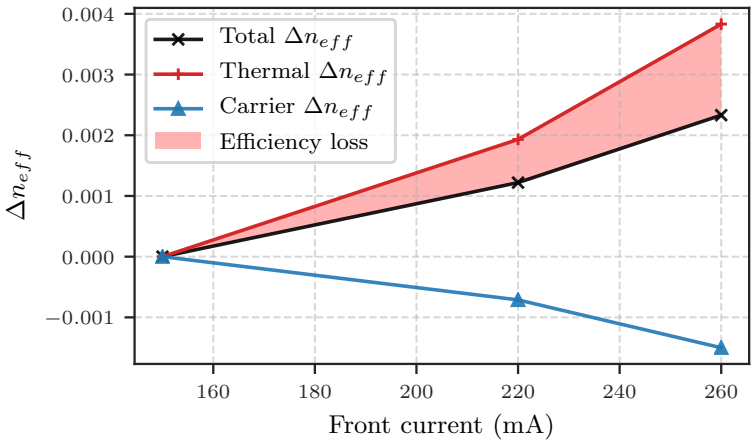

Figure 5.36: Individual contribution of physical effects to the overall tuning.

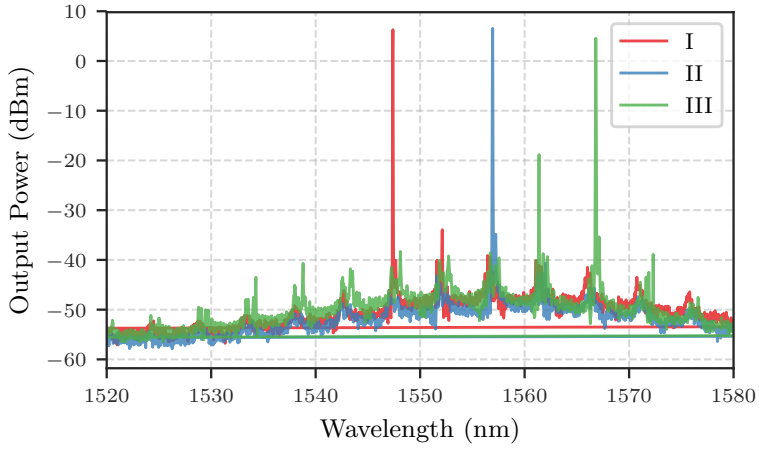

Figure 5.37: Simulated lasing spectrum for the three supermodes labelled in Figure 5.35.

Front period 70 µm Back period 80 µm with micro-heaters

One potential method of avoiding high carrier density effects (spontaneous emission and wavelength tuning) while tuning is to employ thin film micro-heaters. This involves fabricating a resistive element near the cavity which can be used to tune the laser cavity via resistive heating. Implementing such micro-heaters near the Front and Back mirrors, we can simulate the tuning pattern of the laser as shown in Figure 5.38. The design of such micro-heaters is beyond the scope of this thesis, however, it is possible to take previous implementations as a gauge of the potential tuning performance. Han et al. [73] demonstrated a DBR with extend the tuning range using micro heaters which where capable of inducing a temperature change ΔT of 60 °C at 0.5 W. We can include a heat source in the thermo-optic model capable of achieving the same temperature and simulate the tuning performance. The result of this can be seen in Figure 5.38, where the laser has been simulated at an injection current of 300 mA, injected uniformly over the Front, Gain and Back sections, with the micro-heater power being increased in order to induce a temperature change.

Plotting the tuning maps against the average Front and Back section temperature from this simulation results in Figure 5.38. This map reveals the tuning performance when the carrier dynamics are constant. The simulation suggests that in order to tune into the available channels a ΔT of ≤ 40 °C is needed. The simulated change in SMSR performance, relative to the direct injection method, is shown in Figure 5.40, where we have specified a minimum SMSR performance of 40 dB (values below 40 dB are shaded red). In order to make the comparison valid the SMSR is taken over equivalent wavelength tuning ranges in both maps. The simulation suggests that the purely thermal tuning improves the SMSR performance, particularly at the higher tuning currents. Given that the removal of carrier dynamics from the tuning process results in a higher SMSR, it is likely that the degraded SMSR performance at higher injection currents is due to the associated high carrier densities.

Though promising, it should however be noted that thin film micro-heaters may require more input power and as such, the overall wall plug efficiency of the device may be reduced. Further research is required in regard to designs involving such heating elements, and this is discussed in chapter 7

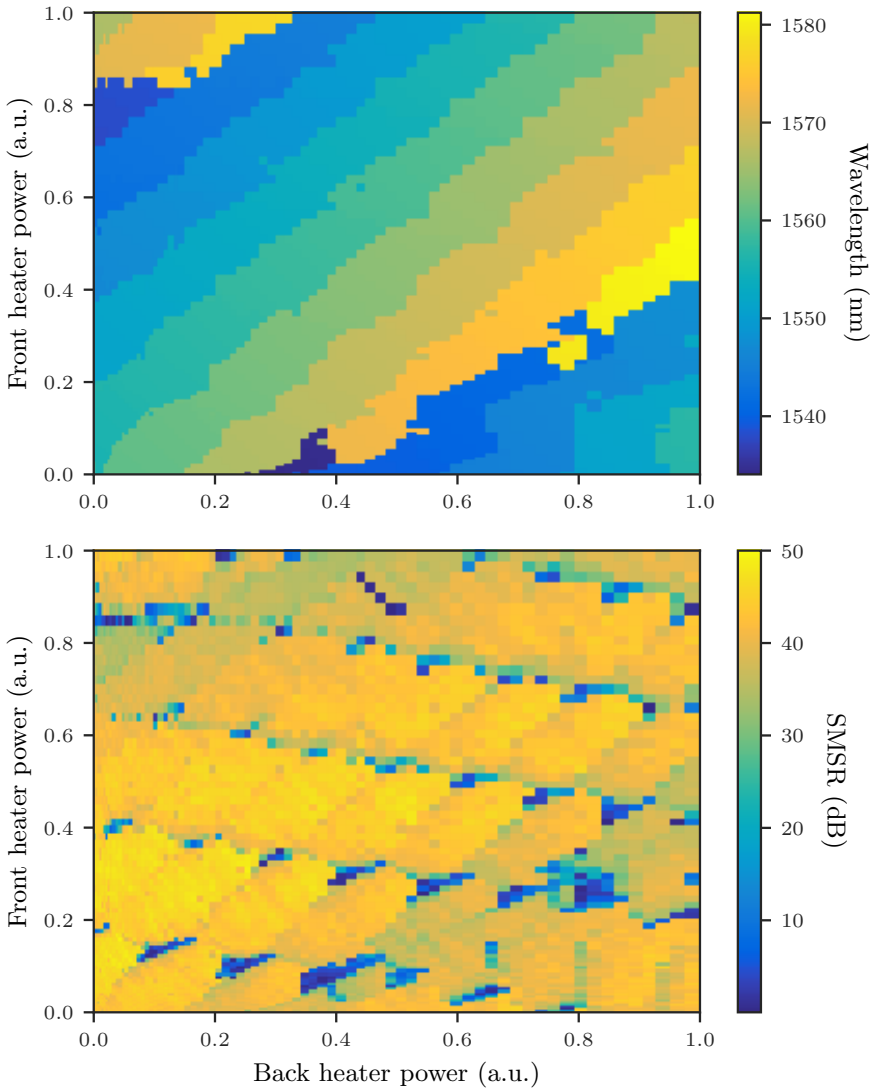

Figure 5.38: Simulated tuning map of wavelength (top) and SMSR (bottom) for a vernier laser biased uniformly at 300 mA with varying Front and Back section micro-heater power.

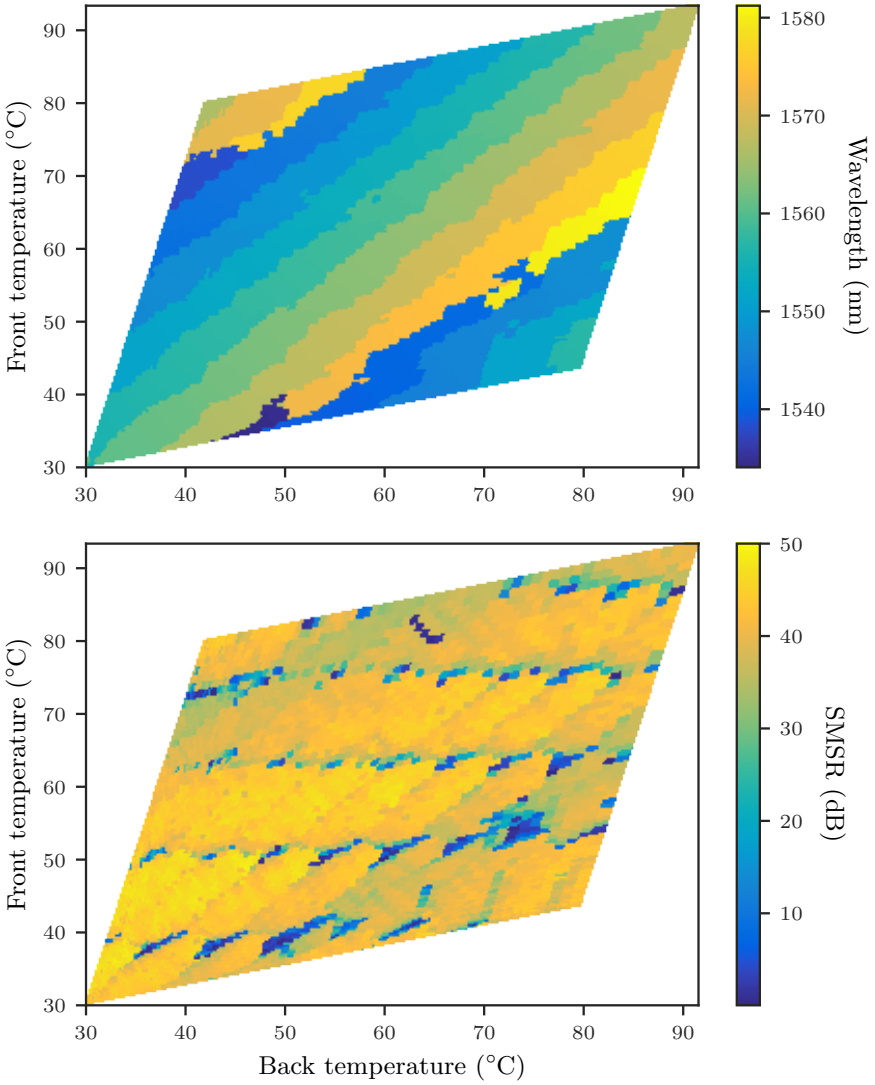

Figure 5.39: Simulated tuning map of wavelength (top) and SMSR (bottom) for a vernier laser biased uniformly at 300 mA with varying Front and Back section average temperatures.

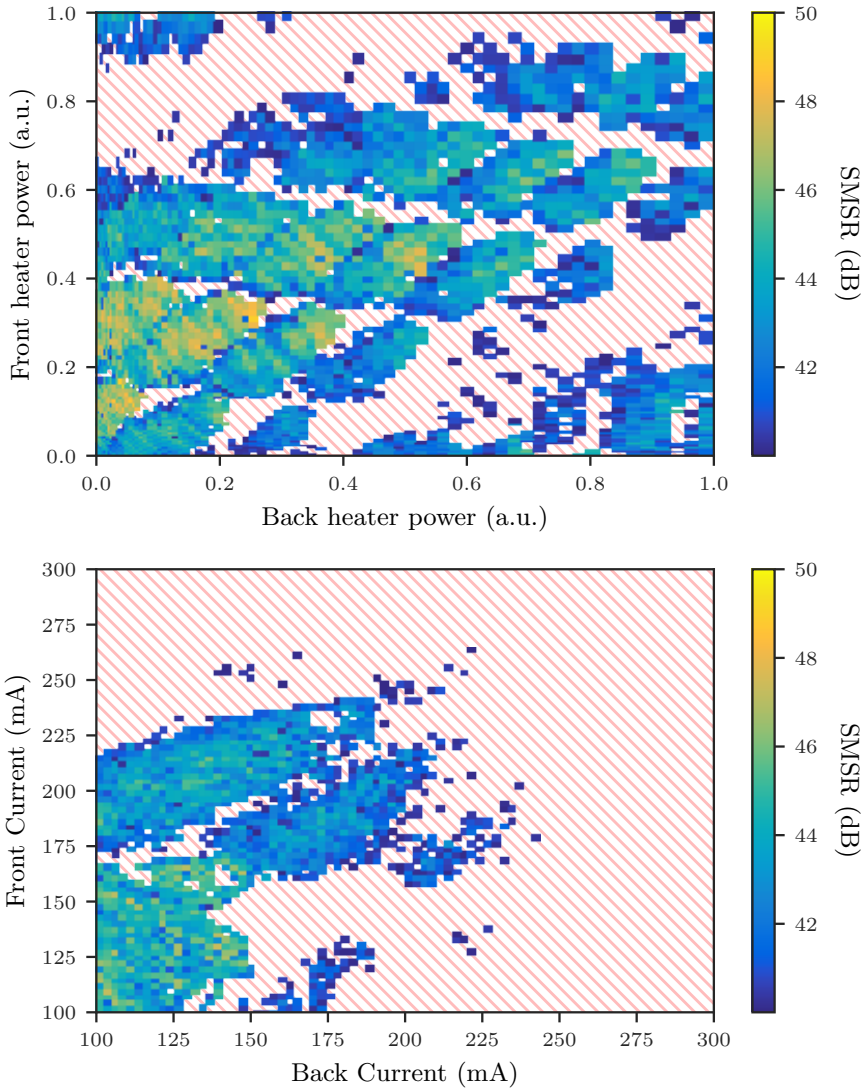

Figure 5.40: Simulated SMSR map of micro-heater tuning (top) and direct current injection (bottom) over an equivalent tuning range. Shaded regions are below 40 dB.

Front 97 µm Back 108 µm — asymmetric case

In this section we consider a vernier laser with slot periods of 97 µm for the front mirror and 108 µm for the back mirror. The FSRs are 3.8 nm and 3.5 nm for the front and back mirror, respectively. Unlike the previous example this designs has 5 slots for the front grating and 9 resulting in a front grating of 485 µm length and a back of 972 µm length. Figure 5.41 is the experimentally measured wavelength and SMSR of the laser, compared with simulated values in Figure 5.42. The result of a shortened front section is seen in the map in terms of asymmetry. From subsection 5.6.1, the heating term Q is proportional to the current density j. As we have shortened the front grating, j and Q are higher relative to the back grating. This results in a faster rate of tuning with front current, as seen in Figure 5.41 where the tuning map has in effect been compressed relative to the previous symmetric device.

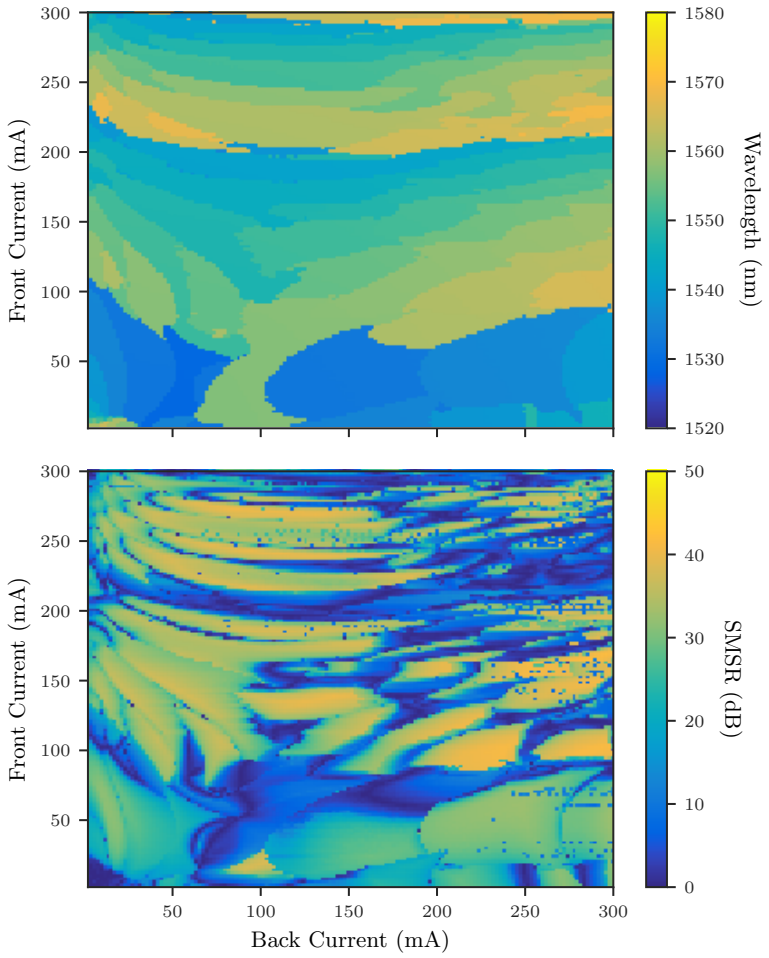

Figure 5.41: Experimental tuning map of wavelength (top) and SMSR (bottom).

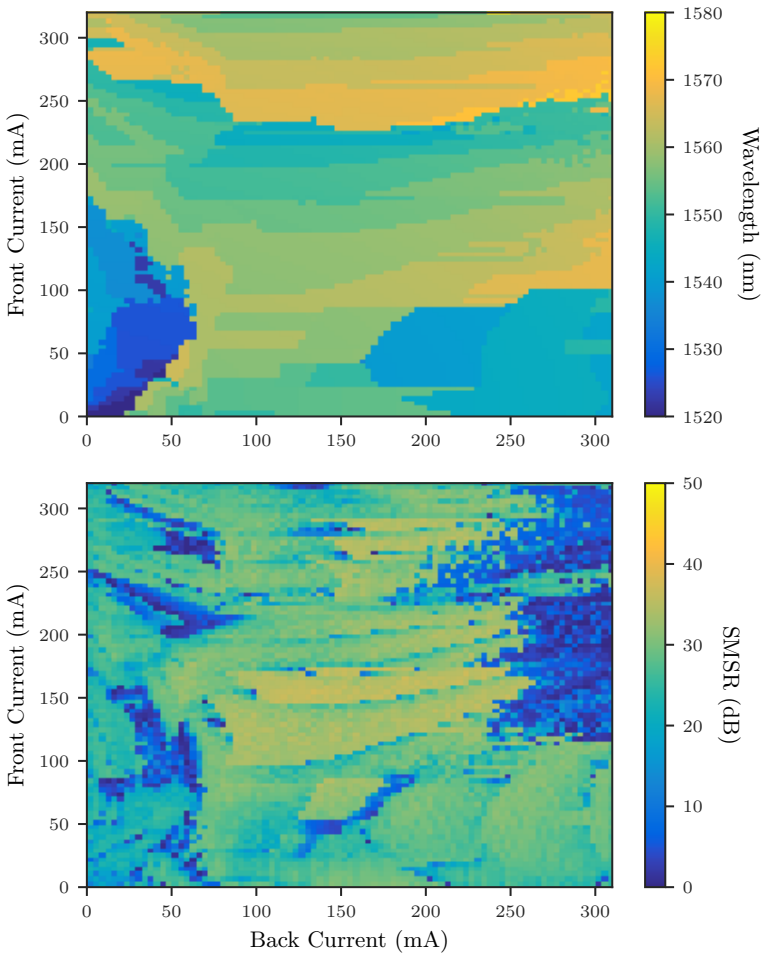

Figure 5.42: Simulated tuning map of wavelength (top) and SMSR (bottom)

Vernier linewidth

The linewidth of widely tunable lasers is another parameter which is of importance. Generally speaking, the desired linewidth should be $\leq 1\,\text{MHz}$. Given that the vernier lasers have relatively long cavity lengths in excess of 1500 µm one anticipates a relatively low linewidth, which is inversely proportional to the cavity length. Contrary to this expectation the linewidth experimentally measured from such Vernier lasers was at best $\sim 2\,\text{MHz}$. The cause of this was not fully understood and whether this was due to device fabrication or inherent to the design is a question which needs to be answered before the next iteration of designs. In order to gain an insight into this we apply the TD-TMM thermo-optic model as a diagnostic tool to simulate the theoretical linewidth performance compared with the experimentally measured linewidth. To this end, we consider a vernier laser from the most recent fabrication run, which attained reasonable linewidth performance over the range of channels. The grating period of this laser is 52 µm for the front mirror and 57 µm for the back mirror, which leads to FSRs of 6.6 nm and 6.02 , respectively. This laser was measured to have eleven wavelength channels which could be tuned to, each channel having good SMSR $\geq 30\,\text{dB}$ from 1520 nm to 1570 nm with an average linewidth of $\sim 7.5\,\text{MHz}$ [23].

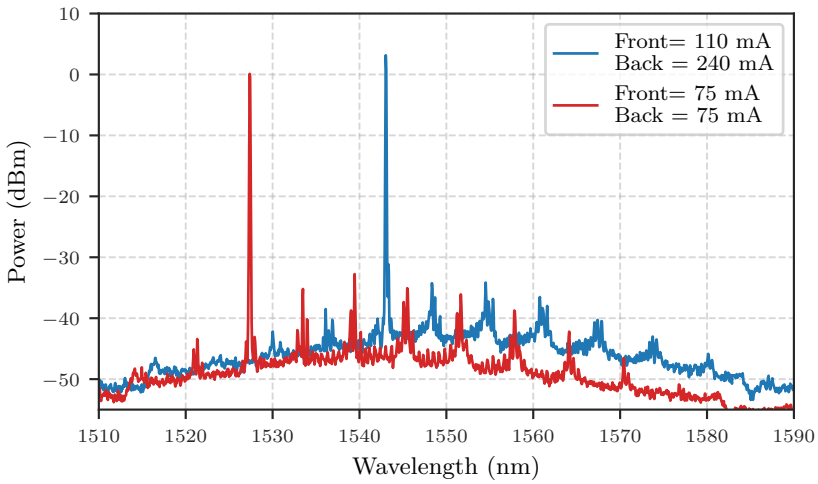

Figure 5.43: Simulated lasing spectrum of a vernier laser tuned to two different channels.

Taking the 1525 nm channel which was tuned with front and back currents of 75 mA each, a gain section current of 120 mA and an SOA current of 30 mA; the linewidth was measured using the self-heterodyne method [58]. The thermo-optic model was then run with the same injection currents, the resulting spectrum correctly predicting the laser channel as shown in Figure 5.43. The TD-TMM was then run for

sufficient iterations (as described in section 5.4.1) in order to attain a good frequency resolution of the line-shape from which the FWHM was extracted via a Lorentzian fit. The results of this are shown in Figure 5.44. The simulation predicts a somewhat higher linewidth of 5.96 MHz compared with the experimentally measured value of 4.97 MHz. Importantly, the relatively poor linewidth performance was reproduced in the simulation

We also consider a second wavelength channel tuned to approximately the centre of the C-band at 1545 nm. The comparison between simulation and experiment is seen in Figure 5.45. The simulation in this case provides a closer match with experiment predicting a FWHM of 7.36 MHz versus the measured 7.16 MHz. The high theoretic linewidth implies that the vernier design requires alterations in order to achieve linewidth on the order of 1 MHz.

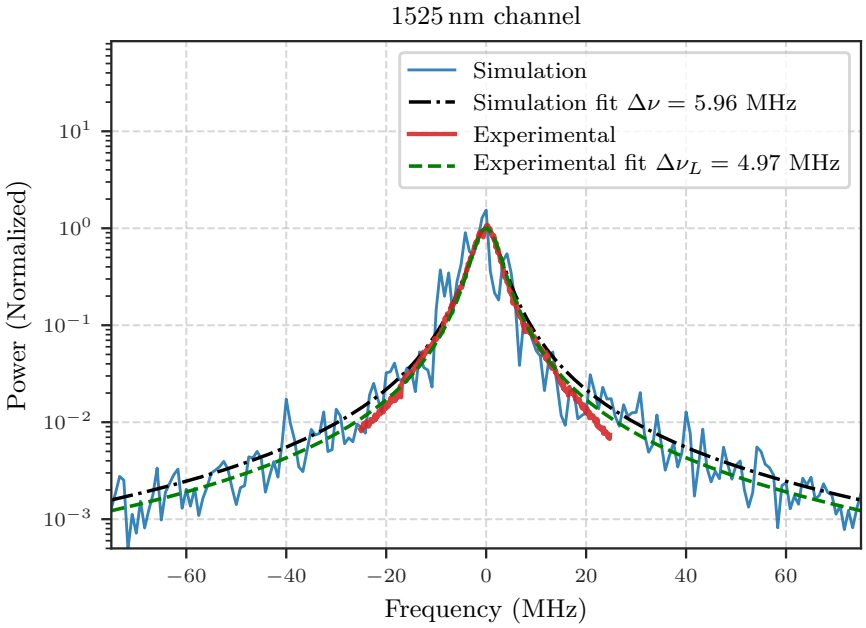

Figure 5.44: Experimental and simulated linewidth of a vernier laser with front and back currents of 75 mA each; gain section current of 120 mA.

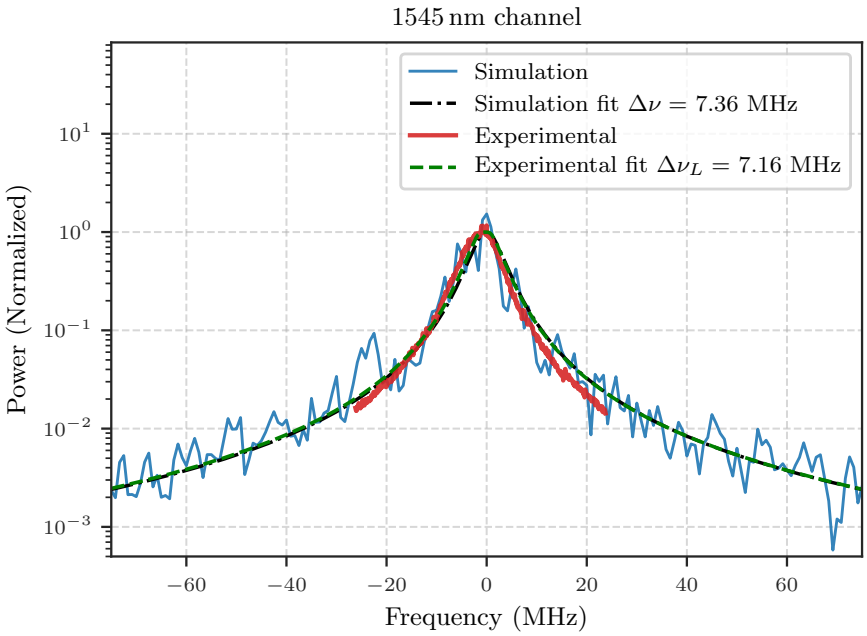

Figure 5.45: Experimental and simulated linewidth of a vernier laser with front and back currents of 110 mA and 240 mA respectively; gain section current of 120 mA.

5.7 Conclusion

This chapter has built on the previously introduced analytic model by developing a high fidelity thermo-optic numerical model. This numerical model allows for the analysis of static laser performance as well as a range of transient optical dynamics. Simulation results have, where possible, been compared to experimentally measured results, with good agreement. To the author's knowledge, we present the first direct comparison of simulated laser temperature to spatial temperature maps through use of the CCD-TR method. Despite challenges of varying fabrication parameters the model is seen to agree well with experimental results, in part due to the previously experimentally determined physical parameters [20, 23]. Additionally, to the best of our knowledge this is the first such thermo-optic model that has been implemented using exclusively free and open source software.

The model has been used to gain a better understanding of the tuning effects of both single mode and widely tunable vernier lasers, explaining all the tuning regions observed and the physical reasons behind them. For the Vernier lasers, the model has been used to analyse the fundamental reasons behind the high tuning currents which are required. From this we have concluded that the use of direct current injection results in significant increases in carrier density, counteracting the desired thermal tuning. In addition, the linewidth performance of the Vernier lasers was investigated and found to agree with experimental measurements. From this we can conclude that future designs require further optimization if the linewidth is to be reduced.

In terms of the general scope of our work, we have now developed an accurate model with which to predict laser performance. Although gaining a physical understanding of the lasers is a key aim of our work, an important aspect of our research is ultimately to improve the overall performance of the slotted laser diodes. Any such performance improvements require us to precisely optimise the next iteration of laser designs. With this in mind, we will now look to leverage the TD-TMM to precisely optimise designs, with the goal of improving over previous iterations, as well as exploring potential new laser designs for specific applications.

Chapter 6

Laser optimization

6.1 Introduction

Chapter 3 contained a discussion of the current slotted laser design and fabrication, on which the experimental measurements of this thesis would be based. These lasers have achieved good overall performance, with stable single mode performance, high SMSR, low linewidth and full C-band coverage when implemented as laser arrays [21].

This chapter builds on the previous design run with two primary goals in mind. Firstly, we wish to improve laser performance, however, as there are several performance criteria such as SMSR, linewidth and output power, we need to develop a method whereby we can quantitatively define the performance of a given laser design. As will be seen, the previous design iteration falls short of some of the aforementioned performance criteria which we wish to rectify in our next design iteration. Specific aims are to improve the output power and the single mode stability at higher temperatures. This leads to our second goal, we wish to generate new laser diode designs with as few assumptions or arbitrary design decisions as possible. Ideally a laser design should be purely a function of the performance requirements and design restrictions which we initially define. Such a process will allow for fine-tuned lasers which are not over or under optimized in regard to any one performance criterion. This will also facilitate future design iterations, as once a laser design is defined in terms of performance requirements, subsequent designs can be easily modified to take into account feedback from experimental measurements.

6.2 Slotted laser diode optimization

Optimizing slotted laser diodes poses a number of challenges generally not encountered when optimizing lasers with buried gratings. Chief among these challenges, is the fact that etching into the laser ridge necessarily introduces radiation loss, as a portion of

the field profile will overlap with the etched slot and be radiated from the waveguide. As a result, the grating structure needs to be carefully optimized, and although one cannot entirely avoid loss, it is crucial to optimize the laser such that radiation loss is minimized, while also achieving sufficiently high reflectivity and narrow bandwidth from the Bragg peak.

In addition to radiation loss, mode competition from free spectral range (FSR) reflection peaks introduces further complexity into the design of slotted lasers. A particular challenge arises from our previous optimization in which the 37th order grating period — coinciding with high reflectivity — has a relatively narrow FSR of $\sim 40\,\text{nm}$. This narrow FSR results in adjacent reflection peaks competing with the main lasing mode, particularly at elevated temperatures where the gain peak may be detuned from the designed lasing wavelength. The reflection spectrum must be engineered such that these side peaks are either suppressed or are located at an appropriate wavelength not overlapping the gain spectrum.

As discussed in chapter 3, previously multiple period gratings have been employed to overcome competition from FSR reflection peaks. However, the question remains whether this is the most effective approach. Indeed, it may be more efficient to simply reduce the period order thereby increasing the FSR spacing. This approach may, however, have negative impacts on linewidth and threshold as lower grating orders have been simulated to have lower reflectivity.

The previous grating design consist of a 24 slot grating etched to a depth of $1.35\,\mu\text{m}$. The grating has three different periods of ~ 8.48, 9.93 and 11.38 µm, each consisting of 8 slots. In the proceeding sections we will compare newly optimized lasers to this previous iteration of designs.

6.2.1 Simulated parameters

A primary difficulty in optimizing new lasers is the interdependence of the laser performance criteria. If we consider our previous design which had lower than optimal output power, one obvious approach would be to simply reduce the etch depth to reduce loss and thus increase output power. This would, however, reduce the reflectivity and thus increase the linewidth. To counteract this, the cavity length could be increased, thereby reducing the linewidth, however, this in turn would decrease the mode spacing resulting, in a reduced SMSR. Suffice it to say, the complex interdependence of the various performance criteria requires accurate simulation of all these parameters simultaneously in order to accurately asses their values for a given design. To this end, we employ some of the modelling concepts previously covered in

chapter 5. We will consider four main performance criteria: output power, SMSR, linewidth and maximum operating temperature, in order to asses designs. These criteria will be used to define a figure of merit (FOM) returned by an evaluation function $f(x)$ which we wish to minimize. Analytical approaches are used to approximate the linewidth and SMSR values as the time domain simulation is too time-consuming. In addition, the thermal dynamics are not simulated via the FEM method during the optimization, as to do so would increase the run time exorbitantly (though it will be used in the analysis of optimized designs).

Output power and linewidth

Methods to calculate laser output power and linewidth have previously been discussed in chapter 5. Some changes are required in these methods in order to reduce the run-time of the evaluation function when optimizing. In chapter 5, L-I curves were produced by simulating the laser at each injection current, which for the purposes of optimization is too time-consuming. To reduce run time, we simply simulate the output power at two currents above threshold and as the output power is approximately linear we use these two points to estimate slope efficiency and threshold. The same approach is taken for the linewidth simulation where the photon density in the gain section at two currents above threshold is linearly fitted and subsequently used in the modified Schawlow-Townes linewidth equation given by Equation 5.31 from chapter 5. This allows us to quickly calculate linewidth and output power values over a sufficient range of injection currents, with the accuracy afforded by the TD-TMM.

SMSR

Although it is possible to calculate the SMSR via the TD-TMM, this requires a long run time in order to accurately simulate the side mode power. Furthermore, the issue of cleave error makes evaluating the SMSR performance somewhat more complicated, as the SMSR of a given laser will change as a function of cleave error. Given that this cleave error is random in nature, we calculate the theoretical single mode yield of a cleaved laser, i.e. the fraction of fabricated lasers which under uniform current injection are expected to have an SMSR greater than a minimum value.

The SMSR can be approximated using the equation

$$SMSR(I) \approx 10 \log_{10} \left(\frac{\Delta\alpha_m + \Delta g}{\delta_G} + 1 \right), \tag{6.1}$$

where $\Delta\alpha_m$ is the difference between the lasing and competing modes mirror loss, Δg is the difference between the lasing and competing modes gain and δ_G can typically be taken as

$$\delta_G \sim 10^{-3} \frac{I_{th}}{I_{th} - I}, \tag{6.2}$$

where I_{th} is the threshold current and I is the injection current [25]. These parameters are illustrated in Figure 6.1. The change in SMSR with cleave error is then calculated by shifting the wavelength of the longitudinal modes over one mode spacing. The percentage of SMSR greater than a defined minimum is the single mode yield.

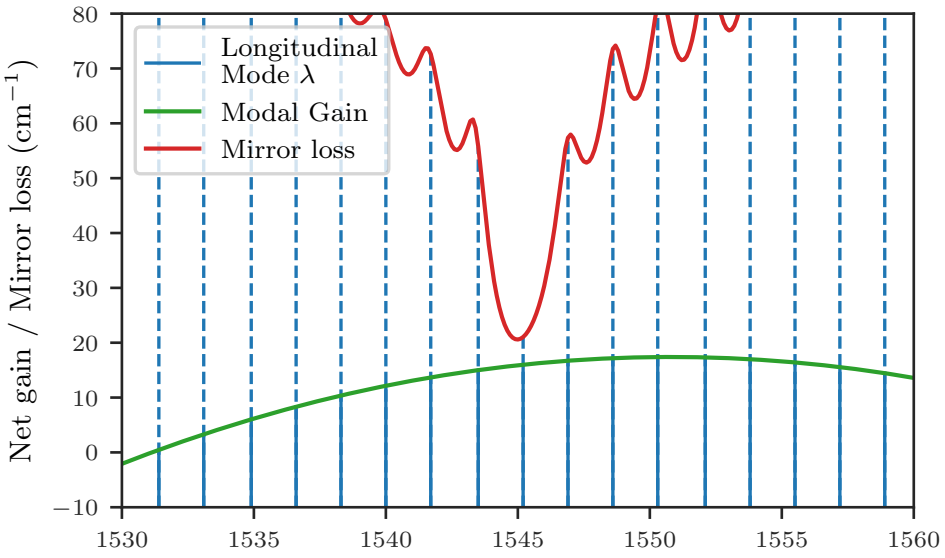

Figure 6.1: Mirror loss, net gain and longitudinal mode positions with variables relating to Equation 6.1.

Figure 6.2 shows the result of this yield calculation for a 37$^{\text{th}}$ order, 24 slot, 700 µm length laser biased at 100 mA where we have set the minimum SMSR condition at 40 dB. In this case $\sim$ 75 % of the laser diodes will have an SMSR above 40 dB. The single mode yield can be calculated for each individual injection current, the result of doing so is shown in Figure 6.3. This allows us to evaluate the SMSR performance as a function of injection current, whilst also taking into account the statistical nature of the cleaving processes. For comparison purposes, the required yield is kept on par with or better than our previous design.

Setting the required yield too high may result in SMSR being over-optimized at the expense of other parameters. From chapter 4 we have developed a method for reducing the impact of cleave error in multi-section devices which can be used to compensate in devices which have sub-optimal SMSR. However, adding two contact

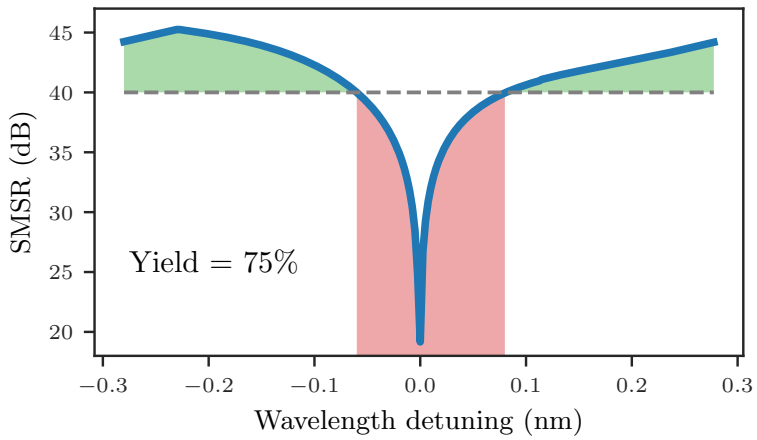

Figure 6.2: Simulated SMSR versus wavelength detuning over one mode-spacing. Red shading corresponds to SMSR below a defined minimum, and green is above.

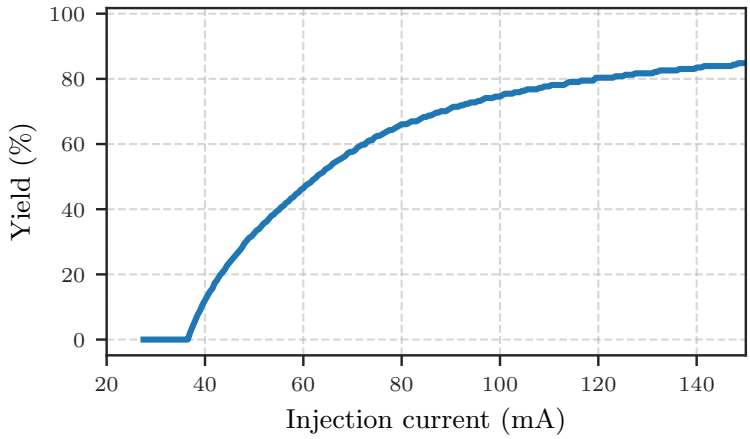

Figure 6.3: Simulated yield versus injection current for previously designed single mode 700 µm cavity length laser.

pads in the multi-section case introduces further complexities in terms of packaging the lasers; in so far as increasing the number of contact pads increases the chance of wire bonding failures. Such issues are beyond the scope of our optimization and are difficult to quantify without the availability of larger scale fabrication and packaging statistics.

Temperature tuning

In previous chapters we touched upon the concept of temperature tuning whereby laser arrays were tuned thermally in order to fully cover the C-band. In chapter 5,

Figure 5.26, it was demonstrated that changes in the laser temperature can also lead to unintended mode competition due to the red shift of the gain peak. Thus, it is necessary to include temperature tuning as a criterion in our evaluation function. Excluding this from the optimization process will result in optimized devices which may have little or no tolerance to changes in temperature. Additionally, in the case of a laser array, each laser needs to tune over a minimum temperature-tuned wavelength range in order to fully cover the C-band.

In order to asses the laser's temperature tuning, the lasing wavelength over a required temperature range can be calculated. This calculation is performed by obtaining the maximum of the round trip gain from Equation 4.5, over a range of temperatures. We define the maximum operating temperature as the highest temperature at which the maximum round trip gain coincides with the designed wavelength.

6.3 Optimization algorithms

We have defined the methods whereby various performance criteria may be evaluated and now can define a function $f(x) = FOM$, where x is a laser design and FOM is the figure of merit. The optimization process now either minimized or maximizes $f(x)$, depending on the definition of the FOM. Of critical importance is choosing an appropriate optimization method suitable to our particular problem. The evaluation function $f(x)$ can then be tailored to the chosen optimization method.

Broadly speaking, we can categorise optimization methods as either local or global. Local search methods typically are initialized with an initial guess solution and evaluate nearby solutions in the optimization space. Such optimizations can be guided by direct or gradient based methods. Direct based methods, guided only by the evaluated function and its constraints, are generally slow requiring a large number of function evaluations. Gradient based methods which use the first or second-order derivatives to guide the solution on the other hand are prone to becoming stuck in local minimum. In particular, functions with severable variables, as in the case of slotted lasers, are prone to getting stuck in such localized minimum. Figure 6.4 illustrates the potential pitfalls of such local optimization methods when applied to slotted lasers. The reflectivity and transmission of a slotted grating is simulated over a range of slot depths and period orders using the 2D-SMM. The maps show a number of local minimum and maximum with the optimized results likely being dependent on the initial guess. Given that this complex behaviour is seen for a two-dimensional problem of slot depth

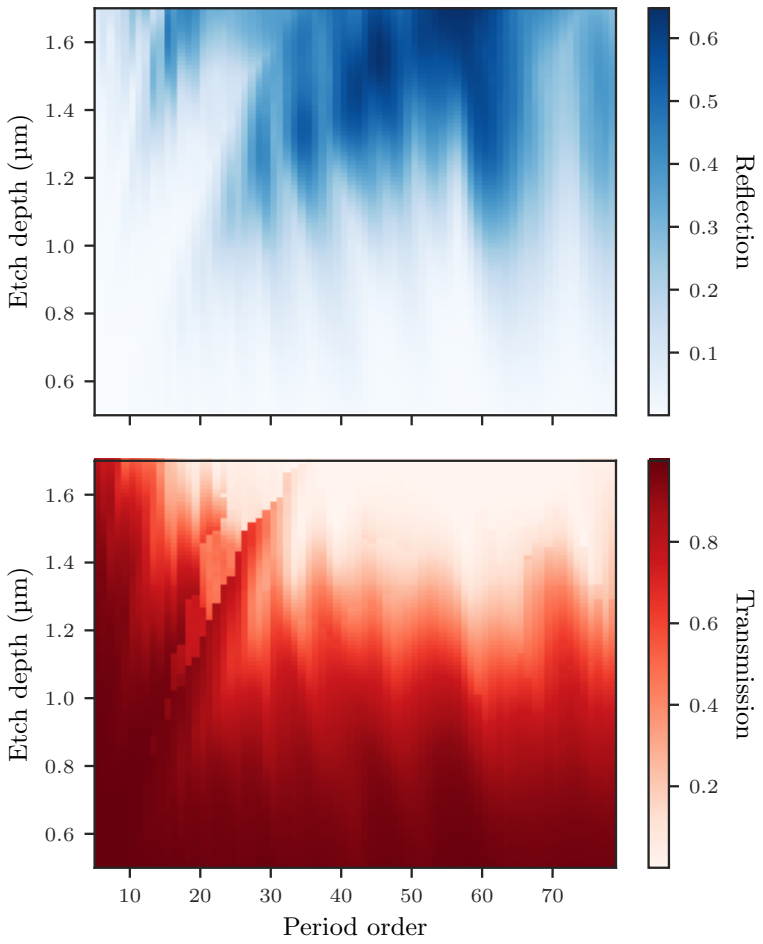

Figure 6.4: SMM simulation of grating reflection (top) and transmission (bottom). Slot width is constant at $\sim 1.1\,\mu m$ (slot order of 4.5).

and period order it can be inferred that the higher dimensional functions we wish to evaluate will be not well served by local optimization methods.

In contrast, global optimization methods are effective at finding the maximum or minimum over all input values. Such global methods include basin-hopping, brute force and particle swarm optimization. As our function evaluation times are relatively long (on the order of seconds) and a large number of evaluations are performed, we require a method which can return adequate solutions with a limited number of function evaluations. Genetic algorithms fulfil this requirement and are effective at solving high dimensional optimization problems [74]. For these reasons we choose the genetic evolution method to optimize our laser structures.

6.4 Genetic algorithm theory

Genetic algorithms are a form of evolutionary computation which can be used to maximize or minimize a particular function. This optimization method operates by replicating the process of biological evolution. As in biological evolution, genetic algorithms are rooted in random processes and operate on a population basis. The random and population based nature of genetic algorithms helps overcome a number of limitations of direct and gradient based local optimization methods [75]. We will briefly describe the implementation of the genetic algorithm and some considerations needed in tailoring our evaluation function in a manner compatible with genetic optimization.

6.4.1 Nomenclature and theory

As genetic algorithms are based on the biological principle of evolution, much of the terminology is inherited from biology. When discussing the genetic algorithm we will use the following terms and concepts.

Individual: a single laser design.

Gene: the variables associated with an individual. In our case, slot depth, slot number, period order, period number, period spacing, slot order/width and cavity length are the *genes* of an individual.

Population: a group of individuals.

Fitness function: the function $f(x)$ which returns a fitness value for each individual x. In this case we are minimizing the function.

Fitness: a measure of the quality of a given individual, as per a defined figure of merit.

Mutation: a mutation is an event in which an individual's genes are altered in some random process.

Cross over: a cross over event involves two individuals, whereby certain genes are exchanged between individuals.

Selection: selection involves choosing individuals from a population based on their fitness values.

Figure 6.5 shows the general schematic of the genetic algorithm. The algorithm starts by seeding the population with a random set of individuals. This initial population may be seeded with designs which are known to have good fitness values in order to help the optimization converge faster. Once an initial population is generated each individual is passed to the fitness function and a fitness value is returned. Once each individual within the population has a computed fitness value, a selection process removes individuals with low fitness. A new generation of individuals is now created by randomly mutating a number of surviving individuals as well as randomly crossing over genes between a number of individuals. Once this new generation has been defined, the individuals are once again evaluated for fitness and the process repeats until a satisfactory solution has been found. Care needs to be taken when defining each of the previously mentioned steps which is now discussed in detail.

Fitness / Figure of merit

We have described the various performance criteria that we will calculate for each individual in the optimization. It is now necessary to formulate these criteria into an appropriate FOM with which the genetic algorithm can evaluate an individual's overall fitness, and over the course of the optimization minimize. The output power, yield and linewidth have all intentionally been formulated as functions of injection current which allows us to use the concept of an operating current, I_{op}. This operating current is defined as the minimum current for which all the specified performance targets are met. This definition avoids the over optimization of certain performance criteria at the expense of others. The concept is illustrated in Figure 6.6 for a hypothetical optimization problem in which we wish to optimize a laser with linewidth $\leq 2\,\mathrm{MHz}$, output power $\geq 7\,\mathrm{mW}$ and SMSR $\geq 40\,\mathrm{Bm}$. A laser with the performance shown in Figure 6.6a, although capable of meeting the SMSR and linewidth requirements below 60 mA, must nonetheless be biased at 100 mA in order to achieve the desired output power. As such, the operating current is 100 mA and the laser is not particularly well optimized — that is to say, the various performance criteria are not suitable balanced with one another in order to minimize the operating current. A better optimized laser is shown in Figure 6.6b, whereby SMSR and linewidth performance have been sacrificed (as would be the case when reducing mirror reflectivity) in order to increase the slope efficiency. As a result, all performance criteria are now met simultaneously at a lower injection current of 70 mA, thus reducing the operating current of the device. By basing the FOM which we are minimizing on the operating current, our

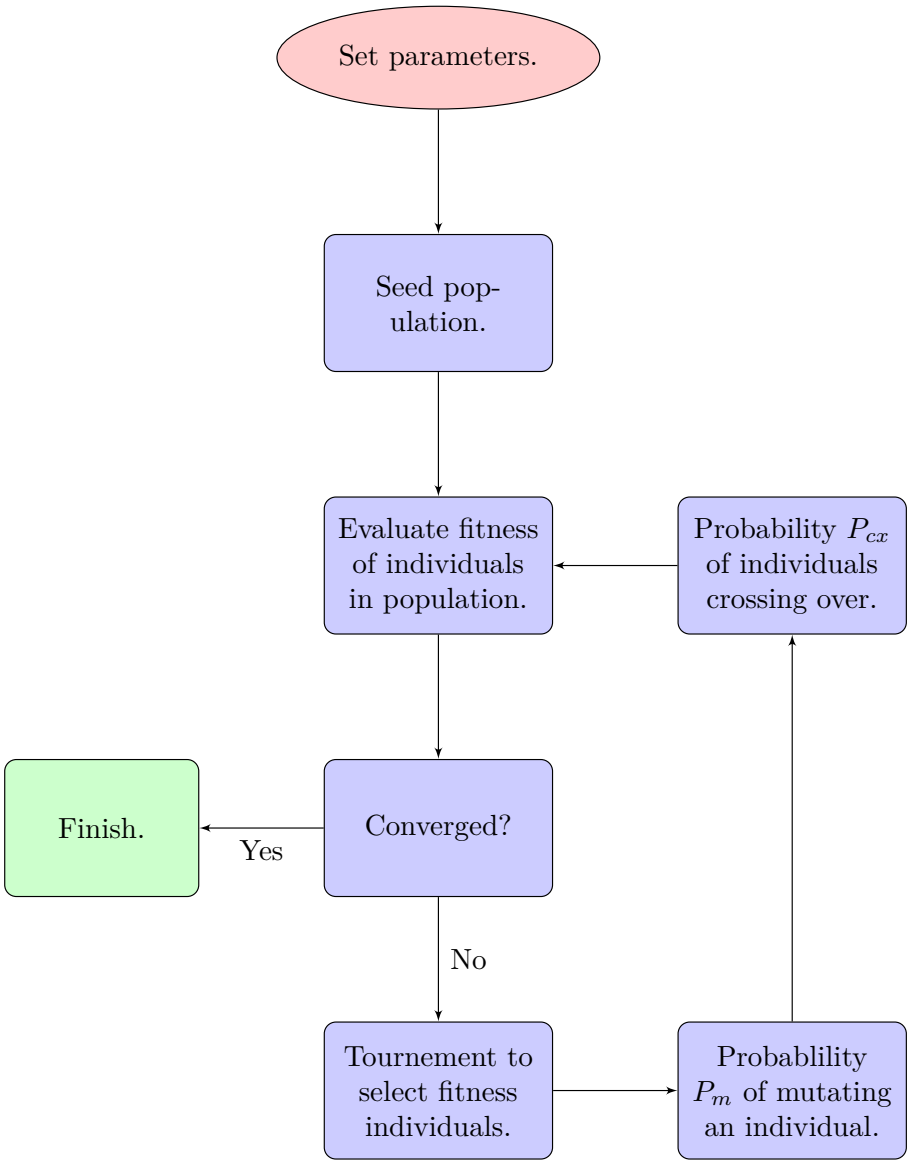

Figure 6.5: Flowchart illustrating the genetic algorithm.

optimization will naturally balance the performance targets against one another as shown in Figure 6.6.

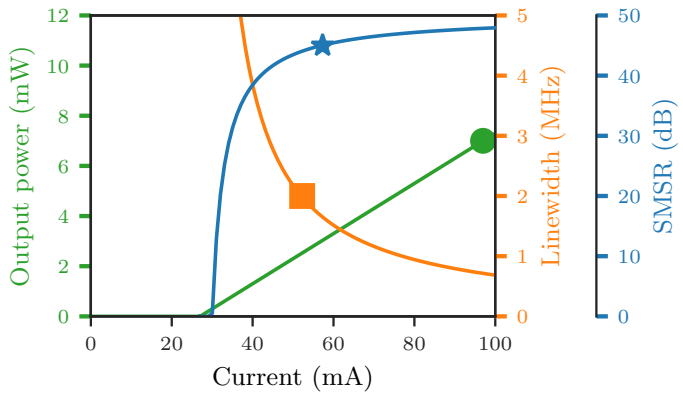

(a)

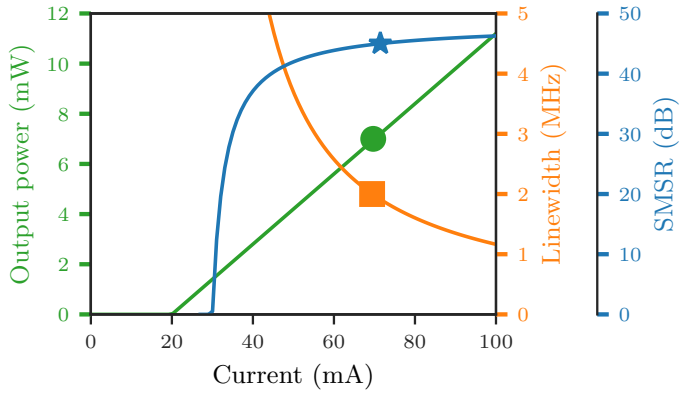

(b)

Figure 6.6: Illustration of optimization process. Markers on each line represent specific performance requirements. Figure (a) represents an unoptimized case and figure (b) represents the optimized case where the various requirements have been balanced against one another.

The temperature performance also needs to accounted for in the FOM. The simplest approach is to evaluate the lasing wavelength over the required temperature range and if the calculated lasing wavelength deviates from the designed wavelength at any temperature; set the FOM equal to a large value to reduce the fitness of the individual. However, such discontinuous approaches can be deleterious to the convergence of the optimization. Alternatively we can describe the temperature performance in a manner such that individuals are punished proportional to the fraction of the temperature range they fail to cover. This is achieved by setting the figure of

merit as

$$FOM = I_{op} + I_{op}(1 - \eta_T) \cdot w, \tag{6.3}$$

where I_{op} is the operating current as previously defined and η_T is the fraction of the temperature range over which the correct lasing wavelength is maintained and w is a weighting parameter with which we can set the priority of covering the temperature range. The FOM which is being minimized, is now continuous and temperature stability is taken into account proportionally.

Mutation

Each individual in the population has a probability P_m to undergo a mutation event. When such a mutation event occurs, each of the genes that are free to vary have an individual probability p_m of having their values altered. This change is implemented by adding a random value, determined by a Gaussian with mean of $\mu = 0$ and a standard deviation σ defined for each parameter. This ensures variability within the population, enabling the optimization to find new solutions and escape local minimums.

Cross over

After a mutation event, each individual has probability P_{cx} to undergo a cross over event with another individual in the population. In this case we implement a simple uniform cross over function. This takes two individuals of the population with each of the genes which are free to vary having a probability p_{cx} to be switched with that of the other individual. This results in advantageous traits being shared throughout the population improving the rate of convergence.

Selection

Finally, a method whereby selective pressure is applied to the population is required. We implement a simple *tournament selection* function to apply this selective pressure. The function takes a population and runs N tournaments with P participants. Each tournament selects the fittest individual from the participants and replaces the less fit individuals with the fittest individual. Increasing the number of participants increases the selective pressure, however if this is set too high the optimization runs the risk of converging prematurely. In general the participant number is kept < 5 to avoid this.

The values typically used for the genetic algorithm parameters are shown in Table 6.1. The values were chosen through trial and error to provide a good rate of convergence and solutions.

Table 6.1: Genetic algorithm parameters. N_g is the number of free varying genes.

Parameter	Value
Population size	$20 \times N_g$
Mutation event probability P_m	0.2
Gene mutation probability p_m	~ 0.15
Cross over probability C_{cx}	0.15
Gene cross over probability c_{cx}	0.1
Tournament size	3

Grating definition

In order to limit the convergence time, measures are taken to limit the number of possible designs. In particular, the inclusion of multiple period gratings results in a very large number of possible grating structures. The number of possible gratings is limited by defining the grating in terms of *period number* and *period spacing*. The period number defines the number of different periods within a grating while the period spacing defines the difference in period between each of these. This definition results in an equal number of slots for each individual period within the grating. For example, a multiple period grating G_T with period = 30, period number = 3, period spacing = 5 and slot number = 30 would be composed of the sub-gratings shown in table Table 6.2. For convenience the gratings subsequently presented will be expressed in terms of period number and spacing, and will not be expanded into constituent gratings as in Table 6.2. The gratings can be expanded via

$$G_T = \sum_{i=0}^{n} \left((m_0 + i\Delta m) \frac{N}{n} \right), \tag{6.4}$$

where m_0 is the period order, Δm is the period order spacing, n is the period number, and N is the total slot number.

Table 6.2: Example of a multiple period grating composition.

	G_1	G_2	G_2
Period order	30	35	40
Slot number	10	10	10

6.5 Optimization results

6.5.1 Single mode lasers at 1550 nm

A single laser tuned to a single wavelength approximately centred on the gain spectrum at 1550 nm is optimized first. Several of the design parameters are allowed to vary freely, namely etch depth, period order, slot order, slot number, period number, period spacing and cavity length. The initial population is randomly seeded by assigning uniformly distributed random values to each individual's genes. Bounds are placed on the initial seeding process as shown in Table 6.3. Subsequent mutations are unbounded except for the slot width which is required to be greater than 1 µm in order to facilitate lower resolution fabrication processes such as photo-lithography.

Table 6.3: Initial population specifications.

Parameter	Seeding bounds
Etch depth µm	0.7 to 1.6
Slot number	10 to 90
Period order	15 to 70
Period number	1 to 7
Period spacing	0 to 7
Slot order	4 to 7
Cavity length µm	300 to 1200

The population size is set to $\sim \times 20$ the number of free variables in order to ensure a sufficiently even distribution over the optimization space. Table 6.4 shows the parameters of the resulting best laser design from the optimization process. The etch depth is shallower than the previous optimization with a larger number of slots at a shorter period. The 2D-SMM simulated reflection and transmission spectra are shown in Figure 6.7a with a peak reflectivity and transmission of ~ 0.3 and 0.7, respectively. Figure 6.7b shows the resulting lasing spectrum at the operating current, simulated via the TD-TMM.

Relative to the previous optimization process the genetic algorithm tends to be more opaque, in so far as it is not immediately clear how the solution was reached and whether the optimization space has been covered efficaciously. It is instructive to examine the convergence process to gain an understanding of the laser optimization. Figure 6.8 shows the convergence process in terms of FOM versus generation number. Importantly, the genetic algorithm is capable of returning suitable designs in a relatively short number of generations, with most of the performance to be gained being achieved by the 10^{th} generation.

Table 6.4: Optimization result for a single laser at 1550 nm.

Minimum linewidth Minimum power	$\Delta\nu_{min} = 2.0\,\text{MHz}$, $P_{min} = 20\,\text{mW}$
Lasing Wavelength nm	1550
Etch depth µm	1.05
Slot number	49
Period order	29
Period number	1
Period spacing	-
Slot order	4.5
Cavity length µm	619.9
Slope efficiency W/ A	0.146
Threshold mA	22.19
Operating current mA	125

Figure 6.9 provides a visual insight into the optimization in the form of 2D-histograms for each of the free laser design variables, as well as the figure of merit. All the laser design variables are seen to have a uniform distribution early on in the optimization process and as the optimization progresses each variable starts to converge. We can make certain inferences from the convergence of each parameter. For instance, in the case of period order, the individuals with order greater than ~ 35 are relatively quickly eliminated from the population. This is as a result of higher order gratings having closer spaced FSR peaks, which detrimentally affects the temperature tuning range of the lasers. We can also see that the grating configuration quickly tends towards a high number of slots with a shallower etch depth relative to previous designs. In other words, the grating is optimized to be longer than previous designs with a smaller reflectivity per unit distance. Deeper etched gratings up to 1.4 µm are seen to propagate initially within the population, however past the 10^{th} generation these are seen to decline in number.

Varying performance requirements

We are also interested in seeing how the optimal design varies with defined performance requirements. Table 6.5 shows various optimized lasers for different required linewidth performance. In keeping with the Schawlow-Townes equation, the optimized designs are seen to increase the cavity length with decreasing required linewidth. In general, we observe that the slot depth is consistently close to $\sim 1\,\mu\text{m}$. Table 6.6 shows various optimized lasers for different required output power. Similar designs

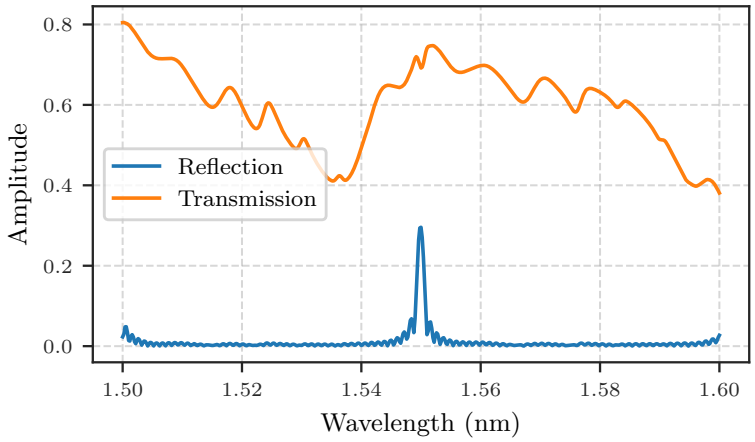

(a) Grating reflection and transmission spectra of an optimaized laser

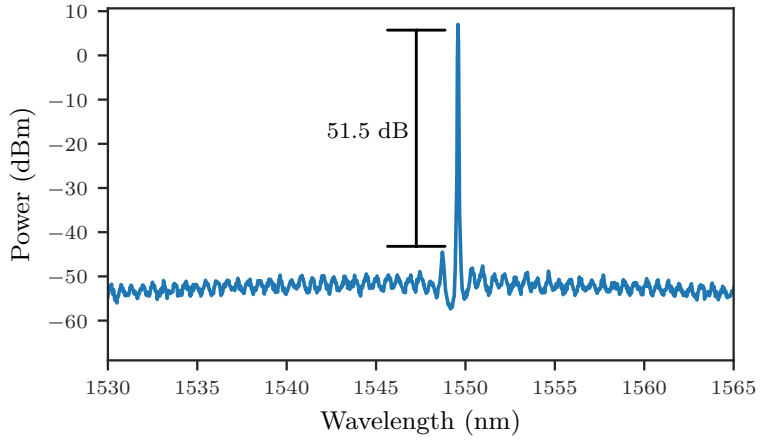

(b) Lasing spectrum.

Figure 6.7: Simulated laser properties optimized by the genetic algorithm.

are again observed with etch depth $\sim 1\,\mu m$. We can see that as the required output power increases, the algorithm sacrifices threshold performance for slope efficiency in order to achieve the required power. The operating current is also seen to increase, a natural consequence of requiring more output power.

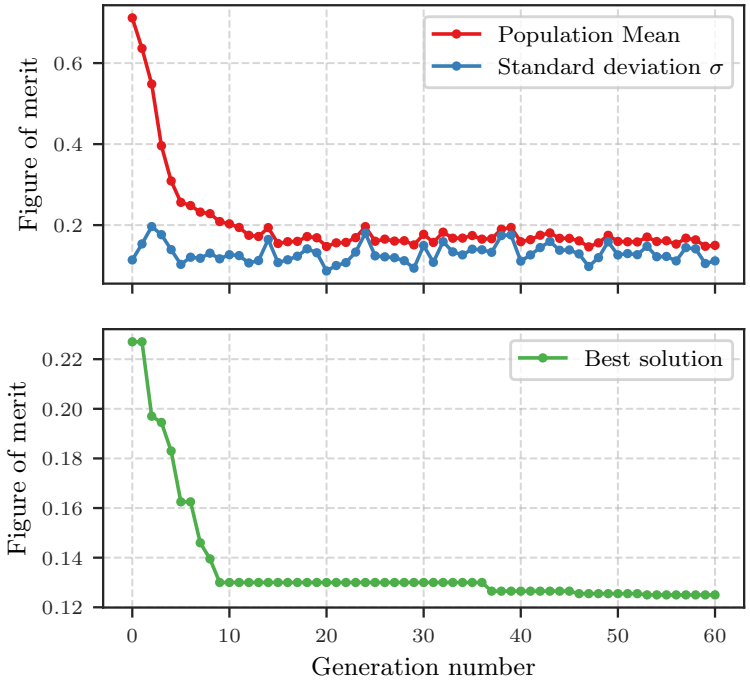

Figure 6.8: Convergence of population FOM (top) and the best solution within the population (bottom).

Table 6.5: Optimization results for varying linewidth requirements.

Minimum linewidth	0.5 MHz	1 MHz	2 MHz	4 MHz
Minimum power		12.5 mW		
Etch depth (µm)	0.9702	0.928	0.972	0.88
Period order	26	25	31	30
Slot order	4.5	4.5	4.5	6.5
Slot number	66	56	37	54
Period number	2	7	1	2
Period spacing	1	1	–	1
Cavity length (µm)	1000	855	627	668
Slope efficiency (W/ A)	0.112	0.154	0.180	0.180
Threshold (mA)	36.4	39.7	44	41.7
Operating current (mA)	164	136	117	113

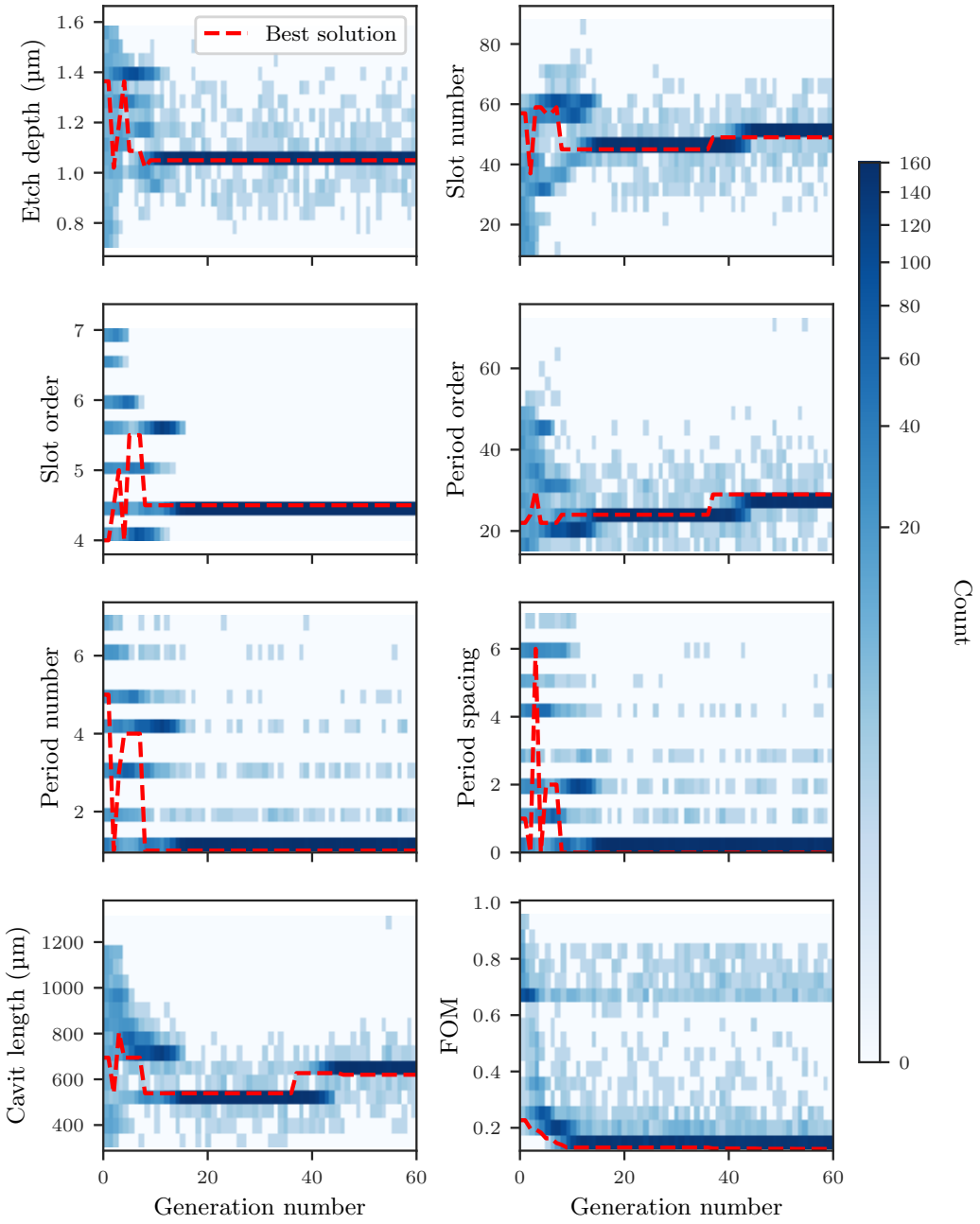

Figure 6.9: Convergence of parameters represented by 2D histograms. The population at generation 0 has a uniform distribution for each of the parameters — as the population evolves each parameter converges around a favourable value.

Table 6.6: Optimization results for varying output power requirements.

Minimum linewidth	1 MHz			
Minimum power	5 mW	7.5 mW	12.5 mW	17.5 mW
Etch depth (µm)	1.042	1.118	0.976	0.981
Period order	25	24	23	23
Slot order	4.5	5	4.5	4.5
Slot number	78	72	56	44
Period number	5	2	7	4
Period spacing	1	1	2	3
Cavity length (µm)	918	767	705	590
Slope efficiency (W/ A)	0.106	0.131	0.157	0.171
Threshold (mA)	36.7	41.6	43.2	46.1
Operating current (mA)	84	99	125	146

6.5.2 Optimizing Laser Arrays

In chapter 2 the concept of tunable laser arrays was touched upon. Previously, such lasers arrays have been designed with the goal of full C-band coverage from 1530 nm to 1565 nm. Subsequent fabrication of these designs yielded arrays with full C-band coverage, low linewidth and good SMSR. However, a number of outstanding issues remain with these designs. Primarily the laser arrays had lower output power than desirable. In addition, the longer cavity lasers of length 700 µm and 1000 µm used to reach lower linewidth, had sub-optimal performance at elevated temperatures due to competition from the higher wavelength FSR reflection peak. With this in mind we wish to use the genetic optimization process to overcome these issues.

6.5.3 700 µm / 1 MHz array

In order to asses the effectiveness of the genetic algorithm it is instructive to directly compare a newly optimized array with previous arrays. One factor which makes this difficult is that many of the performance criteria in the previous optimization, such as slope efficiency and yield were not explicitly defined to the same degree as in the genetic optimization. However, one specific goal for the 700 µm laser array was to achieve $\leq$ 1 MHz linewidth which can be use as a performance criteria to compare with. Thus, the operating current of the previous design is defined as the current at which 1 MHz linewidth is reached. The yield and output power at this operating current are then calculated for the array, and the average of these values is used as performance requirements for the genetic algorithm. The maximum designed operating temperature is taken as 40 °C which is the theoretical maximum operating temperature of the 1530 nm channel laser. In this way, the previously designed lasers are re-optimized with similar performance goals, allowing for a valid comparison. The cavity length is also set constant at 700 µm. This optimization, undertaken using the aforementioned conditions, will be referred to as *optimization 1* henceforth.

The performance parameters for optimization 1 may not be ideal for operation at 1 MHz, and as such these are primarily used as a method to compare with the previous design. A newly optimized design from scratch would naturally adjust the parameters in order to enforce higher performance of the resulting laser. With this in mind the desired maximum operating temperature is increased to 70 °C, minimum output power to 12.5 mW and the minimum yield to 75 %. This optimization run will be referred to as *optimization 2*.

Finally, *optimization 3* is defined as identical to *optimization 2*, but with a reduced yield requirement equal to 25 %. The reasoning behind this being that for multi-section section lasers we have the ability to correct for cleave error via current tuning, reducing the requirement for high single mode yield.

Each array of lasers consists of 12 individual lasers each designed to operate at linearly spaced wavelengths from 1530 to 1565 nm in order to cover the C-band. Optimizing for a range of wavelength lasers on a single chip imposes certain restrictions on our optimization parameters. As etching a different depth for each laser is not practical in terms of fabrication, it is necessary to first determine an ideal etch depth for the array. Additionally, as the chip has a set length, all lasers in the array must have the same length. In order to determine a set etch depth and cavity length for the entire array, the 1530 nm laser is first optimized, with the reasoning that this laser has in the past proved to have lower performance and was most susceptible to competition from FSR peaks at high temperatures [20]. Once an optimal etch depth and cavity length has been determined for the 1530 nm laser, these values are set as constant for all subsequent lasers in the array. The resulting etch depth and cavity length may not be optimal for the entire array; however, ensuring good performance for the 1530 nm channel laser is a priority — the laser array is only as good as its weakest performing laser. In order to shorten the convergence time for subsequent lasers in the array, each optimization is started by seeding the population with a small portion of individuals from the previous optimized laser in the array. As the wavelength channels are closely spaced, these seed individuals should in general be close to the optimal design for the laser being optimized.

The final designs and performance for these optimization runs is included in Table C.1, Table C.2 and Table C.3; Appendix C.

Simulated performance

The performance of the re-optimized laser designs can be seen in Figure 6.10. Optimization 1, which has the same theoretical performance requirements as the previous design, shows improvement in performance with an average increase of 45 % for the slope efficiency, 62 % for the output power at operating current, while the average operating current increases marginally by less than 1 %. In both cases the lasers have ≤ 1 MHz linewidth at their respective operating currents.

Optimization 2, which has higher performance requirements is seen to have a significantly increased slope efficiency. As a higher output power requirement was defined, the operating current is also naturally higher, although the average increase

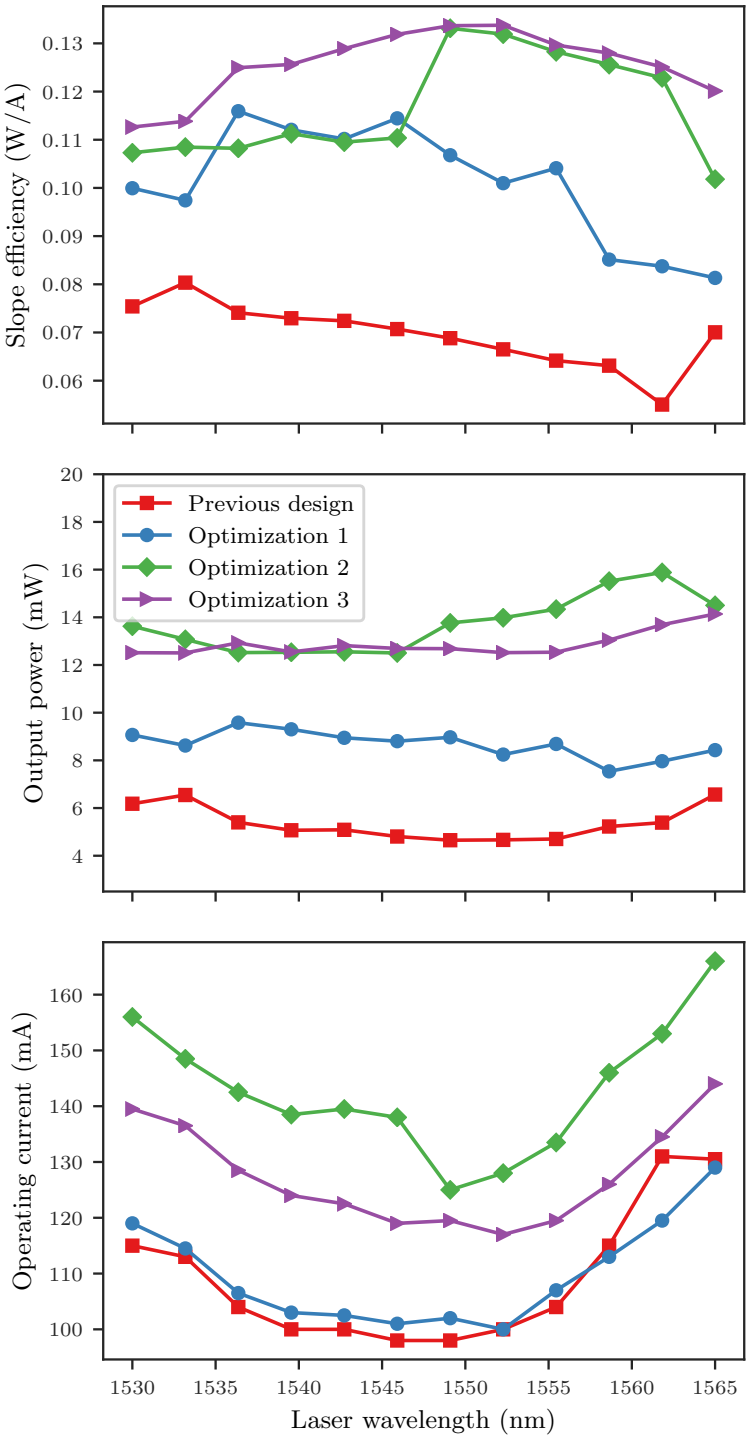

Figure 6.10: Simulated performance of the optimized and previous laser arrays: slope efficiency (top), output power at respective operating current (middle), operating current (bottom).

in operating current of $\sim 35\,\%$ yields an average increase in output power of $\sim 200\,\%$. The effect of reducing the yield requirement is seen from Optimization 3, where the operating current is notably reduced and the slope efficiency is generally higher across the array.

In order to accurately asses the benefits of the genetic algorithm, it is also instructive to optimize the previous design for higher output power and compare this to the genetic algorithm's result. Taking the previous 700 µm cavity length design, its operating current can be defined for similar conditions as Optimization 2, namely at linewidth and output power equal 1 MHz and 12.5 mW respectively. The cavity length is then reduced until the minimum operating current is found, at which point the linewidth and output power have been balanced, similar to the balancing of design parameters achieved by the genetic algorithm. Figure 6.11 shows the result of this with the minimum operating current being reached at 172 mA compared with the genetic algorithm solution of 124 mA an improvement of 30 % over previous designs. The improvement in performance can be attributed to the altered grating design which is more suitable for higher output power.

The genetic algorithm optimization also results in improved SMSR/single mode yield and temperature performance. Figure 6.12 compares the previous design yield and maximum operating temperature. The newly designed lasers have a consistent yield $\geq 70\,\%$ at 150 mA. The effect of explicitly defining a minimum temperature tuning range can also be seen. Optimization 1 and the previous design are seen to have a maximum operating temperature of $\sim 40\,^{\circ}\mathrm{C}$ for the 1530 nm laser while Optimization 2 has a theoretical maximum temperature of $\geq 70\,^{\circ}\mathrm{C}$.

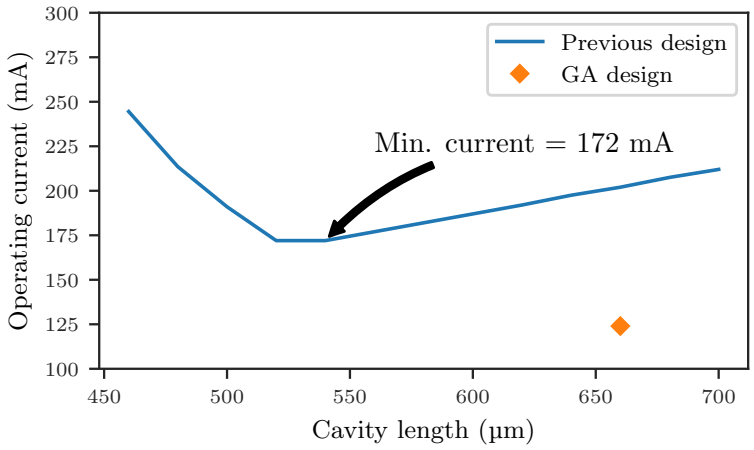

Figure 6.11: Operating current as a function of cavity length.

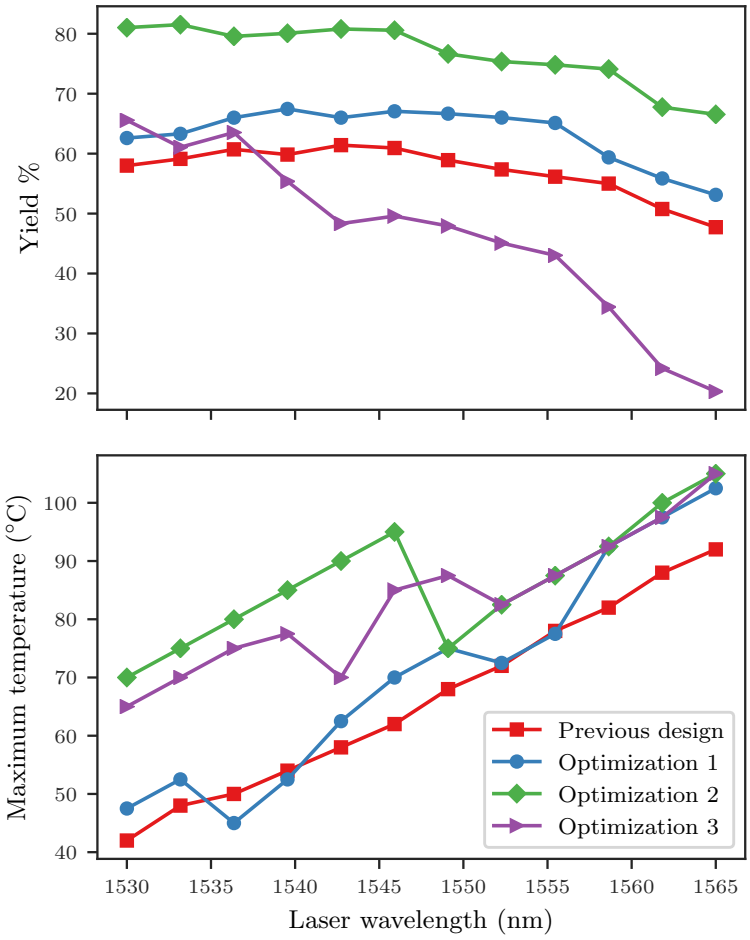

Figure 6.12: Simulated performance of the previous 700 µm cavity length array design and the optimized design: single mode yield (top) and maximum operating temperature (bottom).

It is also instructive to examine the lasing performance using the thermo-optic model developed in chapter 5 to evaluate the spectral properties of the optimized design compared with previous designs. The top plot in Figure 6.13 shows the experimental spectrum of a 700 µm cavity laser with a designed wavelength of $\sim$ 1536 nm at 50 °C. The laser operates at the designed lasing wavelength, however, between 1570 nm to 1580 nm mode competition from the FSR peak is seen. Although experimental data for a 1530 nm laser of this kind is not available, the bottom plot in Figure 6.13 shows the simulated lasing performance for a 1530 nm laser of the previous grating design. The simulated spectrum suggests that at a heatsink temperature of 50 °C the previous laser design will operate at the incorrect wavelength.

The performance of our optimized laser is contrasted in Figure 6.14. The top plot shows the simulated spectrum of the optimization 1 at 50 °C and 65 °C for the

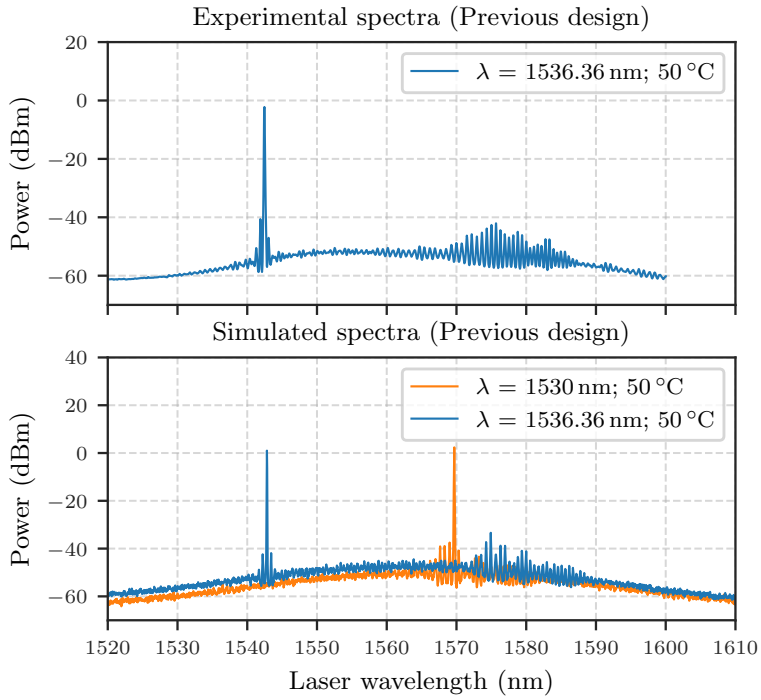

Figure 6.13: Experimental measurement of a 700 µm length laser designed for room temperature operation at 1536.36 nm (top), simulated spectra of a 700 µm length laser designed for room temperature operation at 1530 nm and 1536.36 nm (bottom).

blue-most laser at 1530 nm. This simulation suggests an improved performance, with the 1530 nm laser being capable of maintaining the correct wavelength at elevated temperatures. However, as a high temperature tolerance was not explicitly required for optimization 1, at 65 °C the lasing wavelength is located at the FSR reflection peak. In contrast, optimization 2 in which we explicitly set our required temperature tolerance to be $\geq$ 75 °C shows markedly improved spectral properties at a heatsink temperature of 65 °C, maintaining the designed wavelength channel.

Etch tolerance

Thus far, the performance improvements of explicitly defined parameters have been examined: output power, linewidth, yield and maximum temperature. Another aspect of design is fabrication tolerance. Simulations suggest that the etch depth in particular affects the performance of the laser. Figure 6.15 shows the fractional increase in operating current over a range of etch errors. Negative etch errors correspond to the slot being etched too shallow, while positive etch error corresponds to etching the slot deeper than intended. The simulation suggests that etching the slot too shallow has a

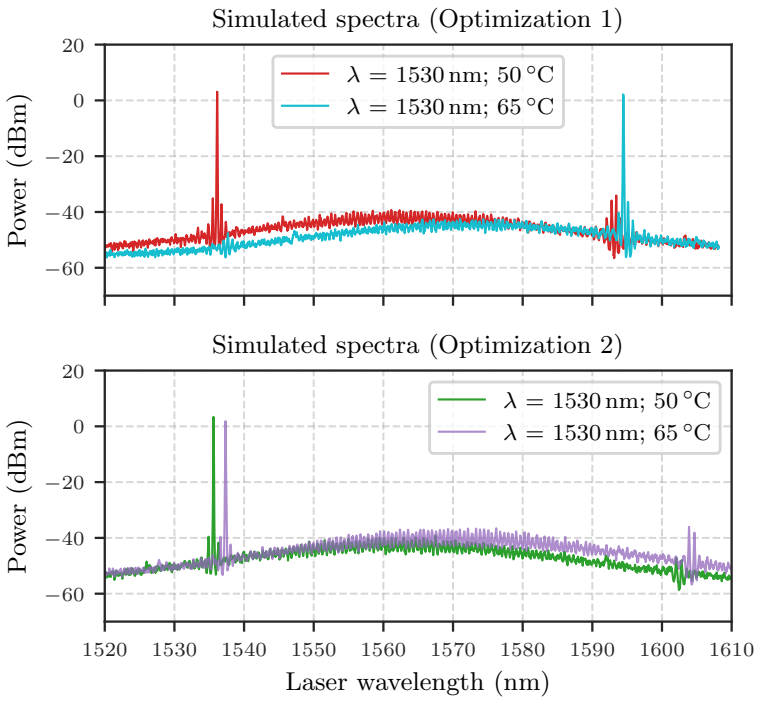

Figure 6.14: Simulated lasing spectra of the optimized lasers.

relatively small effect on the operating current in all cases with optimization 2 being most sensitive to under etching of the slot. In the case of an under etched slot the operating current is seen to increase due to reduced linewidth performance. For the original design, over-etching the slot is simulated to have a severe detrimental effect on the laser performance. A relatively small error of 100 nm in etch depth results in factor of 1.5 increase in operating current, and by 200 nm etch depth this factor increases to 3. In contrast, newly optimized designs are simulated to have a much greater tolerance to over etching of the slot depth.

Whether this improvement in fabrication tolerance is a result of the genetic algorithm is somewhat unclear. The nature of the genetic algorithm may indeed tend towards more tolerant designs for a number of possible reasons. As the entirety of the optimization space in not covered, sharp peaks in fitness in the optimization space which correspond to error sensitive designs may simply not be found by the genetic algorithm. The genetic algorithm may account for fabrication tolerance to some degree, as individuals within a population which are highly sensitive to changes in parameters such as etch depth, are more likely to lose fitness upon a mutation or cross over event. It may be the case that a primary downside of the genetic algorithm approach, namely that the very best design in the optimization space is not necessarily found, may in

this case be beneficial.

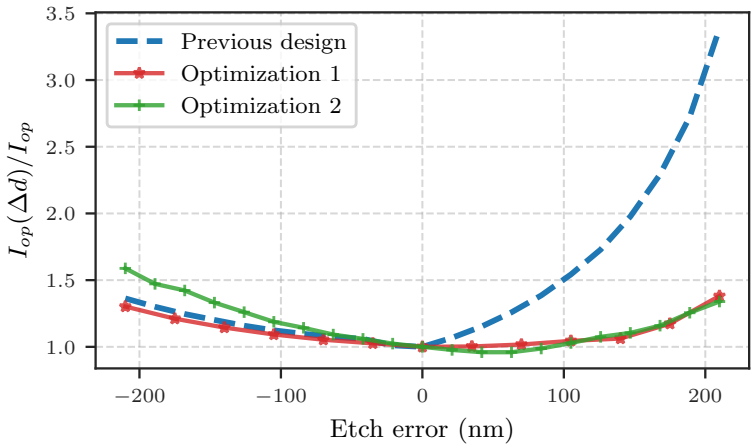

Figure 6.15: Fractional increase in operating current versus etch depth error.

6.5.4 1000 µm / 0.5 MHz array

The genetic algorithm has been demonstrated as being capable of improving both overall performance and temperature tuning ranges. This improved temperature performance is of particular relevance to 1000 µm length lasers which are more difficult to design successfully at the blue end of the C-band. This difficulty arises for two reasons which can be understood from Equation 4.5. Considering the round trip gain, $g_{round}(\lambda) \propto e^{g_{net}(\lambda)L}$ where L is the cavity length and $g_{net}(\lambda)$ is the net gain. From this one can deduce that as the cavity increases in length, the shape of the gain curve plays a greater role in determining the lasing wavelength and the suppression of the FSR peaks becomes less effective. An additional problem is the blue shifting of the gain peak with carrier density. As the cavity length is increased, Equation 4.5 shows that the laser will reach threshold at a lower gain $g(\lambda)$, and thus the carrier density will clamp at a lower value. This lower carrier density results in less blue shifting of the gain peak, and as a result, the red FSR reflection peaks receive more gain than they would for shorter cavities.

As a result of the aforementioned factors, certain previously fabricated 1000 µm lasers have suffered from poor SMSR and thermal tuning ranges. Figure 6.16 shows an experimental spectrum of a 1000 µm cavity length laser at a heatsink temperature of 25 °C. One can see that in this case the laser fails to operate at the designed wavelength due to the reflection peak occurring at one FSR longer wavelength. In order to address

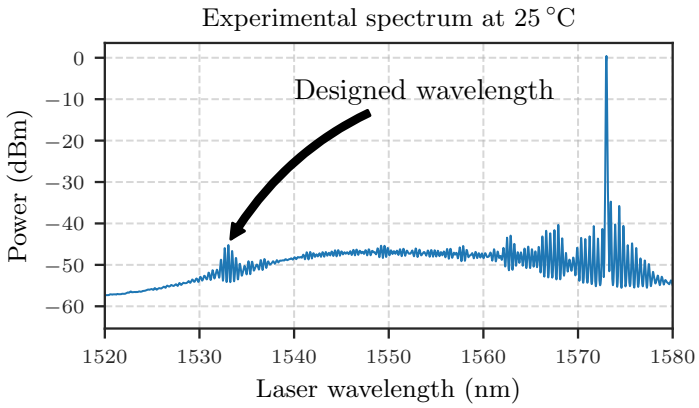

Figure 6.16: Experimental measurement of a 1000 µm cavity length laser designed for ∼ 1533 nm lasing wavelength. The laser is biased at 100 mA with a heatsink temperature of 25 °C.

this issue, a similar approach as discussed for the 700 µm laser is again used, whereby the appropriate performance criteria as defined in our genetic algorithm are first reverse engineered for comparisons purpose. In this case, the required linewidth is defined as 0.5 MHz. The optimization algorithm was run, optimizing each of the individual lasers in the array. The etch depth has been set constant at 1.1 µm, the depth which was optimized for the previous 1 MHz laser arrays. This was done in order to facilitate fabrication of the various optimized arrays during one fabrication run, as the inclusion of multiple etch depths adds to the complexity of the fabrication. The required maximum temperature has been increased to 60 °C in order to rectify the poor performance on the blue end of the C-band (as observed in Figure 6.16), and the required output power has been increased to 10 mW. The final designs and performance for this optimization run is included in Table C.4; Appendix C.

Simulated performance

The optimized performance is illustrated in Figure 6.17. The 1530 nm and the 1533.2 nm laser have notably higher operating currents which can be attributed to the fact that they are being designed in order to maintain correct output wavelength at higher temperature. In these cases the genetic algorithm has effectively sacrificed some performance efficiency in order to enable stable operation, and as such, a higher current is needed to reach ≤ 0.5 MHz and ≥ 10 mW. The average increase in the operating current of the array is 14 % which yields an average increase in slope efficiency of 90 % achieving our stated goal of increasing laser power output.

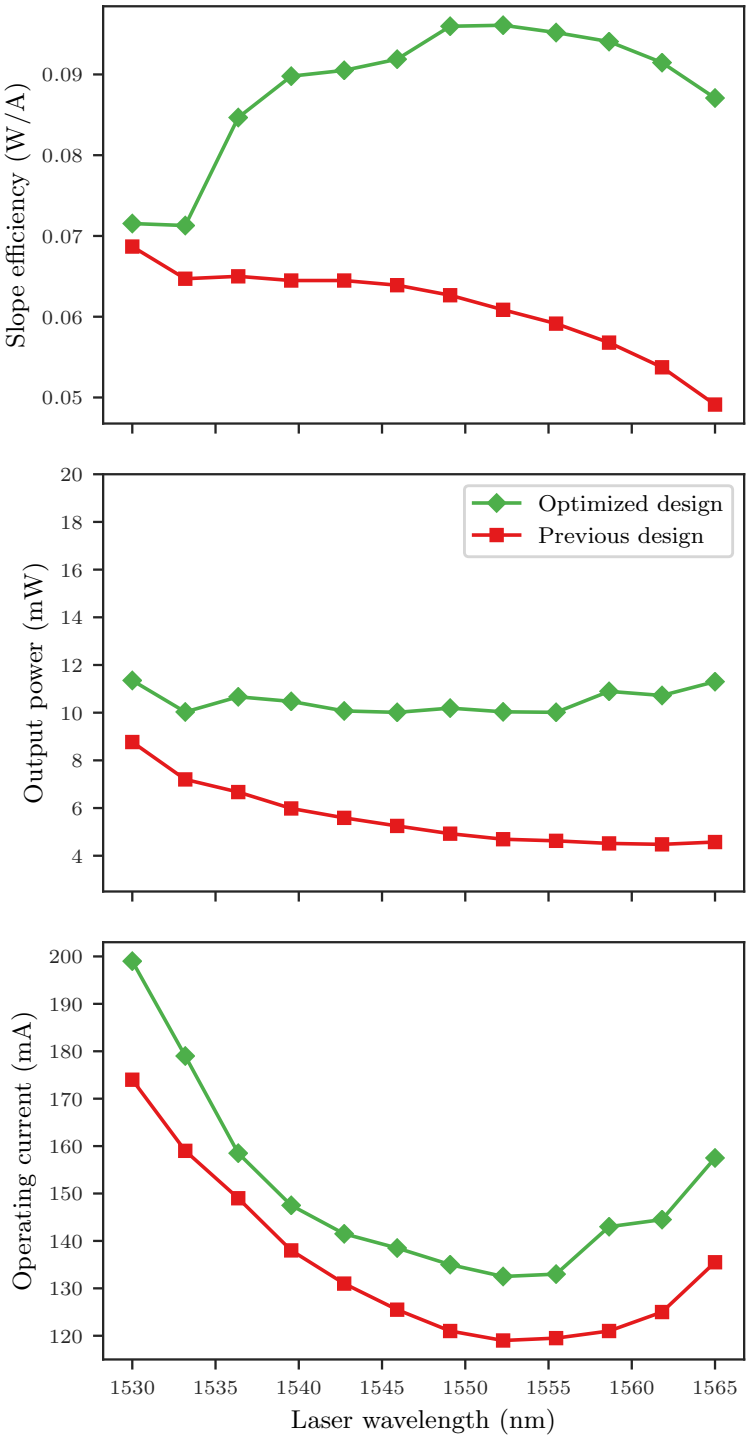

Figure 6.17: Simulated performance of the previous 1000 µm cavity length array design and the optimized design: slope efficiency (top), output power at respective operating current (middle), operating current (bottom).

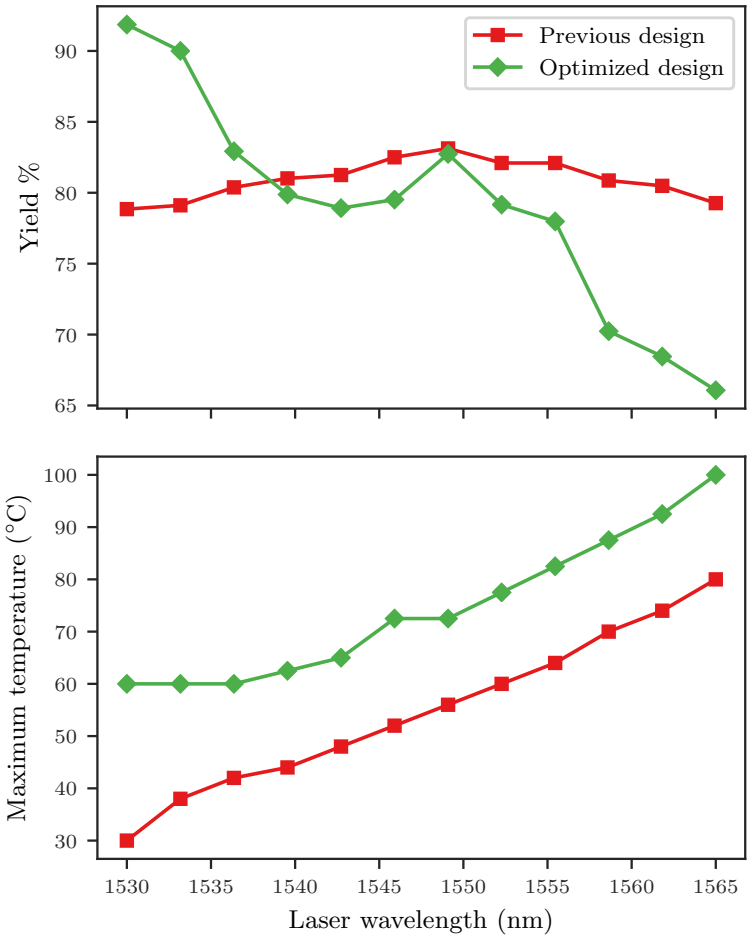

Figure 6.18: Simulated performance of the previous 1000 µm cavity length array design and the optimized design: single mode yield (top) and maximum operating temperature (bottom).

The most notable improvements come in terms of temperature stability. Figure 6.18 shows the maximum operating temperature of the laser as calculated via the maximum of the round trip gain. The optimized design is seen to have the same trend as the previous design above 1539.5 nm, below which the optimized design is altered in order to maintain the maximum operating temperature above 60 °C. This can be seen in Figure 6.19 where the thermo-optic model from chapter 5 has been used to simulate the laser spectrum at different heatsink temperatures. The previous design (top) is seen to operate at the incorrect wavelength, and in contrast, the optimized design is seen to maintain the correct wavelength at a heatsink temperature of 25 °C. Additionally, the optimized laser is seen to maintain the correct lasing wavelength at a significantly elevated heatsink temperature of 55 °C, albeit with a reduced SMSR of 31.5 dB. The single mode yield of both designs is shown in Figure 6.18 at 170 mA for

a minimum SMSR of 30 dB.

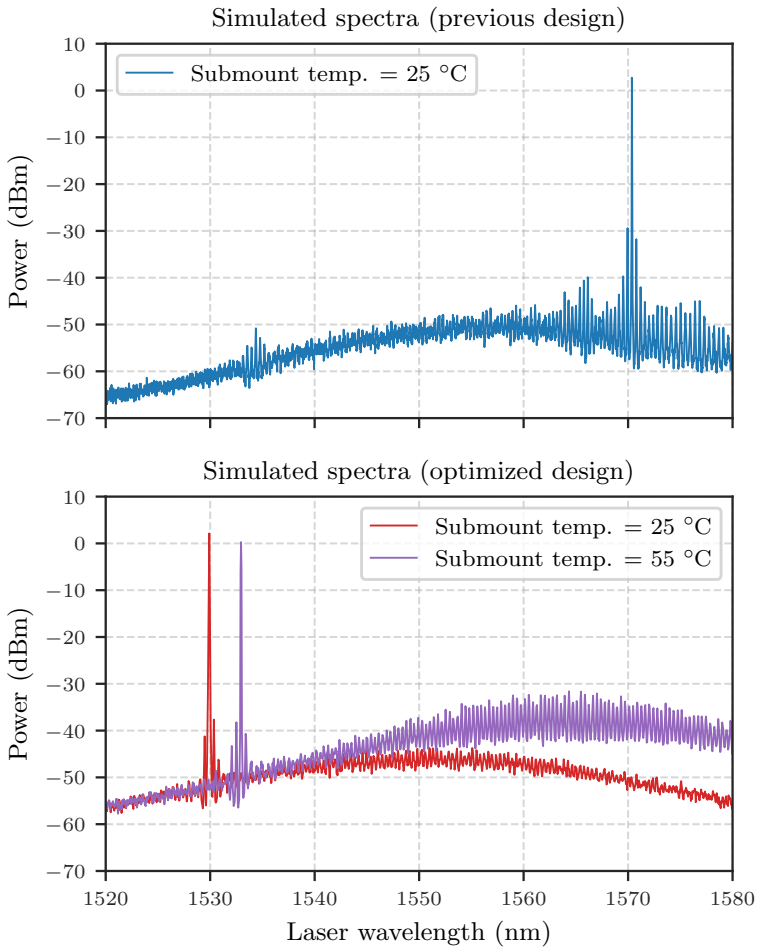

Figure 6.19: Simulated lasing spectra: previous 1000 µm cavity length design (top), optimized laser design (bottom).

The simulated reflection and transmission spectra of the 1530 nm channel laser, for both previous and optimized designs, can be seen in Figure 6.20. Although the previous design can be seen to have suppressed reflection peaks, this suppression is not sufficient particularly for the 1000 µm laser. The genetic algorithm solves this by reducing the grating period order to 24, resulting in an increased FSR of 65 nm. Interestingly, the genetic algorithm has also found a solution with a suppressed FSR peak without using multiple periods in the grating. The increased FSR combined with a suppressed FSR reflection peak yields a solution which can maintain the correct lasing wavelength at elevated temperatures.

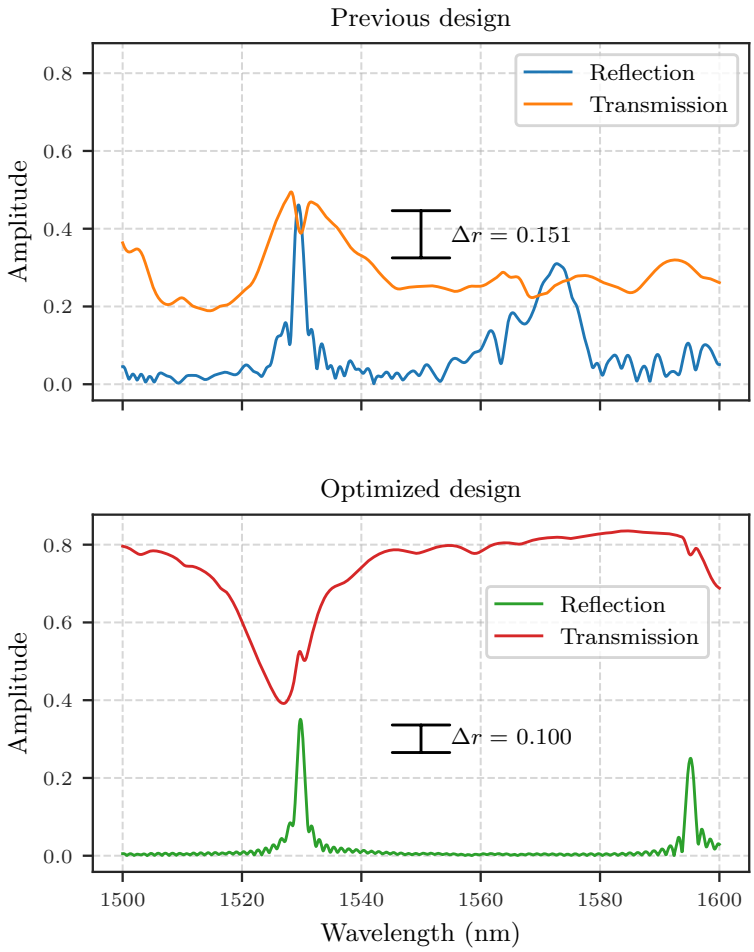

Figure 6.20: SMM simulated grating reflection and transmission spectra: previous design (top), optimized laser design (bottom).

6.5.5 Linewidth optimization

Advanced modulation formats with coherent detection are increasingly seen as an effective method of improving spectral efficiency. Such advanced modulation formats utilise phase-shift keying (PSK), a process whereby the carrier phase is modulated to encode data. As these modulation formats require the recovery of signal phase, certain minimum linewidths are required, with maximum data rates increasing with decreasing linewidth [76]. Table 6.7 shows the required linewidth in order to transmit at 40 Gbit/s for numerous modulation formats [77]. Thus far, lasers arrays have been optimized achieving linewidths compatible with both 8PSK and Star 16QAM formats. For modulation formats such as 16PSK and Square 16QAM, however, substantially lower linewidths are required. The genetic algorithm can be utilised to evaluate the potential of slotted laser designs to reach suitable low linewidths and optimize a laser with this application in mind.

Table 6.7: Linewidth requirements for a range of modulation formats [77].

Modulation format	Minimum linewidth @ 40 Gbit/s
QPSK	10 MHz
8PSK	1.6 MHz
16PSK	240 kHz
Star 16QAM	1.6 MHz
Square 16QAM	120 kHz
Square 64QAM	1.2 kHz

As per the modified Schawlow-Townes equation (Equation 5.31), the laser linewidth can be reduced by increasing the power within the cavity and by reducing waveguide loss α_i. The latter is not possible as the wafer's material properties in this case are constant. In order to increase the power within the cavity, another design parameter is allowed to vary during this optimization, namely the anti-reflective coating on the output facet. Increasing the facet reflectivity will increase the power within the cavity but will also reduce the slope efficiency and SMSR. Again, there is a need to balance various design parameters and performance criteria, which is achieved using the genetic algorithm.

The convergence of the optimization can be seen in Figure 6.21. Solutions with cavity length $< 1000\,\mu m$ are quickly eliminated from the population. Gratings with an etch depth of $\sim 1.2\,\mu m$ are initially seen in the population but after generation 20 are replaced by shallower slot designs. The final design and performance is included in Table C.5; Appendix C.

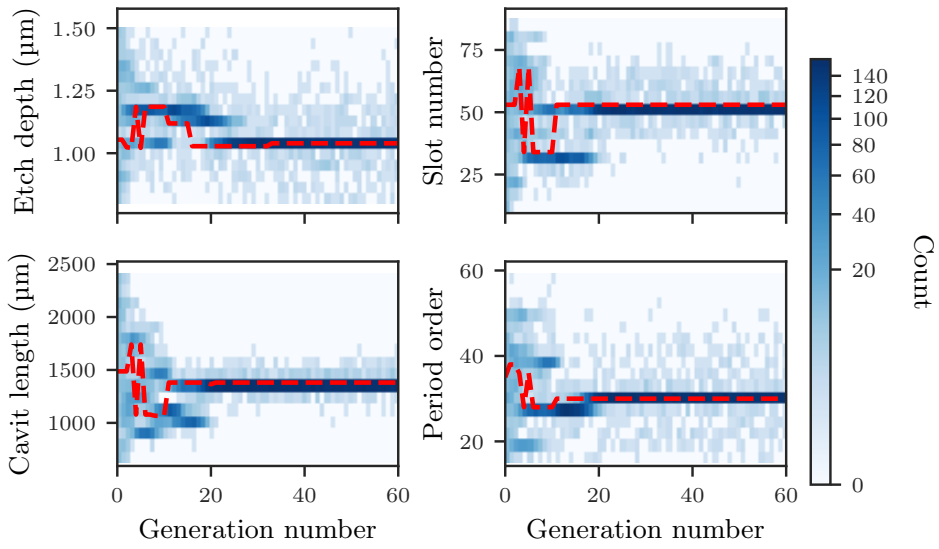

Figure 6.21: Distribution of parameters during optimization of a low linewidth laser. Red line represents parameters of the best individual in a given generation.

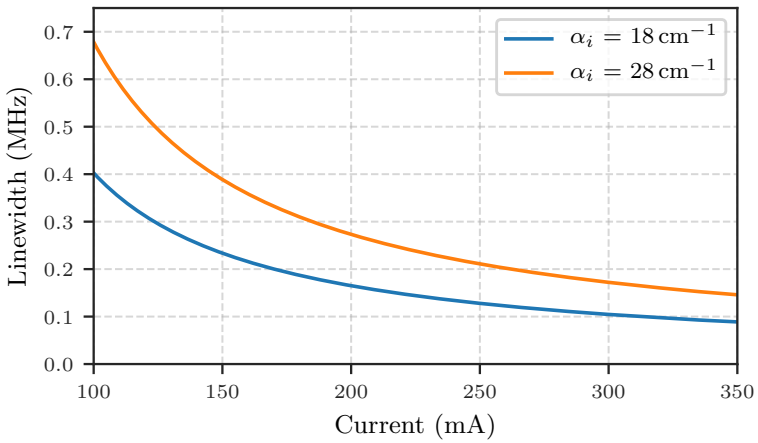

Figure 6.22: Simulated linewidth of the optimized design. A waveguide loss of $28\,\mathrm{cm}^{-1}$ used in the optimization corresponds to the most recent waveguide loss measurement, waveguide loss of $18\,\mathrm{cm}^{-1}$ corresponds to the lowest waveguide loss which has been measured for our devices.

The resulting simulated linewidth (using the method described in section 5.4.1) is seen in Figure 6.22. Simulations with a waveguide loss of $\alpha_i = 18\,\mathrm{cm}^{-1}$ and $\alpha_i = 28\,\mathrm{cm}^{-1}$ have been included, corresponding to the lower and higher ranges of experimentally measured values respectively [23]. For $\alpha_i = 28\,\mathrm{cm}^{-1}$ a linewidth of $\leq 200\,\mathrm{kHz}$ can potentially be achieved at $\sim 265\,\mathrm{mA}$, opening up the potential for

applications in 16PSK modulation systems. For $\alpha_i = 18\,\mathrm{cm}^{-1}$ the simulation suggests that the minimum linewidth for Square 16QAM of $\leq 120\,\mathrm{kHz}$ can be achieved at $\sim 265\,\mathrm{mA}$.

The lasing spectrum of the optimized design is also simulated in Figure 6.23. The increase in facet reflectivity is not seen to significantly impact the lasing spectrum with an SMSR of $\sim 48\,\mathrm{dB}$ being predicted at 260 mA. Although a relatively low power of 5 mW was specified for the design, the final design far exceeds this with a slope efficiency of ~ 0.078 W/A giving an output power of $\sim 16\,\mathrm{mW}$ at 25 °C under 265 mA injection current.

In general, comparing with other laser designs' performance is not straight forward. For instance, a surface etched grating laser designed for low linewidth is presented in Dridi et al. [78]. For a 1500 µm long laser diode, SMSR of $\geq 50\,\mathrm{dB}$, output powers of $\geq 7\,\mathrm{mW}$ and a minimum linewidth of 184 kHz at 300 mA and 25 °C were presented. Our design has comparable theoretical linewidth performance with higher output power and somewhat lower SMSR. However, there are considerations for both designs which help or hinder the ease of fabrication. The main differences are that Dridi et al. [78] use a lower third-order grating etched on the sides of the ridge and in this regard our slotted higher order gratings may be easier to fabricate. However, our design uses HR and AR coatings to improve output power and linewidth, adding another step and cost to the fabrication. Nonetheless, the simple monolithic fabrication, high output power and low linewidth of this design makes it a potentially attractive solution for linewidth sensitive applications.

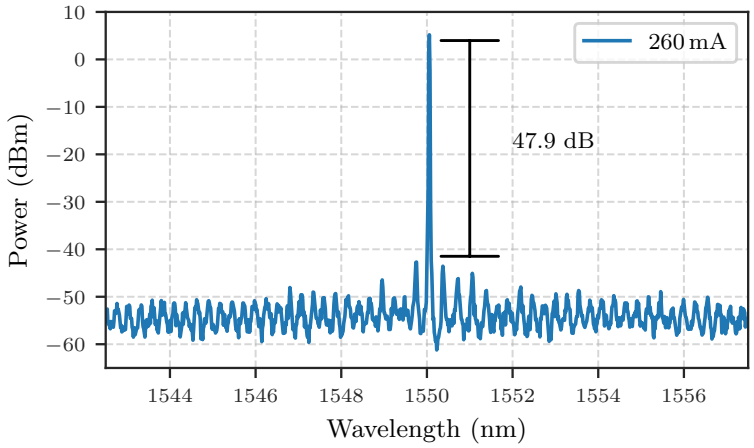

Figure 6.23: Simulated lasing spectrum, biased at 265 mA.

6.5.6 Directly modulated laser optimization

In recent years, data centres and other short-haul applications have experienced a significant increase in traffic. Conventional transceivers have employed electro-absorption modulated lasers (EMLs) to encode data at high bit rates. However, EMLs tend to be a relatively costly solution, with lower output power, more complicated fabrication and a larger spacial footprint. Directly modulated lasers (DMLs), more widely used in the 1.3 µm window, are now being implemented in the 1.55 µm window in order to drive down cost and complexity of transceivers for short haul applications [79, 80]. Recently, systems incorporating such DMLs have demonstrated capabilities of 100 Gb/s transmission using four lasers at 25 Gb/s each [81].

Given the slotted laser's simple monolithic fabrication, investigating the potential use of such lasers for direct modulation applications is of interest. Specifically, the genetic algorithm is used to optimize the performance achievable for use in 4 × 25 Gb/s systems, which can be used to achieve 100 Gb/s Ethernet (100GbE).

In order to optimize for improved direct modulation, a measure of the modulation response is needed, which can guide the genetic algorithm toward an appropriate solution. To this end the modulation response is simulated by modulating each laser in the population at a defined required frequency: set to 30 GHz in this case. Once the modulation response at this frequency is known, the FOM from Equation 6.3 is adjusted as follows:

$$FOM = I_{op} + I_{op}(1 - \eta_T) \cdot w + I_{op}\eta_f \cdot w_f, \tag{6.5}$$

where w_f is a weighting factor, and

$$\eta_f = (E_r + 3)/3, \tag{6.6}$$

for $E_r \leq -3$, where E_r is the simulated modulation response at the defined frequency. This term results in the FOM being proportional to the difference between the simulated modulation response and the −3 dB response. In short, designs which have a modulation bandwidth less than the desired bandwidth have their fitness' negatively weighted.

In order to achieve high direct modulation rates, the relaxation oscillation frequency of the laser needs to be increased. This frequency has the relation

$$f_r \propto \left(\frac{\Gamma dg/dN}{LwN_wL_w}(I - I_{th}) \right)^{1/2}, \tag{6.7}$$

where Γ is the confinement factor dg/dN is the differential gain, L is the cavity length, W is the active region width, N_w is the number of quantum wells, L_w is the well thickness, I is the bias current and I_{th} is the threshold current [82]. Again, material properties are not altered in the optimization process as the lasers are to be fabricated using the IQE wafer previously introduced. A number of properties already make this wafer ideal for direct modulation. Specifically the high differential gain, $dg/dN \sim 1.0 \times 10^{-15}\,\mathrm{cm}^{-3}$ and narrow well thickness $L_w = 0.03\,\mu\mathrm{m}$ results in a relatively high frequency response, per Equation 6.7.

The result of the optimization can be seen in Figure 6.24. Contrasting to all the previous genetic algorithm optimized designs, in this case shallower etched gratings are not seen to propagate within the population. In order to improve the modulation response, shorter length cavities are favoured in line with Equation 6.7. As a result the grating must also be designed shorter, the number of slots decreasing in order to do so. As such, the reflectivity for each slot needs to be larger and hence deeper etch depth are favoured. The total cavity length is optimized as 273 µm with the grating consisting of 18 slots with a length of 162 µm and an etch depth of 1.4 µm.

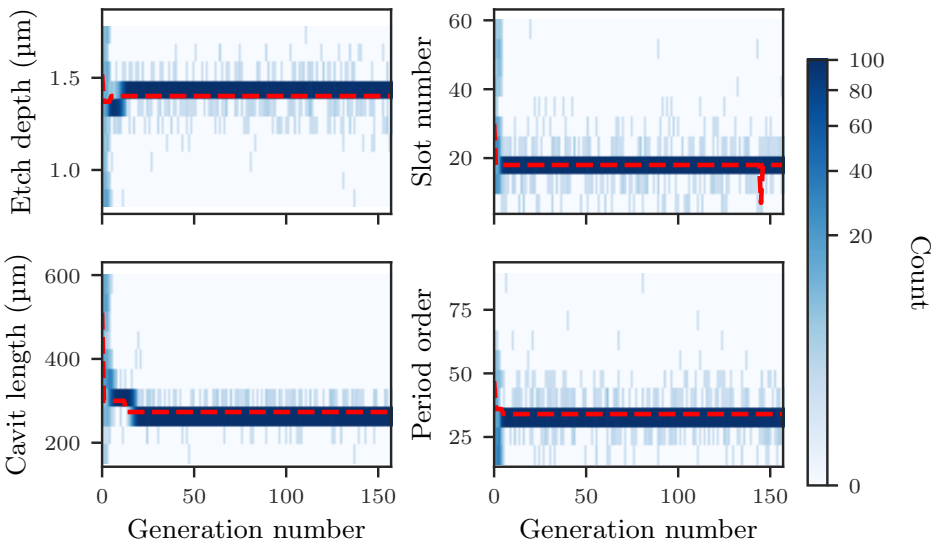

Figure 6.24: Distribution of parameters during optimization of a directly modulated laser. Red line represents parameters of the best individual for a given generation.

The simulated modulation response versus frequency is shown in Figure 6.25. The defined goal modulation bandwidth of 30 GHz is reached at a bias of 87.5 mA. The performance of the optimized laser is evaluated by simulating the eye pattern at a symbol rate of 28 GBd, slightly higher than 25 GBd in order to accommodated forward

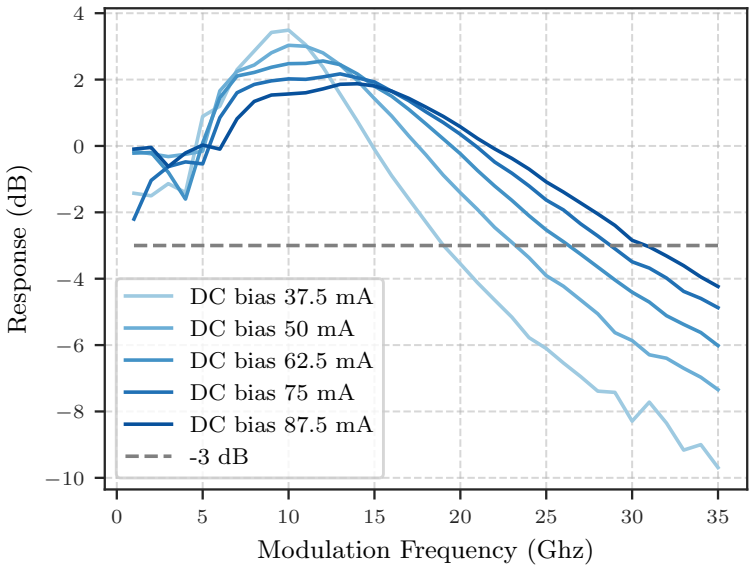

Figure 6.25: Simulated modulation response of the optimized DML.

error correction overhead. In order to maximize the eye-opening, only the gain section is modulated and the grating section is left unbiased. In practice, the grating may be biased at transparency to increase the output power. The eye patterns are generated by modulating the laser with a pseudo random binary sequence and accumulating the signal over 1000 waveforms. Figure 6.26 shows the resulting eye pattern for a range of bias currents. The simulation suggests that the optimized slotted DML can potentially achieve good eye-opening at a bias current of 80 mA, similar to performance reported for slotted DMLs in the 1.3 µm window [18].

The optimized DML also is also capable of operating at high active region temperatures[1] as shown in Figure 6.27, albeit with an increased bias current required in order to maintain an open eye pattern. Such performance at high temperatures may enable un-cooled operation in coarse wavelength division systems, a key goal for implementing low energy budget solutions. However, the high injection currents required to maintain an open eye pattern may be an obstacle in this regard.

[1]It should be noted that the temperatures in these simulations do not refer to ambient/heatsink temperatures, but rather the waveguide/active region temperatures. This is because the 3D-thermal distributions were not simulated in this case, to reduce complexity.

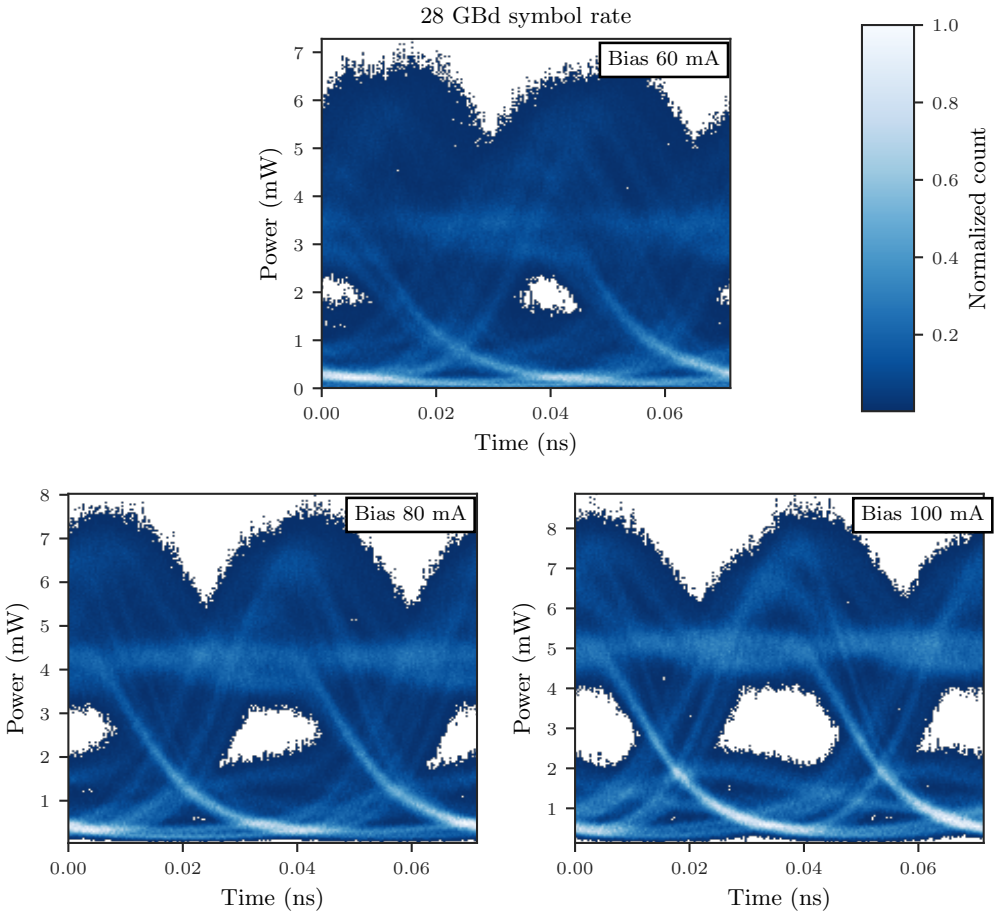

Figure 6.26: Simulated eye diagrams of the optimized DML at 28 GBd symbol rate at a constant active region temperature of 25 °C under varying bias currents.

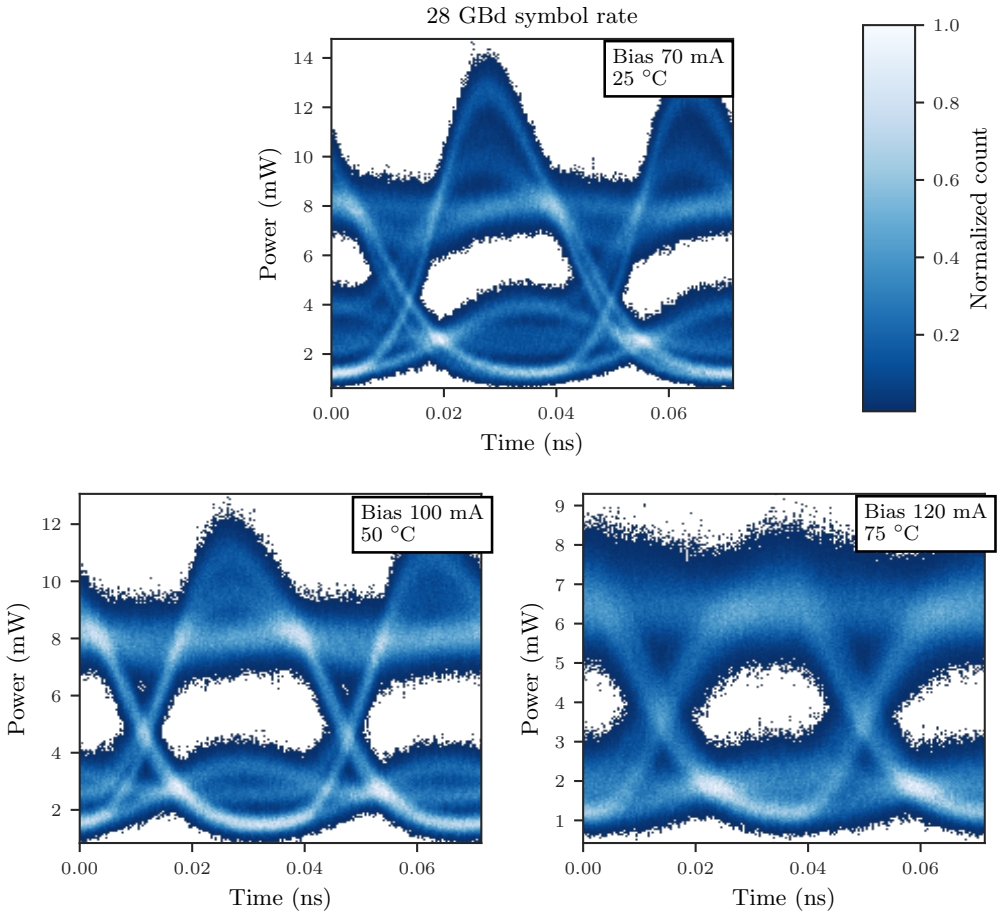

Figure 6.27: Simulated eye diagrams of an optimized DM laser modulated at 28 GBd symbol rate for a range of active region temperatures.

6.6 Conclusion

In this chapter, the challenges inherent in designing and optimizing slotted laser diodes have been examined. In order to overcome these obstacles, a genetic algorithm has been implemented and the optimization problem for slotted lasers formulated accordingly. This results in an optimization where explicit performance requirements are balanced with one another in order to design a laser which achieves said requirements at the lowest possible injection current. This procedure has yielded optimized lasers for a number of specific use cases. A new iteration of laser arrays has been designed to improve upon the previously reported 700 µm and 1000 µm lasers arrays. For such laser arrays, a shallower etch depth of 1.1 µm was found to be optimal for increasing slope efficiency. This shallower etch depth is also predicted to improve tolerance to errors in etch depth. The genetic algorithm was also used to rectify poor wavelength stability of lasers designed towards the blue end of the C-band. Notably, the longer cavity laser arrays of 1000 µm are re-optimized to have significantly improved performance at elevated temperatures and are simulated to maintain single mode performance at heatsink temperatures of up to 55 °C. This is a large improvement over the previous 1000 µm design, which was susceptible to multi mode behaviour at 25 °C.

Furthermore, the feasibility of slotted lasers with more niche performance requirements were investigated. A laser for low linewidth applications was optimized using the genetic algorithm. Simulations suggest that the optimized design is capable of sub 200 kHz linewidth, with an SMSR $\sim$ 48 dB and a slope efficiency of $\sim$ 0.078 W/A. This performance was found to be comparable with similar surface etched grating lasers [78].

Finally, a slotted laser was designed in order to optimize direct modulation performance. This laser is designed with next generation 100 GbE short haul systems in mind with such systems having been previously implemented using x4 25 Gb/s DMLs. The optimized design is simulated to have a clear eye-opening at 28 GBd over a range of temperatures up to 75 °C. Given the simple fabrication of slotted lasers, such a design may be suitable for future 100 GbE solutions where the deployment and running costs are a key factors determining adoption.

Chapter 7

Conclusions and outlook

7.1 Conclusions

This work was undertaken with a number of objectives. Obtaining a detailed understanding of the tuning dynamics as well as the general physical behaviour of multi-section slotted laser diodes was a primary aim. In order to achieve this, the tuning behaviour was first experimentally investigated which revealed a number distinct region where mode-hops were occurring. This experimental characterisation yielded a more rigorous tuning scheme of the various laser sections, replacing the previous ad hoc approach of avoiding mode hops. This tuning method was subsequently adopted to athermalize the laser relative to changing ambient temperatures. This method yielded continuously tuned athermal operation from 8 °C to 47 °C with a wavelength stability of ± 0.04 nm/± 5 GHz and a minimum SMSR of 37.5 dB. Utilizing dis-continuous tuning (mode hops), extended athermal operation was possible from 10 °C up to 85 °C, with a wavelength stability of ± 0.01 nm/± 1.25 GHz and a minimum SMSR of 38 dB. An analytic predictive model for laser tuning was also developed utilizing surface temperature profile data measured via the CCD-TR method. This model predicted tuning maps which matched experimental maps to a high degree of accuracy. The analytic model was also used to ascertain the effect of cleave error on the tuning map, accounting for the variation in tuning maps experimentally observed.

A thermo-optic numerical model was subsequently developed in order to more accurately predict laser performance. This method utilized the time-domain transfer matrix method to simulate the laser performance and a 3-D FEM thermal solver to simulate the on-chip temperature distribution. This multi-physics thermo-optic model was compared with experimental measurements for a range of laser parameters including, slope efficiency, threshold, linewidth and wavelength tuning, agreeing well with experimentally measured devices. Furthermore, laser surface temperature measurements, obtained with the CCD-TR method, were compared with simulated

values and also resulted in close agreement. The model was used to explain the various regions of mode-hopping observed in the experimentally measured tuning maps of single mode lasers.

In addition to single mode lasers, widely tunable slotted Vernier lasers were simulated reproducing experimentally observed tuning maps. The model was used to explain the observed tuning maps, establishing that tuning at low injection currents was due to the free carrier plasma effect, with thermal tuning dominating at higher injection currents. The relatively high tuning currents required for these lasers was attributed to the increase in carrier density which offset the thermal tuning. The model was finally used as a diagnostic tool to investigate Vernier laser linewidth — the close agreement between simulation and experiment suggests that the current Vernier laser design, as opposed to fabrication issues, is limiting linewidth performance and as such a re-examination of the Vernier design is warranted.

The final chapter of this thesis focused on maximizing the performance of single mode slotted laser diodes. To this end, a new optimization procedure was defined building upon the modelling framework outlined in previous chapters to simulate a range laser performance criteria. A genetic algorithm was developed in order to cover the complex optimization space associated with slotted lasers and the optimization problem was formulated accordingly. This method was then applied to a number of designs. The previous iteration of designed laser arrays were re-optimized with an emphasis on improving slope efficiency. This re-optimization yielded laser arrays with significantly improved output power and improved single-mode yield. A particularly important result of the re-optimization is the rectification of issues with single mode stability experienced in previous designs. Lasers which previously failed to maintain the correct wavelength under room temperature conditions (25 °C heatsink temperature) now theoretically are capable of operating at 55 °C heatsink temperature. The laser arrays were also found to have a higher theoretical tolerances to errors in etch depth, potentially improving fabrication yield.

The genetic algorithm was also applied to two additional specific applications: a laser optimized for low linewidth operation and a laser design for direct modulation. The low linewidth design is theoretically capable of achieving linewidth of $\leq$ 120 kHz opening up the potential for advance modulation formats such as 16PSK and 16QAM. A directly modulated laser design also showed good theoretical performance with a -3 dB bandwidth of 30 GHz at 87 mA and opening in simulated eye-patterns at $\sim$ 60 mA injection current. Importantly all designs were limited to a slot width of $\geq$ 1.0 µm enabling simple fabrication potentially using photo-lithography.

7.2 Future work

7.2.1 Athermal and laser tuning

The research presented has developed a good understanding of the tuning dynamics in slotted single mode lasers and applied this understanding in some proof of concept tuning schemes. The next step in this regard is to test the tuning schemes in a packaged device. Ultimately, a full data transmission test should be carried out to determine the reliability of the improved tuning paths and the athermal stabilization. Over longer time scales, the effect of device *burn in* on the wavelength map may be an issue. If the tuning pattern changes significantly over time, the chosen path may no longer be ideal and as such, this also is worth investigating.

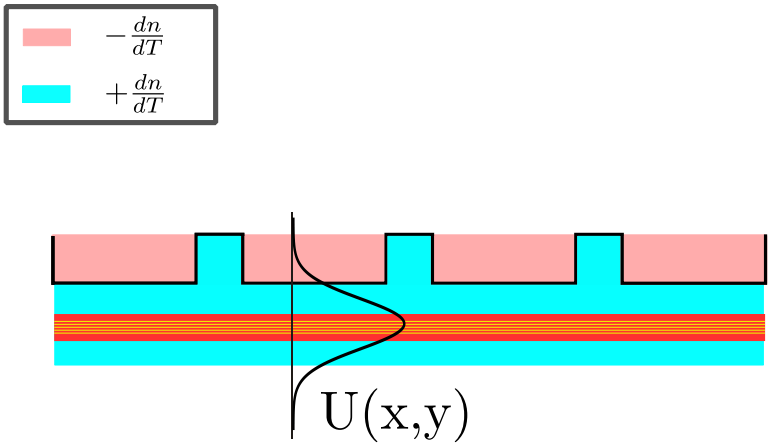

Figure 7.1: Potential athermal grating design.

Another route which athermal research may take is the application of material based athermalization. Bovington, Srinivasan, and Bowers [39] have proposed a laser inherently athermal by design. This is possible by incorporating a material with a negative thermo-optic coefficient, dn/dT, to offset the positive coefficient associated with the laser material. Such a material may be polymer based or, for more compatibility with CMOS processes, TiO_2 is also potential candidate [39]. The scattering matrix method can be used to simulate potential structures with reduced or fully negated thermally induced wavelength shift. Depending on the outcome of such simulations, devices incorporating negative thermo-optic coefficient materials may be fabricated and experimentally investigated. Such designs could also potentially leverage the slotted laser design by filling the slots with negative thermo-optic materials as envisioned in Figure 7.1. The pink shaded region represents a wide-etched slot, which can be filled with a negative thermo-optic coefficient material, thus counteracting the positive thermo-optic coefficient of the InP. Depending on the material used, the ratio between

slot width and spacing will need to be carefully chosen in order to balance positive and negative dn/dT. As only certain slot widths and spacings produce good reflection spectra, this may also be applicable to the genetic algorithm, albeit with a some re-formulation required as the problem is somewhat different to that of optimizing a single mode laser.

7.2.2 Laser modelling

The thermo-optic model presented in this work was compared thoroughly against static laser parameters. However, experimental data on transient laser behaviour was not available for comparison. It would be instructive to experimentally measure transient effects such as laser turn on delay, modulation response and wavelength switching, in order the further verify the model. In terms of thermal transient behaviour the model currently only considers the thermal steady state. The model can be further developed relatively simply by including the time dependent terms in the heat equation (Equation 5.32)

$$\frac{\partial T(x,y,z,t)}{\partial t}. \tag{7.1}$$

Such numerical modelling may be applied to the issue of thermally induced transient wavelength drift in burst mode operation in time-wavelength division PON systems.

7.2.3 Optimization

This research has focused to a large extent on the numerical simulation of slotted lasers. As such, the next phase of the research is recommended to focus more on experimental investigation and applying some of the results in this thesis. The most obvious course of action is to fabricate the designs optimized via the genetic algorithm. The laser arrays have specifically been designed with a single etch depth in mind for the slots such that these arrays can both be easily fabricated in a single run. These devices can then be compared with predicted performance and the previous design's performance in order to evaluate the success of the optimization process. Furthermore, the low linewidth design and directly modulated design are worth investigation experimentally, though extra fabrication steps may be involved due to the differential slot depths.

Future work involving the Vernier lasers should focus on further optimization. The design of the laser should be altered to enhance the linewidth. Naively, this can be achieved by simply lengthening the laser cavity. For instance, a Vernier design with a larger gain section length of 1000 µm (double the previous length) is predicted to have

linewidth on the order of 1 MHz as shown in the simulation in Figure 7.2. However, a natural extension of this work would be to apply the genetic algorithm in order to optimize the Vernier lasers.

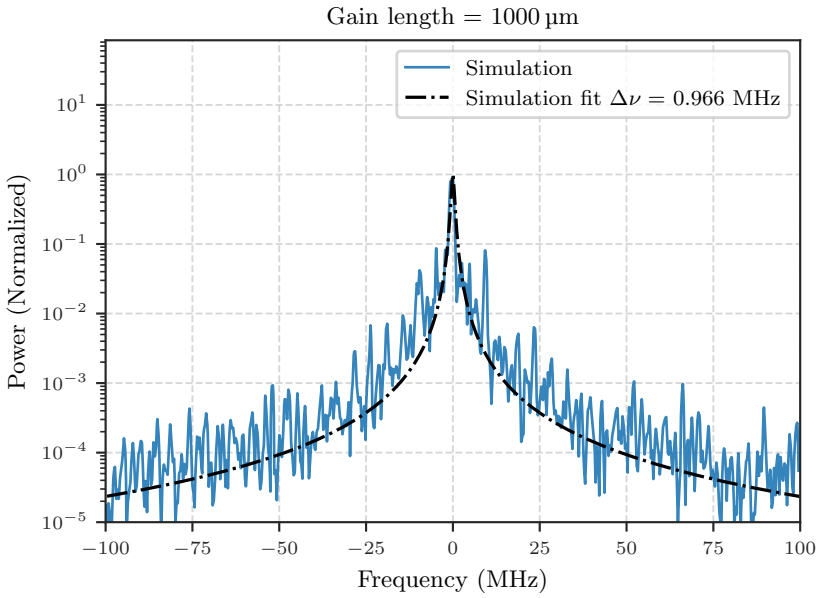

Figure 7.2: Simulated linewidth of a Vernier laser with a gain section length of 1000 µm.

One limiting aspect of the present Vernier design was the use of direct current injection for tuning. Simulations in this thesis have revealed that the direct injection of current into the mirror section has the un-desired effect of increasing the carrier density. This carrier density increase counteracts the thermal tuning and as such, a rather large injection current is needed for the thermal tuning to take effect. The large injection current within the grating sections results in increased spontaneous emission as well as longitudinal gradients in refractive index, both of which effect the SMSR and linewidth negatively.

To overcome this, the potential use of thin-film micro-heaters in place of direct current injection was introduced in chapter 5. The use of micro-heaters avoids the counteractive tuning induced by carrier injection and hence avoids the high injection currents required for the Vernier lasers. This would avoid large carrier densities (and hence increased spontaneous emission) within the mirror sections potentially lowering the SMSR and linewidth. Simulations have shown good tuning behaviour is attainable with such micro-heaters. This approach has been demonstrated in conventional SG-DBRs using platinum thin film heaters, achieving sub 500 kHz linewidth [83] and as such, should be applicable to the slotted Vernier lasers.

Future research may focus on building upon these simulations to further investigate the use of micro-heaters. Specifically the potential efficiency of such tuning versus the present direct injection approach should be studied. In addition, the differences in laser performance between the two tuning approaches should be investigated. Also, the exact design of such micro-heaters should be optimized. Such devices can then be fabricated and their performance compared with the direct current injection approach. In order to further increase the tuning efficiency, novel designs may be implemented to increase the thermal resistance in the mirror sections. These could, for instance, include air gap structures which have been previously used to such an effect [84]. The thermo-optic model can readily be used to design such lasers.

Appendix A

IIR filter

A.1 Introduction

The two main types of digital filters used is digital signal processing are finite impulse response (FIR) filters and infinite impulse response (IIR) filters. FIR filters do not have any feedback and as such are finite in nature. IIR filters on the other hand are recursive and therefore infinite in their response i.e. an IIR filter applied to and impulse 1 will return an infinite number of non-zero values. In the TD-TMM we utilized a simple first order IIR filter to approximate the shape of the gain curve.

A.2 IIR filter

The magnitude response of the IIR filter — applied to approximate the gain dispersion in chapter 5 — was given as

$$|\mathcal{H}(\omega)|^2 = \frac{(1-\eta)^2}{1+\eta^2-2\eta\cos[(\omega+\delta_g dt)]}. \tag{A.1}$$

As our IIR filter in this case is a relatively simple first order filter the difference equation is $y[n] = ay[n-1] + bx[n]$, where we have used the coefficients

$$\begin{aligned} a &= \eta e^{i(\delta_g)dt}, \\ b &= 1-\eta, \end{aligned} \tag{A.2}$$

where η determines the bandwidth of the response. In order to prove that these coefficients yield the correct response as per Equation A.1 we take the z-transform of the difference equation

$$Y(z) = az^{-1}Y(z) + bX(z), \tag{A.3}$$

or

$$Y(1 - az^{-1}) = bX(z). \tag{A.4}$$

From this, the system function can be given as

$$H(z) = \frac{Y(z)}{X(z)} = \frac{b}{1 - az^{-1}}. \tag{A.5}$$

The relation between magnitude response and system function is

$$\mathcal{H}(\omega) = H(z)\Big|_{z=e^{i\omega}} = H(e^{j\omega}), \tag{A.6}$$

$$\mathcal{H}(\omega) = H(e^{i\omega}) = \frac{b}{1 - ae^{-i\omega}}, \tag{A.7}$$

$$|\mathcal{H}(\omega)| = \frac{b}{\sqrt{(1 - ae^{-i\omega})(1 - ae^{i\omega})}}, \tag{A.8}$$

and inserting the coefficients from Equation A.2 gives

$$\begin{aligned} |\mathcal{H}(\omega)| &= \frac{1 - \eta}{\sqrt{(1 - \eta e^{-i\delta_g dt} e^{-i\omega})(1 - \eta e^{i\delta_g dt} e^{i\omega})}}, \\ &= \frac{(1 - \eta)}{\sqrt{1 + \eta^2 - 2\eta \cos[(\omega + \delta_g dt)]}}, \end{aligned} \tag{A.9}$$

which results in the original magnitude response

$$|\mathcal{H}(\omega)|^2 = \frac{(1 - \eta)^2}{1 + \eta^2 - 2\eta \cos[(\omega + \delta_g dt)]}. \tag{A.10}$$

As such, the coefficients from Equation A.2 produce the correct response, as per Equation A.1.

Appendix B

Stabilization algorithm

One challenge in taking high magnification thermal images with the CCD-TR technique arises from vibrations from the sample. As the CCD-TR technique functions by measuring the change in reflectivity and inferring from that a temperature change, any movement of the sample will be measured as a change in temperature, particularly at feature boundaries, i.e. the laser ridge. In order to reduce this effect we implement an image stabilization algorithm. To this end we use the OpenCV library implementation of the Lucas Kande method for estimating optical flow [85]. The optical flow associated with a video feed is the apparent motion of objects in between the consecutive frames. By measuring the optical flow of objects within the image, we can average their motion and thus correct for any movement.

A flow chart of the algorithm can be seen in Figure B.1. We start the algorithm with a reference frame from which relative movement will be measured. A number of parameters associated with detecting objects within the frame are selected, including: number of objects, threshold for detection, minimum distance between objects. Within this frame a number of features are detected using the "good features to track" algorithm [86]. Once these features are selected, a new frame can be captured: the motion of this frame can be estimated based on the movement of the selected features relative to the original frame. The motion of each feature is calculated using the Lucas Kande method [87] from which an average motion of the frame can be estimated. This procedure now allows us to stabilize the frame by truncating the border of the frame and moving a sub frame in the opposite direction of the calculated average frame shift. However, the range we can shift our frame is limited by the resolution, i.e. one pixel is the smallest distance we can shift our frame. This limitation will result in discontinuous behaviour, for instance, if the calculated flow in the x direction is 0.6 pixels, and the algorithm then shifts the frame by 1 pixel, a discontinuity will be measured resulting in a false temperature measurement. In order to overcome this limitation we first take a 2-D cubic interpolation of the image to a higher resolution, which we

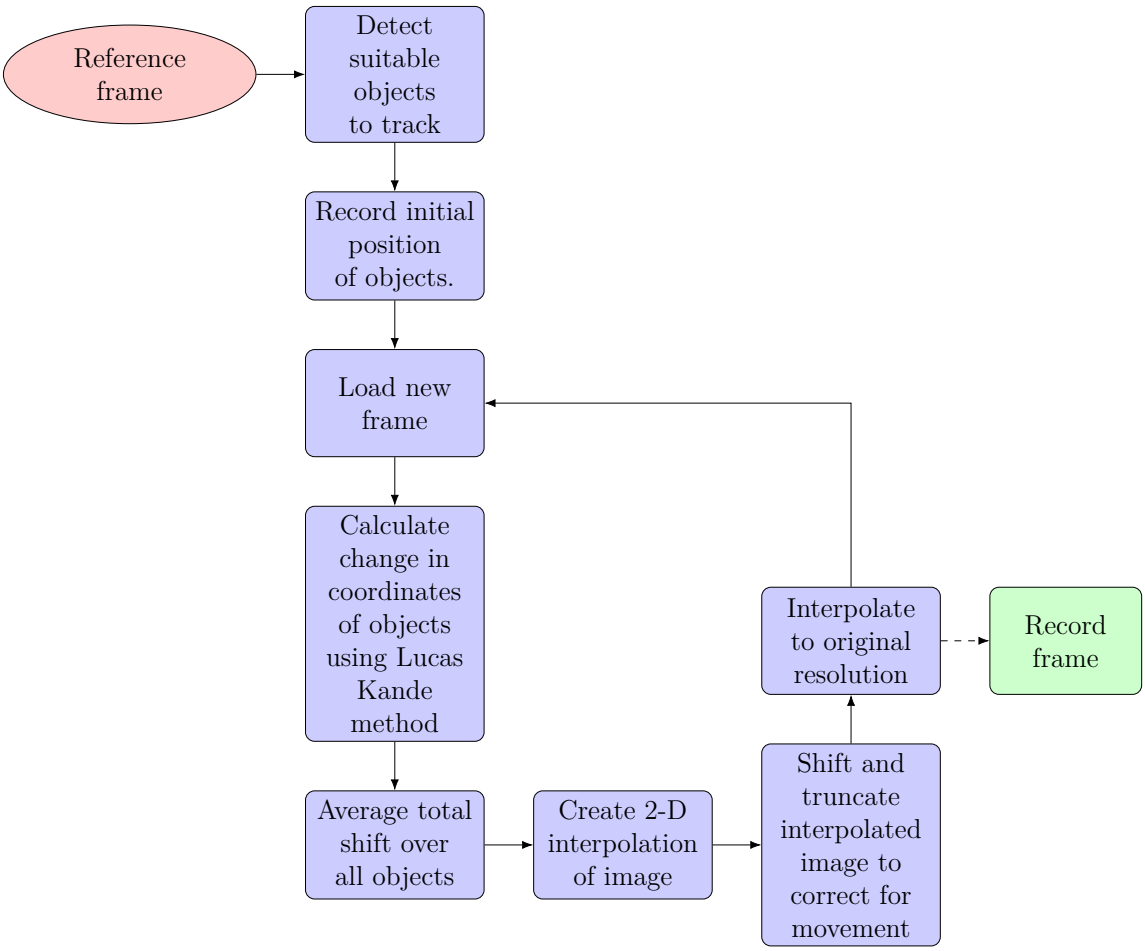

Figure B.1: Stabilization algorithm.

can then shift by sub pixel values. Once corrected, the image is *de-interpolate* to the original resolution and the frame is saved to memory. The process is relatively computationally intensive and although at lower frame rates we can run it in real time, for use in the CCD-TR a number of frames are first loaded into a buffer, over which the stabilization algorithm is run before the measurement continues.

The results of applying this algorithm can be seen in Figure B.2b compared to the un-stabilized case in Figure B.2a.

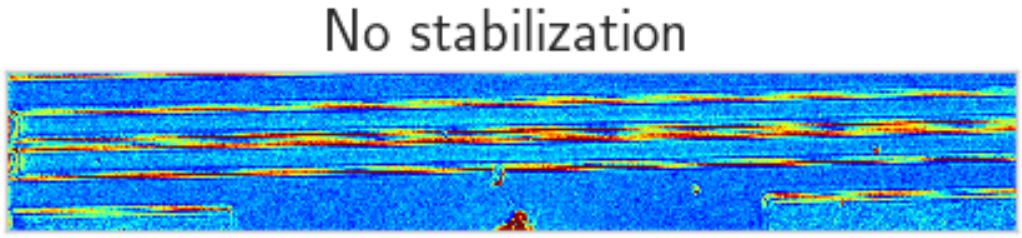

(a) Original CCD-TR measurement with no stabilization (1000 frames)

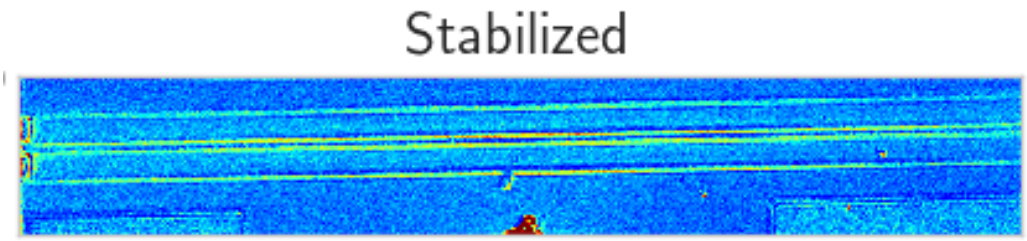

(b) Stabilized CCD-TR measurement (1000 frames)

Figure B.2: Result of applying the stabilization algorithm. Artefacts near edge features are significantly reduced.

Appendix C

Optimization results

The following tables are the results of the optimization described in chapter 6.

Table C.1: Optimization 1.

Lasing Wavelength nm	1530	1533	1536	1540	1543	1546	1549	1552	1555	1559	1562	1565
Etch depth µm	1.195											
Slot number	31	31	26	26	31	31	31	27	27	32	31	31
Period order	28	28	36	36	29	29	29	35	35	28	28	28
Period number	2	2	1	1	1	1	1	1	1	1	1	1
Period spacing	1	1	–	–	–	–	–	–	–	–	–	–
Slot order	4.5											
Cavity length µm	700											
Slope efficiency W/A	0.100	0.097	0.116	0.112	0.110	0.114	0.107	0.101	0.104	0.085	0.084	0.081
Threshold mA	28.29	26	23.85	19.98	21.29	24.07	18.03	18.38	23.53	24.45	24.39	25.35
Operating current mA	119	114.5	106.5	103	102.5	101	102	100	107	113	119.5	129

Table C.2: Optimization 2.

Lasing Wavelength nm	1530	1533	1536	1540	1543	1546	1549	1552	1555	1559	1562	1565
Etch depth µm						1.1						
Slot number	45	45	43	43	43	43	33	33	33	33	31	33
Period order	24	24	24	24	24	24	29	29	29	29	29	28
Period number	1	1	1	1	1	1	1	1	1	1	1	1
Period spacing	–	–	–	–	–	4	–	–	–	–	–	–
Slot order						4.5						
Cavity length µm						660						
Slope efficiency W/A	0.107	0.109	0.108	0.111	0.109	0.110	0.133	0.132	0.128	0.126	0.123	0.102
Threshold mA	29.01	27.97	26.81	25.86	24.85	24.72	21.6	22.01	21.68	22.48	23.73	23.58
Operating current mA	156	148.5	142.5	138.5	139.5	138	125	128	133.5	146	153	166

Table C.3: Optimization 3 — Lower single mode yield.

Lasing Wavelength nm	1530	1533	1536	1540	1543	1546	1549	1552	1555	1559	1562	1565
Etch depth µm						1.05						
Slot number	40	38	37	34	28	28	28	27	27	26	25	25
Period order	24	24	24	24	28	26	26	29	29	29	29	29
Period number	1	1	3	3	1	4	4	1	1	1	1	1
Period spacing	–	–	1	1	5	1	1	4	4	–	–	–
Slot order						4.5						
Cavity length µm						710						
Slope efficiency W/A	0.113	0.114	0.125	0.126	0.129	0.132	0.134	0.134	0.129	0.128	0.125	0.120
Threshold mA	28.39	26.64	25.03	24.14	23.1	22.74	24.61	23.42	22.81	24.08	25.07	26.28
Operating current mA	139.5	136.5	128.5	124	122.5	119	119.5	117	119.5	126	134.5	144

Table C.4: Optimization results, 0.5 MHz.

Lasing Wavelength nm	1530	1533	1536	1540	1543	1546	1549	1552	1555	1559	1562	1565
Etch depth µm						1.1						
Slot number	52	47	30	30	30	30	31	29	29	26	26	26
Period order	24	24	26	26	26	26	29	29	29	29	29	29
Period number	1	1	4	5	2	2	1	1	1	1	1	1
Period spacing	–	–	1	1	3	3	–	–	–	–	–	–
Slot order						4.5						
Cavity length µm						995						
Slope efficiency W/A	0.072	0.071	0.085	0.090	0.091	0.092	0.096	0.096	0.095	0.094	0.092	0.087
Threshold mA	40.32	38.31	32.52	30.87	30.21	29.53	28.8	28.06	27.79	27.19	27.28	27.72
Operating current mA	199	179	158.5	147.5	141.5	138.5	135	132.5	133	143	144.5	157.5

Table C.5: Optimization results for low linewidth laser.

Lasing Wavelength nm	1550
Etch depth µm	1.039
Slot number	53
Period order	30
Period number	1
Period spacing	–
Slot order	4.5
Cavity length µm	1381
AR reflectivity	0.169
Slope efficiency W/A	0.079
Threshold mA	35.81
Operating current mA	266.5

Table C.6: Optimization results for a DM laser.

Lasing Wavelength nm	1540
Etch depth µm	1.40
Slot number	18
Period order	34
Period number	2
Period spacing	5
Slot order	4.5
Cavity length µm	273
Slope efficiency W/A	0.191
Threshold mA	22.91

Bibliography

[1] R. N. Hall et al. “Coherent Light Emission From GaAs Junctions”. *Phys. Rev. Lett.* 9 (9 Nov. 1962), pp. 366–368. DOI: 10.1103/PhysRevLett.9.366. URL: http://link.aps.org/doi/10.1103/PhysRevLett.9.366.

[2] Zhores Alferov. “Double heterostructure lasers: early days and future perspectives”. *IEEE Journal of Selected Topics in Quantum Electronics* (2000), pp. 832–840.

[3] K.C. KAO and G.A. Hockham. “Dielectric-fibre surface waveguides for optical frequencies”. *Electrical Engineers, Proceedings of the Institution of* 113.7 (July 1966), pp. 1151–1158. DOI: 10.1049/piee.1966.0189.

[4] Erik Agrell et al. “Roadmap of optical communications”. *Journal of Optics* 18.6 (2016), p. 063002. URL: http://stacks.iop.org/2040-8986/18/i=6/a=063002.

[5] P. J. Winzer. “Spatial Multiplexing in Fiber Optics: The 10X Scaling of Metro/-Core Capacities”. *Bell Labs Technical Journal* 19 (2014), pp. 22–30. DOI: 10.15325/BLTJ.2014.2347431.

[6] M. Fiorani et al. “Energy-Efficient Elastic Optical Interconnect Architecture for Data Centers”. *IEEE Communications Letters* 18.9 (Sept. 2014), pp. 1531–1534. DOI: 10.1109/LCOMM.2014.2339322.

[7] ITU-T. “G.694.1 (02/2012), Spectral grids for WDM applications: DWDM frequency grid”. *Series G.694.1* (2012), pp. 1–16. URL: http://www.itu.int/rec/T-REC-G.694.1-201202-I/en.

[8] K. Kudo et al. “1.55 μm wavelength-selectable microarray DFB-LDs with integrated MMI combiner, SOA, and EA-modulator”. *Optical Fiber Communication Conference. Technical Digest Postconference Edition. Trends in Optics and Photonics Vol.37 (IEEE Cat. No. 00CH37079)*. Vol. 1. Mar. 2000, 190–192 vol.1. DOI: 10.1109/OFC.2000.868411.

[9] Koji Horikawa et al. *Development of ITLA Using a Full-Band Tunable Laser*. Tech. rep. Furukawa, Mar. 2009. URL: http://www.furukawa.co.jp/review/fr035/fr35%5C_01.pdf.

[10] V. Jayaraman, Z. M. Chuang, and L. A. Coldren. "Theory, design, and performance of extended tuning range semiconductor lasers with sampled gratings". *IEEE Journal of Quantum Electronics* 29.6 (June 1993), pp. 1824–1834. DOI: 10.1109/3.234440.

[11] B. Mason et al. "Design of sampled grating DBR lasers with integrated semiconductor optical amplifiers". *IEEE Photonics Technology Letters* 12 (July 2000), pp. 762–764. DOI: 10.1109/68.853492.

[12] Y. A. Akulova et al. "Widely tunable electroabsorption-modulated sampled-grating DBR laser transmitter". *IEEE Journal of Selected Topics in Quantum Electronics* 8.6 (Nov. 2002), pp. 1349–1357. DOI: 10.1109/JSTQE.2002.806677.

[13] Jan-Olof Wesström et al. "State-of-the-art performance of widely tunable modulated grating Y-branch lasers". *Optical Fiber Communication Conference*. Optical Society of America, 2004, TuE2. URL: http://www.osapublishing.org/abstract.cfm?URI=OFC-2004-TuE2.

[14] L. A. Coldren et al. "Tunable semiconductor lasers: a tutorial". *Journal of Lightwave Technology* 22.1 (Jan. 2004), pp. 193–202. DOI: 10.1109/JLT.2003.822207.

[15] A. J. Ward et al. "Widely tunable DS-DBR laser with monolithically integrated SOA: design and performance". *IEEE Journal of Selected Topics in Quantum Electronics* 11.1 (Jan. 2005), pp. 149–156. DOI: 10.1109/JSTQE.2004.841698.

[16] H. Yang et al. "Monolithic Integration of Single Facet Slotted Laser, SOA, and MMI Coupler". *IEEE Photonics Technology Letters* 25.3 (Feb. 2013), pp. 257–260. DOI: 10.1109/LPT.2012.2233197.

[17] K. Shi et al. "Self-coherent optical transmission using a narrow linewidth tunable slotted fabry-perot laser". *2010 Conference on Optical Fiber Communication (OFC/NFOEC), collocated National Fiber Optic Engineers Conference*. Mar. 2010, pp. 1–3. DOI: 10.1364/NFOEC.2010.JWA35.

[18] W. Sun et al. "Design of 1.3- μm High-Performance Directly Modulated Lasers Based on High-Order Slotted Surface Gratings". *IEEE Journal of Quantum Electronics* 53.5 (Oct. 2017), pp. 1–9. DOI: 10.1109/JQE.2017.2730160.

[19] M. Li et al. "A Hybrid Single-Mode Laser Based on Slotted Silicon Waveguides". *IEEE Photonics Technology Letters* 28.9 (May 2016), pp. 967–970. DOI: 10.1109/LPT.2016.2522399.

[20] Azat Abdullayev. "Characterization of single-mode laser and tunable laser array based on etched high order surface gratings". PhD thesis. Trinity College Dublin, 2014. URL: http://www.tara.tcd.ie/handle/2262/77841.

[21] Azat Abdullaev et al. "Improved performance of tunable single-mode laser array based on high-order slotted surface grating". *Optics express* 23.9 (2015), pp. 12072–12078.

[22] Qiaoyin Lu et al. "Single mode lasers based on slots suitable for photonic integration". *Opt. Express* 19.26 (Dec. 2011), B140–B145. DOI: 10.1364/OE.19.00B140.

[23] Marta Nawrocka. "Design and characterization of widely tunable semiconductor lasers based on etched slots". PhD thesis. Trinity College Dublin, 2014. URL: http://www.tara.tcd.ie/handle/2262/80420.

[24] A. R. Adams. "Strained-Layer Quantum-Well Lasers". *IEEE Journal of Selected Topics in Quantum Electronics* 17.5 (Sept. 2011), pp. 1364–1373. DOI: 10.1109/JSTQE.2011.2108995.

[25] L.A. Coldren, S.W. Corzine, and M.L. Mashanovitch. *Diode Lasers and Photonic Integrated Circuits*. Wiley Series in Microwave and Optical Engineering. Wiley, 2011. DOI: 10.1002/9781118148167.

[26] L.D. Westbrook. "Measurements of dg/dN and dn/dN and their dependence on photon energy in λ =1.5μm InGaAsP laser diodes". *Optoelectronics, IEE Proceedings J* 133.2 (Apr. 1986), pp. 135–142. DOI: 10.1049/ip-j:19860022.

[27] C. Henry. "Theory of the linewidth of semiconductor lasers". *IEEE Journal of Quantum Electronics* 18.2 (Feb. 1982), pp. 259–264. DOI: 10.1109/JQE.1982.1071522.

[28] M.C. Amann and J. Buus. *Tunable Laser Diodes*. Artech House optoelectronics library. Artech House, 1998. URL: http://uk.artechhouse.com/Tunable-Laser-Diodes-P459.aspx.

[29] J. P. Weber. "Optimization of the carrier-induced effective index change in InGaAsP waveguides-application to tunable Bragg filters". *IEEE Journal of Quantum Electronics* 30.8 (Aug. 1994), pp. 1801–1816. DOI: 10.1109/3.301645.

[30] J. E. Zucker et al. "Quaternary quantum wells for electro-optic intensity and phase modulation at 1.3 and 1.55 μm". *Applied Physics Letters* 54.1 (1989), pp. 10–12. DOI: 10.1063/1.100821.

[31] Takeshi Kobayashi and Yoshitaka Furukawa. "Temperature Distributions in the GaAs-AlGaAs Double-Heterostructure Laser below and above the Threshold Current". *Japanese Journal of Applied Physics* 14.12 (1975), p. 1981. URL: http://stacks.iop.org/1347-4065/14/i=12/a=1981.

[32] Y. Tohmori et al. "Broad-range wavelength-tunable superstructure grating (SSG) DBR lasers". *IEEE Journal of Quantum Electronics* 29.6 (June 1993), pp. 1817–1823. DOI: 10.1109/3.234439.

[33] J. O. Wesstrom et al. "Design of a widely tunable modulated grating Y-branch laser using the additive Vernier effect for improved super-mode selection". *IEEE 18th International Semiconductor Laser Conference.* 2002, pp. 99–100. DOI: 10.1109/ISLC.2002.1041137.

[34] G. Morthier, B. Moeyersoon, and R. Baets. "A sampled or superstructure grating tunable twin-guide laser for wide tunability with 2 tuning currents". *OFC 2001. Optical Fiber Communication Conference and Exhibit. Technical Digest Postconference Edition (IEEE Cat. 01CH37171).* Vol. 2. Mar. 2001, TuB2–TuB2. DOI: 10.1109/OFC.2001.927293.

[35] Q.Y. Lu et al. "Analysis of Slot Characteristics in Slotted Single-Mode Semiconductor Lasers Using the 2-D Scattering Matrix Method". *Photonics Technology Letters, IEEE* 18.24 (Dec. 2006), pp. 2605–2607. DOI: 10.1109/LPT.2006.887328.

[36] E. Silberstein et al. "Use of grating theories in integrated optics". *Journal of the Optical Society of America A* 18 (Nov. 2001), pp. 2865–2875. DOI: 10.1364/JOSAA.18.002865.

[37] P. Bienstman. "Rigorous and efficient modelling of wavelength scale photonic components". PhD thesis. University of Ghent, Department of Applied Mathematics, Computer Science and Statistics, May 2001. URL: http://photonics.intec.ugent.be/download/phd%5C_104.pdf.

[38] Qiaoyin Lu et al. "Design of Slotted Single-Mode Lasers Suitable for Photonic Integration". *Photonics Technology Letters, IEEE* 22.11 (June 2010), pp. 787–789. DOI: 10.1109/LPT.2010.2045888.

[39] Jock Bovington, Sudharsanan Srinivasan, and John E Bowers. "Athermal laser design". *Optics express* 22.16 (2014), pp. 19357–19364.

[40] A. E. W. Phillips, R. V. Penty, and I. H. White. "Integrated passive wavelength athermalisation for vertical-cavity semiconductor laser diodes". *IEE Proceedings - Optoelectronics* 152.3 (June 2005), pp. 174–180. DOI: 10.1049/ip-opt:20045048.

[41] S. H. Lee et al. "Self-configuring athermal tunable DS-DBR laser for passive optical networks". *Lasers and Electro-Optics (CLEO) and Quantum Electronics and Laser Science Conference (QELS), 2010 Conference on*. May 2010, pp. 1–2. DOI: 10.1364/CLEO.2010.CWN5.

[42] J. Zhu et al. "Athermal Colorless C-Band Optical Transmitter System for Passive Optical Networks". *Journal of Lightwave Technology* 32.22 (Nov. 2014), pp. 4253–4260. DOI: 10.1109/JLT.2014.2354058.

[43] Markus Roppelt et al. "Tuning Methods for Uncooled Low-Cost Tunable Lasers in WDM-PON". *Optical Fiber Communication Conference/National Fiber Optic Engineers Conference 2011*. Optical Society of America, 2011, NTuB1. DOI: 10.1364/NFOEC.2011.NTuB1.

[44] Jock Bovington et al. "Thermal stress implications in athermal TiO2 waveguides on a silicon substrate". *Opt. Express* 22.1 (Jan. 2014), pp. 661–666. DOI: 10.1364/OE.22.000661.

[45] D. Bosc et al. "Temperature and polarisation insensitive Bragg gratings realised on silica waveguide on silicon". *Electronics Letters* 33.2 (Jan. 1997), pp. 134–136. DOI: 10.1049/el:19970091.

[46] I. Mathews et al. "Reducing thermal crosstalk in ten-channel tunable slotted-laser arrays". *Opt. Express* 23.18 (Sept. 2015), pp. 23380–23393. DOI: 10.1364/OE.23.023380.

[47] ITU-T. "40-Gigabit-capable passive optical networks 2 (NG-PON2): Physical media dependent (PMD) layer specification". *ITU-T Recommendation G.989.2* 2 (2014), G.114.

[48] M Farzaneh et al. "CCD-based thermoreflectance microscopy: principles and applications". *Journal of Physics D: Applied Physics* 42.14 (2009), p. 143001. URL: http://stacks.iop.org/0022-3727/42/i=14/a=143001.

[49] G. Tessier et al. "High resolution thermal imaging inside integrated circuits". *Sensor Review* 27.4 (2007), pp. 291–297. DOI: 10.1108/02602280710821425.

[50] R. B. Wilson et al. “Thermoreflectance of metal transducers for optical pump-probe studies of thermal properties”. *Opt. Express* 20.27 (Dec. 2012), pp. 28829–28838. DOI: 10.1364/OE.20.028829.

[51] F. Bello et al. “Traveling Wave Analysis for a High-Order Grating, Partially Slotted Laser”. *IEEE Journal of Quantum Electronics* 51.11 (Nov. 2015), pp. 1–5. DOI: 10.1109/JQE.2015.2485219.

[52] M.G. Davis and R.F. O’Dowd. “A new large-signal dynamic model for multielectrode DFB lasers based on the transfer matrix method”. *Photonics Technology Letters, IEEE* 4.8 (Aug. 1992), pp. 838–840. DOI: 10.1109/68.149880.

[53] X. Han et al. “Thermal analysis of an SOA integrated in SG-DBR laser module”. *2015 International Conference on Numerical Simulation of Optoelectronic Devices (NUSOD)*. Sept. 2015, pp. 107–108. DOI: 10.1109/NUSOD.2015.7292845.

[54] Hosni Saidi et al. “Self-consistent optimization of [111]-AlGaInAs/InP MQWs structures lasing at 1.55 μm by a genetic algorithm”. *Superlattices and Microstructures* 112 (2017), pp. 200–209. DOI: https://doi.org/10.1016/j.spmi.2017.09.020.

[55] Wei Li, Wei-Ping Huang, and Xun Li. “Digital filter approach for Simulation of a complex integrated laser diode based on the traveling-wave model”. *IEEE Journal of Quantum Electronics* 40.5 (May 2004), pp. 473–480. DOI: 10.1109/JQE.2004.826436.

[56] Wei-Hua Guo et al. “Fourier series expansion method for gain measurement from amplified spontaneous emission spectra of Fabry-Perot semiconductor lasers”. *IEEE Journal of Quantum Electronics* 40.2 (Feb. 2004), pp. 123–129. DOI: 10.1109/JQE.2003.821535.

[57] Pearu Peterson. “F2PY: a Tool for Connecting Fortran and Python Programs”. *Int. J. Comput. Sci. Eng.* 4.4 (Nov. 2009), pp. 296–305. DOI: 10.1504/IJCSE.2009.029165.

[58] T. Okoshi, K. Kikuchi, and A. Nakayama. “Novel method for high resolution measurement of laser output spectrum”. *Electronics Letters* 16.16 (July 1980), pp. 630–631. DOI: 10.1049/el:19800437.

[59] X. Han et al. “Thermal analysis of an SOA integrated in SG-DBR laser module”. *2015 International Conference on Numerical Simulation of Optoelectronic Devices (NUSOD)*. Sept. 2015, pp. 107–108. DOI: 10.1109/NUSOD.2015.7292845.

[60] Martin S. Alnæs et al. "The FEniCS Project Version 1.5". *Archive of Numerical Software* 3.100 (2015). DOI: 10.11588/ans.2015.100.20553.

[61] Anders Logg, Kent-Andre Mardal, Garth N. Wells, et al. *Automated Solution of Differential Equations by the Finite Element Method*. Springer, 2012. DOI: 10.1007/978-3-642-23099-8.

[62] Anders Logg and Garth N. Wells. "DOLFIN: Automated Finite Element Computing". *ACM Transactions on Mathematical Software* 37.2 (2010). DOI: 10.1145/1731022.1731030.

[63] Anders Logg, Garth N. Wells, and Johan Hake. "DOLFIN: a C++/Python Finite Element Library". *Automated Solution of Differential Equations by the Finite Element Method, Volume 84 of Lecture Notes in Computational Science and Engineering*. Ed. by Anders Logg, Kent-Andre Mardal, and Garth N. Wells. Springer, 2012. Chap. 10.

[64] Robert C. Kirby and Anders Logg. "A Compiler for Variational Forms". *ACM Transactions on Mathematical Software* 32.3 (2006). DOI: 10.1145/1163641.1163644.

[65] Anders Logg et al. "FFC: the FEniCS Form Compiler". *Automated Solution of Differential Equations by the Finite Element Method, Volume 84 of Lecture Notes in Computational Science and Engineering*. Ed. by Anders Logg, Kent-Andre Mardal, and Garth N. Wells. Springer, 2012. Chap. 11.

[66] Kristian B. Ølgaard and Garth N. Wells. "Optimisations for Quadrature Representations of Finite Element Tensors Through Automated Code Generation". *ACM Transactions on Mathematical Software* 37 (2010). DOI: 10.1145/1644001.1644009.

[67] Martin S. Alnæs et al. "Unified Form Language: A domain-specific language for weak formulations of partial differential equations". *ACM Transactions on Mathematical Software* 40.2 (2014). DOI: 10.1145/2566630.

[68] Martin S. Alnæs. "UFL: a Finite Element Form Language". *Automated Solution of Differential Equations by the Finite Element Method, Volume 84 of Lecture Notes in Computational Science and Engineering*. Ed. by Anders Logg, Kent-Andre Mardal, and Garth N. Wells. Springer, 2012. Chap. 17.

[69] Robert C. Kirby. "Algorithm 839: FIAT, a New Paradigm for Computing Finite Element Basis Functions". *ACM Transactions on Mathematical Software* 30.4 (2004), pp. 502–516. DOI: 10.1145/1039813.1039820.

[70] Robert C. Kirby. "FIAT: Numerical Construction of Finite Element Basis Functions," *Automated Solution of Differential Equations by the Finite Element Method, Volume 84 of Lecture Notes in Computational Science and Engineering*. Ed. by Anders Logg, Kent-Andre Mardal, and Garth N. Wells. Springer, 2012. Chap. 13.

[71] Martin S. Alnæs et al. "Unified Framework for Finite Element Assembly". *International Journal of Computational Science and Engineering* 4.4 (2009), pp. 231–244. DOI: 10.1504/IJCSE.2009.029160.

[72] Martin S. Alnæs, Anders Logg, and Kent-Andre Mardal. "UFC: a Finite Element Code Generation Interface". *Automated Solution of Differential Equations by the Finite Element Method, Volume 84 of Lecture Notes in Computational Science and Engineering*. Ed. by Anders Logg, Kent-Andre Mardal, and Garth N. Wells. Springer, 2012. Chap. 16.

[73] L. Han et al. "DBR Laser With Over 20-nm Wavelength Tuning Range". *IEEE Photonics Technology Letters* 28.9 (May 2016), pp. 943–946. DOI: 10.1109/LPT.2016.2518806.

[74] K. F. Man, K. S. Tang, and S. Kwong. "Genetic algorithms: concepts and applications [in engineering design]". *IEEE Transactions on Industrial Electronics* 43.5 (Oct. 1996), pp. 519–534. DOI: 10.1109/41.538609.

[75] Kalyanmoy Deb. "An introduction to genetic algorithms". *Sadhana* 24.4 (Aug. 1999), pp. 293–315. DOI: 10.1007/BF02823145.

[76] K. Gao et al. "Local oscillator linewidth limitation on 16 QAM coherent optical transmission system". *CLEO/QELS: 2010 Laser Science to Photonic Applications*. May 2010, pp. 1–2. DOI: 10.1364/CLEO.2010.JThE64.

[77] M. Seimetz. "Laser Linewidth Limitations for Optical Systems with High-Order Modulation Employing Feed Forward Digital Carrier Phase Estimation". *OFC/NFOEC 2008 - 2008 Conference on Optical Fiber Communication/National Fiber Optic Engineers Conference*. Feb. 2008, pp. 1–3. DOI: 10.1109/OFC.2008.4528637.

[78] K. Dridi et al. "Narrow Linewidth 1550 nm Corrugated Ridge Waveguide DFB Lasers". *IEEE Photonics Technology Letters* 26.12 (June 2014), pp. 1192–1195. DOI: 10.1109/LPT.2014.2318593.

[79] Sung Hyun Bae, Kim Hoon, and Yun Chur Chung. "Transmission of 51.56-Gb/s OOK Signal over 15 km of SSMF Using Directly-Modulated 1.55-mm DFB Laser". *Optical Fiber Communication Conference*. Optical Society of America, 2016, Tu2J.5. DOI: 10.1364/OFC.2016.Tu2J.5.

[80] A. S. Karar and J. C. Cartledge. "Generation and Detection of a 56 Gb/s Signal Using a DML and Half-Cycle 16-QAM Nyquist-SCM". *IEEE Photonics Technology Letters* 25.8 (Apr. 2013), pp. 757–760. DOI: 10.1109/LPT.2013.2249059.

[81] Z. Zhou et al. "Experimental Demonstration of Symmetric 100-Gb/s DML-Based TWDM-PON System". *IEEE Photonics Technology Letters* 27.5 (Mar. 2015), pp. 470–473. DOI: 10.1109/LPT.2014.2377271.

[82] M. C. Tatham et al. "Resonance frequency, damping, and differential gain in 1.5 mu;m multiple quantum-well lasers". *IEEE Journal of Quantum Electronics* 28.2 (Feb. 1992), pp. 408–414. DOI: 10.1109/3.123267.

[83] H. Ishii et al. "Narrow spectral linewidth under wavelength tuning in thermally tunable super-structure-grating (SSG) DBR lasers". *IEEE Journal of Selected Topics in Quantum Electronics* 1.2 (June 1995), pp. 401–407. DOI: 10.1109/2944.401222.

[84] X. Han et al. "Numerical Analysis on Thermal Tuning Efficiency and Thermal Stress of a Thermally Tunable SG-DBR Laser". *IEEE Photonics Journal* 8.3 (June 2016), pp. 1–12. DOI: 10.1109/JPHOT.2016.2558042.

[85] G. Bradski. "The OpenCV Library". *Dr. Dobb's Journal of Software Tools* (2000).

[86] Jianbo Shi and C. Tomasi. "Good features to track". *1994 Proceedings of IEEE Conference on Computer Vision and Pattern Recognition*. June 1994, pp. 593–600. DOI: 10.1109/CVPR.1994.323794.

[87] G. R. Bradski and J. Davis. "Motion segmentation and pose recognition with motion history gradients". *Proceedings Fifth IEEE Workshop on Applications of Computer Vision*. 2000, pp. 238–244. DOI: 10.1109/WACV.2000.895428.